

UNIVERSITE DE STRASBOURG

THESE DE DOCTORAT

Présentée par :

Benny SIEGERT

Filling of carbon nanotubes for the preparation of nano-energetic formulations

Discipline : Chimie-Physique

Directeur de Thèse : Geneviève POURROY, Directeur de Recherches, CNRS

Unité de Recherche : UMR 7504

Institut de Physique et Chimie des Matériaux de Strasbourg

Jury de thèse :

Thomas M. KLAPÖTKE	Professeur, LMU München	(Rapporteur externe)
Pascale LAUNOIS	Directeur de Recherches, LPS Orsay	(Rapporteur externe)
Cuong PHAM-HUU	Directeur de Recherches, LMSPC Strasbourg	(Examinateur)
Marc COMET	Chercheur, NS3E, Saint-Louis	(Examinateur)
Denis SPITZER	Directeur, NS3E, Saint-Louis	(Examinateur)

The first essential in chemistry is that you should perform practical work and conduct experiments, for he who performs not practical work nor makes experiments will never attain the least degree of mastery.

— Abu Musa Jabir ibn Hayyan (721–815)

Acknowledgements

I have to thank many persons for making this work possible. Many of these could not be mentioned here, but I thank all of them.

First of all, I would like to express my sincere gratitude to my parents for supporting me all my life, and for enabling me to continue my studies until this point. I would also like to thank my girlfriend, Janina Möller, for always being by my side, supporting me and also for helping with the preparation of this manuscript.

Secondly, I acknowledge financial support from the CNRS through a “BDI” scholarship, and I thank Geneviève Pourroy from the IPCMS (Institut de Physique et de Chimie des Matériaux de Strasbourg) for being my advisor during this thesis, for giving insightful ideas, and for extensive corrections to this manuscript. Furthermore, I would like to thank the ISL for receiving me in the framework of the common laboratory NS3E (Nanomatériaux pour les Systèmes Sous Sollicitations Extrêmes), UMR 3208 ISL–CNRS. Everybody from NS3E gave me a warm welcome in their middle, and I feel that we did some excellent work together. In this context, I have to express my very special thanks to Denis Spitzer and Marc Comet, without whom all this work would never have been possible, and who did everything they could to bring this work forward, to give new ideas as well as quick help and insight in case of problems.

Many people from other groups in the ISL also did their share in this work. I have to thank Fabrice Ciszek (PEM) for mechanical sensitivity measurements, Florence Moitrier (ECN) for help with X-ray diffraction, and Yannick Boehrer and Yves Suma (DMI/EM) for their excellent photos and videos of the TRC experiments. The TRC experiments themselves were made possible by Olivier Muller and Jens Kokot (OAL).

A special thanks also goes to Markus Dürrenberger from the ZMB (Zentrum für Mikroskopie) of the University of Basel, who allowed me to use two of their transmission electron microscopes. I feel honored to be allowed to work by myself on these instruments. The people I worked with from the ZMB (Gianni Morson, Ursula Sauder and Vesna Olivieri) were always there to help.

I am also grateful to Cathie Vix-Guterl from the IS2M (Institut de Science des Matériaux de Mulhouse) for allowing me to use some characterization techniques not available at our lab at the time, especially the Raman spectrometer. Thanks also go to Simon Grée for practical support with the Raman measurements and to Dris Ihiawakrim (IPCMS) for doing HRTEM observations on many CNT/metal oxide nanocomposites.

Finally, I would like to thank all the members of the jury, especially the two rapporteurs, for taking the time to read this manuscript, and, I hope, for some interesting discussion about its contents.



Résumé étendu

Les nanotubes de carbone (NTC) suscitent un intérêt sans cesse croissant des chercheurs en science des matériaux depuis presque vingt ans. Comme il s'agit de structures creuses, l'espace intérieur peut être rempli avec un autre matériau, ce qui conduit à des structures « unidimensionnelles » telles que des nanofils. Le matériau à l'intérieur est protégé de son environnement par la paroi carbonée, ce qui peut stabiliser des structures qui n'existeraient pas sous forme libre.

Les thermites sont des matériaux énergétiques composés d'un oxydant, le plus souvent un oxyde métallique, et d'un réducteur, comme l'aluminium ou le phosphore. Les deux composants réagissent dans une réaction d'oxydoréduction fortement exothermique pour former l'oxyde le plus stable. L'utilisation de nanoparticules permet d'accélérer ces réactions par un facteur de 100 ou plus, et de rapprocher les vitesses de combustion de celles d'un explosif en déflagration.¹ Le problème restreignant l'utilisation pratique des nanothermites est leur sensibilité souvent très élevée aux sollicitations de friction ou de décharge électrostatique.

Vu que la sécurité d'utilisation est devenue le principal critère pour le choix de matériaux énergétiques susceptibles d'applications industrielles, la désensibilisation de ces matériaux est primordiale.

Il a été récemment démontré dans notre laboratoire qu'un explosif peut être désensibilisé de façon importante vis-à-vis de sollicitations d'impact et de friction par son incorporation dans une matrice poreuse. De même, il est envisageable d'obtenir des nanothermites moins sensibles en utilisant un oxyde incorporé dans un nanotube de carbone. Le but de ce travail de thèse a donc été de remplir des nanotubes de carbone avec des oxydes métalliques et d'utiliser ces nanocomposites pour l'élaboration de nanothermites à sensibilité réduite.

Ce manuscrit se divise en sept chapitres. Après l'introduction générale (chapitre 1), une bibliographie (« Etat de l'art », chapitre 2) introduira les nanotubes de carbone, les techniques et effets de remplissage et les nanomatériaux énergétiques. Dans la partie expérimentale (chapitre 3), les protocoles expérimentaux de synthèse de nanotubes de carbone

¹Une *déflagration* est un mode de décomposition rapide caractérisé par une onde de choc qui se propage à vitesse subsonique dans le matériau, contrairement à une *détonation*; cf. section 2.7.1, p. 31.

remplis, d'élaboration des nanothermites par mélange physique et de synthèse de nanoparticules de dioxyde de manganèse (MnO_2) seront donnés. Dans un deuxième temps, nous expliquerons les techniques de caractérisation des matériaux et des nanothermites.

Les trois chapitres suivants traiteront des résultats de nos travaux et de leur discussion. Chacun de ces chapitres sera fondé sur les résultats du chapitre précédent : chapitre 4 introduira les quatre types de nanotubes commerciaux utilisés et montrera les traitements d'oxydation, qui permettent d'ouvrir les extrémités des NTC et/ou de fonctionnaliser leurs surfaces avec des groupements chimiques qui favorisent le remplissage. Dans le chapitre 5, nous utiliserons les nanotubes traités dans des réactions d'infiltration afin de remplir leurs cavités avec un oxyde métallique. Le chapitre 6 proposera une application des nanotubes remplis pour la pyrotechnie, à savoir l'élaboration des nanothermites à sensibilité réduite.

Finalement, la conclusion générale (chapitre 7) résume rapidement les résultats des autres chapitres et décrit les perspectives qu'ouvre cette étude. Quant à l'annexe A, il décrit trois logiciels développés dans le cadre de ce travail de thèse et en donne le code source complet. L'annexe B contient des caractérisations supplémentaires sur certains produits.

Etat de l'art

Nous présentons les techniques de synthèse des nanotubes de carbone à haute température (arc électrique, ablation laser) et à basse température (CVD et autres) ainsi que les techniques de dispersion dans les solvants organiques et à l'aide de surfactants en solution aqueuse. Ensuite, des recherches réalisées par d'autres équipes sur l'effet de différents traitements d'oxydation sur les NTC sont présentés, constituant la base de nos investigations dans le chapitre 4. Nous donnons également une vue synoptique sur la littérature scientifique concernant le remplissage des nanotubes de carbone, en montrant les techniques utilisées et les produits encapsulés pour chaque système.² L'agent de remplissage peut être

- soit le produit souhaité,
- soit un précurseur qui est ultérieurement décomposé pour former le produit souhaité après l'avoir infiltré dans les nanotubes.

Plusieurs méthodes pour remplir la cavité des nanotubes de carbone ont été décrites. Pour les nanotubes monoparoi, qui ont des diamètres très petits, la plupart des synthèses décrites ont été réalisées dans des ampoules sous vide. Pour une infiltration en milieu fondu, les nanotubes sont mélangés à l'agent de remplissage souhaité. Le mélange est ensuite chauffé sous vide pendant des durées prolongées (jusqu'à une semaine). La

²Le tableau 2.1 (page 22) donne une vue synoptique sur la littérature sur le remplissage des nanotubes de carbone.

viscosité et la tension de surface, qui doit être inférieure à 200 mN/m, sont les facteurs déterminants pour qu'un liquide entre dans un nanotube par l'effet de nanocapillarité. L'infiltration des tubes peut également être réalisée à partir d'une solution du produit souhaité ; cette méthode a notamment été utilisée pour élaborer des nanotubes multiparois remplis avec différents oxydes métalliques à partir de nitrates ou oxalates métalliques utilisés en tant que précurseurs. Cependant, les rendements obtenus restent relativement faibles pour ces systèmes à cause d'un effet de volume mort important et de problèmes liés à la mouillabilité de la surface des nanotubes.

En fonction du diamètre du nanotube, la structure de la phase confinée peut être modifiée. Il y a, en effet, une compétition entre les interactions des atomes dans le cristal et les interactions avec la paroi carbonée. Avec une taille de cavité décroissante, on passe ainsi de nanoparticules ayant des structures semblables au « bulk » à une phase dite de couche de contact (ou les atomes forment des couches concentriques sur les parois) et finalement à des colonnes ou hélices atomiques.

Dans la partie finale de ce chapitre, nous introduisons un certain nombre de définitions venant de la science des matériaux énergétiques, qui seront utiles lors de la description des expériences avec les nanothermites. Par la suite, l'effet de la nanostructuration des matériaux énergétiques est rapidement résumé. Ainsi, le RDX (cyclotriméthylènetrinitramine, un explosif secondaire)³ se décompose avant d'atteindre son point de fusion s'il est confiné dans une matrice poreuse d'oxyde de chrome(III), et il ne peut détoner si les nanoparticules d'explosif sont réparties de manière discontinue dans la matrice.

La littérature mentionne plusieurs approches pour obtenir des nanothermites à sensibilité réduite. L'enrobage des nanoparticules d'aluminium par un polymère réduit considérablement la sensibilité du mélange à la décharge électrostatique. En revanche, des nanothermites insensibles ont été élaborées par un procédé d'enrobage de l'oxydant par le réducteur (appelé EOR), breveté par l'ISL.

Caractérisation et traitement des nanotubes de carbone

Les nanotubes de carbone utilisés pour les essais de remplissage ont été achetés chez différents fournisseurs commerciaux : des nanotubes monoparoi (SWNT), double paroi (DWNT), multiparoi (MWNT) et des nanofibres creuses (CNF) de type « arête de poisson » commercialisées sous le nom Pyrograf-III. Malgré le traitement de purification auquel sont soumis les SWNT, DWNT et MWNT après leur synthèse, leurs extrémités demeurent généralement fermées. Or, l'accès à l'espace poreux intérieur suppose que ces

³La figure 2.16 (page 33) montre les structures moléculaires des explosifs les plus importants.

dernières soient ouvertes. L'ouverture s'opère par un traitement d'oxydation, fondé sur le fait que les atomes de carbone appartenant aux sites présentant une courbure forte (comme c'est le cas aux extrémités) sont les plus réactifs. Selon la littérature, ce comportement est corrélé à l'état d'hybridation sp^3 partielle desdits atomes. L'étude bibliographique a montré qu'un grand nombre de réactifs oxydants ont été utilisés pour ouvrir des NTC. Cependant, les publications se limitent pour la plupart aux nanotubes SWNT, ce qui fait que les conditions opératoires décrites ne sont pas directement applicables aux autres types de tubes.

Nous avons donc étudié des méthodes d'oxydation et d'ouverture des nanotubes multiparois et de type « arête de poisson ». Outre les observations de microscopie électronique à transmission, dont le traitement des images ne donne jamais une vue statistique sur l'ensemble de l'échantillon, l'adsorption d'azote à 77 K s'est avérée une bonne méthode pour suivre l'ouverture des NTC. Un modèle simple, fondé sur une géométrie cylindrique, a été développé pour corréler la surface BET au pourcentage de nanotubes ouverts.

En ce qui concerne les attaques par des acides oxydants, le mélange sulfonitrique à chaud détruit rapidement la structure des NTC. Par contre, l'acide nitrique seul conduit à des MWNT bien ouverts après 16 heures de traitement à 120°C. Le même traitement a été mis en œuvre pour oxyder la surface des nanotubes de type arête de poisson. Sur ces derniers, l'attaque acide augmente fortement la proportion de mésopores ayant une taille proche de 4 nm, ce qui est dû à une désolidarisation entre la couche extérieure graphitisée et la couche intérieure, qui est composée de coupelles graphitiques superposées donnant la structure « arête de poisson ». Cette composition en deux couches provient du mécanisme de croissance de ces fibres. Il en résulte des propriétés de surface qui sont différentes entre la face intérieure et extérieure des nanofibres : alors que la surface intérieure est formée d'extrémités de structures graphitiques, c'est le système π qui est exposé à l'extérieur de la fibre. En conséquence, l'oxydation à l'acide nitrique fonctionnalise fortement la surface intérieure des fibres mais pas la surface extérieure, ce qui favorise ensuite le remplissage de la cavité par rapport à la « décoration » de l'extérieur lors des infiltrations avec les sels précurseurs.

Une autre méthode classique pour l'oxydation des matériaux carbonés est le traitement thermique sous atmosphère oxydante (air). Après avoir identifié la gamme de température par des mesures à vitesse de chauffe constante, nous avons analysé la cinétique de l'oxydation isotherme des nanotubes MWNT à différentes températures par l'analyse thermogravimétrique entre 350 et 500°C. Il s'agit d'une cinétique de pseudo-premier ordre – car la pression partielle d'oxygène reste constante – qui est caractérisée par une énergie d'activation de 114 kJ/mol. Une bonne sélectivité de l'oxydation est observée

pour des températures inférieures ou égales à 400°C. A 350°C, l'évolution de la masse de l'échantillon correspond à une somme de deux termes exponentiels avec deux constantes de temps différentes (400 min pour $\sim 10\%$ de la masse et 3000 min pour les 90% restants) ; ceci peut être dû à l'existence de sites de réactivité différente aux extrémités et à des défauts structuraux des parois.

Finalement, un traitement d'ouverture plus original a été développé. Il consiste à faire réagir les MWNT avec de la potasse (KOH) fondue à 400°C dans un creuset de nickel. Une fois refroidi, le résidu est lavé à l'eau, les nanotubes sont alors remplis de potasse. Ces derniers sont lavés à l'acide chlorhydrique pour éliminer la totalité de la base ainsi que les particules de catalyseur (impureté), puis séchés. Une partie des groupements oxygénés de surface ainsi formés peut être éliminée par un traitement thermique additionnel à 950°C sous une atmosphère rigoureusement inerte (flux d'argon). Ce traitement donne des nanotubes ouverts et raccourcis avec un bon rendement en carbone.

Remplissage des NTC par des oxydes métalliques

Dans ce chapitre, nous présentons le remplissage des quatre différents types de NTC avec quatre oxydes métalliques :

- l'oxyde de manganèse (MnO_x avec $1,6 < x < 2,0$),
- l'oxyde de chrome(III),
- l'oxyde de vanadium(IV) et (V),
- l'oxyde de cuivre(II).

Les travaux de remplissage ont surtout été axés sur des oxydes pouvant entrer dans la formulation de nanothermites. Les méthodes choisies pour le remplissage des NTC sont toutes fondées sur l'imprégnation par un sel métallique, ce précurseur étant ensuite décomposé thermiquement en oxyde métallique. Trois méthodes ont été mises au point pour remplir les NTC par les sels précurseurs :

- La première consiste à mettre en contact les nanotubes préalablement ouverts avec une solution aqueuse du précurseur, qui est ensuite évaporée lentement.
- La seconde méthode est le mélange du sel précurseur en fusion (s'il peut être fondu sans se décomposer) avec les nanotubes ouverts, suivi d'un lavage avec un alcool.
- La troisième méthode, que nous appellerons « infiltration réactive », consiste à chauffer des nanotubes bruts dans une solution concentrée du précurseur nitrate dans l'acide nitrique. L'excès de solution est alors éliminé par filtration sur une membrane résistant aux acides. Ce procédé permet d'ouvrir les nanotubes et d'en assurer le remplissage en une seule étape ; en effet, dès que la paroi extérieure d'un tube est percée par l'attaque acide, la solution peut diffuser dans le volume poreux qui lui est

offert.

Dans ces trois méthodes, la force motrice est l'effet de nanocapillarité, gouverné à la fois par la tension de surface de la phase liquide, qui doit être inférieure à 200 mN/m, et par la viscosité. Les précurseurs utilisés sont les nitrates métalliques ou un sel d'ammonium :

- le nitrate de manganèse tétrahydraté $\text{Mn}(\text{NO}_3)_2 \cdot 4 \text{H}_2\text{O}$, qui fond à environ 30°C et se décompose à partir de 130°C en un oxyde MnO_y ($y \leq 2$) et en NO_x ;
- le nitrate de chrome nonahydraté $\text{Cr}(\text{NO}_3)_3 \cdot 9 \text{H}_2\text{O}$, qui a un comportement chimique très proche de celui du nitrate de manganèse et fond à 78°C ;
- le nitrate de cuivre hémi(pentahydraté) $\text{Cu}(\text{NO}_3)_2 \cdot 2.5\text{H}_2\text{O}$ – ce sel se décomposant avant la fusion et sa solubilité dans l'acide nitrique étant inférieure à celle des autres nitrates étudiés, nous avons privilégié l'étude de l'infiltration par une solution aqueuse.
- Finalement, nous avons rempli des NTC d'oxyde de vanadium(V), en utilisant le métavanadate d'ammonium NH_4VO_3 comme précurseur. La thermolyse de ce dernier se produit avant sa fusion, ce qui a permis d'exclure l'infiltration en milieu fondu. En outre, NH_4VO_3 présente la particularité de précipiter d'une solution aqueuse lorsque l'on acidifie cette dernière. Pour cette raison, l'acide nitrique ne peut pas être utilisé en tant que solvant pour réaliser une infiltration réactive. La seule voie possible consiste donc à infiltrer les nanotubes par une solution aqueuse.

Le taux maximal que l'on peut obtenir pour des NTC complètement remplis a été déterminé théoriquement par un calcul géométrique simple. Malgré leurs diamètres différents, tous les types de nanotubes de carbone employés – SWNT, DWNT, MWNT et CNF – ont des ratios D/d entre leur diamètre extérieur et leur diamètre intérieur qui sont semblables, ce qui conduit à des taux de remplissage similaires. Compte tenu qu'il existe toujours une distribution de diamètres dans un échantillon donné, nous donnerons une estimation optimiste et une estimation pessimiste, afin de définir la gamme des taux que l'on peut obtenir. Il s'est avéré que le taux de remplissage maximal obtenu pour tous les types de NTC avec de l'oxyde de manganèse ($\rho \approx 5,1$) se situe entre 20 et 60% en masse.

En règle générale, les nanotubes les plus larges se remplissent plus facilement. En conséquence, les meilleurs taux de remplissage ont systématiquement été obtenus avec les nanofibres Pyrograf ($\text{MO}_x@\text{CNF}$). Un nanotube plus large ne conduit pas forcément à des particules d'oxyde métallique de taille plus importante. Ainsi, dans le cas de $\text{MnO}_x@\text{CNF}$, les particules d'oxyde de manganèse sont plus petites (entre 10 et 20 nm) que la cavité du nanotube (environ 40 nm). L'oxyde adhère à la paroi intérieure de la nanofibre, ce qui est attribué au fait que celle-ci est fortement fonctionnalisée avec des groupements oxygénés tels que des acides carboxyliques —COOH. Ces groupements constituent des « points d'ancrage » pour le nitrate utilisé en tant que précurseur – par le biais de la

formation d'un carboxylate métallique – et pour l'oxyde après la calcination. De même, sur les MWNT, nous avons observé une germination préférentielle de particules d'oxyde de manganèse au niveau des extrémités et des défauts, qui constituent les sites les plus richement fonctionnalisés.

Dans le cas de $V_2O_5@CNF$, l'oxyde de vanadium(V) occlus dans la cavité interne de la nanofibre forme une mousse dont les bulles sont probablement constituées par les gaz libérés lors de la décomposition du précurseur. Lorsqu'elles sont observées au microscope électronique en transmission, ces mousses recristallisent sous le faisceau d'électrons, et l'on observe un grossissement des cristaux. Par contre, l'oxyde de cuivre(II) forme des cristaux larges et facetés dans les nanocomposites de type $CuO@CNF$. Ces cristaux occupent toute la largeur de la cavité, avec un diamètre typique de 40 nm. Notons que selon la littérature, l'élaboration de nanotubes remplis à l'oxyde de cuivre par l'infiltration de nitrate de cuivre hémipentahydraté donne un taux de remplissage nul ; les travaux décrits ci-dessus montrent donc un progrès par rapport aux résultats rapportés par la littérature.

Dans l'ensemble des produits, l'existence de nanotubes remplis a été montré par microscopie électronique en transmission (MET). Malheureusement, dans les images enregistrés à faible tension d'accélération (80 kV), les particules de carbone amorphe – « débris » provenant de l'oxydation du carbone – se confondent facilement avec des particules d'oxyde. Pour identifier ces particules, nous avons pris en compte uniquement les images sur lesquelles les particules à l'intérieur des NTC sont observées avec un contraste plus élevé que la paroi carbonée. Dans la plupart des cas, la nature et/ou la phase cristalline de ces particules a été déterminée plus explicitement par des observation à haute résolution (HRTEM), par la mesure de la distance entre les plans de diffraction apparaissant sur les images ou par des spectres de rayons X à dispersion d'énergie (EDS) localisés ; dans ces derniers, chaque élément est identifiable grâce à ses raies d'énergies caractéristiques. La diffraction des rayons X (DRX) ainsi que la microspectrométrie Raman sont également utilisées pour caractériser les oxydes métalliques dans les nanocomposites. Ces techniques apportent notamment des informations sur l'état d'oxydation des atomes métalliques. La plupart des oxydes métalliques dans les nanocomposites sont sous-oxygénés, surtout dans le cas de l'oxyde de manganèse. Les déficits d'oxygène les plus faibles ont été observés dans les nanocomposites à base de CNF, qui sont aussi ceux avec le taux le plus faible d'oxyde exocristallisé, c'est-à-dire à l'extérieur des nanotubes de carbone. Il semblerait donc qu'il existe une corrélation entre le déficit en oxygène et le ratio d'oxyde à l'extérieur et à l'intérieur des tubes : plus ce ratio est petit, plus la stœchiométrie de l'oxyde est proche de sa valeur idéale. Par exemple, dans le composite $MnO_x@DWNT$ ($x \approx 1,6$), la majeure partie de l'oxyde est exocristallisé alors que dans $MnO_x@CNF$ ($x \approx 1,9$), l'oxyde de manganèse est essentiellement dans les nanotubes.

Ce phénomène s'explique par le mécanisme de décomposition des nitrates métalliques *confinés dans le nanotube*. La décomposition d'un nitrate produit des quantités stœchiométriques d'acide nitrique et/ou de NO_x. Ces molécules sont confinées dans la cavité, qui constitue une sorte de nanoréacteur, et la réaction se déroule alors dans des conditions « pseudo-hydrothermales » fortement oxydantes. Le point d'ébullition de l'acide est augmenté sous l'effet de l'accroissement de pression produit *in situ*.

Les produits les plus intéressants, c'est-à-dire ceux pour lesquels avec le taux de remplissage est le plus élevé, ont été sélectionnés pour l'étape suivante : l'élaboration de nanothermites.

Nanothermites à sensibilité réduite contenant des nanotubes de carbone

Ce chapitre est dédié à l'étude de nanothermites, qui sont des mélanges nanostructurés d'un oxydant et d'un réducteur. Les systèmes examinés sont :

- MnO_x/Al,
- VO_y/Al,
- CuO/P.

Deux types de formulations contenant des nanotubes de carbone ont été étudiés : ceux dans lesquels l'oxydant (l'oxyde métallique) est remplacé par des NTC remplis – ce qui constitue l'idée de base de ce travail de thèse – et deux formulations dans lesquelles des nanotubes non remplis ont été mélangés physiquement à des nanoparticules d'oxydant et de réducteur (MWNT/MnO₂/Al et CNF/MnO₂/Al).⁴

L'élaboration se fait par mélange physique du nanocomposite et du réducteur dans un non-solvant, qui peut être le *n*-hexane ou l'acétonitrile. L'utilisation d'acétonitrile a pour effet de rendre le mélange plus homogène, ce qui a été démontré récemment dans la thèse de Nicolas LE HOUX.

Les mélanges sont formulés à partir de nanoparticules d'aluminium Al 50 P (Novacentrix, Austin, TX). Celles-ci possèdent un cœur d'aluminium ayant un diamètre d'environ 50 nm, recouvert d'une couche superficielle d'alumine de 3,4 nm. Les proportions du mélange sont définies à partir de la teneur en oxyde du nanocomposite et de la teneur en aluminium métallique de l'Al 50 P, déterminées à l'aide d'une analyse thermogravimétrique sous atmosphère oxydante. L'aluminium est en excès de 20% par rapport à la réaction (M = métal) :



⁴Le tableau 6.1 (page 130) montre les formulations de nanothermites avec leurs sensibilités.

Pour MnO_2/Al et CuO/P , des compositions dites de référence, qui ont été décrites dans des articles récents publiés par notre laboratoire, sont présentées. Ces matériaux sont très sensibles notamment aux sollicitations de friction et de décharge électrostatique (ESD). Leurs sensibilités sont proches de celles des explosifs primaires. Les mélanges CuO/P figurent même parmi les matériaux les plus sensibles aux décharges électrostatiques décrits dans la littérature.

Lors du test de sensibilité à la friction,⁵ l'échantillon se trouve entre une plaque rugueuse et un bâtonnet en porcelaine. Le fait d'encapsuler l'oxydant dans un nanotube de carbone conduit à une séparation physique des deux phases. Comme il n'y a pas de frottement direct entre les particules d'oxydant et de réducteur, on peut s'attendre à ce que la sensibilité à la friction diminue. Nous trouvons effectivement une *absence de sensibilité à la friction* pour tous les mélanges (seuil de première réaction > 360 N), tandis qu'une nanothermite comparable contenant des nanoparticules de MnO_2 et de l'aluminium y est extrêmement sensible (seuil de réaction < 5 N). Le mélange $\text{CuO}@\text{CNT}/\text{P}$ ne réagit pas aux sollicitations maximales de choc et de friction et possède une insensibilité à la décharge électrostatique *300 fois supérieure* à celle d'un simple mélange CuO/P . Cette désensibilisation est remarquable dans la mesure où de tels niveaux d'insensibilité n'ont jamais été atteints pour ce type de matériaux !

La sensibilité à la décharge électrostatique est également réduite d'au moins un ordre de grandeur. L'explication la plus probable est le fait que les nanotubes de carbone sont des bons conducteurs électriques, ce qui fait que la décharge passe rapidement par ce que l'on appelle des chemins de percolation sans créer de points chauds dans le matériau. La sensibilité au choc des formulations oxydoréductrices avec des NTC est également raisonnable. Certains des produits à base d'oxyde de manganèse sont plus sensibles à l'impact que la formulation MnO_2/Al pur, notamment celles contenant des nanotubes non remplis. Ce phénomène s'explique par une concentration de contrainte à certains points dans l'échantillon, qui crée ainsi un point chaud. Par exemple, la surface de contact entre deux cylindres croisés est quasiment nulle ; si des particules d'oxydant et de réducteur se retrouvent confinées entre deux nanotubes croisés, la force de l'impact se concentre en un seul point, ce qui amorce plus facilement la réaction thermitique dans le matériau.

Afin d'évaluer leurs performances, les formulations ont été comprimées dans une presse hydraulique à trois niveaux de pression (44, 95 et 210 MPa).⁶ Les pastilles ainsi formées (diamètre ≈ 4 mm) sont initiées par un laser CO_2 ($\lambda = 10.6 \mu\text{m}$) focalisé ayant une puissance optique de $P = 7$ W, et la combustion est observée à l'aide d'une caméra ultra-rapide (1000 images par seconde) et d'un oscilloscope, qui enregistre l'énergie délivrée

⁵Le résultat du test est la sollicitation minimale pour une réaction positive en six essais. Plus la valeur est grande, moins l'échantillon est sensible.

⁶Le tableau 6.2 (page 131) donne tous les résultats des compressions et des caractérisations réactives.

par le laser ainsi que la luminosité de la combustion. Cette expérience – appelée *cinématographie à résolution temporelle* (CRT)⁷ – permet de déterminer le délai d’initiation (IDT), l’énergie d’activation E_A et la vitesse de combustion v si celle-ci est régulière. La vitesse est déterminée en analysant les vidéos de la combustion. Dans ces vidéos, la pastille se trouve toujours à la droite, et le laser vient horizontalement de la gauche. Pour analyser ces données plus aisément, deux logiciels ont été développés pendant ce travail de thèse, permettant de mieux suivre le front de combustion $x = f(t)$ et de déterminer des vitesses de combustion instantanées. Pour ceci, une ligne de pixels, correspondant à la hauteur du point focal du laser, est extraite de chaque image de la vidéo, de façon que le résultat soit un diagramme $x-t$. Le front de combustion peut facilement être distingué par la luminosité de la réaction. Cette technique permet de reconnaître un certain nombre de phénomènes pendant la combustion d’une pastille de nanothermite, par exemple la progression parabolique de la combustion, due à une accélération de la combustion, dans le cas des mélanges MnO_2/Al et l’oscillation du front de combustion dans $MnO_x@CNF/Al$ et $V_2O_5@CNF/Al$. Un deuxième logiciel permet une analyse numérique de la progression du front de combustion, par exemple par régression linéaire.

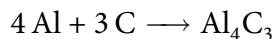
La nanothermite $MnO_x@MWNT/Al$ brûle de façon très irrégulière ; par contre, la combustion du mélange $MnO_x@CNF/Al$ est beaucoup plus régulière, ce qui est dû à la proportion plus importante d’oxyde exocristallisé dans le premier cas. Comparé au mélange de référence MnO_2/Al , le délai d’initiation passe de 3,6 à 11,2 ms, ce qui correspond à une désensibilisation thermique considérable. La vitesse de combustion est également diminuée fortement, elle passe de 730 mm/s à 3,5 mm/s pour une compression à 95 MPa. Ce résultat n’est pas surprenant car le produit contient près de 50% d’espèces pyrotechniquement inactives (nanotubes de carbone et alumine à la surface des nanoparticules d’aluminium). Afin d’augmenter les vitesses de combustion, il faudra donc augmenter le ratio oxyde/carbone. En comparaison, la nanothermite $V_2O_5@CNT/Al$ brûle plus rapidement que le produit à base d’oxyde de manganèse (jusqu’à 12 mm/s) et à une température plus élevée. La combustion de la formulation contenant des nanotubes non remplis, dans laquelle tous les réactifs sont à l’extérieur des nanotubes, est trois à cinq fois plus rapide que celle à base de nanotubes remplis à l’oxyde de manganèse. Ceci montre que malgré l’effet très bénéfique sur les sensibilités de la séparation spatiale de l’oxydant du réducteur, celle-ci rend la réaction d’oxydoréduction considérablement plus difficile.

Quant au $CuO@CNT/P$, la combustion est régulière et peu lumineuse, sans flamme visible. Par contre, cet effet rend la détermination de la vitesse de combustion plus difficile.

Pendant la combustion des nanothermites contenant des nanotubes de type « arête de poisson », le comprimé gonfle le long de l’axe du comprimé ; les résidus ressemblent à

⁷Un schéma de l’expérience est montré dans la figure 3.8, page 57.

des cendres de cigarette. Dans les résidus, on trouve le métal correspondant à l'oxyde (Mn ou V), des oxydes partiellement réduits, de l'alumine ainsi que du carbure d'aluminium, formé d'après la réaction :



Vu que la quantité d'aluminium consommé par cette réaction secondaire n'est plus disponible pour la réaction avec l'oxyde métallique, l'excès de 20% en aluminium, qui est utilisé pour des mélanges nanothermites « classiques », est probablement insuffisant pour des formulations contenant des nanotubes de carbone. L'augmentation de la teneur en aluminium permet notamment de gagner en vitesse de combustion, alors que la durée d'initiation reste à peu près constante.

Les formulations décrites dans ce chapitre ont des vitesses de combustion fortement réduites par rapport aux nanothermites classiques, ce qui n'exclut cependant pas d'utiliser ces matériaux pour des applications spécifiques. Il existe actuellement un besoin industriel de trouver de nouvelles compositions pyrotechniques de retard ; dans un tel contexte, les vitesses de propagation relativement faibles sont idéales. Néanmoins, il faudrait arriver à une plus grande régularité ainsi qu'à des délais d'initiation et des vitesses de combustions plus reproductibles pour ces applications.

Contents

1	Introduction	1
2	State of the art	3
2.1	Carbon nanotubes (CNTs)	3
2.2	Synthesis of CNTs	7
2.2.1	High-temperature methods	7
2.2.2	CVD synthesis	8
2.2.3	Other methods	12
2.2.4	Sorting by chirality	13
2.3	Dispersion/solution	13
2.3.1	Dispersion in organic solvents	14
2.3.2	Surfactant-assisted dispersion	15
2.4	Oxidation treatments	17
2.4.1	Functionalization	20
2.4.2	Defunctionalization	20
2.5	Filling of carbon nanotubes	21
2.5.1	In-situ syntheses	23
2.5.2	Ex-situ syntheses	24
2.5.2.1	Gas phase synthesis: peapods	24
2.5.3	Liquid route: molten salts or metals, solutions	24
2.5.3.1	Filling with halides	25
2.5.3.2	Infiltration with solutions	25
2.5.3.3	Filling with preformed nanoparticles	27
2.6	Effects of confinement and encapsulation	28
2.7	Energetic nanomaterials	31
2.7.1	Introduction to energetic materials	31
2.7.2	Nanostructuration	35
2.7.3	Desensitization of energetic nanomaterials	36
3	Experimental techniques	39
3.1	Filling of carbon nanotubes	39
3.1.1	Reactive infiltration	39

3.1.2	Infiltration of opened nanotubes with aqueous solutions	40
3.1.3	Infiltration of opened nanotubes with melts	40
3.1.4	Infiltration of opened nanotubes with melts, simplified procedure	40
3.2	Preparation of nanothermites by physical mixing	40
3.3	Synthesis of manganese dioxide nanoparticles	41
3.4	Characterization methods	41
3.4.1	Thermal analysis (TG/DTA/DSC)	41
3.4.2	Nitrogen adsorption	45
3.4.3	Raman spectroscopy	50
3.4.4	Zeta potential	53
3.5	Pyrotechnical characterizations	54
3.5.1	Mechanical sensitivity	54
3.5.2	Electrostatic discharge (ESD) sensitivity	55
3.5.3	Time-Resolved Cinematography (TRC)	56
4	Characterization and treatment of carbon nanotubes	61
4.1	Structural characterization of the as-received nanotubes	61
4.1.1	SWNT (BuckyUSA)	61
4.1.2	DWNT (CNT&F21)	63
4.1.3	MWNT (FutureCarbon)	63
4.1.4	Herringbone nanotubes, “CNF” (Pyrograf-III)	65
4.2	Opening the ends of CNTs by oxidation	67
4.2.1	Acid treatments	68
4.2.2	Thermal oxidation in air	70
4.2.2.1	Study of the isothermal oxidation kinetics	70
4.2.2.2	Furnace treatments	75
4.2.2.3	Morphology of air-oxidized MWNT	77
4.2.3	Filling with KOH	79
4.2.4	Aqueous KOH treatment	85
4.3	Conclusion of this chapter	87
5	Filling of carbon nanotubes with metal oxides	89
5.1	Study of the thermal stability of the metal oxide precursors	91
5.1.1	Manganese nitrate tetrahydrate	91
5.1.2	Chromium nitrate nonahydrate	94
5.1.3	Ammonium metavanadate	97
5.1.4	Copper nitrate hemi(pentahydrate)	99
5.2	Filling with manganese oxide	101
5.2.1	Reactive infiltration: comparison of CNT types	101

5.2.2	Infiltration of MWNTs with molten manganese nitrate	113
5.2.3	Infiltration of herringbone CNFs with molten manganese nitrate	114
5.3	Filling MWNTs with chromium(III) oxide by reactive infiltration	116
5.4	Filling with vanadium oxide	118
5.4.1	Filling MWNT with vanadium oxide	118
5.4.2	Filling Pyrograf CNF with vanadium oxide	120
5.5	Filling with copper(II) oxide	125
5.5.1	Filling MWNT with copper oxide	125
5.5.2	Filling CNF with copper oxide	126
5.6	Conclusion of this chapter	127
6	Reduced-sensitivity nanothermites containing carbon nanotubes	129
6.1	Reference systems (without CNTs)	130
6.1.1	MnO ₂ /Al	130
6.1.2	CuO/P	133
6.2	Nanothermites containing manganese oxide-filled CNTs	135
6.2.1	MnO _x @MWNT/Al	135
6.2.2	MnO _x @CNF/Al	141
6.3	MnO ₂ /Al nanothermites physically mixed with CNTs	146
6.4	Nanothermites containing vanadium oxide-filled CNTs	149
6.5	Phosphorus-based nanothermites: CuO@CNF/P	156
6.6	Conclusion of this chapter	159
7	Conclusion	161
7.1	Opening of carbon nanotubes	161
7.2	Filling of carbon nanotubes with metal oxides	162
7.3	Reduced-sensitivity nanothermites containing carbon nanotubes	164
7.4	Perspectives	166
A	Software	169
A.1	An algorithm for calculating atomic positions in carbon nanotubes	169
A.1.1	Implementation in Limbo under Inferno	170
A.1.2	The source code	172
A.1.2.1	vector.m	172
A.1.2.2	vector.b	172
A.1.2.3	nanotube.b	173
A.2	Extracting “timeline” images of nanothermite combustion movies	177
A.2.1	Implementation in Go	178
A.2.2	The source code	178

Contents

A.2.2.1	nt-timeline.go	178
A.2.2.2	w32glob.go	181
A.3	Decoding combustion front images for numerical analysis	182
A.3.1	The source code: nt-decode.go	182
B	Supplementary characterization results	187
B.1	Manganese dioxide nanorods	187

Chapter 1

Introduction

For almost 20 years, carbon nanotubes (CNTs) have been subjected to an ever-increasing interest by scientists in fields such as materials science, chemistry, biology and physics. As carbon nanotubes are hollow structures, their endohedral (inner) space can be filled with other compounds, leading to “one-dimensional” structures like nanorods or even atomic chains. The material inside the CNT is protected from its environment by the carbonaceous wall [1], which can stabilize structures that would not be able to exist in freestanding form. At the same time, the filling material can modify the electronic and transport properties of their nanotube hosts, leading to new physical phenomena.

Thermites (from greek θερμος, “hot”) are energetic materials composed of an oxidizer – in most cases a metal oxide – and a fuel (a reducing agent) like aluminum or phosphorus. The two components react in a redox reaction to form the more stable oxide, with the development of considerable amounts of heat. The reaction can be used to prepare molten metals like iron, which makes them useful for welding. The use of nanoparticles for both oxidizer and fuel allows to accelerate these reactions by a factor of 100 or more and to reach combustion velocities comparable to deflagrating explosives.¹ These systems are called nanothermites, superthermites or Metastable Intermolecular Compounds (MIC) [2, 3]. Today, nanothermites find applications in microthrusters [4], igniters, actuators, lead-free electric primers for ammunition [5], micro- and nanoelectromechanical systems (MEMS/NEMS) and other fields. The reactivity, reaction velocity and temperature can be tuned by choosing an appropriate metal oxide.

The problem that restricts the practical use of nanothermites is their sensitivity to mechanical stress (especially friction) and electrostatic discharges, which is often very high. This means that the thermite reaction may be triggered accidentally, presenting considerable danger. There are international norms [6] defining minimum thresholds for a reaction on mechanical impact, friction stress and electrostatic discharge. *As safety has become one of the main criteria for selecting energetic materials for industrial use, the search for insensitive energetic materials is crucial.*

Recently, it was demonstrated in our laboratory [7] that an explosive can be strongly desensitized to impact and friction stress by incorporating it into a porous matrix. In the same vein,

¹For a detailed explanation of the term, see section 2.7.1, page 31ff.

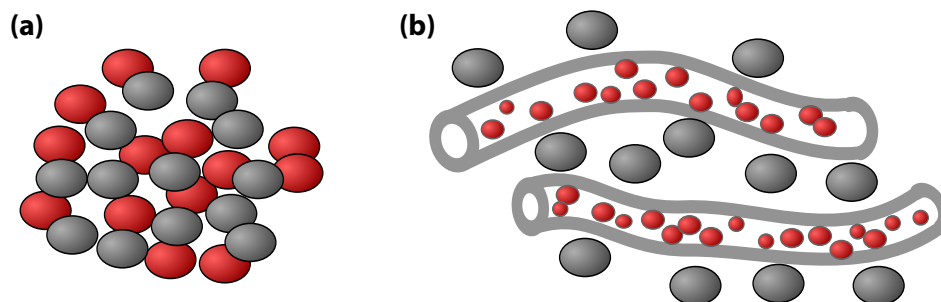


Figure 1.1 Mixture of spherical oxidizer (red) and fuel particles (grey) for a classical nanothermite formulation (a) and use of metal oxide-filled carbon nanotubes as the oxidizer (b).

in this work, we want to obtain less sensitive nanothermite mixtures by using metal oxide-filled carbon nanotubes mixed with aluminum nanoparticles. In such a system, the oxidizer and the fuel are spatially separated (Figure 1.1b), and their contact surface is greatly reduced compared to a simple mixture of particles (Figure 1.1a).

Chapter 2 will present the background of this work, including a bibliographical overview on the fields of carbon nanotubes and energetic nanomaterials.

In chapter 3, we will present the experimental techniques used for the preparation and the characterization of the investigated materials.

Chapter 4 deals with the structural characterization of the as-received carbon nanotubes, which have been bought from commercial suppliers. We will also present the techniques used for treating the CNTs before subjecting them to filling reactions. To understand the oxidation reactions better, we will investigate the isothermal oxidation kinetics of carbon nanotubes.

In chapter 5, we will present the preparation of metal-oxide filled carbon nanotubes, for various oxides and various types of CNTs. Two approaches are used for filling: the infiltration of solutions or melts and a technique which we call “reactive infiltration”, combining opening and filling in a single step. The goal is to achieve the highest possible oxide loading in the composite materials in order to have as little pyrotechnically inert material as possible in the nanothermites later. The products are characterized by a range of different techniques.

In chapter 6, the filled CNTs are used to prepare reduced-sensitivity nanothermite mixtures. Where appropriate, they will be compared to reference systems which do not contain carbon nanotubes. Their sensitivity and reactive behavior will be tested using some programs developed in the framework of this work.

Appendix A presents three software programs that were developed for this work, with their full source code. Appendix B contains additional characterization results.

State of the art

2.1 Carbon nanotubes (CNTs)

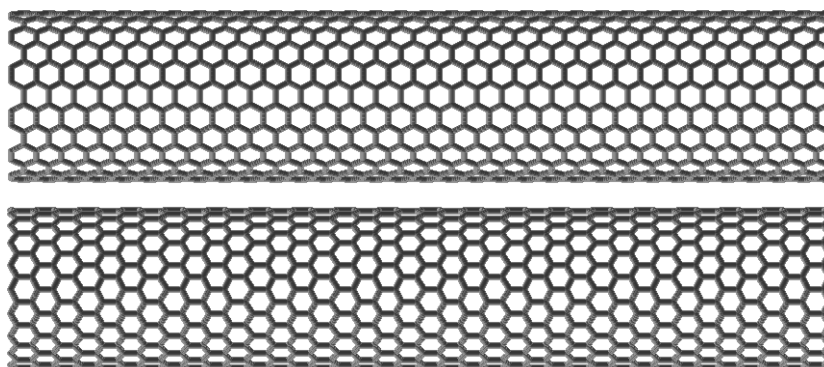


Figure 2.1 Side-on view of an armchair (12,12) nanotube (top) and of a zigzag (20,0) nanotube (bottom). Images generated with RasMol, atomic coordinates calculated with the software in appendix A.1.

Carbon nanotubes (CNTs, Figure 2.1) are hollow, tubular carbon nanostructures composed exclusively of graphitic carbon. The structure can be derived from a graphene sheet by rolling it up and joining it at the seam.¹ Two equivalent points in the graphene lattice are connected by the *roll-up vector* \mathbf{R} , which is mapped to the cylinder circumference when the plane is rolled up to give the nanotube. This vector is expressed as the sum of the two primitive lattice vectors \mathbf{R}_1 and \mathbf{R}_2 (see Figure 2.2) multiplied by two indices (n,m) or (n_1,n_2) .

The roll-up vector is thus

$$\mathbf{R} = n_1\mathbf{R}_1 + n_2\mathbf{R}_2, \quad (2.1)$$

and the tube radius is

$$r = \frac{|\mathbf{R}|}{2\pi}. \quad (2.2)$$

¹Even though this is only a *gedankenexperiment*, the reverse process—i. e. longitudinally cutting carbon nanotubes—is actually being used for synthesizing graphene nanoribbons.

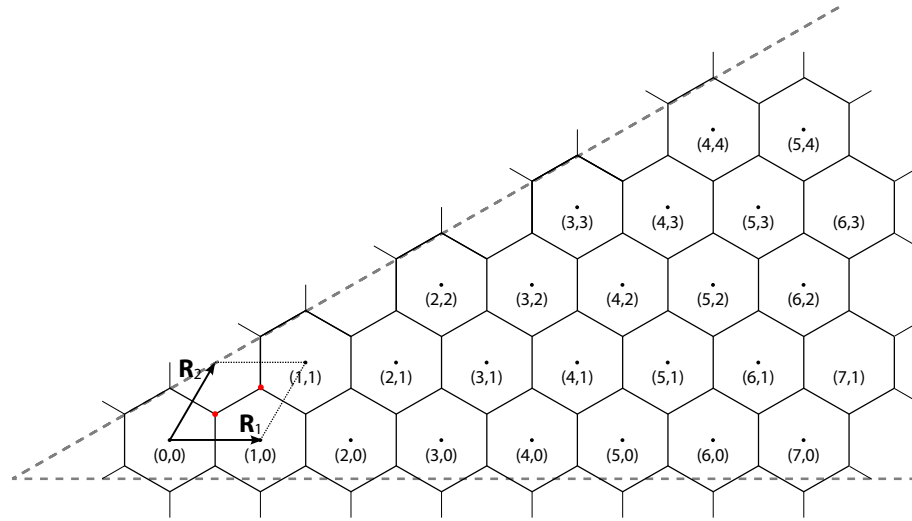


Figure 2.2 Drawing of the “irreducible wedge” in the graphite lattice, containing the definition of the vectors \mathbf{R}_1 and \mathbf{R}_2 . Dotted lines denote the (0,0) unit cell. The two highlighted atoms are the basic motif for the symmetry operations. Drawn after [8].

For symmetry reasons, 1/12 of the possible vectors (the *irreducible wedge*, Figure 2.2) are sufficient to describe every possible carbon nanotube with a right-handed helicity; the constraints on the indices are thus

$$n_1 > 0 \quad (2.3)$$

and

$$0 \leq n_2 \leq n_1. \quad (2.4)$$

The electronic structure of the nanotube is determined by the values of the (n_1, n_2) indices. A CNT is metallic if and only if

$$(n - m) \bmod 3 = 0.$$

If $(n - m) \bmod 3$ is 1 or 2, the CNT is a semiconductor and is said to belong to the “family” 1 or 2, respectively. (n, n) nanotubes are called “armchair” and are always metallic, while $(n, 0)$ nanotubes are called “zigzag”. These names come from the shape of the circumferential edges, as shown in Figure 2.1.

Depending on the number of concentric layers, the names “single-walled”, “double-walled” and “multi-walled carbon nanotube” (more than two layers), or “SWNT”, “DWNT” and “MWNT”, respectively, are used.

Contrary to popular belief, CNTs have not been discovered in 1991 by Iijima *et al.* They had been known for some time before – for instance, Radushkevich and Lukyanovich [9] published TEM images of what we now call multi-walled carbon nanotubes (MWNT) in 1952 – but it was

the Iijima paper, where the author found MWNTs in the residues of fullerene production, that research in this area became active [10].

From an early stage, the question how to fill a nanotube was treated by different groups. In one such experiment, where the carbon electrode for the arc-discharge production process had been doped with cobalt, single-wall carbon nanotubes (SWNT) were obtained for the first time – a more or less accidental discovery!

Double-wall carbon nanotubes (DWNTs) are a relatively recent but very interesting material. They share many of the properties of SWNTs but they are more resistant to drastic treatments, for example with concentrated acids. Their outer wall can be functionalized without affecting the inner tube.

For some years, carbon nanotubes have been the most hyped topic in materials science and research. Even though some of this interest recently shifted to graphene and graphene-based materials, this resulted mostly in a slower *increase* in interest in CNTs.² Real applications exist on the market now, especially for multi-walled carbon nanotubes (MWNT). Bayer (Germany) and Nanocyl (Belgium), to cite just two examples, each produce several hundred tons of MWNT per year. Almost all of this is used by the industry for the preparation of structural materials and polymer composites. For example, most new cars have bumpers made of MWNT-filled polymer, which can be used as an electrode for powder lacquer coatings. In the future, there is potential for even more widespread adoption [11], which will then concern also SWNT-based products. Possible applications for SWNT and their composites include

- ▶ electronics (such as field emission displays or transistors),
- ▶ composite materials, especially with polymers [12, 13],
- ▶ AFM cantilevers [14] and
- ▶ biomedical applications [15].

Recently, the “blackest” material known to date – i. e. with the highest absorption and the lowest reflectivity – has been prepared, based on a low-density aligned array of carbon nanotubes [16]. Such layers are used, for instance at NIST, in a concrete application for thermal detectors which absorb infrared radiation.

Applications in nanoelectromechanical systems (NEMS) are also reported, such as the motion of a cargo (for example a nanoparticle) by using two concentric CNTs, by an AFM cantilever or by Joule heating: if a current is passed through the nanotube “rail”, a temperature gradient causes moving the target [17].

Molecular flow through CNTs has been studied both theoretically [18] and practically [19, 20, 21]; membranes of aligned CNTs can be used for “perfect” filtration and separation of gases and/or

²Cf. Mildred Dresselhaus’s talk at the NT10 conference, Montreal, QC (2010).

liquids. Among the proposed applications of such membranes is water desalination. It was found that the flow does not obey macroscopic capillary dynamics, and that molecules like water can traverse the nanotube two orders of magnitude faster than predicted by Knudsen diffusion [20]. This effect is regarded as a result of the smoothness of the potential energy surface on the interior of the tubes.

Toxicity. The question of CNT toxicity remains an important obstacle to widespread adoption of CNT-based materials and devices today. The public reception of this question must be seen in the context of a larger debate about the use of nanoparticles and nanotechnologies in the daily life.

It has been shown that CNTs generate reactive oxygen species (e. g. superoxide anions, hydroxyl radicals, hydrogen peroxide) in cells, which places considerable stress on them. Additionally, they may induce DNA damage, as shown in embryonic stem cells from mice [22,23]. Thus, nanotubes have to be considered toxic, and appropriate protection—such as respirative masks—has to be applied when handling them.

The consensus of the participants of the NT10 conference was that claims about an asbestos-like toxicity of CNTs are probably exaggerated. It is, however, very difficult to assess this problem in a completely neutral way, as researchers with enough knowledge about CNTs can be said to be biased in favor of this material. Existing research is highly controversial, and contradictory results are reported by different groups. For example, one such study with SWNT in the blood of mice revealed no toxic behavior at all after four months [24]. Indeed, it has been suggested that the differences in results may come from different test methodologies—such as the use of surfactants, which may be toxic themselves, to suspend the nanotubes [23]. Residual catalyst particles in the samples used may be another explanation, since it has been known for a long time that many heavy metal nanoparticles are toxic [25]. It has also been suggested [26] that the cellular uptake of CNTs is governed by physical parameters (especially their length) and essentially independent of functional groups on the surface. The internalization does not involve endocytosis but rather a needle-like penetration after adsorption of the nanotube on the cell membrane; this process is easier for shorter tubes.

Finding a way of reducing the toxicity is all the more important as applications for CNTs in drug delivery are being researched [27]. There are also applications for carbon nanotubes for cancer therapy by hyperthermia. In a recent study using nitrogen-doped MWNT, Torti and coworkers [28] determined whether the nanotubes are pro-coagulant in blood. They obtained the lowest response for non-functionalized CNTs. However, *in vivo* tests show that any coagulation is relatively weak and transient (the maximum being at 3 hours after injection), even at very large doses above the therapeutic ones. Suspensions were made using Pluronic, which is an FDA-approved surfactant. Tests on mice with kidney cancer showed no obvious toxicity of the MWNTs, and after one irradiation treatment of 30 seconds at $\lambda = 1064$ nm, an 80% survival rate was achieved.

2.2 Synthesis of CNTs

Many different methods are used for synthesizing CNTs. Among them are:

- ▶ electric arc discharge
- ▶ laser ablation
- ▶ chemical vapor deposition (CVD)
- ▶ sonification synthesis
- ▶ electrochemical methods
- ▶ sonochemical production
- ▶ low-temperature solid pyrolysis
- ▶ template synthesis
- ▶ carbonization of polymers

Arc discharge and laser ablation are high-temperature methods (1500–3000°C), while the others, of which CVD is by far the most important one, take place at a lower temperature. Most of these processes produce agglomerates of randomly entangled nanotubes with a very low bulk density, which can be around 0.05 g/cm³ or even lower. A review describing SWNT production techniques can be found in Ref. [29].

2.2.1 High-temperature methods

The **arc-discharge process**, which is similar to fullerene synthesis [30,31], was the first method for producing CNTs. Arc-discharge SWNTs are commercialized by CarboLex, a spin-off company of the University of Kentucky, led by Peter Eklund.³ In this process, two graphite electrodes are placed at a distance of a few millimeters in an inert atmosphere, and a high voltage generates an arc discharge. One of the electrodes is consumed and a fluffy deposit is formed. The main impurities in the product are amorphous carbon, fullerenes, residual metal catalyst particles and polyhedral carbon nanoparticles (PCNs) (also called “carbon onions”). Some of the catalyst particles are surrounded by carbon shells after the oxidation, making their removal difficult. Such carbon onions can be more stable towards oxidation than the carbon nanotubes themselves.

In the **laser ablation** process, a high-powered laser acts on a heated carbon target in an inert atmosphere. Some of the carbon is vaporized and transported via a gas stream to a water-cooled

³However, the current faith of the company is unclear since Eklund passed away in the fall of 2009.

deposition area. Doping the target with the right amount of metal catalyst gives good yields of (single-walled) carbon nanotubes.

In these two processes, unlike in the low-temperature ones, multiple SWNTs can grow out of one single catalyst particle with a much larger diameter. The quantity of defects (such as kinks and bends in the structure) in high-temperature methods is generally lower than in CVD syntheses [32] because the conditions provide a kind of *in situ* annealing. The higher thermal activation allows the reconstruction of the lattice to remove defects.

2.2.2 CVD synthesis

Chemical Vapor Deposition (CVD) is the commercially most important method of carbon nanotube synthesis. It can generate large volumes of nanotubes, comparatively cheaply, without the presence of contaminating nanoparticles [33]. The cost benefits mainly come from a much lower growth temperature. CVD reactors can be upscaled very well for production on an industrial scale. Thus, in the last few years, CVD methods have gained in importance over the high-temperature routes, to the point that they are now the most favored process of CNT synthesis.

The CVD synthesis of carbon nanotubes consists in the pyrolytical conversion of a carbonaceous molecule – such as CO or a hydrocarbon like toluene, *n*-hexane, or acetylene – into carbon. The precursor vapor is brought into a hot oven with a carrier gas stream, where it is subsequently decomposed. Contrary to the high-temperature growth methods, catalyst-free nanotube syntheses are not possible under CVD conditions. The catalyst can be used in two forms, either “floating” or in the form of particles on a substrate.

The most important method of preparing catalyst substrates is to sputter or evaporate a thin metal layer (about 0.3–3 nm) on its surface. The reaction itself then consists of two steps, a catalyst pre-treatment step followed by a nanotube growth step [34]. In the first step, the thin film is converted to isolated nanoparticle islands by dewetting of the substrate. The morphology changes are governed by the minimization of the surface and interface energies. Introducing a reactive gas like NH₃ in this phase can be used to control size and shape of the catalyst particles by adsorbate-induced changes in surface energy of certain crystal facets. The active particles are metallic; if the catalyst films are deliberately oxidized before, they show a lower CNT yield upon exposure to acetylene [35]. This technique allows for example the preparation of aligned nanotube forests. Patterned deposition of the catalyst allows nanotubes to be grown selectively [36].

In the “floating catalyst” method, a suitable catalyst precursor molecule is dissolved in the liquid carbon source, and the solution is sprayed into the reactor, or it is evaporated and mixed into the gas stream. Metallocenes are the main catalyst precursor molecules for these syntheses. For example, ferrocene decomposes in the CVD reactor to directly give the iron particles necessary for CNT growth [37].

Today, while many research groups have their own CVD synthesis methods, there are three

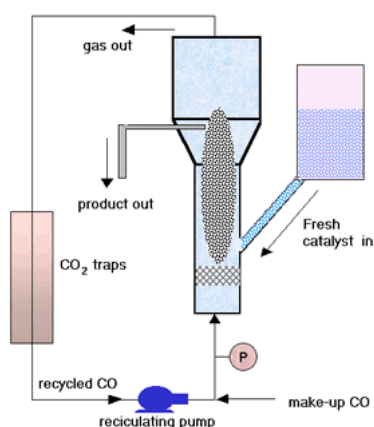


Figure 2.3 Schematic illustration of the CoMoCAT process. From [38].

commercially established CVD synthesis processes for producing high-quality SWNTs:

- ▶ The **HiPCO process** (High Pressure Carbon Monoxide) was developed by the group of R. E. Smalley at Rice University [39,40]. It is a gas-phase method that uses $\text{Fe}(\text{CO})_5$ and CO as the feedstock and a reaction temperature of 800–1200°C. The iron pentacarbonyl dissociates to form iron clusters, and the carbon monoxide undergoes a disproportionation following the reaction

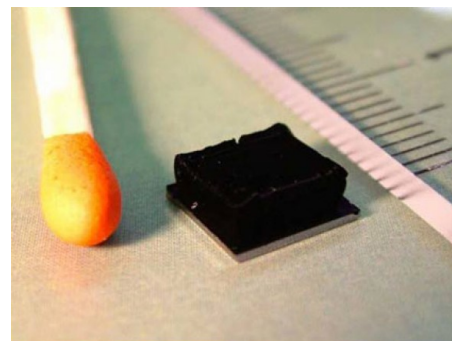


The products are high-quality SWNTs with diameters of 0.7–1.4 nm. They are commercialized by Carbon Nanotechnologies, Inc., which is now a part of Unidym.

- ▶ The **CoMoCAT process** (see Figure 2.3) was developed at Oklahoma University. It is based on the disproportionation of pure CO on cobalt/molybdenum catalyst particles in a vertical fluidized-bed reactor. A high flow rate is selected so that only a small part of the CO reacts and so that the catalyst particles are lifted off the quartz frit by the gas flow. The resulting SWNTs are very small in diameter (0.6–1.1 nm).⁴ CoMoCAT nanotubes are commercialized by South West NanoTechnologies (SWeNT).
- ▶ **Supergrowth** (water-assisted growth) SWNTs [41, 42], are very long, pure SWNT forests grown by ethylene CVD on substrates with such different catalysts as Fe, Al/Fe, $\text{Al}_2\text{O}_3/\text{Co}$ on Si wafers, quartz, or metal foils. A controlled amount of water vapor is introduced into the system and acts as a weak oxidizer. The inventors think that an amorphous carbon coating on the catalyst particles is an important growth termination mechanism. H_2O selectively etches the amorphous carbon and increases catalyst lifetime. Impressive growth rates of up to 2.5 mm total forest height in 10 min have been achieved (Figure 2.4).

⁴The smallest ones of these nanotubes are even smaller in diameter than a C_{60} fullerene, which has a diameter of 0.7 nm.

Figure 2.4 Vertically aligned SWNT forest on a 7×7 mm silicon wafer, product of the Supergrowth process. A height of 2.5 mm was achieved after 10 min of CVD. A match and a ruler have been added as size references. Taken from [42].



Several explanations are proposed for the underlying **growth mechanism**. The formation of carbides in nickel catalyst nanoparticles has been disproven by in-situ selected area electron diffraction during nucleation and growth, where no carbide formation was seen [43]. The other explanation offered is called the bulk-diffusion growth mechanism. It assumes that under the synthesis conditions, the metallic nanoparticles are in a quasi-liquid state. They remain crystalline during the reaction but show fast self-diffusivity like a liquid. Step edges on the nickel surface are stabilized by the graphitic carbon coating, which also facilitates the rapid shape change [34]. The catalytic decomposition of a hydrocarbon gas (acetylene, methane or similar) forms carbon adatoms, which diffuse through the bulk of the particle, driven by the concentration gradient. At the same time, Ni atoms diffuse away from the interface with the graphitic layer, contributing to the elongation of the particle that can be observed during growth (Figure 2.5).

The growth itself takes place in three regimes: Initially, there is an induction period with very slow growth. In this period, a graphene layer is formed from the diffusing carbon adatoms, the driving force being the gain in free energy compared to isolated carbon atoms. This seeding is the slow step from a kinetic point of view. Depending on the diameter of the particle and the conditions, the seed evolves either into a round cap, which will continue to grow into a nanotube, or into a graphitic layer that coats the particle, forming a carbon onion. This effect can be likened to the models for molecular beam epitaxy (the matter flux coming from the segregation of diffusing carbon atoms): carbon onion formation corresponds to a layer-by-layer growth or Frank-van der Merwe process, while the formation of carbon nanotubes corresponds to island formation (Volmer-Weber or Stranski-Krastanov process) [44]. On particles with a diameter of under 6 nm, one SWNT, whose diameter is controlled by the size of the catalyst particle, is formed. The nanotube diameter is comprised between 50 and 100% of the catalyst particle [43, 44].

In the second growth regime, the growth rate and the SWNT length increase. In this phase, carbon atoms migrate on the surface of the catalyst and are incorporated into the base of the SWNT (so-called root growth). In a typical example, up to 250 carbon atoms per second can be incorporated into an SWNT [43].

Finally, a decrease in the growth rate occurs due to catalyst poisoning. This indicates that the

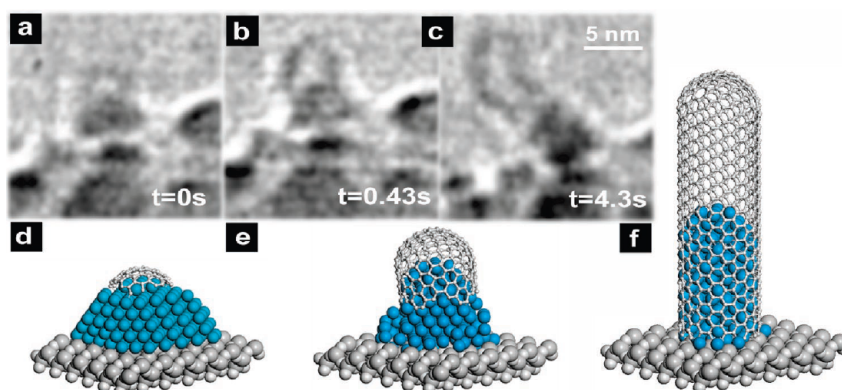


Figure 2.5 ETEM image sequence of Ni-catalyzed CNT root growth recorded in $8 \cdot 10^{-3}$ mbar C_2H_2 at $615^\circ C$ (a–c); schematic ball-and-stick-model of different SWNT growth stages (d–f). Reproduced with permission from [34]. © 2007 American Chemical Society.

active sites on the catalyst have been partially passivated, presumably by the presence of strongly adsorbed carbon atoms on the surface.

Group I–III cations like sodium and aluminum quantitatively inhibit the growth, most likely by blocking the reactive catalytic sites on the metal nanoparticle surface [45].

Growth of herringbone nanotubes. Herringbone nanotubes/-fibers are produced by the catalytic disproportionation of CO according to equation (2.5) on metallic catalyst particles, for example made of a Ni/Fe alloy [46, p. 58f.]. The growth temperatures are between about 500 and $650^\circ C$. The growth mechanism has been described by Audier and Colon in the 1980s [47] and is similar to the recent findings regarding SWNT growth detailed above. It is based on a conical catalyst particle (see Figure 2.6). The CO disproportionation reaction happens on the free side of this particle, and the carbon adatoms diffuse through the particle bulk, driven by the concentration gradient. For certain crystallographic axes, the carbon diffusion is very fast. Finally, segregation of a graphitic carbon layer happens on the “inner” surface of the catalyst particles, and the concentration gradient is restored. The angle of the crystallographic faces where the carbon layer segregates determines the angle of the graphitic planes with the fiber axis.

Pyrograf nanofibers are the most common type of commercially available herringbone carbon nanotubes and are sold by Applied Sciences, Inc (Cedarville, OH, USA). They can be bought in three types, called PS (pyrolytically stripped), LHT (low-temperature heat treated) and HHT (high-temperature heat treated). On the outside surface of these fibers, there is an amorphous overlayer of CVD carbon, which has been graphitized at $700^\circ C$, $1500^\circ C$ or $3000^\circ C$, respectively.

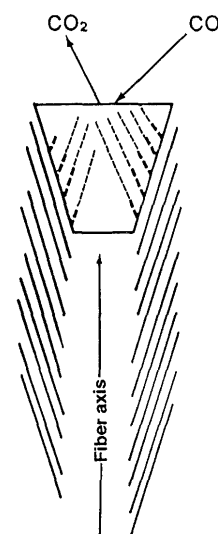


Figure 2.6 Scheme of the growth model for herringbone CNTs grown over a conical metal particle. Reprinted from [47], © 1985, with permission from Elsevier.

2.2.3 Other methods

A very original **electrochemical method** takes place below room temperature: Multi-walled carbon nanotubes are synthesized by electrolysis of an acetylene solution in liquid ammonia at 233 K [48]. The method offers neither very good yields nor a high quality of the product. However, it may allow the incorporation of thermally sensitive molecules into the CNT during the synthesis, under the condition that the molecule is stable in liquid ammonia.

Recently, a very ambitious project for the preparation of single-chirality SWNTs with predefined (m,n) indices has been presented [49, 50]. It is based on the **Diels-Alder** [2 + 4] **cycloaddition** of acetylene to the “bay region” of a polycyclic aromatic hydrocarbon (PAH), as shown in Figure 2.7. This reaction is notoriously difficult as the transition state requires the breaking of aromaticity on two rings. However, calculations show that the larger the PAH, the lower the activation energy for this reaction becomes. This has also been proven on a model system using diethyl acetylenedicarboxylate (which is a better dienophile than acetylene) on 4,11-dimesitylbisanthrene and perylene. In a competition experiment, it was found that the addition on the larger hydrocarbon is preferred and, more importantly, that no oxidant was needed in stoichiometric amounts to rearomatize the newly formed ring under H₂ evolution. The final CNT synthesis, which has not yet been realized, starts from a seed of defined chirality, e. g. a “buckybowl” or a piece of cut hydrogen-terminated SWNT, and proceeds over an indefinite number of cycloadditions, the reactive “bay region” being regenerated in each addition product. The chirality and diameter of the seed completely control the ones the product. The concept does not work for $(m,0)$ zigzag nanotubes because their ends do not have a “bay region”.

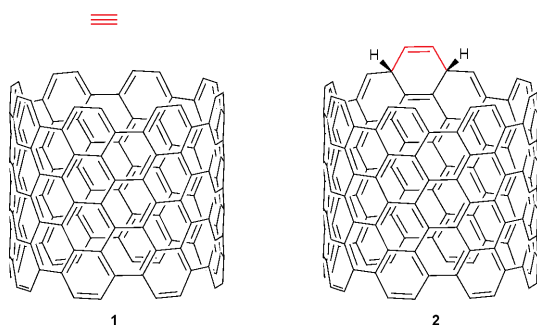


Figure 2.7 Scheme of the Diels-Alder cycloaddition of acetylene to the “bay region” of a (8,8) SWNT. From [49].

2.2.4 Sorting by chirality

All known synthesis methods for SWNT give tubes of mixed diameters and chiralities. There is active research on synthesizing nanotubes with defined chiralities or on separating them depending on the chirality—that is, upon the (n,m) indices. For electronic applications such as field-effect transistors and transparent conductive layers, such a separation process is crucial: Depending on their chirality vector, SWNTs are either metallic or semi-conducting [51].

Recently, a method for “chirality enrichment” based on polyfluorene sheets has been developed by several groups [52]. Depending on the structure of the polymer, the active sites exactly match certain distances on the nanotubes and thus selectively wrap only certain types. A similar treatment method uses phospholipid micelles, in this case lysophosphatidylcholine (LPC), which wraps (and thus disperses) preferentially the SWNT fractions with a smaller diameter [53].

The most mature process for SWNT sorting is based on **Density Gradient Ultracentrifugation (DGU)**, a process that has been in use for a long time in molecular biology for separating sub-cellular material, such as vesicles, fractionation of proteins etc. [54]. The research group around Mark C. Hersam has developed this technique to a high degree of maturity [55, 56, 57, 58, 59], to the point that a spin-off company (NanoIntegris) now offers different types of sorted SWNTs as aqueous dispersions.

2.3 Dispersion/solution

Generally speaking, molecules and salts are *dissolved* in a solvent while particles are *dispersed*. A carbon nanotube can be thought of as either a molecule (albeit a rather large one) or a nanoparticle. Most publications speak of dispersion, however some of the literature about SWNTs uses the term “solution” for the same process.

As-produced SWNT form ropes or “bundles” with a hexagonal arrangement of the tubes. These ropes can be very hard to separate as they are held together by multiple van-der-Waals interactions. The interaction energy is in the order of 500 eV per μm of tube–tube contact [60].

Another factor that decreases the dispersibility of carbon nanotubes is their high aspect ratio,

which can be 1000 or more, leading to entanglement of molecules. This effect is seen in investigations of the viscosity of aqueous nanotube dispersions [33]. The viscosity dramatically increases at a concentration of oxidized MWNT near 0.7 vol-%; a similar phenomenon is observed in polymer solutions, and attributed to an **entanglement transition**. The apparent viscosity of the nanotube dispersions increases with concentration and may be fitted to the Schulz-Blaschke formula for polymer solutions

$$\frac{\eta_{sp}}{c} = [\eta] + k[\eta]\eta_{sp},$$

where η_{sp} is the specific viscosity and $[\eta]$ and k are constants. The strength of the entanglement of the nanotubes in the dispersion depends on their flexibility, which is related to the number of defects, and especially their length. All other factors being equal, shorter nanotubes are better dispersible [61].

For nanotube dispersions, the UV-VIS absorption A obeys the Lambert-Beer law

$$A = \log \frac{I_0}{I} = \epsilon cd,$$

where ϵ is the extinction coefficient, c the concentration (here as a mass concentration) and d the thickness of the sample. For MWNT, an extinction coefficient $\epsilon = 35.10 \text{ mL mg}^{-1} \text{ cm}^{-1}$ at $\lambda = 800 \text{ nm}$ has been determined experimentally [32]. This property allows the rapid determination of the concentration in a dispersion by a simple photometric absorption measurement.

2.3.1 Dispersion in organic solvents

Liu *et al.* disperse single-walled carbon nanotubes for AFM imaging by achieving stable dispersions ($y = 0.1 \text{ mg/mL}$) in N,N-dimethylformamide (DMF) and other amide solvents like N-methyl-pyrrolidinone (NMP). However, the duration of the ultrasonic treatment is 15 hours so the mean length of the nanotubes is reduced to about $1 \mu\text{m}$ [62]. Other reports also indicate that SWNT are properly wet by highly polar solvents such as N,N-dimethylformamide (DMF), dimethylacetamide (DMAc), N-methylpyrrolidone (NMP), and hexamethyl phosphoramide (HMPA) [60]. These solvents are characterized by

- ▶ high values for the electron pair donicity β ,
- ▶ very low values for the Taft-Kamlet hydrogen bond donation parameter α and
- ▶ high values for the solvchromic parameter π .

Put in simpler terms, they are good Lewis bases (i. e. they have a free electron pair) but are aprotic. However, this is not the whole explanation, as DMSO fulfills the same conditions but does not disperse CNTs well [63]. Presumably, DMSO is a worse solvent for CNTs because it is not as basic (in the Brønsted sense) as DMF or other amides. With its pK_a of 34, the basicity is less than that of ammonia while organic amines are more basic [64, p. 149]. From own experiments, a basic environment tends to help in the dispersion of CNTs.

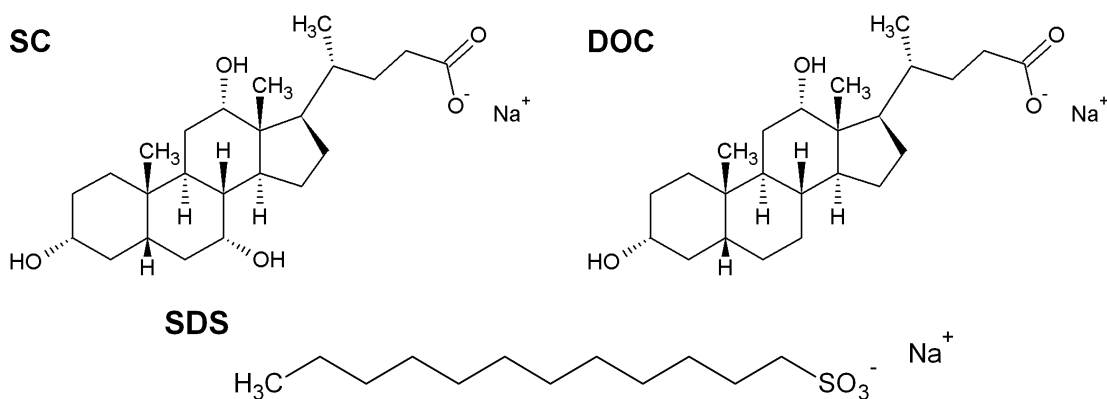


Figure 2.8 Molecular structures of the surfactants sodium cholate (SC), sodium deoxycholate (DOC) and sodium dodecylsulfate (SDS).

2.3.2 Surfactant-assisted dispersion

The role of a surfactant is to produce an efficient coating and induce electrostatic or steric repulsions to counterbalance the van-der-Waals attractions [65]. Surfactants are a quick and easy way to prepare stable dispersions of carbon nanotubes, which are contained inside surfactant micelles.

Many synthetic surfactants represent environmental or health hazards upon inhalation or environmental release. Surfactant toxicity can occur through direct cell membrane damage and may even be the primary cause of observed toxicity when surfactants are used to disperse nanotubes in nanotoxicology assays [23].

One of the most common (anionic) surfactants is **sodium dodecyl sulfate** (SDS, Figure 2.8). A phase diagram for the system SDS–MWNT (see figure 2.9) has been established [66, 67]. In an aqueous solution containing 1% by weight of SDS, MWNT can be quickly and permanently dispersed up to at least 0.5 wt%. However, for too high concentrations of SDS, whose critical micellar concentration (cmc) is 2.49 wt-%, an unstable state called *depletion* is achieved. In fact, when empty SDS micelles are formed, they cannot fit between two CNT bundles close to one another. Effectively, the osmotic pressure created by these micelles creates an additional attractive force called depletion interaction.

In the last few years, the use of SDS is decreasing in favour of **sodium cholate** (SC) and **sodium deoxycholate** (DOC) [68]. Their molecular structures are given in Figure 2.8. These surfactants are extracted from animal livers and gall bladders, where they are naturally found. They are thus relatively cheap, non-toxic and biocompatible. They debundle SWNTs more effectively than SDS, leading to more stable dispersions. Because both are chiral surfactants, they wrap around the nanotubes slightly differently depending on their (n,m) indices, giving slight

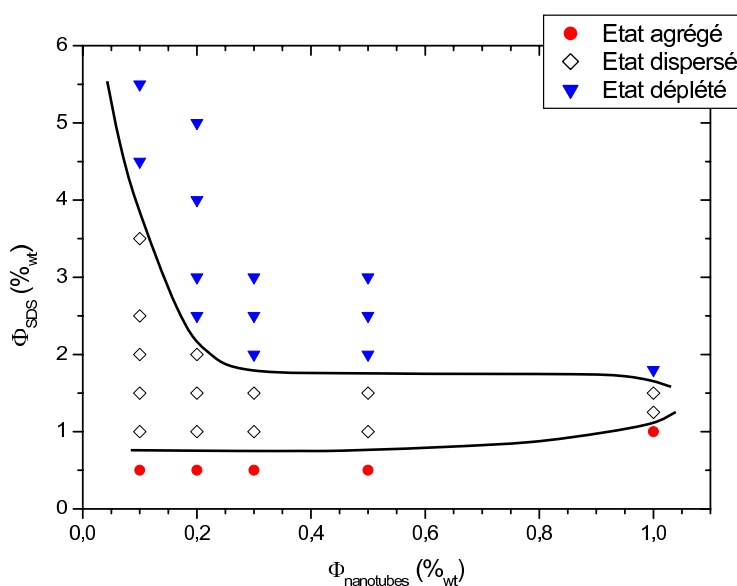


Figure 2.9 Phase diagram of carbon nanotubes and sodium dodecyl sulfate (SDS) in water: aggregated (red circles), dispersed (white diamonds) and depleted state (blue triangles). Reproduced from [66].

differences in buoyant density. This is the base for the chirality separation by DGU.⁵

Triton X-100, a nonionic surfactant, has also been used for nanotube dispersion. The disadvantage of nonionic surfactants is that they tend to lower the value of the zeta potential, thus decreasing electrostatic interactions. The stabilization is only due to steric repulsion in this case. On the plus side, Triton X-100 has also been reported to work in THF as a solvent [60].

Tocopheryl polyethylene glycol succinate (TPGS) is an interesting surfactant for nanotube dispersions. It is normally sold as a water-soluble form of vitamin E (Tocopherol), non-toxic, and even a GRAS (Generally Regarded As Safe)-listed food supplement. Concentrations as low as 3.8 mg/L (2.5 μ M) are sufficient to stabilize a MWNT suspension at 15 mg/L [23].

The same kind of forces that hold nanotube bundles together also act between polyaromatic compounds and nanotube surfaces. This is the reason why TPGS is so effective, and it has been used to promote adhesion of copolymer surfactants, for example by binding pyrene groups to the hydrophobic side [69].

Synthetic **block copolymers** have been used for nanotube dispersion, based on solvent selectivity [70]: A selective solvent that acts as a “good solvent” for one of the blocks dissolves the polymer and increases its spatial dimensions, while it acts simultaneously as a “poor solvent” for the other block that adsorbs onto the nanotube surface. This selective interaction is

⁵see section 2.2.4.

essential for the stabilization of dispersions. A concrete example is that Pluronic, a commercial $(\text{PEO})_m(\text{PPO})_n(\text{PEO})_m$ surfactant, in water (a selective solvent for its blocks), leads to stable SWNT dispersions. Pluronic is non-toxic and approved by the FDA (Food and Drug Administration). The mechanism is called steric stabilization; it is characterized by the redispersability of a colloid: after solvent evaporation, the resulting powder disperses instantly when new solvent is added. It is based on the onset of entropic repulsion; the interaction is weak (of the order of a few kT) but long-range (several tens of nanometers) while the vdW attraction inside a bundle is highly attractive (thousands of kT) but short-ranged.

Steric repulsion can also be achieved by introducing **charged nanoparticles**. Even if they are not really surfactants, they can stabilize a colloid by a “haloing” effect. In principle, by adding charged nanoparticles to negligibly charged micrometric objects, halos occur because it is advantageous for the charged nanoparticles to be near the uncharged surface. Tsai’s group [71] achieves impressive concentrations up to about 20 g/L of MWNT in a 1 wt% aqueous solution of positively-charged alumina-coated silica nanoparticles (ACS).

2.4 Oxidation treatments

As-prepared carbon nanotubes are generally closed with end caps. As in a fullerene, the curvature is induced by the introduction of pentagons into the graphitic lattice. Following Kepler’s rule, six pentagons give a fullerene-type cap [51]. Five pentagons are sufficient for a conical cap [29]. Molecular dynamics simulations show that the pentagons are more reactive [72], so in principle a selective oxidation attacking these sites is possible. The direct attack of a sidewall can take place on the site of a Stone-Wales defect [73]. In such a defect, four hexagons are replaced by two pentagons and two heptagons. Effectively, one C=C bond is rotated by 90 degrees, and the π electrons of the turned bond are not delocalized.

In mild oxidation treatments, the caps are generally removed first; only then is the wall attacked. The attack proceeds mainly at the defect sites such as the opened tips and introduces oxygenated groups (Figure 2.10). Oxidized nanotubes disperse better, particularly in water. The two main approaches are gas phase reactions (e. g. heating in air) and wet chemical reactions.

As-produced nanotubes are generally insoluble; an improved dispersion can be reached by functionalizing the tubes. For SWNTs, there is always the danger of irreparably damaging the walls if the treatment is too excessive. For MWNTs, even if the outer wall is damaged, the inner walls usually stay intact.

Mechanical treatments. A number of different mechanical treatments for opening SWNTs and dissociating their bundles have been described. Ball milling is the most destructive mechanical treatment. After a few minutes of milling, the structure of SWNTs is already severely damaged; after 30 minutes, it is almost completely lost, and only amorphous carbon remains, as evidenced

Figure 2.10 End groups on a carbon nanotube surface: Carboxylic acid and anhydride groups. With kind permission from Springer Science+Business Media: [74]. © Springer-Verlag 2002.

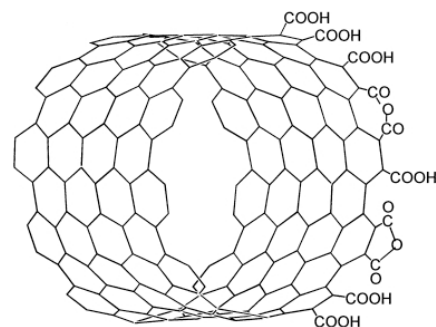
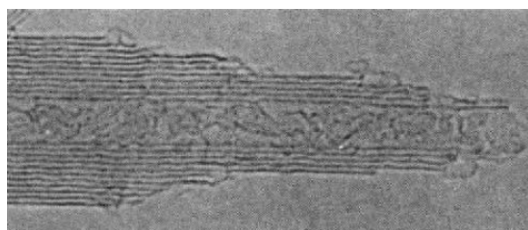


Figure 2.11 HRTEM micrograph of an individual nanotube showing the structural damage that has occurred during oxidation in air. Carbonaceous debris is visible inside the tube. From [76], © 1993 Nature Publishing Group.



by Raman measurements [75]. The tube tips can also be opened by rubbing on diamond lapping discs with 100 nm diamond powder. Diamond particles can also be used for unbundling by sonication. These treatments work well but introduce new impurities—such as diamond or titanium particles from the sonotrode—into the samples [75].

Gas-phase reactions. Ajayan *et al* [76] investigated the oxidation of thick-walled MWNT synthesized by the arc-discharge method in air at temperatures between 680 and 800°C. They see a characteristic damage pattern, as shown in Figure 2.11. The damage is the most intense on the outside walls and progressively less pronounced on the inner walls. On many of the opened tubes, carbonaceous debris seems to have been sucked into the hollow inner cavity, blocking it. Consequently, they find it more difficult to fill pre-opened tubes than to do a one-step opening/filling reaction. They argue that the inside cavities of closed tubes are under vacuum, or near vacuum, and that the pressure difference *at the moment the tube is opened* sucks the filling reagent inside the tube. The meaning of vacuum, however, is not quite clear in a small cavity, given that only about 20 gas molecules would be found in a 1 μm long, 1 nm large tube at 1 atm of pressure. Thus, the macroscopic concept of a gas pressure does not have an obvious meaning at the nanoscale.

In another study on arc-discharge nanotubes, Pillai and coworkers [31] find no tube degradation for temperatures below 450°C. Heating the crude product to 400°C for two hours selectively removes carbonaceous impurities. Contrary to the previous study, the nanotubes start to become damaged at temperatures of 450°C and more.

Marsh *et al* [61] investigate air oxidation on MWNT synthesized by CVD. 20 min of treatment at 500°C lead to a 30% weight loss; after 40 min, the weight loss is 60%. The tubes are observed

to be shortened after the treatment: the longer the annealing time, the shorter the CNTs. After 40 min of oxidation, most nanotubes are under 1 μm in length, compared to tens of microns in the as-received state. IR analyses of the shortened tubes do not show an increase in the number of oxygenated functional groups for the air-oxidized CNTs; the improved dispersibility of these tubes is thus only due to their shorter length. *Shorter nanotubes disperse better.*

Wet chemical methods. The most common wet-chemical oxidation method is the reaction with an oxidizing acid, namely nitric acid HNO_3 or a $\text{HNO}_3/\text{H}_2\text{SO}_4$ mixture [77]. The nanotubes are typically boiled at reflux in the acid for 24 h or more. Depending on the concentration, the reaction mechanisms are different. The concentrated acid opens the nanotubes via an *oxidative cleavage* mechanism. Surprisingly, not much is known about this mechanism, even if it is one of the most common treatments for carbonaceous materials. Although the mixture is the same used for adding $-\text{NO}_2$ groups to aromatic hydrocarbons, no nucleophilic substitution takes place. Nitration of aromatic rings can be excluded from time-resolved XPS measurements, which show no non-hydrolyzable C–N species [78].

Treating MWNT in diluted nitric acid (2.6 mol/L) does not lead to much damage of the carbon skeleton. It does however add large amounts of acidic oxygenated surface functions to the CNT surface [61], more than the oxidation in air. These functional groups – mainly carboxylic acids – facilitate the dispersion in polar solvents such as water.

Other possible wet chemical opening agents used in the literature include:

- ▶ KMnO_4 in acidic or basic solution [77,79],
- ▶ $\text{OsO}_4/\text{NaIO}_4$ at room temperature [77],
- ▶ O_3 [80,81],
- ▶ $\text{K}_2\text{S}_2\text{O}_8$ in diluted H_2SO_4 (on SWNT) [82].

For other forms of carbon – microporous active coal and mesoporous carbons – ammonium persulfate solution ($(\text{NH}_4)_2\text{S}_2\text{O}_8$) has been used for oxidation. For activated carbons, it has been shown that ammonium persulfate treatments give more $-\text{COOH}$ groups on the surface than a nitric acid or H_2SO_4 treatment. The persulfate is used as a solution in 2 M H_2SO_4 with a concentration of up to 1.75 M [83]. A similar treatment, using $\text{K}_2\text{S}_2\text{O}_8$ in dilute sulfuric acid as the oxidizing agent, has also been reported for SWNTs. It is said to oxidize preferentially the amorphous carbon present in the sample, but also to add hydrophilic groups like carboxyls. The product is well dispersible in water and DMF [82].

The **molten hydroxide treatment** [84,85,86] is an interesting method: Single-walled carbon nanotubes are opened and filled at the same time by treating them with molten KOH or CsOH. The hydroxide-filled nanotubes themselves are not very interesting as a material; however, the

hydroxide can be easily washed out with water, giving empty, uncapped tubes. We will revisit this method in section 4.2.3.

2.4.1 Functionalization

Satishkumar and coworkers [77] tried to introduce a high degree of functionalization into MWNTs by refluxing for two hours with a $\text{H}_2\text{SO}_4/\text{HNO}_3$ mixture (3:2 by volume). Such solutions are classically used for adding nitro groups to aromatic hydrocarbons. The result is a white (!) solid residue. SEM images show a nanotube-like structure but the graphene sheets seem to be largely destroyed. Many sulfonic acid ($-\text{SO}_3\text{H}$) groups are found. Most likely, the product is some kind of graphene oxide.

To make them more reactive, the carboxylic acid end groups can also be converted to the corresponding acyl chloride $-\text{COCl}$ by a treatment with thionyl chloride [87, 88, 74]. The chloride can further be treated with amines to give rise to an amide or by an alcohol, resulting in esters. Octadecylamine-functionalized MWNT have been reported to be well soluble in carbon disulfide (CS_2), chloroform, dichloromethane, and aromatic solvents (toluene, benzene, chlorobenzene, 1,2-dichlorobenzene) [88]. The activation of carboxyl groups by $\text{N,N}'$ -dicyclohexylcarbodiimide (DCC) has also been reported for this reaction [82]. The functionalized nanotubes are well dispersible in tetrahydrofuran (THF), chloroform, methylene chloride, and DMF, thus the process can be used as part of a purification cycle.

Hamon and coworkers [74] use octadecanol (ODO) and find a much higher number of reactive SWNT sites than one would expect by a model based only on end-group functionalization, i.e. defect sites on the walls participate in the reaction and are functionalized, too. “The mole fraction of reactive (end-group) sites would be about 0.2% in a perfect 100-nm-long SWNT-COOH” of the (10,10) type. It is also possible that the nanotubes are actually filled (non-covalently) with the amine or alcohol. Filling the tubes with ODA would correspond to a weight percentage slightly less than the actual value. Thus, a combination of filling and end-group reaction seems likely.

2.4.2 Defunctionalization

Most of the oxidizing treatments to open CNTs also add functional groups to the surface, mostly carboxylic acids and other oxygenated moieties. These improve the dispersability in water and other solvents. In a way, opening and dispersing are thus related problems. However, if the inner space is to be filled, these functional groups may “block” the nanotube entries, preventing molecules like N_2 (for BET measurements) or the desired filling reagent from entering the tube.

Worse still, some treatments leave carbon “debris” at the nanotube tips that completely obstruct the entry. This was first observed by Ajayan and coworkers [76] (cf. Figure 2.11) and confirmed by several more recent papers [74, 89, 90]. These flakes of debris left the acid purification and oxidation steps are low-molecular, highly functionalized aromatic and polyaromatic

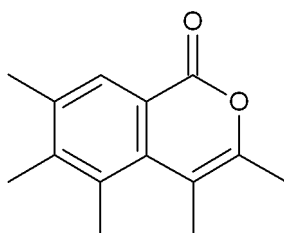


Figure 2.12 Example of an oxygenated functional group of the pyrone type.

molecules. They are strongly adsorbed on the sample surface by π - π stacking and not removed by conventional water washing. In some cases, reactions designed to act on the CNT surface may functionalize the debris instead of the nanotubes themselves.

It may thus be necessary to remove the acidic functionalities (even if the dispersibility decreases) and remove the carbon flakes, either by burning the latter or by converting them to graphite (graphitization). In order to remove a part of the acidic functional groups on the acid-treated CNTs, they can be heated to 950°C under an inert N_2 atmosphere [32]. Under these conditions, most of the carboxylic acid functions are destroyed or converted to pyrone-like functional groups (Figure 2.12). Contrary to carboxylic acids, pyrones are basic functional groups.

Kuznetsova and coworkers [91] heated SWNT in an ultra-high vacuum to remove surface groups. At a temperature above about 600 K, an evolution of CH_4 , CO , CO_2 , and H_2 gases is observed. The infrared peaks of oxygenated groups are seen to decrease. Heating to 800°C produces both an enhanced capacity and rate for xenon adsorption. The saturation capacity is found to be about 20 times higher.

2.5 Filling of carbon nanotubes

Carbon nanotubes can be thought of as a straw-like structure, with an interior that may be filled with other materials—atoms, molecules, or compounds. The result of this endohedral filling is called a “hybrid carbon nanotube” by some researchers, notably by Monthieux [1, 92]. These hybrid nanotubes are part of a larger group called “meta CNTs”, which also contains

- ▶ covalently and non-covalently functionalized nanotubes,
- ▶ “decorated” CNTs (with nanoparticles attached to the outer walls),
- ▶ heterogenous nanotubes (where heteroatoms, such as N, are substituted inside the lattice itself), and
- ▶ doped nanotubes (with electron acceptors or donors intercalated between the graphitic layers of MWNTs).

Nanotubes	Filled with	Method	Ref.
MWNT	metals	in-situ	[97]
MWNT	FeS ₂	in-situ (one-pot)	[98]
MWNT	metals	melt (ampoule)	[99]
MWNT	halides	melt (ampoule)	[100, 101]
SWNT	halides	melt (ampoule)	[102, 103, 104, 105]
SWNT	alkali metal hydroxides	melt (ampoule)	[84, 85, 86]
SWNT	oxides	melt (ampoule)	[106]
MWNT	oxides (V ₂ O ₅)	melt (in air)	[107]
DWNT	halides, C ₆₀	plasma-ion irradiation	[108]
SWNT	calcium	plasma	[109]
SWNT	ionic liquids	melt (ampoule)	[110]
DWNT	AgCl (from precursor)	solution	[111]
SWNT	halides	solution	[112]
MWNT	CdS (from precursor)	solution	[113]
MWNT	metals (from precursor)	solution	[114, 115, 116, 117, 77]
SWNT	metals (from precursor)	solution	[118, 119]
MWNT	oxides	solution	[120, 121, 122, 123, 124]
SWNT	organic molecules	solution	[125, 126]
SWNT	oxides	reactive	[127, 128]
DWNT	ferrocene	gas phase	[129]
SWNT	organic molecules	gas phase	[130]
SWNT	C ₆₀ (peapods)	gas phase	[131, 132, 133, 134, 135, 136]
SWNT	C ₆₀ (peapods)	supercritical fluids	[137]

Table 2.1 Synopsis of literature about the filling of carbon nanotubes.

Table 2.1 presents a non-exhaustive overview of the literature about filling carbon nanotubes. It shows the types of CNTs, the materials with which they have been filled and the corresponding method. Several reviews have been written about the filling of carbon nanotubes [1, 93, 92, 94, 95, 96].

Concerning the nomenclature of endohedrally filled compounds, they are called X@CNT, where X is the filling compound and CNT is the type of carbon nanotube (SWNT, DWNT, MWNT).

Transmission Electron Microscopy (TEM) is the most important technique used to prove that filling has occurred. In effect, it is the only technique that allows looking *through* the nanotubes. Thus, the interior can directly be imaged, at the price of a somewhat local view. Even if a relatively large number of micrographs is used for statistical analysis, the result can never be representative of a sample as a whole.

Two fundamentally different approaches for filling nanotubes can be used: either opening and filling are separate steps or the opening takes place *in situ* at the same time as the filling.

2.5.1 In-situ syntheses

Until recently, no *in situ* syntheses had been described. However, the application of this strategy led to the serendipitous initial discovery of SWNTs. The first (multi-walled) carbon nanotube synthesis had been the arc-discharge method, which is very similar to the synthesis conditions for fullerenes. The growth of these tubes is catalyst-free. To synthesize filled nanotubes, researchers incorporated metal powder into the graphite rod. Instead of filling, the product were single-walled nanotubes (SWNT). The condition for their formation under the synthesis conditions is the presence of a metallic catalyst with a certain size.

Filling with copper. It turns out that the original idea of using metal-containing carbon anodes does work for some systems. Kokai and coworkers [138] obtained copper-filled CNTs by laser vaporization of Cu and graphite under a high-pressure argon atmosphere. Depending on the pressure and the Cu content in the graphite target, different morphologies (capsules, nanotubes) are observed. At 0.9 MPa of pressure and with 20 at-% of Cu in the target, the product contains about 60% of nanotubes. No unfilled nanotubes were observed even for low Cu contents in the target. All carbon nanostructures were completely filled with polycrystalline copper nanowires or -particles, with no interstitial free space.

On the other hand, the thermal decomposition of copper acetylacetonate gives Cu nanowires coated with amorphous carbon instead [139]. The process is carried out in an evacuated, sealed ampoule at 400°C and leads to filled tubular structures with 40–150 nm inner diameter and 100–200 nm outer diameter. Annealing at temperatures above 800°C makes the copper leave the nanotube; the melting point is thus strongly decreased from its bulk value of 1083°C.

Methods based on metallocenes. Pyrolysis of pure metallocene vapors in a CVD reactor at 900–1150°C gives multi-walled carbon nanotubes filled with metallic Fe, Co, or Ni [140, 141]. The precursor contains both the carbon for the shell and the metal for the filling. Filling yields are up to about 50%. The method allows the preparation of filled nanotube “carpets” on a substrate. Fe-filled nanotubes have a significantly higher magnetic coercivity compared to bulk iron [140].

Highly aligned Fe@MWNT forests have been obtained by pyrolysis of an aerosol of a 2.5 wt-% solution of ferrocene in cyclohexane at 850°C [142]. These tubes have a length of almost 1 mm. They contain 2.4 wt-% of iron, which is mainly in the metastable γ -Fe phase. Most of the Fe nanowires have a preferred orientation in the $\langle 110 \rangle$ direction.

By using a solution of ferrocene and nickelocene in dichlorobenzene as the precursor, permalloy-filled nanotubes FeNi@MWNT have been prepared [143, 144]. Interestingly, the chlorine atoms in the carbon source lead to higher internal diameters of the carbon nanotubes and to an improved

filling ratio. With dichlorobenzene as the carbon source, the ratio of outer to inner diameter D/d was about 1.2, while a value of $D/d \approx 2.3$ was observed when using benzene as the carbon source. This is attributed to the etching of the innermost walls, which have the highest curvature strain, by $\text{Cl}\cdot$ radicals during the synthesis.

See ref. [145] for a short review on in-situ metal filling by CVD.

Non-CVD synthesis. A first non-CVD in-situ synthesis of filled CNTs was described in 2006 [98]: Ferrocene, sodium azide, and carbon disulfide were heated together in a stainless steel reactor to 500°C. CS_2 becomes supercritical under these conditions, and pyrite-filled nanotubes $\text{FeS}_2@\text{CNT}$ are obtained.

2.5.2 Ex-situ syntheses

Today, ex situ filling methods—i.e. those where the nanotubes are first synthesized in their empty state and then filled—are the most common approach for endohedral filling of carbon nanotubes. They can be classified after the aggregate state of the filling agent [92]: gas phase, liquid, or solid. The various methods will be described in more detail below.

2.5.2.1 Gas phase synthesis: peapods

The most effective encapsulation methods with filling yields up to 100% is filling over the gas phase, i. e. the filling material enters the nanotube in vapor form. This method has been widely used for the synthesis of so-called “peapods” [131, 132], i. e. single-walled carbon nanotubes filled with fullerenes ($\text{C}_{60}@\text{SWNT}$). Fullerenes can be sublimated at 350°C and enter the nanotube easily. This synthesis method is usually carried out in branched (Y form) glass ampoules. The SWNTs are introduced into one branch and the fullerenes into the other. The ampoule is evacuated, sealed, and put in an oven. The heating periods can be very long, up to a week.

When they are imaged under a TEM, the fullerenes inside the SWNTs slowly coalesce under the influence of the electron beam. After the reaction has finished, a new nanotube wall has been formed, giving rise to a double-walled carbon nanotube (DWNT).

2.5.3 Liquid route: molten salts or metals, solutions

Liquids enter open nanotubes by the force of capillary wetting. High surface tensions prevent the liquid from entering the nanotube. The threshold for entering is near 200 mN/m, depending on the inner diameter of the tube. All organic solvents and water have surface tensions below this threshold, while mercury [146], for instance, has a higher surface tension. Mercury can still be filled into CNTs by an “electrowetting” process, i. e. the liquid mercury can be forced by an electric tension to go inside the nanotube.

2.5.3.1 Filling with halides

Metal halides have been used for filling CNTs in several studies. The use of molten salts enables to obtain high filling yields. One of the first filling reactions demonstrated for SWNTs was the encapsulation of ruthenium chloride [112]. Most of these reactions take place in sealed ampoules, similar to the vapor phase method: the carbon nanotubes are ground with an excess of the filling compound, and the mixture is transferred into an ampoule sealed under vacuum.

For preparing SWNTs filled with potassium iodide, 350 mg of KI are mixed with 30 mg of SWNTs, and the mixture is heated to 781°C for 12h in the vacuum ampoule [84]. Interestingly, the KI filling cannot be washed out with water, except when treating with a molten alkali hydroxide to open the tubes. This is interpreted as a sign that the tube ends re-seal during the cooling process, trapping the KI on the inside. This is difficult to prove by electron microscopy or by nitrogen adsorption experiments, though.

Costa and coworkers [101] filled multi-walled carbon nanotubes with copper iodide by mixing CuI and MWNTs and heating them to 600°C in an evacuated ampoule at 10^{-3} Torr. Single CuI@MWNT have been contacted with gold electrodes to measure $I-V$ curves, and the authors detect the stepwise ejection of CuI from the nanotubes with the voltage sweeps. The ejected quantities are in the 50–100 ag (attogram) range, i. e. 10^{-16} g.

Sloan and coworkers [100] filled arc-discharge MWNTs with uranium tetrachloride and eutectic mixtures of UCl_4 with KCl. The nanotubes are first opened by oxidizing them in boiling HNO_3 for 24 h, then decarboxylated by heating them in air. The salt and the opened MWNTs are mixed in a 1 : 1 ratio in a glove box and put into an evacuated ampoule, which is then heated to 150 K above the melting point of the salt for 30 min. For pure KCl and UCl_4 , no filling is observed as their surface tensions in the molten state (270 and 371 mN/m respectively) are too large for successful capillary filling, where the surface tension has to be below 200 mN/m. However, using binary mixtures, filled MWNTs in good yields are obtained. The 1 : 1 eutectic mixture of KCl and UCl_4 , for instance, allows reducing the infiltration temperature to 750 K, and the encapsulated product also corresponds to this eutectic.

2.5.3.2 Infiltration with solutions

Many compounds cannot be infiltrated in molten form – their melting point is too high, which is often the case with metal oxides, the melt reacts with the CNT, the surface tension is too high or the compound decomposes before melting. In many of these cases, CNTs can be filled with this compound by infiltrating them with a solution. In general, this means preparing a concentrated solution of the filling agent, mixing it with the carbon nanotubes, stirring and/or sonicating for a certain time for the infiltration to take place, and finally purifying the product.

Some authors say that infiltrating the nanotubes with a solution results in bad filling yields (below 1/3). In any infiltration technique, the solvent enters along with the solute molecules and

2 State of the art

Precursor	desired oxide	reaction time (h)	filling yield (%)	aggregate size (nm)
$\text{Bi}(\text{NO}_3)_3 \cdot 5 \text{H}_2\text{O}$	Bi_2O_3	24	10–15	10–30
$\text{Fe}(\text{NO}_3)_3 \cdot 9 \text{H}_2\text{O}$	Fe_2O_3	24	15–20	10–30
$\text{Mn}(\text{NO}_3)_3 \cdot 6 \text{H}_2\text{O}$	MnO	24	10–15	10–30
V_2O_5	V_2O_5	24	30	up to 150

Table 2.2 Results of the filling of MWNT by infiltration of solutions. Reproduced and translated from [147].

Precursor	desired oxide	reaction time (h)	filling yield (%)	aggregate size (nm)
$\text{Ni}(\text{NO}_3)_2 \cdot 6 \text{H}_2\text{O}$	NiO	2, 6, 8, 15, 18, 24	0	
$\text{Cu}(\text{NO}_3)_3 \cdot 5 \text{H}_2\text{O}$	CuO	2, 6, 8, 15, 18, 24	0	
$\text{Bi}(\text{NO}_3)_3 \cdot 5 \text{H}_2\text{O}$	Bi_2O_3	2, 6, 18, 24	20	up to 50
$\text{Fe}(\text{NO}_3)_3 \cdot 9 \text{H}_2\text{O}$	Fe_2O_3	6	10	up to 10
$\text{Mn}(\text{NO}_3)_2 \cdot 6 \text{H}_2\text{O}$	MnO	6	10	up to 10
MnCO_3	MnO	6	0	
$\text{Fe}_2(\text{C}_2\text{O}_4)_3$	Fe_2O_3	6	0	

Table 2.3 Results of the filling of MWNT by reactive infiltration (called “one-step method”). Reproduced and translated from [147].

is effectively trapped inside the nanotube (*dead volume effect*). Worse, it can eject solid material during the evaporation step [122, 123]. In this case, very slow heating is needed to minimize material ejection.

Some progress with the yield problem has been made using supercritical solvents—for example CO_2 [137], whose low viscosity, absence of surface tension and low molecular cross-section may allow it to pass between the wall of the nanotube and the filling agent.

In his Ph.D. thesis, Chancolon [147] investigated the filling of MWNT with an internal diameter of about 5 nm with aqueous solutions of several metal nitrates and of vanadium(V) oxide, which is a water-soluble oxide. The nanotubes are first opened with hot nitric acid, then brought into contact with the solution. Table 2.2 gives the results obtained with this method. The obtained filling yields are reasonable, especially in the case of V_2O_5 , for which nanorods up to 150 nm in length have been observed.

Reactive infiltration. The reactive infiltration method, which we will use in chapter 5, is called “one-step method” by Chancolon [147], as opposed to the “two-step” opening of the MWNTs followed by the infiltration of the solution. Several precursors – again, mostly nitrates – for various metal oxides and varying reaction times have been used to fill the nanotubes, as shown in Table 2.3. In each case, the precursor was dissolved in nitric acid, the pristine MWNTs were added,

and the mixture was heated to reflux for the time given in the table. The products are calcined, however the conditions are not given in the manuscript.

The filling yields are either zero or very low in each case. Notably, no filling is observed for copper and nickel nitrate as well as for non-nitrate precursors (manganese carbonate and iron oxalate). The optimum reaction time found was 6 hours. For shorter times, less nanotubes are filled, while longer reaction times lead to a stronger degradation of the CNT backbone without improving the filling yields. All the products contained a certain amount (which is not given) of exocrystallized metal oxide. The author concludes that this technique is not useful for obtaining homogeneously filled carbon nanotubes.

Infiltration of herringbone nanotubes. Herringbone nanotubes, of which Pyrograf-III fibers are the most common type, present several advantages for filling reactions. They are easy to open and larger in diameter than most types of MWNT. Dangsheng Su's group filled HNO₃-treated Pyrograf-III nanofibers with iron nitrate solution by an incipient wetness technique: 803 mg of Fe(NO₃)₃ · 9 H₂O dissolved in 6 mL of water are added dropwise to 1 g of nanotubes, dried and then calcined at 350°C for 2 h in air. The iron oxides formed are reduced under hydrogen at 400°C to form Fe@CNF nanocomposites. The morphology of the products depends on the heat treatment of the fibers, as shown in Figure 2.13: while 20–60 nm Fe particles are present inside the nanofibers for all samples, very small particles (~ 5 nm) are found on the *outside* surface only in the case of the PS type. This product has only been pyrolytically stripped of hydrocarbons at 700°C and has considerable amounts of oxygenated surface functional groups such as —COOH attached on the outside surface. A “defunctionalization” treatment at 800°C under argon prevents the formation of particles on the outside surfaces.

2.5.3.3 Filling with preformed nanoparticles

Instead of letting a precursor react inside a CNT to form nanoparticles, one can also infiltrate the CNT with solid, pre-formed nanoparticles. The challenge in this case is a) how to attach them to the inner nanotube surface and b) how to prevent them from attaching to the outer surface. A sophisticated method to achieve both goals has been shown by Castillejos and coworkers [149]. They functionalize the outside surface of Pyrograf-III nanofibers with a long-chain alkylamine to prevent the attachment of particles and then fill them with PtRu nanoparticles (2–3 nm) that have 4-(3-phenylpropyl)pyridine as a ligand. The ligand sticks to the inner surface of the carbon nanofibers by a π - π stacking interaction. The filling is carried out by simply stirring the particles and the nanofibers together in THF.

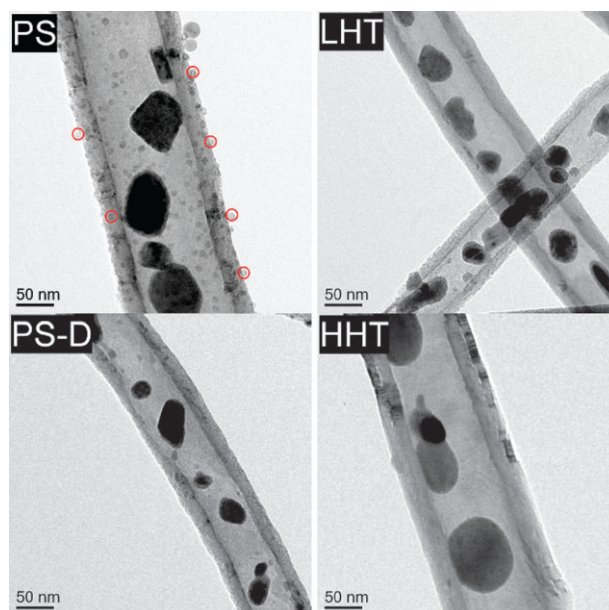


Figure 2.13 Transmission electron micrographs of different types of Fe@CNF samples starting from PS, LHT and HHT types of Pyrograf-III and PS fibers defunctionalized at 800°C (PS-D). The red circles mark 5 nm particles on the outer tube surface. From [148].

2.6 Effects of confinement and encapsulation

Encapsulating materials in a nanotube – or, more generally, in a porous solid – can significantly change its properties; a review that focuses on freezing and melting is found in Ref. [150]. The explanation for these changes comes from thermodynamics.

In classical thermodynamics, the Gibbs-Thomson equation describes how the vapor pressure of a fluid depends on the curvature of the liquid–vapor interface, i. e. the droplet size. Smaller liquid droplets have a higher effective vapor pressure because they have a higher specific surface area. The same reasoning has been applied to the solubility of solids in a solvent depending on its particle size, with the result that nanoparticles have a higher solubility. However, there is some controversy around the validity of the thermodynamic derivation of these laws (see for example Ref. [151]). Similarly, the melting point of a solid depends on its particle size: the smaller the particle, the lower its melting point. For nanoparticles, the decrease in the melting point can be on the order of several hundreds of Kelvins compared to the bulk, to the point that very small gold nanoparticles have been suggested to be in a liquid-like state at room temperature.⁶

Thus, for a material encapsulated in a nanoporous solid, a similar decrease of melting temperature would be expected, as the particle size is limited by the pore diameter. Indeed, this is what experiments on porous silica matrices show. However, an *increase* in the freezing temperature can occur in some systems – particularly for strongly attractive surfaces such as mica or the π system of graphitic carbon [150]. Moreover, in most experiments, a significant hysteresis between

⁶The melting point of 3 nm gold particles is about 35°C.

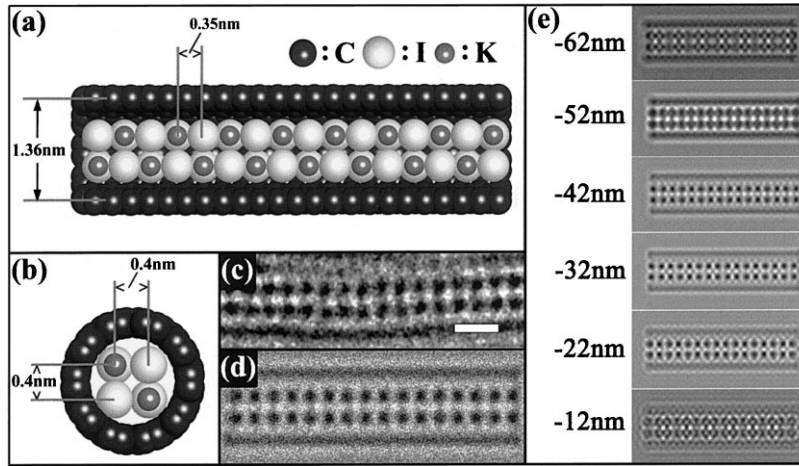


Figure 2.14 Cutaway structural model of a KI@SWNT composite (a) and end-on structural representation (b). TEM micrograph of KI@SWNT (scale bar = 1 nm) (c) and image simulation for -42 nm defocus for an undistorted bilayer KI crystal within a (10,10) SWNT (d). Calculated through focal series of a bilayer crystal within a (10,10) SWNT (e). Reprinted from [102], © 2000, with permission from Elsevier.

the melting and the freezing point are found, suggesting an important role of interactions with the pore walls.

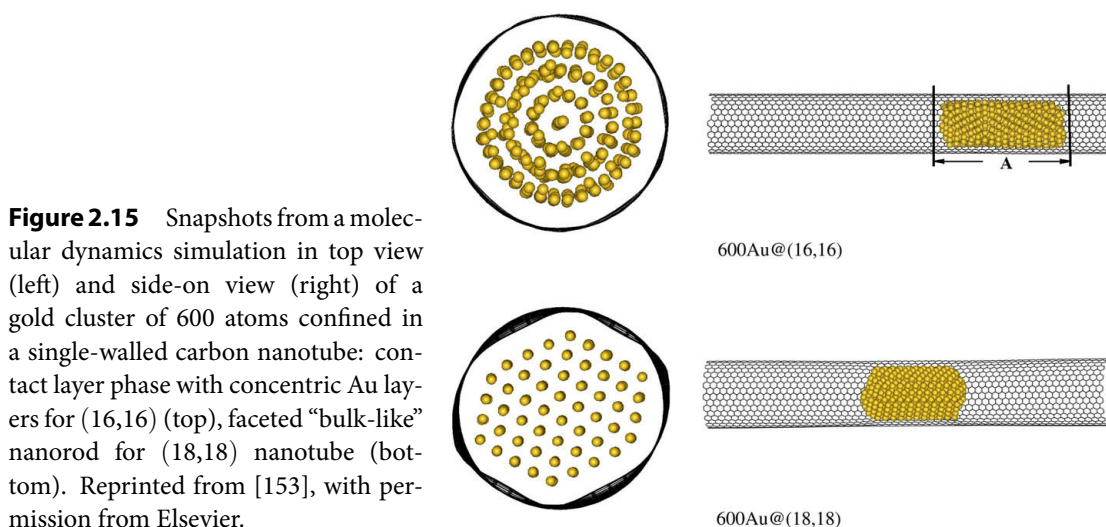
For sufficiently large pores, the difference to the bulk freezing point ΔT_f can again be explained by the Gibbs-Thomson equation, derived by equating the chemical potential of the confined liquid and solid [150]:

$$\Delta T_f = T_{f,\text{pore}} - T_{f,\text{bulk}} = -2 \frac{v(\gamma_{\text{ws}} - \gamma_{\text{wf}})}{d\lambda_{f,\text{bulk}}} \quad (2.6)$$

Here, γ_{ws} and γ_{wf} are the wall–solid and wall–fluid surface tensions, respectively, v is the molar volume of the liquid phase, d the pore diameter and $\lambda_{f,\text{bulk}}$ the latent heat of melting in the bulk. Equation (2.6) predicts that the freezing temperature will decrease compared to its bulk value if the pore wall “prefers” the liquid phase to the solid phase, and vice versa. As this equation is based on macroscopic concepts, such as surface tensions, it breaks down for pores smaller than 15–20 times the molecular diameter (i.e. for pores under 10 nm). But the inner diameter of carbon nanotubes is usually much smaller than this value, for example around 5 nm for typical MWNTs and 0.7–2 nm for SWNTs.

With decreasing pore sizes, the structure of a confined solid goes from a “classical” nanoparticle to a contact layer phase, then to an all-surface crystal or an atomic column.

For example, potassium iodide (KI) “all-surface” crystals (Figure 2.14) with 2×2 atoms thickness have been obtained inside SWNTs of 1.4 nm diameter [102]. These crystals have no internal atoms; they are always observed to form in a preferred orientation relative to the SWNT, with the



$\langle 001 \rangle$ direction parallel to the tube axis. Interestingly, while the lattice spacing along this direction is about 350 pm (the same value as in the bulk crystal), it is increased to 400 pm perpendicular to this direction, i. e. across the nanotube. This is attributed to an attractive interaction between the crystal and the nanotube wall and to the lower coordination number (4 instead of 6) of the atoms in the crystal. Nanotubes with an increased diameter of 1.6 nm give a similar type of crystal with a thickness of 3×3 atoms [152].

Molecular dynamics simulations of gold atoms in SWNT show the formation of cylindrical Au shells parallel to the nanotube axis [153]. The atoms in a shell form helices, depending on the diameter of the nanotube and possibly also its chirality. There is a “critical” diameter for the transition from the purely helical structure (“contact layer phase”) to a bulk-like structure. For a (16,16) nanotube (diameter 2.14 nm), the structure of the gold cluster resembles the bulk fcc structure but retains some cylindrical features. In an (18,18) nanotube however (diameter 2.41 nm), a faceted fcc crystal is obtained. The two structures are shown in Figure 2.15. A similar dependency of the structure on the nanotube diameter has been observed in simulations of Cu@SWNT materials. The reason is that the relative magnitude of the carbon–metal interaction decreases with an increasing nanotube diameter. The “critical diameter” for the transition from the cylindrical to the fcc structure also depends on the length of the nanowire, i. e. the number of encapsulated atoms, also due to the competing carbon–metal and metal–metal interactions. The cylindrical gold nanowires do not exist in a freestanding state.

In the same vein, Hung and coworkers [154] show that frozen nitrobenzene and CCl_4 in MWNTs ($d = 5$ nm) form concentric layers rather than a three-dimensional crystal. The low-temperature phase was found to be inhomogeneous, containing both solid and liquid regions. Simulations show that the freezing temperature of the contact layer is above the bulk value while the one of

the inner layers is below, in agreement with the experiment.

One way to distinguish solid, crystalline organic molecules from liquid-like ones in a pore is by NMR investigations [150]: the line widths for liquid and solid molecules differ by at least one order of magnitude. The reason is that the diffusion coefficient of the liquid-like molecules is higher, thus they can align faster with the magnetic field during the NMR measurement. In an experiment with benzene and cyclohexane in porous silica (SBA-15), it was found that only a part of the molecules, in the inner core of the pore, crystallize. Upon heating, the number of liquid-like molecules gradually increases; this phenomenon is analogous to the pre-melting effects in bulk samples, but the temperature range in which it occurs is much wider. Full crystallization of the encapsulated molecules can only occur in larger pores of 20 times the molecule diameter and above.

For some filling materials, notably halides, it has been demonstrated that only the incorporation into a nanotube stabilizes this nanowire state, which collapses when the outer tube is removed [1]. Furthermore, material inside a carbon nanotube does not have adsorbed molecules or humidity at its surface as it is protected by its sheath. This may lead to the stabilization of some very sensitive phases.

To conclude, *unique properties of the encapsulated materials may result from the one-dimensional confinement, especially for filled single-walled carbon nanotubes (SWNT) with their small diameters of 1–3 nm. The result can be anisotropic lattice distortion or even new structures. Filled SWNTs can give materials with an “ultimate size” in two dimensions.*

2.7 Energetic nanomaterials

2.7.1 Introduction to energetic materials

Energetic materials are materials that can release large amounts of energy relatively quickly when they are initiated. They are a part of the domain of pyrotechnics; the classical categories of energetic materials are explosives, propellants and fuel–oxidizer mixtures such as thermites. These materials have one common property: the energetic reaction does not depend on oxygen from the surrounding atmosphere.

Even though we did not directly use explosives (such as RDX) in this work, we will present some of the basics of these materials, in order to introduce some of the concepts that will be needed for the discussion of nanothermites. A very good overview on explosives (in German) can be found in the book by Köhler and Meyer [155].

Explosives are mostly organic molecules or salts which contain a large amount of nitrogen and oxygen atoms. The nitrogen atoms react to form N_2 gas during the decomposition, while the oxygen atoms react with the organic moieties to CO_2 and H_2O .

The *oxygen balance* of an explosive is the difference (in weight percent) between the quantity of oxygen contained in the molecule and the quantity needed for complete combustion. In the ideal case, i. e. an oxygen balance of zero, there is just enough oxygen in the molecule to oxidize all the other atoms in it (except N). A negative oxygen balance means that there is not enough oxygen for a complete anaerobic combustion; this means that carbonaceous or metallic residues will be formed. A positive oxygen balance means that the decomposition of the molecule will release oxygen.

The decomposition of explosives or other energetic materials is triggered by a stimulus in the form of heat, electrical or mechanical energy. This effect is called **sensitivity**, and it is one of the most important properties to investigate. The sensitivity depends on the molecular structure, but also on the particle size, their shape, the number of defects etc. The thermal sensitivity is given as a decomposition temperature, which is measured by thermal analysis and which can vary depending on the heating rate. The other sensitivity values – electrostatic discharge (electrical), impact and friction (mechanical) – are given as *thresholds*. They follow a sort of Weibull statistic: the higher the stress, the more likely an initiation. Thus, along with a threshold, the corresponding probability must be given. At ISL, we give the threshold for one positive pyrotechnic event in six consecutive tests (1/6); this value corresponds to a “safe” stress level that can be applied during handling. Other laboratories use the so-called Bruceton “up/down” 50 : 50 method: starting from an arbitrary level, the stress is increased by one step for each negative reaction and decreased for each positive one. After a while, the method converges around a threshold where the probability of initiation is 1/2.

Depending on their sensitivity, these materials are classified as *primary* or *secondary explosives*. Primary explosives are very sensitive to impact, friction and/or heat. The idea is that small quantity of primary explosive, which is often combined with a booster in a blasting cap, can initiate a much larger quantity of secondary explosive, which is much safer and easier to handle. The two are combined just before starting the reaction.

Primary explosives are often heavy metal salts, such as lead azide $\text{Pb}(\text{N}_3)_2$ and mercury fulminate $\text{Hg}(\text{CNO})_2$. A few important organic secondary explosives are given in Figure 2.16. The most important ones are RDX, TNT, PETN and ammonium nitrate (NH_4NO_3). Some sensitivity values of explosives are given in Table 2.4.

The decomposition of an energetic material follows one of the following two basic mechanisms:

► Deflagration

A deflagration is a decomposition reaction that propagates at a subsonic velocity through the material, without involving oxygen from the ambient air. It propagates through diffusion of the heat released by the reaction, while the reaction products (mostly gases) are transported away in the opposite direction.

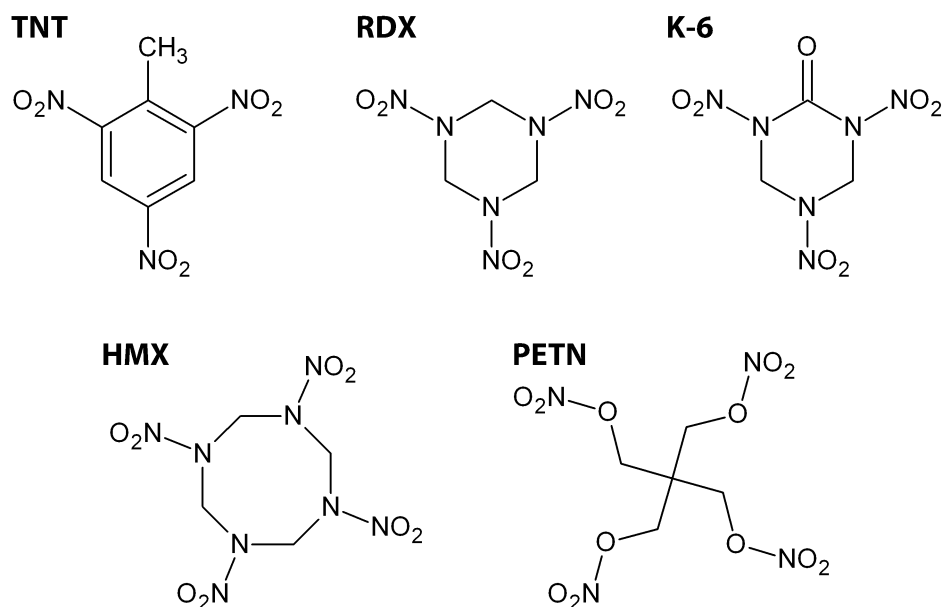


Figure 2.16 Molecular structures of some important secondary explosives: 2,4,6-trinitrotoluene (TNT), cyclotrimethylenetrinitramine (hexogen, RDX), "keto-RDX" (K-6), cyclotetramethylenetetranitramine (octogen, HMX) and pentaerythroltetranitrate (PETN).

product	impact sensitivity (J)	friction sensitivity (N)
TNT	360	22
RDX (hexogen)	160	3.5
HMX (octogen)	108	3.5
PETN	72	2.9
Pb(N ₃) ₂ (lead azide)	2.5–6	0.1–1
Hg(CNO) ₂ (mercury fulminate)	1–2	< 1

Table 2.4 Impact and friction sensitivity of some secondary (top) and primary (bottom) explosives. Data on secondary explosives are ISL measurements, the sensitivities of primary explosives are taken from [155].

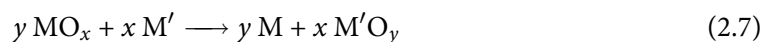
► Detonation

A decomposition reaction which propagates through a supersonic shock wave in the material is called a detonation. At the front of the shock wave, temperature and pressure change strongly and suddenly, initiating the decomposition of the material. The shock wave in a detonation propagates with a velocity between about 1500 and 9000 m/s.

Propellants are energetic materials that do not detonate but show a rapid deflagration under gas release. They are used e. g. for the acceleration of projectiles and rockets. Most propellants in use today are based on nitrocellulose mixed with stabilizers and plasticizers.

Fuel–oxidizer mixtures are mixtures between a reducing agent, called the fuel, and an oxidizer. For example, mixtures of potassium chlorate KClO_3 and organic fats or oils (such as diesel oil) used to be called cheddites; they are no longer in use due to the dangerous and erratic sensitivity of chlorate-based mixtures. ANFO (ammonium nitrate fuel–oxidizer) formulations are widely used safe explosives, for example in mining.

Thermites are also fuel–oxidizer mixtures, in which the fuel is a metal or metalloid (such as aluminum) and the oxidizer is a metal oxide whose corresponding metal is more “noble” according to the electrochemical series. The two components react to form the more stable oxide:



A well-known thermite mixture is composed of aluminum and iron oxide and has the reaction



This reaction generates so much heat that liquid iron is produced, which makes it useful (and common) for welding applications. However, many other metals and oxides can be used as thermites. Fischer and Grubelich [156] published a theoretical survey of thermite and intermetallic reactions, giving the adiabatic reaction temperature,⁷ with and without taking phase changes into account, as well as the heat of reaction. Some of these systems can reach extremely high temperatures; the $\text{Y/I}_2\text{O}_5$ mixture, for instance, can reach up to 12000°C.

The principal disadvantage of thermites is their slow energy release, with reaction times on the order of minutes. Furthermore, their reaction creates no gases or only small amounts. We will see in the next section how the use of nanomaterials can eliminate these deficits.

⁷neglecting the heat loss with the environment

2.7.2 Nanostructuring

The relation between energetic materials and nanomaterials is twofold. On the one hand, the use of nanoparticles and nanocomposites for energetic formulations allows to improve their properties, which can lead to completely new applications, and to gain insight into the fundamental physical processes. On the other hand, energetic reactions – detonations and thermite reactions – can be used to synthesize new materials. The most interesting example for this is the detonation synthesis of nanodiamonds [157]: A hexolite (70 wt-% TNT + 30 wt-% RDX) charge is detonated in a detonation chamber. This formulation has a negative oxygen balance, which leads to the formation of carbonaceous residues. Under the conditions of the detonation (10–30 GPa of pressure, temperatures of 3000–4000 K), diamond is formed; as these conditions only exist for a few microseconds, their growth quickly terminates, leading to particles with a size of 2–5 nm. To complete the circle, nanodiamond can be used as a fuel in a fuel–oxidizer mixture based on potassium chlorate [158].

Nanostructured explosives can be pelletized by compression without the addition of a polymer binder. The incorporation of RDX in a porous matrix, such as chromium(III) oxide [7], leads to interesting *confinement effects*. For an RDX loading of the matrix of under 10 wt-%, the explosive forms independent, discontinuous nanoparticles inside the mesopores of the matrix. Between 10 and 40 wt-% of RDX, explosive particles are also found on the oxide surface outside the pores, but they are still independent. Between 40 and about 75 wt-% of RDX, the explosive is continuous but in the form of a nanometric layer. For more than 75 wt-% RDX, the explosive completely surrounds the matrix, resulting in a behavior almost like the pure substance.

The decomposition of these products, as measured by DSC (Figure 2.17), is very different depending on the microstructure. The topmost curve is the same as in pure, microcrystalline RDX. It melts at 204°C (endothermic peak), immediately followed by the decomposition. On the other hand, all the nanostructured products shown in the figure decompose *before* melting. The confined nanoparticles (bottom curve) react in a single exothermic peak starting at about 130°C. The non-confined nanoparticles react at a slightly higher temperature, which results in two exothermic peaks in the curves at 14.3, 25 and 40 wt-% of RDX. A similar behavior was seen when infiltrating RDX into the porosity of activated carbon [159].

Nanothermites, also called superthermites or Metastable Intermolecular Compounds (MICs), have many advantages compared to classical thermite formulations [2]. In these mixtures, both oxidizer and fuel are used in the form of nanoparticles, creating a much more intimate mixture. Because of this, the reaction velocity is increased by a factor of 100 or more, which places them in the range of deflagrating explosives. For MoO_3/Al mixtures, for example, burning rates of around 350 m/s have been found experimentally [3]. Today, nanothermites find applications in microthrusters [4], igniters, actuators, lead-free electric primers for ammunition [5], micro-

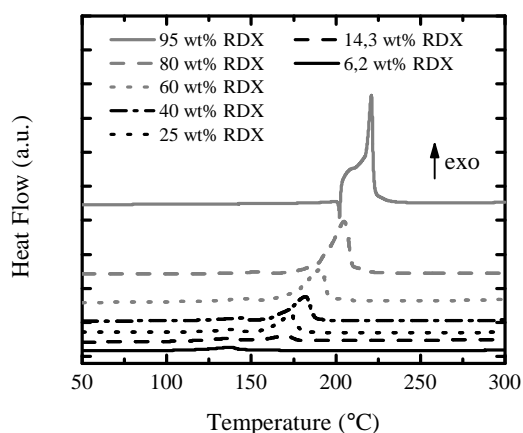


Figure 2.17 DSC curves of $\text{Cr}_2\text{O}_3/\text{RDX}$ nanocomposites with different weight contents of RDX, showing the strong dependency of the decomposition temperature from the particle size and confinement. Reproduced from [7].

and nanoelectromechanical systems (MEMS/NEMS) and other fields. Contrary to thermites prepared from micron-sized particles, nanothermite formulations can be easily pelletized without the addition of a binder. The higher homogeneity also leads to a better reproducible properties and thus to a more reliable operation.

Aluminum nanoparticles are commercially available; the aluminum used in this work, for instance, was bought from NovaCentrix (Austin, TX). Alas, the USA have been considering aluminum nanoparticles as “strategic material” for about three years, which leads to severe export restrictions. As there are currently no european suppliers for good nano-Al, this means that it is very difficult for European researchers to get the needed raw materials.

2.7.3 Desensitization of energetic nanomaterials

Several strategies to decrease the sensitivity of nanothermites and other energetic nanomaterials have been proposed in the literature. To understand how they work, we must consider the initiation mechanism associated with each type of sensitivity. The mechanical sensitivity of a nanothermite is caused by friction *between* the oxidizer and the fuel particles. This friction causes local heating and the formation of “hot spots”, where the reaction is initiated. The rapid absorption of the energy of an impact gives the same local heating effect. Furthermore, the protective oxide layer on the aluminum particles can be broken off, exposing the highly reactive bare aluminum metal.

To decrease the importance of this mechanism, the **EOR process** has been developed in our laboratory and patented by the ISL. It consists of the deposition of aluminum metal *around* tungsten trioxide nanoparticles to create WO_3/Al composite particles. This morphology can be clearly distinguished in the TEM micrograph in Figure 2.18. To achieve the deposition, a solution of alu-

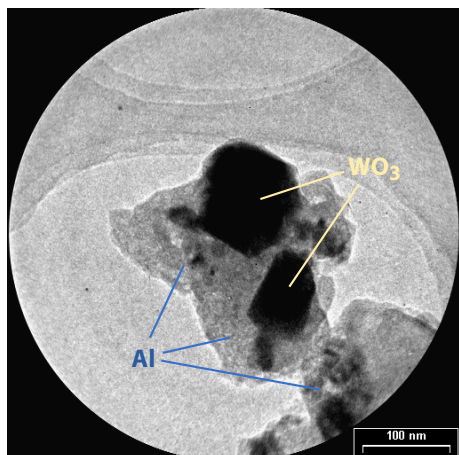


Figure 2.18 Transmission electron micrograph of tungsten trioxide (WO_3) particles coated with metallic aluminum, prepared by the EOR process.

aluminum hydride AlH_3 in diethylether is prepared by the reaction



The oxide is added to the solution, and the hydride is decomposed by gentle and careful heating. The product is an WO_3/Al nanothermite in which there can be no friction between oxide and metal. It is insensitive to impact ($> 49 \text{ J}$) and friction ($> 360 \text{ N}$).

Kwok and coworkers [160] coated aluminum nanopowders with polyethylene and polypropylene by a Ziegler-Natta process. The coated particles contain between 7 and 25 wt-% of polymer. They mixed the nano-Al with organic explosives – TNT, RDX and glycidyl azide polymer – in order to lower their initiation temperature. Such mixtures are usually highly sensitive to electrostatic discharge (ESD), just like the aluminum nanoparticles themselves. With a threshold of 6 mJ, the products can easily be initiated accidentally by an ungrounded operator.⁸ The polymer-coated aluminum particles however are insensitive to electrostatic discharges (threshold $> 156 \text{ mJ}$).

⁸The human body can deliver electrostatic discharges up to 156 mJ. See section 3.5.2 (page 55) for detailed explanations.

Experimental techniques

3.1 Filling of carbon nanotubes

The straightforward way of filling nanotubes is to bring them in contact with a liquid, which will enter the nanotubes through capillarity. The way that this works at the nanoscale is different from the macroscopic behavior. For the derivation of the macroscopic capillarity laws, it is necessary to have a large number of liquid molecules that can move freely in the liquid phase, without having direct contact with the capillary walls. However, for a nanoscale capillary that is sufficiently small, a large part or even *all* liquid molecules are in direct contact with the wall. Thus, the smaller the capillary diameter (i. e. the inner diameter of the nanotube), the more difficult it is to fill it over a large distance. Another factor to take into account is the viscosity of the liquid.

When infiltrating nanotubes with a solution, a majority of the molecules entering the tube will be solvent molecules. This fact limits the maximum filling yields attainable for such systems.

Fortunately, in many cases, molten compounds can be used. Many metal oxides are ceramics with a high melting point. Chromium oxide, for example, melts at 2435°C [161]. However, instead of directly melting the oxide, we can melt a precursor salt, which can then be decomposed by further heating.

3.1.1 Reactive infiltration

2.0 g of precursor are dissolved in 5 mL of concentrated nitric acid HNO_3 (68–70%, Acros) in a 50 mL one-neck flask. The as-received carbon nanotubes (without pretreatment, contrary to the other methods detailed above) are added, and a water-cooled reflux condenser is fitted on the flask. Under magnetic stirring, the contents are brought to a gentle reflux (bath temperature of 123°C) for 16 hours.

After cooling down to room temperature, the suspension is filtered over an acid-resistant OMNIPORE 450 nm membrane (Millipore). The residue is transferred into a quartz boat and calcined as above without any further drying.

3.1.2 Infiltration of opened nanotubes with aqueous solutions

The opened, dried carbon nanotubes are put in a beaker. The precursor solution is added, and the suspension is magnetically stirred on a hot plate which is held at 60–70°C. The liquid is left to evaporate very slowly from the open beaker (about 12–16 hours).

After complete evaporation, the resulting dry paste is transferred into a tubular furnace in a quartz boat. There, it is calcined under an argon flow of 200 mL/min, using a heating rate of 1 K/min and a hold time of one hour at the final temperature (second column in Table 5.1).

3.1.3 Infiltration of opened nanotubes with melts

The opened nanotubes are put into a 50 mL two-neck flask. One of the necks is closed by a septum, while the other one is connected to a rotary-vane vacuum pump via a stopcock and a liquid nitrogen trap. The flask is heated to 150°C for 1 h while the vacuum system is running. The end pressure is below $3 \cdot 10^{-2}$ mbar. The molten precursor is injected through the septum with a syringe. The flask is transferred to a heated ultrasonic bath, where the suspension is sonicated for 5 min. Then, it is transferred back to a magnetic hot plate, where it is stirred at 50°C (for manganese nitrate) for 16 h.

The resulting paste is washed onto a 450 nm filter (White Nylon, Millipore) with cooled isopropanol and filtered immediately. The filter cake is transferred into a quartz boat and calcined in a tubular furnace as above.

3.1.4 Infiltration of opened nanotubes with melts, simplified procedure

The chosen quantity of the precursor is heated to 50°C in a flask until it is completely molten. The carbon nanotubes are added, and the mixture is stirred in the stoppered flask at 50°C for 72 h. The black slurry is transferred to a 450 nm OMNIPORE filter (Millipore) on a vacuum filtration apparatus and washed two times with 1–2 mL of isopropanol. The filter cake is transferred into a quartz boat and calcined in a tubular furnace.

3.2 Preparation of nanothermites by physical mixing

Procedure A. A pear-shaped flask is filled with the dispersant (*n*-hexane or acetonitrile), then with the calculated amounts of oxidizer and fuel. The dispersant is chosen so that it does not react with nor dissolve any of the components. For the nanotube-containing formulations, the quantity of dispersant added is chosen so that the nanotube concentration is on the order of 1–2 g/L. The dispersion is magnetically stirred for 15 min, then sonicated in a bath for 15 min. Finally, the dispersant is removed on a rotary evaporator. At the end of this operation, the recuperation flask is emptied, and the sample is held for 1 h under vacuum. The final pressure, using a rotary vane

vacuum pump, is below 1 mbar. The product is carefully collected from the wall of the flask using a spatula.

Procedure B. The oxide-filled carbon nanotubes and the dispersant (acetonitrile) are mixed in a pear-shaped flask. The slurry is sonicated for 30 min using a sonotrode (80% power, 20% pause time). Then, the aluminum nanoparticles are added, and the preparation is continued as in procedure A.

3.3 Synthesis of manganese dioxide nanoparticles

The “reference” nanothermite used for comparing the mechanical sensitivities is composed of aluminum nanoparticles (Al 50 P) and manganese dioxide nanorods. Their synthesis, which has been described in an earlier publication of our group [162], is explained below.

In a 250 mL flask, 6.0 g (38 mmol) of potassium permanganate KMnO_4 (Prolabo) are dissolved in 120 mL of H_2O . The flask is placed in an ultrasonic bath, and 12 mL of concentrated sulfuric acid H_2SO_4 are added dropwise while sonicating the solution. After cooling down to 20°C , 60 mL (1.03 mol) of absolute ethanol (Rectapur, Prolabo) are added dropwise during about 40 min while sonicating continuously. The suspension is centrifuged at 4000 rpm for 5 min, and the supernatant solution is decanted. The brown precipitate is washed five times (in sonication–centrifugation cycles) with ultrapure water until a neutral pH in the supernatant is observed. The product is washed three more times with acetone. Finally, the dispersant is evaporated, and the product is dried for 3 h under vacuum.

Characterization. The product of the synthesis is a fine brown powder without any visible aggregates. Its BET surface is $248 \text{ m}^2/\text{g}$. X-ray diffraction¹ shows that the product only contains the $\alpha\text{-MnO}_2$ phase; the peaks are large and correspond to crystallite sizes of 3–7 nm. Observation of the product with TEM² shows a rod-like morphology. The lateral dimension of the manganese dioxide particles is about 3 nm while the length varies from about 40 to 80 nm.

3.4 Characterization methods

3.4.1 Thermal analysis (TG/DTA/DSC)

One of the most important analysis methods used in this work is thermal analysis. In these experiments, a small quantity of sample (1–20 mg) is heated under a controlled atmosphere according to a given program. Most often, this program is a ramp, where the sample is heated at a constant

¹Shown in Figure B.1, page 187.

²Figure B.2, page 188.

rate until a target temperature is reached. Isothermal experiments, where the sample is held at a certain temperature for a given amount of time, are also common.

There are three basic types of measurement, several of which can be combined in one instrument:

- ▶ TG or TGA (Thermogravimetric analysis) measures the weight of the sample depending on the temperature. These measurements are always carried out in open crucibles to allow gaseous reaction products to escape and the sample to react with the atmosphere.
- ▶ DTA (Differential Thermal Analysis) measures the temperature difference between the crucible containing the sample and an empty reference crucible. When an exothermal reaction happens, the sample will heat up more than the reference, which is only heated by the surrounding furnace. In an endothermal reaction, the temperature of the sample stays the same (e.g. at the melting point) until the reaction is finished. The temperature difference signal can be used to see reactions even when the weight of the sample does not change, e. g. melting of the sample.
- ▶ DSC (Differential Scanning Calorimetry) measures not the temperature difference between sample and reference but the *heat flow* (in W) required to keep both at the same temperature. This allows the calculation of reaction enthalpies by integrating the area under a reaction peak. The *modulated DSC* technique, where the ramp is overlaid with a sinusoidal temperature variation, permits to distinguish the reversible heat flow (due to the heat capacity C_p of the sample) from the irreversible one (due to reactions). This allows to see glass transition in polymers, for example.

Three machines were used in this work, each with different characteristics:

- ▶ a Q1000 DSC by TA Instruments. This high-precision instrument only measures the heat flow, not the sample weight. We used sealed hermetic gold-plated crucibles provided by the Swiss Institute of Security, which can withstand several hundred bars of pressure. This guarantees an exact enthalpy determination even for reactions with gaseous products as they cannot leave the crucible. In open crucibles, like those used in TG experiments, hot gases can evacuate some of the heat generated by the reaction.
- ▶ a Q600 TG/DSC by TA Instruments, which uses alumina crucibles located on horizontal alumina beams for the sample and reference. The sample weight is measured with a nominal precision of 0.1 μg . The measured heat flow is very precise, however the baseline is not as flat as in the Q1000. The instrument has an entry for the admixture of a reactive gas. This allows measurements under “artificial air”, i. e. an 80/20 mixture of argon and oxygen. In case of an overheating during the oxidation (burning) of a sample, the oxygen content of the atmosphere can be reduced to slow down the reaction.

- ▶ a Seiko TG/DTA 6200, which is very similar to the Q600 described above. It allows measurements under nitrogen, argon or under ambient air. The values for the combustion residue are more reproducible with this machine than on the Q600.

Combustion of carbon materials. When heated under an oxidizing atmosphere, carbon burns completely, giving CO_2 and/or CO as gases. After complete combustion, a certain amount of residue is left.

For “pure” samples, the residue is the amount of inorganic impurities, given as the corresponding oxide. For example, the FutureCarbon MWNTs³ contain Co nanoparticles used as catalyst in the synthesis. After the carbon is oxidized, these particles are also oxidized, giving Co_3O_4 .

For carbon nanotubes filled with metal oxides, the combustion residue is equal to the relative amount of metal oxide in the composite. However, the oxide phase in the combustion residue may be different from the one in the original composite, for example due to carbothermal reactions or thermal decomposition of the oxide.

For assessing the thermal stability of carbon materials, the “oxidation temperature” T_o [163] is defined as the maximum of the first derivative of the mass

$$T_o = \left. \frac{dm}{dT} \right|_{\max} .$$

This temperature depends on the experimental conditions, especially on the heating rate used. For this reason, in this manuscript, we only compare relative T_o values for samples before and after different treatments. We always use the same heating rate, 5 K/min, which is the one recommended by the NIST (National Institute of Standards and Technology) [163] to avoid spontaneous and uncontrolled combustion of the samples.

Aluminum content of nano-Al. All forms of aluminum particles are covered by a layer of oxide. In aluminum nanoparticles, the oxide content is especially high due to their specific surface area. Additionally, a certain amount of water is usually adsorbed on the particle surface. For correct nanothermite formulations, we thus need to know the precise content of metallic aluminum in the particles.

For analyzing nano-Al, we use a relatively slow ramp (5 K/min) and artificial air that is depleted in oxygen (90 + 10) in order to prevent an overheating effect during the combustion. When overheating occurs, some sample is often lost due to convection, giving inaccurate measurements.

Figure 3.1a shows a typical thermogravimetric analysis result for Al 50 P particles. There is a small weight decrease at low temperatures, corresponding to the desorption of surface water and of hydroxyl groups on the surface of the particles. For higher temperatures, we see a weight

³See section 4.1.3, page 63.

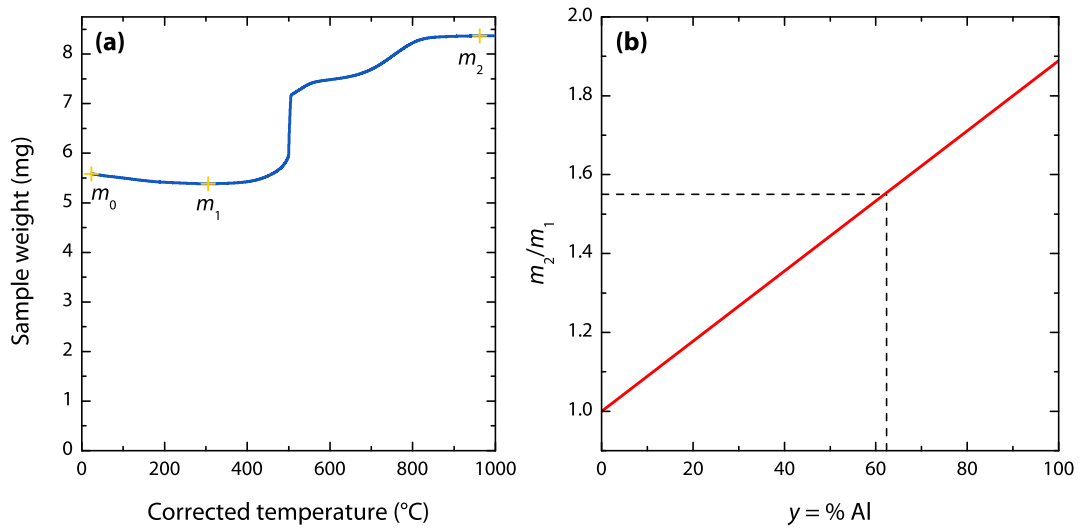
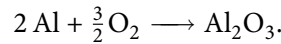


Figure 3.1 Thermogravimetric oxidation of a sample of Al 50 P aluminum nanoparticles (batch 2/10) at 5 K/min (a). The masses m_0 , m_1 and m_2 are defined in the text. Linear interpolation for determining y from m_2/m_1 (b).

increase due to the oxidation of aluminum to alumina



Thus, during heating, there is a minimal mass corresponding to Al and Al_2O_3 without adsorbed water. At high temperatures, there is a maximum mass corresponding to complete oxidation. We thus define three masses, as indicated in Figure 3.1:

- ▶ $m_0 = 5.5836$ mg: initial sample mass (adsorbed water, Al and Al_2O_3)
- ▶ $m_1 = 5.3847$ mg: minimum mass (Al and Al_2O_3)
- ▶ $m_2 = 8.3692$ mg: maximum mass (completely oxidized)

In the following derivation, let Y denote the mass percentage of the component given as an index (H_2O , Al, Al_2O_3). Furthermore, let $y = Y_{\text{Al}} / (Y_{\text{Al}} + Y_{\text{Al}_2\text{O}_3})$ be the aluminum content *in the dry matter*.

The amount of adsorbed water in the sample is obviously

$$Y_{\text{H}_2\text{O}} = \frac{m_0 - m_1}{m_0}. \quad (3.1)$$

The factor m_2/m_1 directly allows to calculate the percentage of metallic aluminum by linear interpolation between two extreme cases (Figure 3.1b): If the sample consisted completely of alumina

($y = 0$), we would have

$$m_2/m_1 = 1,$$

as there would be no mass increase due to oxidation. If we had only aluminum ($y = 1$), we would have

$$m_2/m_1 = \frac{M_{\text{Al}_2\text{O}_3}}{2M_{\text{Al}}} = \frac{101.96}{2 \cdot 26.98} = 1.889.$$

This means that the aluminum content in the dry matter can be calculated by linear interpolation between the two:

$$y = \frac{Y_{\text{Al}}}{Y_{\text{Al}} + Y_{\text{Al}_2\text{O}_3}} = \frac{(m_2/m_1) - 1}{0.889} \quad (3.2)$$

Finally, correcting for the water contents gives:

$$\begin{aligned} Y_{\text{Al}} &= \frac{m_1}{m_0} y \\ Y_{\text{Al}} &= \frac{m_1}{m_0} \cdot \frac{(m_2/m_1) - 1}{0.889} \end{aligned} \quad (3.3)$$

Inserting the numerical values given above for batch 2/10 of Al 50 P nanoparticles gives

$$Y_{\text{Al}} = 60.125 \text{ wt-\%}.$$

3.4.2 Nitrogen adsorption

The adsorption of nitrogen near its boiling point (77 K) onto a solid is one of the most common methods of characterizing its surface area and porosity. The graph of the amount of gas adsorbed V_{ads} (usually measured in cm^3/g) against the relative pressure p/p_0 (where p_0 is the saturation pressure at the measurement temperature) is called an *adsorption isotherm*. The basic framework for interpreting the isotherm and getting the specific surface area (in m^2/g) was given by Brunauer, Emmett and Teller in 1938 [164] and is thus called the *BET theory*. They presume that the same forces that produce condensation are also responsible for multilayer adsorption, i. e. that the heat of adsorption for the second and all subsequent layers are equal to the heat of liquefaction of the gas. They obtain the isotherm equation

$$V_{\text{ads}} = \frac{V_m c p}{(p_0 - p) \{1 + (c - 1)(p/p_0)\}}, \quad (3.4)$$

which can be linearized as

$$\frac{p}{V_{\text{ads}}(p_0 - p)} = \frac{1}{V_m c} + \frac{c - 1}{V_m c} \frac{p}{p_0}. \quad (3.5)$$

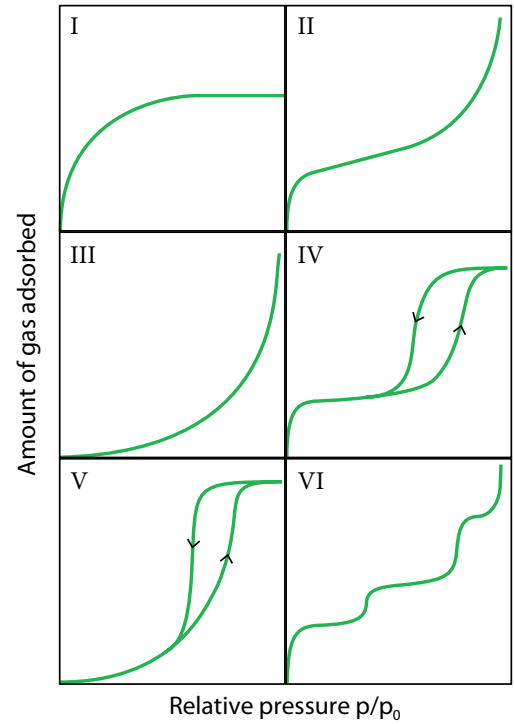


Figure 3.2 Classification of the types of gas adsorption isotherms on solid surfaces. Types I to V as classified by Brunauer *et al*, type VI is the stepped isotherm. Drawn after [167].

Linear regression on a plot of $p/V_{\text{ads}}(p_0 - p)$ against p/p_0 gives the values of the two constants V_m and c ; the former is the volume of gas required to form a complete unimolecular adsorbed layer, which is used to calculate the specific surface area S_{BET} . The constant c is

$$c \approx \exp\left(\frac{E_1 - E_L}{RT}\right), \quad (3.6)$$

where E_1 is the heat of adsorption of the first layer and E_L is the heat of liquefaction of the gas.

If the thickness of the adsorbed layers cannot be greater than a finite number n (for example in a pore of finite diameter), the isotherm equation is

$$V_{\text{ads}} = \frac{V_m c x}{1 - x} \left\{ \frac{1 - (n + 1)x^n + nx^{n+1}}{1 + (c - 1)x - cx^{n+1}} \right\} \quad (3.7)$$

with $x = p/p_0$. This equation reduces to (3.4) for $n = \infty$.

Five standard types of isotherms have been defined by Brunauer, Deming, Deming and Teller (“BDDT”) [165]; a sixth one, the stepped isotherm, has been added by the IUPAC [166]. Their typical form is shown in Figure 3.2. They correspond to the following types of solids:

- A type I isotherm (Langmuir adsorption isotherm) is obtained if only a monolayer of gas

can be adsorbed on the solid, such as for microporous samples. This corresponds to putting $n = 1$ in equation (3.7).

- ▶ A type II isotherm (S-shaped or sigmoidal isotherm) is typical for multilayer adsorption in a non-porous solid or if the porosity is only located between the particles. In nitrogen adsorption experiments, it is the most common type of isotherm. It implies that $c \gg 1$ as defined in equation (3.6), i. e. that adsorption on the solid is preferred over adsorption on another gas particle.
- ▶ A type III isotherm occurs when $c < 1$ in equation (3.4), i. e. $E_1 < E_L$. This means that liquefaction of the adsorbate is preferred over adsorption on the surface, indicating an unfavorable adsorbent–adsorbate interaction. It is usually not observed for nitrogen adsorptions; the example given by Brunauer and coworkers is bromine adsorption on silica gel at 79°C.
- ▶ A type IV isotherm indicates a mesoporous solid, where capillary condensation happens inside the pores. The desorption branch shows a hysteresis behavior. It is obtained from equation (3.7) for a finite value of $n > 1$.
- ▶ A type V isotherm is analogous to type III and IV isotherms in that it occurs for a finite $n > 1$ (i. e. limited pore sizes with capillary condensation) and $c < 1$ (i. e. weak interactions between the adsorbent and the adsorbate). It is observed for example in water vapor adsorption on charcoal at 100°C.
- ▶ The type VI isotherm is also very rare in practice. It is indicative of a very homogeneous, non-porous surface on which each adsorption layer is completed before the next one begins.

BJH. In 1951, Barrett, Joyner and Halenda introduced the theoretical framework for determining the pore size distribution (PSD) from the desorption branch of the isotherm [168,169], known today as the *BJH method*. It is based on the assumptions that

- ▶ the pores are cylindrical (more precisely that pore volume and capillary volume are related to each other as the square of some adequate measure of their cross sections), and
- ▶ that the amount of adsorbate in equilibrium with the gas phase is retained by the adsorbent by two mechanisms:
 - ▷ physical adsorption *on* the pore walls, and
 - ▷ capillary condensation *in* the inner capillary volume.

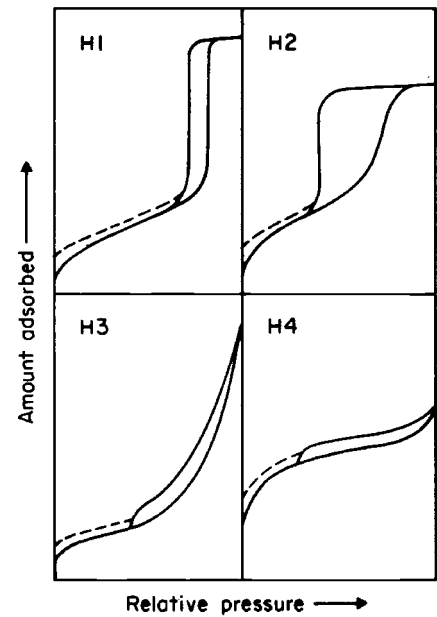


Figure 3.3 IUPAC classification of the hysteresis between the adsorption and the desorption branch of an isotherm. Reproduced from [166], © 1985 IUPAC.

All pores are filled with liquid adsorbate at a relative pressure $p/p_0 \approx 1$. Stepwise desorption results in two processes: the pores are emptied in the order of their size – the largest pores first – and the thickness t of the adsorbed layer in the partially filled pores is reduced. For each relative pressure, there exists a critical pore radius representing the largest filled pores at this pressure. This radius is calculated from the classical Kelvin equation

$$\ln \left(\frac{p}{p_0} \right) = - \frac{2\sigma V_m}{RT r_k}, \quad (3.8)$$

where σ is the surface tension of liquid nitrogen at 77 K, V_m is its molar volume and r_k is the radius of the capillary.

Porosity in a solid usually gives a hysteresis loop between the adsorption and desorption branch of the isotherm. As the desorption branch represents an equilibrium process, this branch is used for PSD calculations. Four types of hystereses have been standardized by the IUPAC, as shown in Figure 3.3. Their precise meaning is not quite understood. The interpretation given by Condon [170, p. 13] is the following:

- ▶ H1 (nearly vertical and parallel adsorption/desorption branches): regular, even pores without interconnecting channels.
- ▶ H2 (sloping adsorption and nearly vertical desorption branch): pores with narrow and wide sections and possible interconnecting channels.

- ▶ H3 (sloping adsorption and desorption branches covering a large range of p/p_0 with underlying type II isotherm): slit-like pores, adsorbent-adsorbate pair that would give a type II isotherm without pores.
- ▶ H4: similar to H3 but with underlying type I isotherm.

In the case of H2 hysteresis, it is not recommended to calculate a pore size distribution (PSD) from the desorption branch [166]. Carbon nanotubes and their composites most often result in H3 hystereses, although much of the porosity seems to be interparticular rather than due to their endohedral space.

Particle size determination from the BET surface, spherical particles. The specific surface area S_{BET} allows determining a mean particle size if some assumptions are made about the nature and shape of the particles. The easiest approach (which is, of course, not applicable to carbon nanotubes) is to consider the particles as non-porous spheres.

The specific surface area S_{BET} is the surface of the sample per unit mass, while the density ρ is the mass per unit volume. Multiplying the two gives

$$\rho S_{\text{BET}} = \frac{S}{m} \frac{m}{V} = \frac{S}{V}. \quad (3.9)$$

For a sphere of radius r , inserting the well-known expressions for surface and volume, one obtains:

$$\begin{aligned} \rho S_{\text{BET}} &= \frac{4\pi r^2}{\frac{4}{3}\pi r^3} \\ &= \frac{3}{r} \\ d &= \frac{6}{\rho S_{\text{BET}}} \end{aligned} \quad (3.10)$$

As real powders are usually not monodisperse but have a distribution of particle sizes, the resulting particle diameter d is a fictitious “mean” diameter. This calculation method does not give any information about the size distribution. Moreover, for nanopowders, care must be taken about the value for ρ , which may not be the same as the bulk density of a compound. The real density of the substance can be determined by helium pycnometry, although the method is experimentally challenging in the case of nanopowders.

Size determination for carbon nanotubes. Carbon nanotubes are obviously not spherical particles. However, equation (3.9) stays valid. Let us consider a cylindrical model for a nanotube of length l , external diameter $D = 2R$ and internal diameter $d = 2r$. The wall thickness is then $R - r$. We postulate that $L \gg D$, so that the mass and the surface of the end caps is negligible.

If both ends of the nanotube are closed and there is no hole in the sidewall, the inner surface is not accessible to the gas being adsorbed. The surface S is then equal to the outer surface area, while the volume V is equal to the cylindrical graphitic shell:

$$\begin{aligned}\rho S_f &= \frac{2\pi Rl}{\pi(R^2 - r^2)l} \\ \rho S_f &= 2\frac{R}{R^2 - r^2}\end{aligned}\quad (3.11)$$

If, however, at least one of the tube ends is open, gas will adsorb on the inner surface of the nanotube, too. This gives a larger surface area:

$$\begin{aligned}\rho S_o &= \frac{2\pi(R+r)l}{\pi(R^2 - r^2)l} \\ &= \rho S_f + 2\frac{r}{R^2 - r^2} \\ \rho S_o &= \frac{2}{R - r}\end{aligned}\quad (3.12)$$

This surprising result means that the BET surface area of completely opened tubes only depends on the number of walls, not on the diameter. A single-walled nanotube, with $\rho = 2.25$ like graphite and $R - r = 335$ pm, would have $S_{\text{BET}} = 2650$ m²/g, a double-walled one ($R - r = 2 \cdot 335$ pm) 1325 m²/g etc. These values are never reached in practice; this is mainly due to bundling, especially for small nanotubes. Bundling decreases the surface free energy due to the favorable π - π interaction between two tubes. MWNT show little bundling, so that the relations derived above are approximately valid. Other effects that influence the specific surface area are impurities (which have a higher density ρ in the case of catalyst particles) and amorphous carbon.

3.4.3 Raman spectroscopy

Like in infrared spectroscopy, Raman spectroscopy measures vibrational energies in a sample. However, the principle is not direct absorption but *inelastic scattering* (Figure 3.4): a laser beam with a wavelength in the visible, NIR or UV range is used to excite the sample. Most of the light is elastically scattered (so-called Rayleigh scattering) while a small proportion of the photons decrease (Stokes lines) or increase (anti-Stokes lines) their energy by a certain amount, corresponding to the energy of vibrational mode of the molecule.

While a transition has to change the *dipole moment* of the molecule to be IR-active, it must change the *polarizability* of the molecule to appear in a Raman spectrum. In group theory, the dipole moment transforms as a linear function while the polarizability transforms as a quadratic function. Thus, the selection rules for Raman spectra are different than for IR spectra. Thus, while sp² carbon materials (graphite, graphene and carbon nanotubes) are normally IR-silent, they have

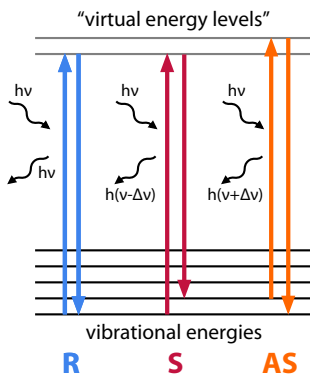


Figure 3.4 Scheme of the energy levels and transitions involved in Raman spectroscopy: Rayleigh (R), Stokes (S) and anti-Stokes (AS) scattering.

several characteristic Raman modes. Ref. [171] by Dresselhaus, Saito and coworkers gives a good overview on the characterization of sp^2 nanocarbons by Raman spectroscopy. Another review, focusing on functionalized SWNT, is found in Ref. [172].

Raman spectroscopy gives extensive information on the carbon skeleton. Pure, defect-free graphene has two main Raman-allowed modes, called G and G'.

The **G band** (for Graphite) or tangential band is due to C—C bond stretching and is found at about 1580 cm^{-1} . All forms of sp^2 carbon show this band. In SWNT, curvature effects give rise to a split of this band into up to six symmetry-allowed phonons. The two dominating ones are called G^+ ($\tilde{\nu} \approx 1590\text{ cm}^{-1}$) and G^- ($1540\text{ cm}^{-1} < \tilde{\nu} < 1580\text{ cm}^{-1}$, depending on the tube diameter). For metallic SWNTs only, there is a considerable interaction between the phonons and the continuum electronic states near the Fermi energy E_F , leading to a low-frequency shift and broadening of the G^- band [173,174]. The line shape can be expressed by the Breit-Wigner-Fano (BWF) resonance shape, which is a non-symmetrical variant of the Lorentzian shape, typically applied in the case of interaction between a discrete state and a continuum, a so-called Fano resonance [175]. The G peak(s) are quite sensitive to strain effects due to external forces or interactions between adjacent layers that are not well understood today [171].

The intercalation and doping of carbon nanotubes modify the G band frequencies. For electron donors, such as K or Rb, this mode is shifted to lower frequencies [46, p. 100], which is evidence for a charge transfer between the nanotube and the dopant. Following the same principle, there is an upshift in frequency when doping with electron acceptors, for example Br_2 , I_2 or even concentrated HNO_3 or H_2SO_4 [176].

The **G' band** is the result of a second-order double resonance process. Its position depends on the incident laser wavelength (*dispersive peak*). It is very sensitive to perturbations of the electronic and/or vibrational energy structure. For SWNTs, the number of peaks and their frequencies depend on the (m,n) indices due to strain induced by the curvature and quantum confinement effects.

Disordered, defect-containing graphite has a lower symmetry, thus the selection rules apply

less strictly. This makes another peak, the **D band** (for Disorder, $\tilde{\nu} \approx 1345 \text{ cm}^{-1}$), appear in the Raman spectrum. The intensity ratio A_D/A_G is a measure for the degree of order or crystallinity in the sample. A second disorder-induced band, the **D' band**, is observed in defect-containing graphene samples at $\tilde{\nu} = 1626 \text{ cm}^{-1}$. Both peaks are dispersive. The $\tilde{\nu}$ values given here are for $\lambda = 514 \text{ nm}$.

For single-walled carbon nanotubes, another mode, the so-called **Radial Breathing Mode (RBM)** appears at Raman shifts below 250 cm^{-1} . The vibration excited by this transition is an expansion–contraction motion of all the carbon atoms in the nanotube. This mode is thus very sensitive to the tube diameter d_t . In fact, from the position of a RBM peak, the diameter of the corresponding nanotube can be calculated using the empirical formula

$$\tilde{\nu}_{\text{RBM}} = \frac{227 \text{ nm cm}^{-1}}{d_t} \sqrt{1 + C_e d_t^2}, \quad (3.13)$$

where d_t is the tube diameter in nm and $\tilde{\nu}_{\text{RBM}}$ is frequency in wavenumbers (cm^{-1}) of the RBM peak [171, 53]. C_e is a parameter describing environmental effects that cause an upshift of the RBM. “Supergrowth” SWNTs have $C_e = 0$, consistent with

$$\lim_{d_t \rightarrow \infty} \tilde{\nu}(\text{RBM}) = 0.$$

Typical values for solutions (HiPCO SWNTs in SDS)⁴ are about 0.05, or about 0.07 for freestanding tubes. Bundling is known to increase the effective value of C_e [75]. The RB modes of SWNT are known to shift by about 8 cm^{-1} per GPa of pressure, which is a result from high-pressure Raman experiments under hydrostatic conditions [177].

Resonance. If the energy of the laser used for exciting the sample is near the energy of an optical transition, the inelastic scattering process no longer involves a “virtual” but a “real” energy level. As a result, the intensity of the Raman peaks is greatly enhanced, and the sample is said to be *in resonance*. This effect is especially important in SWNT, as they have intense optical transitions from a valence band in the corresponding conduction band, whose energies are in the visible range.

The plot of the optical transition energies E_{ij} against the diameter of the corresponding tube is called the *Kataura plot* [179]. It has been presented by Hiromichi Kataura in 1999 and subsequently refined by Riichiro Saito, who also introduced the term. Figure 3.5 shows the Kataura plot with the tube diameter d_t and with the corresponding RBM peak position as the x axis. The latter was calculated by taking equation (3.13) with $C_e = 0.07$. The two photon energies (1.96 eV for 633 nm and 2.4 eV for 514 nm) of the two lasers we used for Raman measurements are shown

⁴For an explanation of the HiPCO and Supergrowth processes, see section 2.2.2 on page 8ff. The formulas of SDS and other surfactants are given in section 2.3.2 on page 15ff.

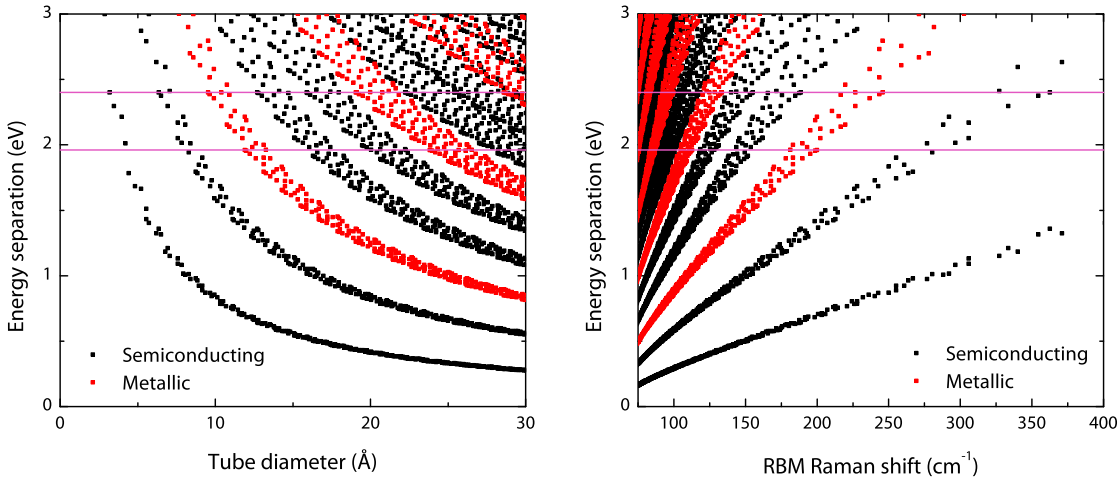


Figure 3.5 Kataura plots showing the optical transition energies E_{ii} of semiconducting (black) and metallic (red) SWNT, depending on either their diameter (left) or the Raman shift of their RBM mode (right), calculated from equation (3.13) with $C_e = 0.07$. The energies for the 514 nm and the 633 nm laser are indicated by horizontal lines. Peak energies are taken from the data files available on Shigeo Maruyama’s homepage [178].

as horizontal lines in the graph. The main contribution to the Raman spectrum for the two energies come from the tubes in resonance, which correspond to the points on or near the horizontal line. If the A_D/A_G ratio varies with the laser energy,⁵ this means that different populations of nanotubes with a different electronic structure or a different number of defects are imaged.

3.4.4 Zeta potential

The zeta (ζ) potential of a particle in a colloidal solution is the potential at the so-called “slipping plane”. A charged particle in solution is surrounded by a cloud of oppositely-charged ions.

Pristine, as-received multi-walled carbon nanotubes have their iso-electric point (i. e. $\zeta = 0$ mV) at about $pH = 4.5$ in water [71]. At a pH of 2, the potential reaches about +30 mV while even a slightly basic solution ($pH = 8$) contains nanotubes with $\zeta = -30$ mV.

Zeta potential measurements are often combined with size measurements by dynamic laser scattering (DLS). However, these methods always give the hydrodynamic radius of the particles. For rod-shaped particles like CNTs, there is essentially no transport in lateral direction. The hydrodynamic radius R_H is thus given by the equation

$$R_H^3 = \frac{3}{4}LR^2, \quad (3.14)$$

⁵See Table 4.1 on page 61.

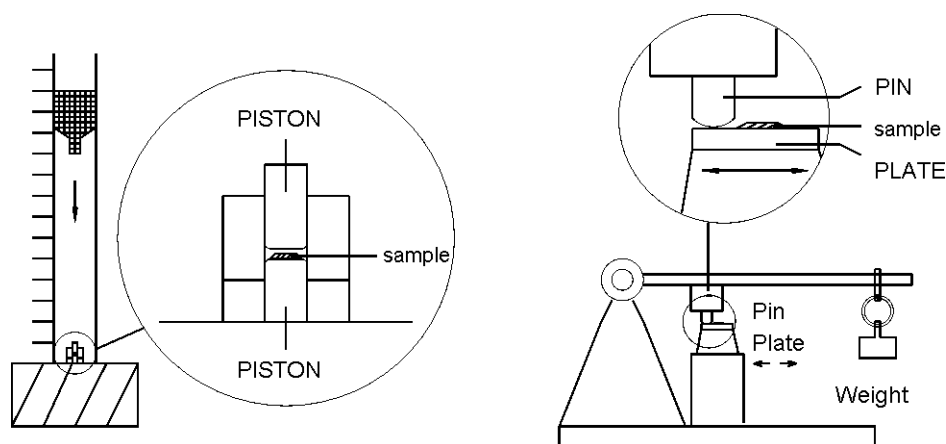


Figure 3.6 Principle of the measurement of impact (left) and friction sensitivity (right) with the BAM devices.

where L is the length and R the radius [180].

3.5 Pyrotechnical characterizations

3.5.1 Mechanical sensitivity

Impact and friction sensitivity are one of the most important criteria for determining whether an energetic material is safe to handle. These kinds of stress occur notably during the transport of such materials, but also while handling them: friction when removing material from a flask, when compressing a pellet, etc. The accepted theory for mechanical initiation is the so-called “hot spot” theory; it states that dynamic mechanical stress induces local heating at certain points, called *hot spots*, inside the material, which initiate the pyrotechnical reactions.

The value measured in these tests is a threshold, i. e. a minimum stress for a pyrotechnic reaction to take place. In the ISL tests, the result given is always the minimum stress for at least one positive reaction in six tests. Other methodologies—for example the Bruceton up/down method—are common in different laboratories, and sometimes the threshold values are given for a 50% ignition probability. The 1/6 thresholds given here will thus be a little lower.

The United Nations created a norm [6] which defines minimum values for the impact (2 J) and friction sensitivity (80 N). If the threshold of an energetic material is below these values, it is deemed as too sensitive for the transport on public roads.

The testing methods are explained very nicely in the book by Sućeska [181]; we will describe them briefly here for the sake of completeness.

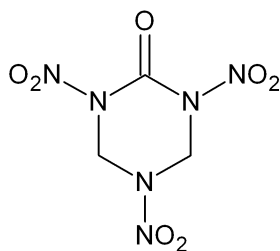


Figure 3.7 Structure of K-6, or Keto-RDX, a brisant explosive.

Impact sensitivity. This test is carried out in a so-called *fall hammer* device [181, p. 23] designed by the BAM (Bundesanstalt für Materialprüfung, Germany). It consists of a drop weight of either 1 or 5 kg that impacts on the sample from a height of up to 1 m. The sample itself (40 μL of powder) is placed between two steel rollers inside a hollow steel cylinder (Figure 3.6). The two rollers are gently pushed together until they touch the sample, the piston device is placed on an anvil, and the weight is dropped by a mechanism. A positive reaction is determined by sound, light effects or smoke. When the reaction is difficult to discern (such as in the case of the nanotube-containing nanothermites), a paper disk in the form of an “O” is placed in the piston device directly under the sample. After the impact, the paper is visually inspected for signs of an initiation [7].

The impact energy E is equal to the potential energy of the weight; it is calculated using the well-known formula

$$E = mgh,$$

where m is the mass of the weight, h is the height and g is the earth acceleration. The measurable threshold values range from 49 J (5 kg, 1 m) down to about 0.981 J (1 kg, 10 cm).

Friction sensitivity. Like the impact sensitivity measurement, the friction sensitivity tests are carried out on a machine designed by the BAM [181, p. 28]. Friction is generated between a ceramic rod with a rough porcelain pistil with a spherical end and a rough ceramic plate (Figure 3.6). The pistil moves forward and backward over the sample (some tens of microliters of powder) that has been put on the plate surface. The normal force with which the pistil presses on the plate is determined by the weight put on a loading arm and its position on the arm; the force corresponding to each pair of parameters is tabulated. A positive pyrotechnical reaction is indicated by sound (crackling), sparks or even a breaking of the plate in the case of very brisant explosives, such as K-6 (Figure 3.7).

3.5.2 Electrostatic discharge (ESD) sensitivity

Electrostatic discharges (sparks) can initiate the reaction of an energetic material. This danger is often underestimated. The energy of a discharge depends on the capacity C of the charged body – which can be a metal container, a human body or other object – and the potential difference U

of the discharge. It is calculated by the formula

$$E = \frac{1}{2}CU^2. \quad (3.15)$$

According to estimations by SME, the largest producer of explosives in France, the human body can deliver up to 156 mJ of ESD energy – enough to ignite many energetic materials. The French legislation on pyrotechnic security contains a long paragraph on protective measures against electrostatic discharges, but no standardized tests for ESD sensitivity exist.

ESD sensitivities are measured in our lab using an ESD 2008 testing device from OZM Research, Czech Republic. A small amount of sample is introduced between two metal electrodes; the sample volume is constant, as it is limited by a polymer ring around the sample. The capacity of the circuit can be set in several steps by introducing known capacitors, while the voltage is controlled by a regulator. At least 4 kV are needed to achieve a repeatable discharge over the distance of the electrodes, which is always kept constant at exactly 1 mm. As in the mechanical sensitivity tests, the higher the energy of the discharge, the more likely an initiation. The value that will be given is the threshold for one positive pyrotechnic event in six tests. In order to distinguish the effect of the discharge itself (ejection of sample) from a positive pyrotechnic initiation, the experiment can be repeated with an inert material (quartz sand) for comparison.

3.5.3 Time-Resolved Cinematography (TRC)

Time-Resolved Cinematography is a method for observing the reactivity and the burning behavior of a nanothermite under conditions similar to real use. It is based on laser ignition of a compressed pellet (Figure 3.8).

In a typical test, 50 mg of nanothermite material are compressed in a steel mold in a hydraulic press to obtain a pellet with a diameter of 4 mm and a height of 1.5–6 mm. Several different pressures are used to determine the influence of the compression. To get information about the apparent density, the dimensions of the pellet are measured with a caliper. The pellet is glued to a duraluminum disk and placed horizontally in the experiment, where it is initiated by a CO₂ laser ($\lambda = 10.6 \mu\text{m}$) operating at a power of $P = 7 \text{ W}$. The pathway of the beam is opened by a mechanical shutter for an adjustable time interval, usually 2 s. At the same time, the optical power arriving on the sample and the light output from the combustion are recorded on an oscilloscope (hence the time resolution). The opening of the shutter also triggers a high-speed camera (Photron FASTCAM) capable of recording up to 50 000 frames per second.

The TRC test gives several pieces of information at once. From the time difference between the start of the laser illumination and the start of the luminous phenomenon, the *ignition delay time (IDT)* is determined. The IDT is not directly proportional to the activation energy E_A of the composition; the laser needs a certain time to go to its full intensity due to the movement of the mechanical shutter. Figure 3.9 shows the beginning of an oscilloscope trace for an

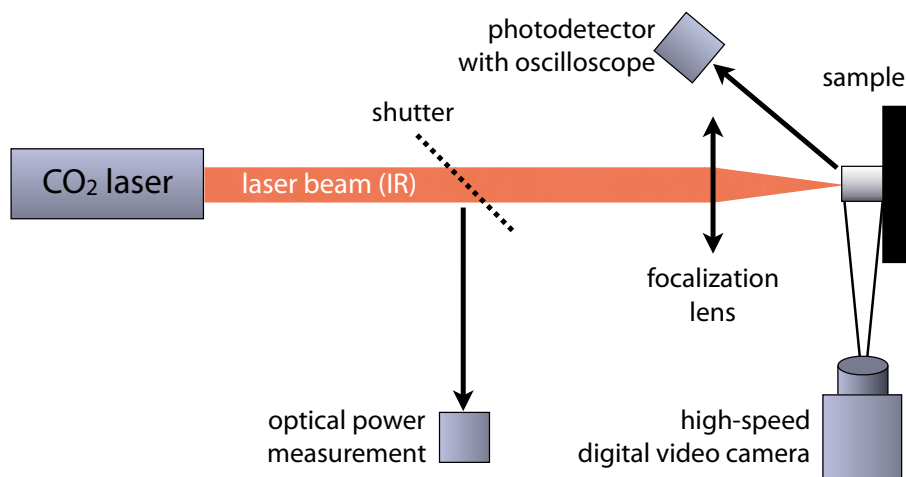


Figure 3.8 Principle of the measurement of the reactivity of nanothermites by Time-Resolved Cinematography (TRC).

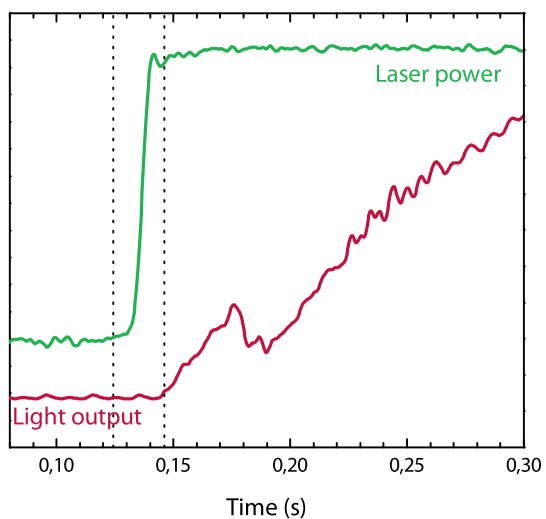


Figure 3.9 Example of the oscilloscope traces (excerpt) of the laser power (—) and the light output from the combustion (—) for an MnO_x @MWNT/Al nanothermite. The area between the dotted vertical lines is the ignition delay time (IDT).

MnO_x@MWNT/Al nanothermite. The IDT is the Δt between the point where the laser intensity starts to rise and the point where the light output starts to rise; the two points are indicated by dotted vertical lines in the graph. The energy dispersed on the sample during this time is obtained by integrating the laser power (the green curve) for the duration of the ignition delay.

Furthermore, the high-speed video allows a qualitative assessment of the burning of the sample. Is the material consumed continuously or rather in short “bursts”? Are solid particles or molten material ejected? As the original dimensions of the pellet are known, the magnification of the video (in pixels per mm) can be calibrated. In the case of a regular and continuous combustion, this allows to determine the propagation velocity of the combustion front through the pellet. In the case of ejected material, the velocity can be estimated.

The measurement of the mean combustion velocity on the high-speed videos is carried out by selecting two arbitrary points (t_1, x_1) and (t_2, x_2) , where x_i is the position of the combustion front, and calculating

$$\bar{v} = \frac{\Delta x}{\Delta t}. \quad (3.16)$$

This method can lead to errors in the measurement because the combustion is not always completely linear; for example, in some cases, it is slower near the end of the pellet because the laser does not directly heat the reaction zone any more and because the duraluminum support itself absorbs heat. This is why we developed the two programs presented in appendix A.2 and A.3.

The first one, “nt-timeline”, creates “timeline” images of the combustion video by taking one horizontal line from each frame and glues them vertically one below the other. The result is one image, in which the vertical axis corresponds to the time t and the horizontal axis allows evaluating the position x of the combustion front.

For a quantitative evaluation of the reaction velocity, the image is opened in an image manipulation program, e. g. GIMP, and the position of the combustion front is drawn by hand on a transparent layer overlaid on the image. This layer is exported as a new image; it contains only one pixel per line, corresponding to the position of the front. This image is fed into the second program, “nt-decode”, that converts it into a two-column ASCII data file containing all (t_i, x_i) points. This data file can be imported into a graphing software, e. g. ORIGIN, to do linear regressions on the coordinates for finding mean or instantaneous propagation velocities.

Results and discussion

Characterization and treatment of carbon nanotubes

In this chapter, we will first characterize the different types of CNTs that we are using for our experiments. After that, we will investigate different pre-treatments for the CNTs, with the goal of opening their ends for using them in filling reactions.

4.1 Structural characterization of the as-received nanotubes

4.1.1 SWNT (BuckyUSA)

The single-walled carbon nanotubes used in this work (“cleaned SWNT” grade, BU-203) have been bought from BuckyUSA (Austin, TX). They have a purity of at least 95% according to the manufacturer. They are the product of a CVD process, however the detailed process conditions are not known. They have been cleaned with acid to remove residual catalyst particles. Accordingly, the ash content is too low to be measured in a TG experiment, i. e. below the experimental error (cf. Table 4.1). The BET surface of 610 m²/g is about 1/4 of the theoretical maximum value for perfectly isolated, opened SWNT, which is 2650 m²/g.¹ This means that there is considerable

¹from equation (3.12), page 50.

Type	D (nm)	d (nm)	S_{BET} (m ² /g)	ash content (wt-%)	T_o (°C)	A_D/A_G (Raman)
SWNT	0.7–2.5	0.3–2.1	610	~ 0	562	0.0355 ^a 0.127 ^b
DWNT	~ 5	~ 3.5	380	4.0	532	0.251 ^a 0.367 ^b
MWNT	12–15	~ 5	222	1.5	524	1.12 ^a
CNF (Pyrograf)	~ 100	~ 40	47.8	~ 0	750	0.188 ^a

^a 514 nm excitation; ^b 633 nm excitation

Table 4.1 Overview of the analytical data for the different types of carbon nanotubes used in this work: inner (d) and outer diameter (D), specific surface area S_{BET} , ash content and oxidation temperature (T_o) determined by TGA, A_D/A_G ratio from Raman measurements at 514 nm wavelength.

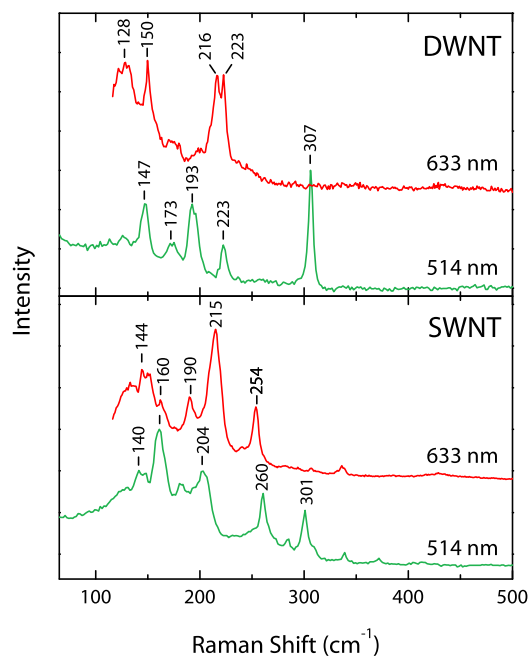


Figure 4.1 Raman spectra of the Radial Breathing Mode (RBM) wavenumber range for the as-received SWNT and DWNT, taken using a 514 nm (green) and a 633 nm (red) laser excitation wavelength. The Raman shift (in cm^{-1}) for the main peaks is indicated.

bundling of SWNTs into larger aggregates in the sample, and that at least a part of the nanotube ends is closed.

The size distribution of the sample can be estimated from the Raman measurements of the radial breathing modes (RBM) shown in Figure 4.1.² Here, we use equation (3.13) with a value of 0.07 for the factor C_e . This approximation neglects changes in RBM frequency due to bundling of CNTs. The tubes with the smallest diameter, giving the RBM peak at 301 cm^{-1} , have a diameter of about 0.7 nm, similar to a fullerene. From the Kataura plot (Figure 3.5, page 53), they most likely have a (6,4) or (7,3) chirality; these nanotubes have an electronic transition near the energy of the green laser ($514 \text{ nm} \equiv 2.4 \text{ eV}$) but not the red one ($633 \text{ nm} \equiv 1.96 \text{ eV}$). This means that the tube is in resonance with the laser excitation, strongly enhancing the Raman peak intensity, consistent with the observation that the peak appears only in the 514 nm spectrum. For the most intense RBM peak at 633 nm excitation, located at 215 cm^{-1} , there is no corresponding chirality in the Kataura plot. This peak is probably upshifted due to bundling and corresponds to tubes with a 1.2 nm diameter. The BWF asymmetry of the G peak, which is due to metallic tubes, is stronger in the 514 nm Raman spectrum than in the 633 nm one; this means that more metallic nanotubes are in resonance in the 514 nm spectrum. Other typical nanotube diameters in the sample are 1.4 nm, 1.6 nm and near 2 nm.

²See section 3.4.3, page 50.

4.1.2 DWNT (CNT&F21)

The double-walled carbon nanotubes used in this work were acquired from CNT&F (Eisenstadt, Austria). Like the SWNT, they are produced by a CVD process. According to the manufacturer, the sample contains at least 50 wt-% of DWNT, the rest consisting mainly of SWNTs and MWNTs. In a TG experiment, we find a relatively high ash content of 4.0 wt% and a slightly lower (-30 K) oxidation temperature (maximum of dm/dT) than for the SWNT sample. The lower T_o is likely caused by a catalytic effect of the inorganic impurities. The A_D/A_G ratio is much higher than for the SWNT sample, which indicates a higher number of defects than in the SWNTs. From geometrical considerations, one would expect a specific surface area about half as high as for SWNTs. The value of $380 \text{ m}^2/\text{g}$ is more than half of the value for the as-received SWNTs. This can be explained by a lower amount of bundling compared to the SWNT sample, mostly due to bigger tube diameters and to their broader distribution.

The analysis of the radial breathing mode (RBM) peaks in the Raman spectrum is more complicated than in the case of SWNTs. There is a separate contribution from the inner and the outer tube of a DWNT, and the RBM of the inner tube can be split or shifted due to different types of electronic interactions between the two incommensurate nanotube lattices [182]. Here, we will only do a basic analysis of typical tube diameters (see Figure 4.1). At low wavenumbers, we find higher peak intensities than for the SWNT, which means that there are more large tubes. For the maximum tube diameter given by the manufacturer (5 nm), the corresponding RBM frequency, calculated from equation (3.13)³ would be at about 75 cm^{-1} , which is too near the cut-off of the spectrographic filter in the Raman spectrometer to be seen clearly. In the 514 nm spectrum, the lowest-wavenumber peak that can be distinguished is at 125.3 cm^{-1} , corresponding to only 1.8 nm of diameter. The 633 nm spectrum shows two intense peaks at 128 and 124 cm^{-1} , just before the cutoff. The double peak at 216 and 233 cm^{-1} indicates a large population of CNTs around 1 nm; these are likely to be the inner tubes of a DWNT. The lowest diameters, again most likely of inner tubes, are found at about 0.7 nm (peak at 307 cm^{-1}), just like in the SWNT sample.

4.1.3 MWNT (FutureCarbon)

The multi-walled carbon nanotubes (MWNT) used in this work (“CNT-MW” grade) were bought from FutureCarbon (Bayreuth, Germany) and are produced by a CVD process. They have been cleaned by an acid wash to remove most of the catalyst particles. According to the manufacturer, the outer diameter is 12–15 nm, with 7–10 concentric layers; this corresponds to an inner diameter of about 5 nm. Their length is typically several micrometers. In the as-received state, they consist of highly entangled micron-sized aggregates, as shown in Figure 4.2a. As CVD is a low-temperature method, these nanotubes have a high defect concentration, leading to permanent kinks and bends in the structure. The high defect concentration is also seen in the Raman spec-

³Page 52.

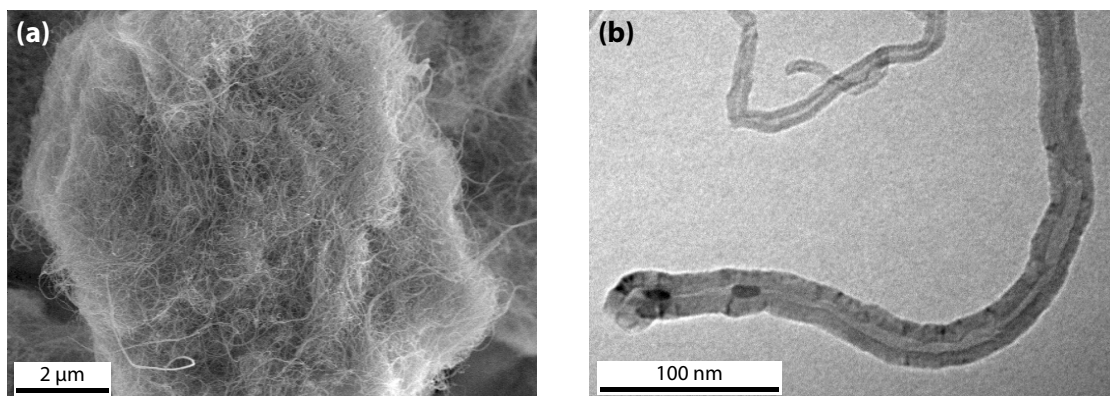


Figure 4.2 Scanning electron micrograph of entangled aggregates present in the as-received CNT sample (a); transmission electron micrograph of the closed end of a MWNT with embedded catalyst particles (b).

trum (Figure 4.3): the D peak is even more intense than the G peak ($A_D/A_G = 1.12$ from the peak areas, for 514 nm excitation), and all the peaks are quite large. The Raman intensity does not even go back to the baseline between the G and the D peak. Due to the high number of defects, the thermal oxidation happens at lower temperatures than for the other as-received nanotube types.

The X-ray diffractogram (Figure 4.4) shows typical peaks for graphite (JCPDS file 56-159). However, the (002) peak is shifted to a lower angle ($2\theta = 25.64^\circ$ instead of 26.54°). As this peak directly indicates the size of the unit cell along c , which is the stacking direction, this means that the mean distance between graphitic planes is higher (347 pm) than for ideal graphite (335 pm). The density of a material is equal to the mass of the atoms in its unit cell divided by its volume, which is proportional to c in this space group ($P6_3/mmc$). The density is then inversely proportional to the c distance. Instead of 2.25 as for graphite, the density of the pure CNT material is thus 2.17 ($2.25 \cdot 335/347$); this is the value that is used for calculating the theoretical maximum densities (TMD) of nanothermite pellets in chapter 6. This effect is most likely due to the curvature of the layers, which creates a geometric distortion of the π system.

We also see sharper peaks that belong to an impurity phase. They are even more intense after annealing the tubes in argon at 1200°C (indicated by orange arrows in Figure 4.4). They correspond exactly to the α phase of cobalt metal (JCPDS file 15-806), which clearly shows a) that the catalyst is metallic cobalt and b) that it has not been completely removed by the acid wash that the manufacturer carried out. This is because most of the tube ends are still closed, and the catalyst particles are embedded inside these closed ends, which means that the acid does not reach them during the cleaning process. Figure 4.2b shows a representative transmission electron micrograph with embedded particles.

In order to use these carbon nanotubes for filling experiments, their ends have to be opened, and they have to be cleaned from catalyst residues. We will look at several ways to do this in

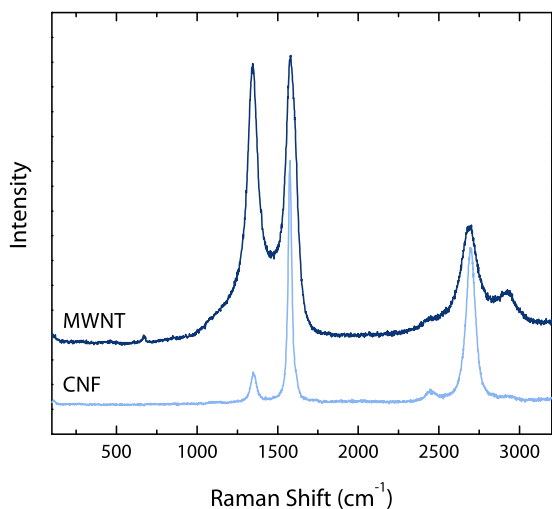


Figure 4.3 Raman spectra of as-received FutureCarbon MWNTs and of Pyrograf-III PR-24-HHT-HD herringbone nanofibers, recorded at 514 nm laser excitation wavelength.

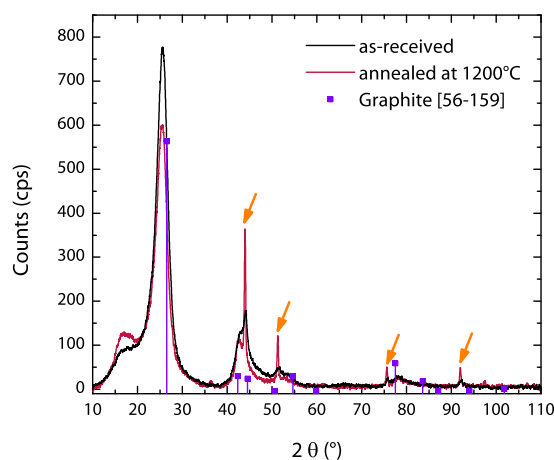


Figure 4.4 X-ray diffractogram using $\text{Cu K}\alpha_1$ radiation of as-received FutureCarbon MWNTs (black) and after annealing at 1200°C under argon. Orange arrows point to peaks of α -cobalt [15-806].

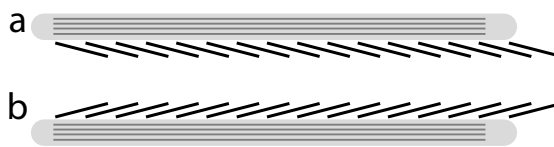
section 4.2.

4.1.4 Herringbone nanotubes, “CNF” (Pyrograf-III)

The herringbone nanotubes used in this study were of the Pyrograf-III type and have been bought from Applied Sciences (Cedarville, OH). They are hollow vapor-grown carbon nanofibers with a hollow core and a CVD carbon overlayer on the outside surface; a schematic side-on view, similar to what would be observed in a TEM, is shown in Figure 4.5. The “herringbone” structure means that the graphitic layers of which the tube is composed lie at an angle relative to the tube axis and thus have a conical form.

This structure has implications both on the mechanical properties and on the chemistry. The exceptional mechanical properties of CNTs are due to the resistance of the graphene sheet itself: in a traction test, rupture of the nanotube occurs only when the graphitic C–C bonds break, which leads to exceptionally high (theoretical) values for the Young modulus and the stress at rupture. On the other hand, the herringbone tubes are held together by π – π stacking between the graphitic layers. This makes the stress required for tube rupture much smaller, and it also makes the tubes easy to cut by mechanical methods such as ball-milling. The chemical reactivity of the sidewall surfaces should also be different: “true” CNTs expose the *surfaces* of the graphene sheets, i. e. the delocalized π system. The herringbone fibers, on the other hand, expose graphene *edges*. To avoid dangling bonds, the edges are saturated with heteroatoms, most likely oxygenated

Figure 4.5 Schematic side-on view of a graphitized Pyrograf nanofiber: graphitized CVD carbon overlayer (a) deposited on the inner herringbone-structured fiber (b) with a hollow core.



functional groups such as carboxylic acids, alcohols, quinones etc.

Whether or not these fibers should be called CNTs depends on the definition of the term. As they are nano-sized, made of carbon and have a hollow tubular structure, it seems reasonable to call them carbon nanotubes. Indeed, numerous examples of articles in which Pyrograf products are called CNTs can be found, for example Ref. [149]. The term CNT can also be defined more strictly as consisting of one or more concentric rolled-up graphitic layers *aligned perpendicularly to the tube axis*. Following this definition, the term “herringbone carbon nanotube” would be a contradiction in terms. In this manuscript, we will use the terms “hollow carbon nanofiber” (CNF) and “herringbone carbon nanotube” interchangeably when referring to the Pyrograf-III material.

Three different types of Pyrograf-III nanofibers exist. They are called PR-19, PR-24 and PR-25; their main difference is the thickness of the CVD overlayer and thus the outer diameter D of the fiber. The outer diameter of PR-19 is about 150 nm, the one of PR-24 about 100 nm. The PR-25 type has no or a minimal carbon overlayer. Each of the types exists in three different grades, corresponding to the temperature at which they were annealed after the synthesis:

- ▶ PS (Pyrolytically Stripped)
treated at low temperature to remove polyaromatic hydrocarbons from the surface;
- ▶ LHT
heat-treated at 1500°C, resulting in partial graphitization of the CVD carbon overlayer;
- ▶ HHT
heat-treated at 3000°C, with a completely graphitized overlayer.

We used a type called *PR-24-HHT-HD*, i. e. having a thin overcoat and treated at 3000°C. TEM observation (Figure 4.6) shows that the vast majority (over 90%) of the as-received tubes have open ends. In most cases, we can distinguish a “convex” and a “concave” end due to the angle of the graphitic plane; for example, the concave end of the two horizontal fibers in the left image of Figure 4.6 is on the left side. This means that *most of the tube ends are the result of tube cleavage between two adjacent graphitic layers*, perhaps by mechanical stress during processing. It also means that treatments to open the nanotube ends are not necessary. The length of most of the nanotubes observed is over 1 μm , often 10 μm and more. On the other hand, short fragments a

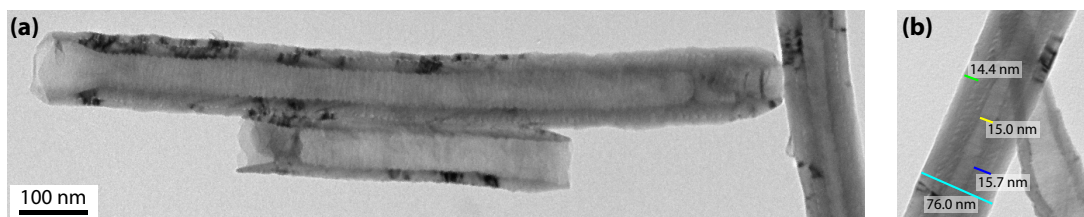


Figure 4.6 Transmission electron micrograph of as-received Pyrograf PR-24-HHT-HD nanofibers, showing “convex” and “concave” open ends and the two-layered structure (a). Measurement of another nanotube, showing a 15 nm CVD overlayer, 15 nm herringbone fiber and 15 nm cavity diameter (b).

few hundred nm in length are also found. A small number of tubes presents a “stacked cup” or “bamboo” morphology, producing barriers on the inside surface. This morphology results from the growing nanofiber entering and leaving the hot reaction zone several times.

On the micrograph, the inner catalytic layer with its herringbone structure, where the steps are clearly visible, can be distinguished from the much smoother outer layer. Measurements of the tube dimensions indicate essentially three populations:

- ▶ smaller tubes with diameters of 40–50 nm and an inner diameter of about 20 nm,
- ▶ tubes with diameters of 100–120 nm and inner diameters ranging from 20 to 50 nm,
- ▶ large tubes with a diameter of 160 nm and more and about 50–60 nm internal diameter.

The Raman spectrum of the as-received carbon nanofibers (Figure 4.3, light blue curve) is characterized by narrow, well-defined peaks compared to the MWNT sample. This indicates a highly homogenous structure and a high crystallinity. The A_D/A_G ratio (given in Table 4.1) is only about 0.2. This result is not surprising, given that the fibers have been graphitized by a heat treatment at 3000°C after their synthesis. It also means that the amount of amorphous carbon, which would enlarge and enhance the D peak, is negligible. The high crystallinity is also seen in the thermal degradation behavior. The nanofibers have the highest oxidation temperature, about 750°C. Their ash content is too low to be measured by TG, the measured residual mass is slightly negative (–0.02 wt-%), which is due to the slight drift of the microbalance.

4.2 Opening the ends of CNTs by oxidation

Contrary to CNFs, the ends of pristine CNTs are generally closed. To make the endohedral (inner) space of carbon nanotubes accessible for reactions—such as filling with other compounds—they have to be opened first. This is achieved by partial oxidation of the carbon.

A carbon pentagon in the wall of a CNT induces a reduction in its diameter. Five pentagons are sufficient for forming a cap. Depending on their relative orientation, the cap is hemispherical (for

example half a fullerene for a nanotube with $D \approx 0.7$ nm), conical or has an irregular shape. Due to the breaking of the six-fold symmetry—and correspondingly the lesser degree of stabilization by mesomery—pentagons are chemically more reactive than hexagons; this has been shown by both simulations [72] and experiments. Thus, any chemical attack that can break C—C bonds will preferentially attack the end caps and other defects on the sidewalls.

Many of the treatments described in the literature use single-walled carbon nanotubes (SWNT) as the substrate. However, there is a fundamental difference between the opening of SWNT and MWNT: To open a MWNT, *all* concentric walls must be opened at the same place. This makes opening on the sidewalls statistically unlikely, as there would need to be a defect on all the walls at the same place. For this reason, experimental methods developed for SWNT ususally have to be adapted for use with MWNT. Herringbone nanotubes are even more different: the tubular structure is essentially held together by π - π stacking interactions, so that they can be easily broken apart.

In this section, we will investigate several experimental techniques for opening the ends of multi-walled carbon nanotubes.

4.2.1 Acid treatments

One of the most often used methods for opening carbon nanotubes is the attack by strong oxidizing acids: nitric acid (HNO_3) or mixture of nitric acid and other acids, e. g. $\text{HNO}_3 + \text{H}_2\text{SO}_4$.

Even if a large number of researchers use this method, not much is known about the reaction mechanism, called *oxidative cleavage* of C—C bonds. Although the $\text{HNO}_3 + \text{H}_2\text{SO}_4$ mixture is the same used for adding $-\text{NO}_2$ groups to aromatic hydrocarbons, no electrophilic substitution takes place. Nitration of aromatic rings in the carbon nanotube can be excluded from time-resolved XPS measurements, which show no non-hydrolyzable C—N species [78].

Acid treatments of MWNT. Even though the opening of MWNTs by heating them in concentrated acids has been used in many literature studies, its results are not as good as for the other opening methods described below (i. e. thermal oxidation and filling with KOH). Furthermore, it gives a relatively high weight loss and strongly damages the graphitic lattice.

Oxidizing MWNTs in a mixture of 50 vol-% of HNO_3 and 50 vol-% of H_2SO_4 at reflux for 2 h leads to their almost complete destruction. The solid residue obtained is only about 1 wt-% of the initial quantity of nanotubes, while the rest is dissolved in the acid in the form of polyaromatic hydrocarbon “debris”, as the brownish-yellow color of the solution shows.

Treating the MWNTs in concentrated nitric acid (65%, Acros) for 16 h at a gentle reflux (123°C) results in a yield of about 50–60 wt-% of oxidized MWNTs (i. e. a 40–50% weight loss). The specific surface area of the oxidized tubes is increased from 222 to 269 m^2/g , corresponding to about 50% of opened nanotubes. The A_D/A_G ratio in the Raman spectrum recorded at 633 nm

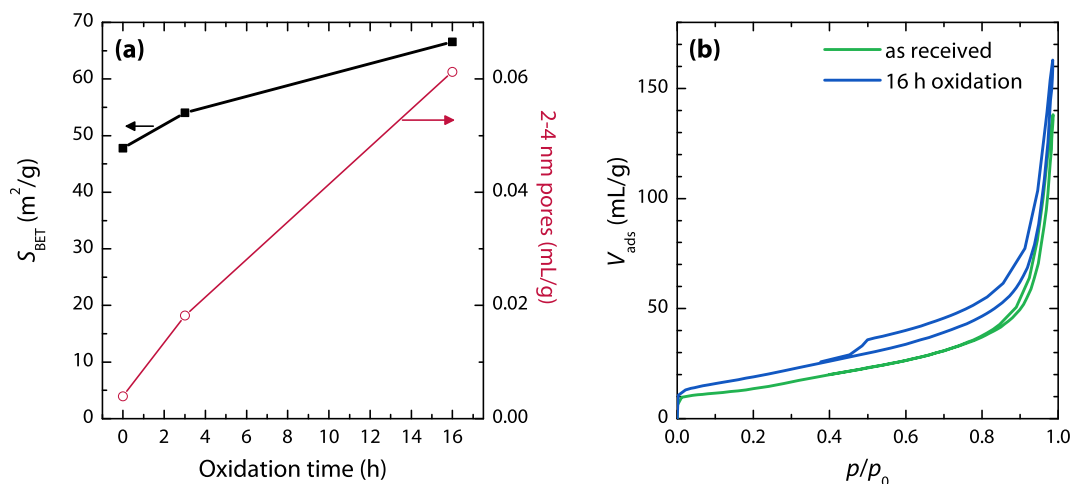


Figure 4.7 Specific surface area S_{BET} of HNO_3 -oxidized herringbone carbon nanotubes and the pore volume for pores of 2–4 nm in diameter depending on the oxidation time (a); Nitrogen adsorption isotherms for as-received CNF and after 16 h of oxidation, showing the stronger hysteresis (b).

excitation increases from 1.80 for the as-received MWNTs to 2.35 for the oxidized ones, indicating that the graphitic lattice has been damaged.

HNO_3 oxidation of herringbone nanotubes. The ends of the herringbone carbon nanotubes (“CNF”) are already opened, so that in principle, no further treatment is necessary. However, we will see in section 5.2.3⁴ that in filling reactions, the adhesion of the oxides and their precursors is improved by prior oxidation of the CNFs. This is because the oxidation by HNO_3 creates a large number of oxygenated functional groups on the tube surface. As the inside surface of a herringbone nanotube consists of the *edges* of graphitic planes, as opposed to the π system on the outside surface, this functionalization effect is stronger on the inside surface. We will see in the next chapter that the oxygenated surface functional groups (especially $-\text{COOH}$) act as “anchoring points” for the nitrate salts.

As in the case of MWNTs, the oxidation is carried out in concentrated nitric acid (HNO_3 , 65%, Acros) at 123°C under magnetic stirring. The flask with the reaction mixture is equipped with a reflux condenser. Depending on the duration of the oxidation reaction, the specific surface area increases (Figure 4.7a) from 47.8 m²/g for the as-received CNFs to 66.5 m²/g after 16 h of oxidation. This is accompanied by a change in the form of the desorption branch in the nitrogen adsorption/desorption isotherms (Figure 4.7b): the oxidized samples show a hysteresis loop with a H3 shape,⁵ whose strength increases with an increasing reaction time. This hysteresis loop in-

⁴Page 114.

⁵For the classification of hysteresis loops, refer to Figure 3.3, page 48, and the accompanying text.

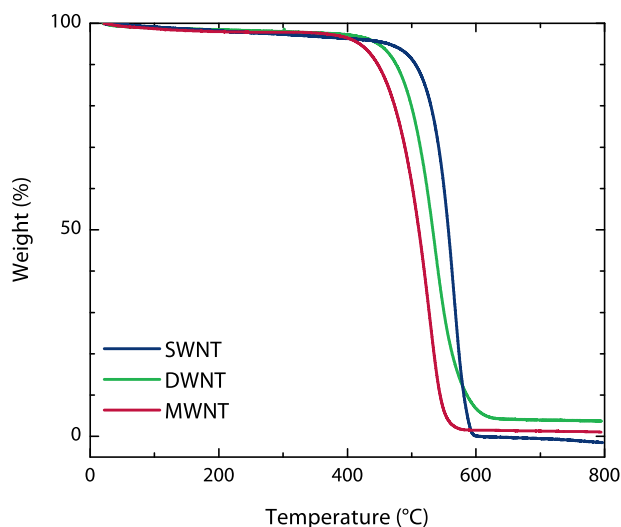


Figure 4.8 Thermogravimetric oxidation of different types of as-received carbon nanotubes at 5 K/min in a flow of 100 mL/min of ambient air.

indicates the creation of mesoporosity. Indeed, the volume of the pores with a diameter between 2 and 4 nm, as determined by BJH analysis, strongly increases with the treatment duration (Figure 4.7a, red curve). TEM observation of the oxidized tubes shows that there are fissurations in the carbon “overlayer”, and that the overlayer is partially detached from the inner herringbone structure. The voids that appear between the overlayer and the herringbone layer are typically 2–5 nm wide, and they act as “slit pores” in the nitrogen adsorption experiments, giving rise to the typical H3 hysteresis shape.

4.2.2 Thermal oxidation in air

It is obvious that carbon nanotubes can be attacked by heating them in air—after all, the primary technical use for carbon (“coal”) is as a fuel for burning. The temperature at which CNTs start to burn depends on the number of walls (single-, double-, multi-walled), the number of defects and metallic impurities that can play the role of a catalyst for oxidation.

It has already been said that the most reactive sites on the CNTs for thermal oxidation are the end caps as well as sidewall defects. The goal is to achieve an optimal *site selectivity*, i. e. to open the ends of the CNTs without consuming too much of the sidewalls. As a general rule in chemistry, a higher selectivity is achieved for a lower reactivity. Useful oxidation temperatures will therefore be situated at the lower end of the oxidation peak measured by TGA.

4.2.2.1 Study of the isothermal oxidation kinetics

Generally speaking, the lower the chosen oxidation temperature of a CNT sample, the longer the sample will have to be kept at this temperature to achieve complete opening. To examine the

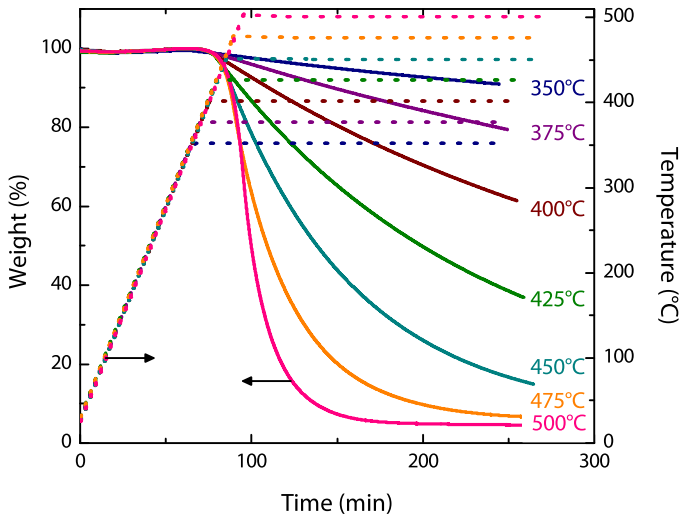


Figure 4.9 Thermogravimetric analysis of MWNT samples for different isothermal temperatures: sample weight (—) and the temperature profile used for the measurement (···) as a function of analysis time.

effect of the treatment time, we did a systematic study in the thermogravimetry analyzer: samples of pristine MWNT were heated in air at 5 K/min up to different temperatures between 350 and 500°C; then they were held isothermally for three hours at this temperature.

Figure 4.9 shows the weight loss of the MWNT samples for different temperatures. At higher temperatures (475 and 500°C), the sample is consumed quickly, and a plateau is reached; it corresponds to the combustion residue, which is due to residual catalyst particles. At the low end (350–400°C), the weight loss is almost a straight line.

From a kinetic point of view, each type of reactive site may be assumed to correspond to a specific rate constant. The total reaction velocity can be written as

$$v = \sum_i k_i \prod_j c_{ij}, \quad (4.1)$$

where k_i is the rate constant and c_{ij} the concentration of each of the reactants.

The purpose of this study is the elucidation of the oxidation mechanism by careful analysis of the thermogravimetric data. Is there more than one type of reactive site, and can we find evidence for the activation of other reactions by varying the temperature?

The oxidation reaction is described by the (trivial) reaction equation



The reaction velocity v for this system is thus described by an equation of the form

$$v = -\frac{d[\text{C}]}{dt} = k[\text{C}][\text{O}_2], \quad (4.3)$$

where k is the rate constant and the brackets signify the concentration of the respective chemical species. As the experiment is carried out under a flow of dry air, the atmosphere is constantly renewed. Thus, $[O_2]$ is (approximately) constant, and the observed kinetics correspond to a pseudo-first order reaction with an *effective rate constant*

$$k' \equiv k[O_2]. \quad (4.4)$$

Instead of the concentration of carbon, which is hard to define for a pure solid after all, we will use the sample mass m in percent of the initial mass, which is directly measured by TGA.

The temperature dependency of the rate constant k' is given by the Arrhenius equation

$$k'(T) = A \exp\left(\frac{E_A}{RT}\right), \quad (4.5)$$

where E_A is the activation energy in kJ/mol and $R = 8.31441 \text{ J K}^{-1} \text{ mol}^{-1}$ is the universal gas constant. The so-called *Arrhenius plot*, where $\ln k'$ is plotted as a function of $1/T$, allows an easy determination of the activation energy. In Figure 4.10, the initial reaction rate (i.e. the slope $-\dot{m}$ at the start of the isothermal phase) is used instead of the rate constant because it can be directly determined from experimental data and because

$$v_o \propto k'.$$

It can be clearly seen in Figure 4.10 that the initial reaction rates follow the Arrhenius law with good accuracy; its validity has thus been confirmed for this system. The slope of the linear regression is equal to E_A/R ; the activation energy of the reaction is thus

$$E_A = 114 \pm 2 \text{ kJ/mol.}$$

Ajayan and coworkers did a similar investigation on arc-discharge MWNT at temperatures around 700°C [76]. They found a much higher activation barrier of $\sim 225 \text{ kJ/mol}$ in air. Due to the high temperatures at which the arc-discharge synthesis takes place, these nanotubes have a lower amount of defects than the CVD tubes investigated in this study. As the oxidation happens more easily on defect sites, the apparent activation energy is lowered. *Thus, it seems that the activation energy barrier E_A for the oxidation of CNTs is also a measure of the number of defects in the graphitic structure, related to the oxidation temperature T_o .*

The shape of the curves in Figure 4.9 (and also a numerical fit) confirms that the oxidation is a pseudo-first-order-process. This is not surprising, as the oxidation is a simple elementary reaction that does not involve intermediate equilibria or multi-body collisions. The equation describing the reaction rate is thus

$$v = -\dot{m} = k' m. \quad (4.6)$$

Temperature (°C)	Initial velocity (wt-%/min)
350	0.05117
375	0.1280
400	0.2697
425	0.5328
450	1.022
475	2.323
500	3.575

Table 4.2 Initial reaction velocities, measured by the rate of weight loss, as a function of the isotherm temperature for MWNT samples.

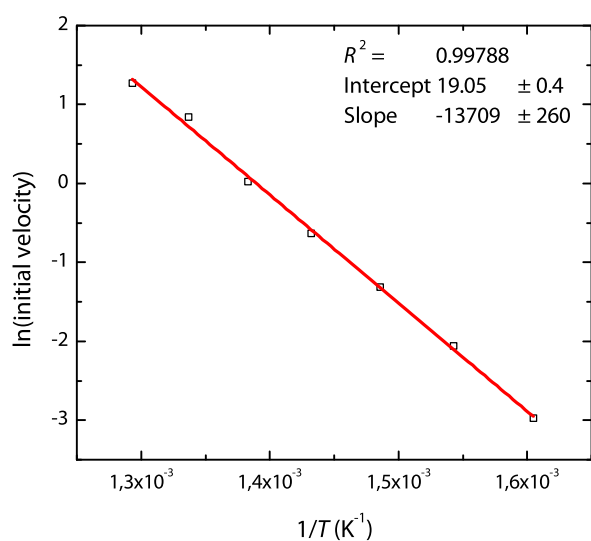


Figure 4.10 Arrhenius plot for the oxidation of MWNT at different temperatures using the initial reaction velocity $v_0(T)$. The slope corresponds to an activation energy of $E_A = 114$ kJ/mol.

4 Characterization and treatment of carbon nanotubes

T (°C)	m_{Res} (wt-%)	τ (min)
350	76.8	379
375	40.1	427
400	21.7	267
425	9.25	154
450	6.83	75.9
475	6.35	34.8
500	4.82	16.4

Table 4.3 Fit results for the oxidation of FutureCarbon MWNTs in air at different temperatures T . A pseudo-first-order kinetic model according to eqn. (4.7) was used to determine the combustion residue m_{Res} and the time constant τ of the reaction.

For solving the differential equation, we have to take into account the existence of a *combustion residue*, i. e. a certain quantity m_{Res} of the sample that never reacts. Solving the differential equation thus gives

$$m(t) = m_{\text{Res}} + (1 - m_{\text{Res}})e^{-k't} = m_{\text{Res}} + (1 - m_{\text{Res}})e^{-t/\tau}. \quad (4.7)$$

Instead of the rate constant k' , we can also use a time constant $\tau = 1/k'$.

Table 4.3 shows the results of numerically fitting eqn. (4.7) to the isothermal part of the curves in Figure 4.9 using free parameter values. The time $t = 0$ was taken at the beginning of the isothermal phase. While the error on the parameters is large for the lower temperature, two different behaviors seem to emerge: at 425°C and above, all the carbon is burned, and m_{Res} corresponds (within experimental error) to the real percentage of metallic impurities. For temperatures of 350–400°C however, the fitted value for m_{Res} is much higher. This effect may be due to the existence of sites of different reactivity. It seems thus that low-temperature oxidation can *selectively* act on these sites.

In order to get more information about the kinetics of this low-temperature oxidation, the same experiment (at 350°C) was performed with an isothermal dwell time of 20 hours. This curve was fitted using a model with an arbitrarily high number of time constants. The fit converged to the sum of two exponential terms with different time constants

$$m(t) = m_{\text{Res}} + m_1 e^{-t/\tau_1} + m_2 e^{-t/\tau_2} \quad (4.8)$$

with a residue of $m_{\text{Res}} = 5.8\%$ and the following numerical values:

$$\begin{aligned} m_1 &= 8.9\%, & \tau_1 &= 401 \text{ min}, \\ m_2 &= 85.3\%, & \tau_2 &= 2876 \text{ min}. \end{aligned}$$

This is an important and interesting result, as it suggests that there exists a small number of sites (about 1/10 of all the carbon atoms) that is much more reactive than the rest. The number is too

4.2 Opening the ends of CNTs by oxidation

Treatment time (min)	Yield (wt-%)	S_{BET} (m ² /g)	Opened tubes (%)
21	79%	309	80–90%
27	34%	326	100%

Table 4.4 Results of thermal oxidation treatments of FutureCarbon MWNTs carried out in a furnace at 450°C: time of treatment, yield, measured BET surface and percentage of opened tubes as calculated from the BET surface.

high for all of these atoms to be part of a closed nanotube end; the edges of incomplete shells or sidewall defects are other possible sites for more reactive atoms.

4.2.2.2 Furnace treatments

In the kinetic study presented in the section above, the amount of opened tubes could not be directly evaluated by measuring the BET surface of the samples, as the amounts of sample used in the DTA/TG measurements (~ 2 mg) are much less than the minimum amount required for a sufficiently precise BET measurement (more than 10 mg). The weight loss alone does not permit to distinguish the opening of the ends from the burning of whole shells or even whole nanotubes.

Table 4.4 shows the conditions and the results obtained for different treatments of FutureCarbon MWNT that have been carried out in an electric muffle furnace or a tubular furnace. The limitation of these methods is the static atmosphere, i. e. there is no forced air circulation. As the amount of sample is much higher than in the DTA/TG experiments (about 200 mg per test), there are two effects that can make the oxidation result inhomogeneous:

- ▶ The atmosphere becomes locally depleted in oxygen, especially inside larger MWNT aggregates, *slowing down* the reaction rate.
- ▶ The reaction of carbon atoms creates heat by itself, heating up the immediate environment and locally *accelerating* the reaction.

These two factors create inhomogeneities in the oxidation result depending on how the sample is placed in the crucible as well as on the shape of the crucible and its cover, if any. When the sample is placed randomly in small heaps on an even surface, the edges of the heaps seem to be attacked first, and the nanotubes there are completely consumed. In addition, other systematical errors are introduced in the measurement of the weight loss of each sample. The most important one is the loss of material when handling the crucible (for example, some tubes may be dispersed in the air due to static electricity), owing to the small density of the CNTs. Additionally, the sample may be polluted due to the accumulation of dust from the ambient air or from inside the furnace if the crucible is kept open.

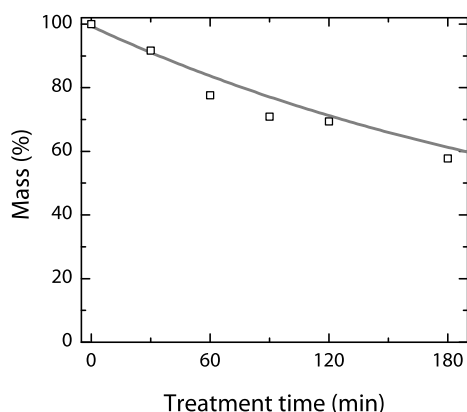


Figure 4.11 Oxidation of MWNT at 400°C: residual weight (in %) of the samples (squares) depending on the oxidation time compared to the isothermal TGA curve (grey line) at the same temperature.

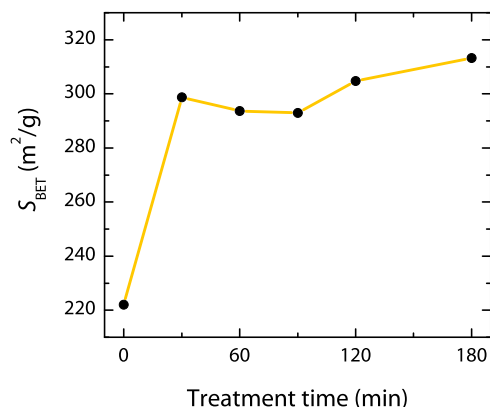


Figure 4.12 Oxidation of MWNT at 400°C: specific surface area of the samples depending on the oxidation time.

A systematic experiment was carried out to evaluate the effect of thermal oxidation at a relatively low temperature (400°C). Five samples of FutureCarbon MWNTs (100 mg each) were placed in a ventilated Heraeus furnace. The samples were put into Petri dishes, with a much larger Petri dish as cover, so that the samples are not carried away by the air flow. The steel grid below the samples still permits the exchange of air. The samples were taken out after 30, 60, 90, 120 and 180 minutes of oxidation respectively. Their residual weight is shown in Figure 4.11. It can be seen that there is a satisfactory but not ideal correspondence between the experimental points and the curve obtained in an isothermal TGA experiment, which is shown in grey. Figure 4.12 shows the evolution of the specific surface area S_{BET} of the samples with time. An interesting effect can be seen: After rapidly rising from 222 m²/g (the value for the as-received product) to about 300 m²/g, there is a sort of plateau at this value up to a time of 90 minutes; for longer times, the BET surface increases further.

The result of these tests allows to postulate a hypothetical reaction mechanism: In the first minutes of oxidation, all the *accessible* easily reacting sites (end caps, sidewall defects) have finished oxidation; in the second phase of the reaction, whole nanotubes are consumed. The further increase at $t \geq 120$ min may be attributed to two effects: when larger aggregates are broken up, more “easy” oxidation sites might be accessible; or the mean wall thickness of the nanotubes decreases, either by burning away single shells while leaving the rest intact or by a preferential oxidation of nanotubes with thicker walls—possibly due to the local heating effect described above. Remember that for completely opened nanotubes, $S_{\text{BET}} \propto (R - r)^{-1}$.

4.2.2.3 Morphology of air-oxidized MWNT

In order to see the influence of the oxidation treatment on the morphology of the MWNTs, we performed TEM observations on the products. The differences between the oxidation temperatures are striking: even for products with similar specific surface areas, different morphologies are obtained.

Figure 4.13 shows a typical micrograph of a sample that has been heated for 20 hours to 350°C. On the right, of the image, a Co catalyst particle is visible; the sidewall is cut next to it so that it could be removed by a mild HCl treatment, for example. All along the lower side of the horizontal nanotube, angled cuts through all of the graphitic layers are visible, the inner space is thus completely accessible. However, we also see that the innermost wall is strongly damaged: it seems to have partially detached from the other layer, which would block an eventual filling. The diagonal piece of nanotube shows carbonaceous debris in the interior, which also prevents a liquid filling from entering the CNT.

The product shown in Figure 4.14 has been oxidized at 400°C for 3 hours. While most of the nanotube ends (estimated at 80–90%) are found to be open, significant quantities of amorphous carbon in the form of spherical particles is observed, especially on the nanotube ends. Many nanotubes are partially filled with what looks like oxidation debris in their channels.

After an oxidation for 3 h at 450°C (Figure 4.15), the MWNTs are even more strongly damaged, as can be seen by TEM. The weight loss for this time of treatment is close to 85%, which makes these conditions not useful for an application. However, we can see what happens in an advanced stage of the oxidation process. Just like in oxidation at 400°C, some amorphous carbon is formed; this is especially visible inside the CNT channels, where a filling with a contrast similar to the walls can be distinguished. The most striking feature of the micrograph though is in the horizontal nanotube: it has large holes with a diameter of over 10 nm in the sidewall. These holes are located at defect sites in the original product. Once the oxidation has started at one point on the sidewall, further reaction is facilitated: the edge of a small hole is itself a structural defect. Material is then removed in a sphere with increasing diameter.

To conclude this part, the oxidation in air has the merit of being easy to perform. However, it tends to convert some of the carbon into amorphous residues that can block the channels and thus make the filling reactions difficult. In some cases, as shown in Figure 4.14, these impurities completely block the entry of the CNTs. It might be possible to remove some of the “debris” by extraction with an organic solvent, such as toluene.

Longer oxidation times and higher temperatures both heavily damage the nanotube structure and give relatively low yields. What's more, it is difficult to compare results from TGA and from oxidation in different types of ovens. The type of air circulation (natural or forced) plays an important role in the yield, as does the placement and amount of sample: the onset of the combustion reaction contributes to self-adiabatic heating of the sample, which accelerates the loss of mass. It seems that despite its simplicity, the air oxidation method is not a good pre-treatment

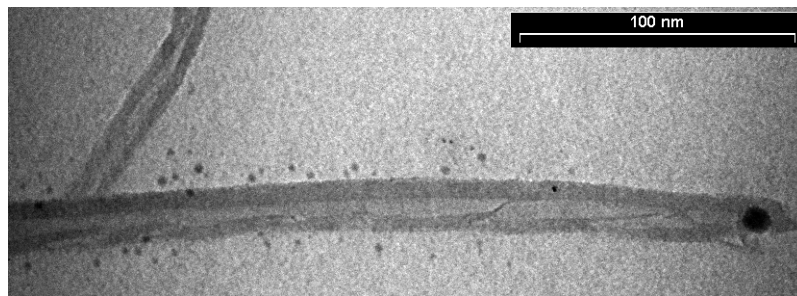


Figure 4.13 Transmission electron micrograph of FutureCarbon MWNT oxidized at 350°C for 20 hours, showing sidewall cuts and a “freed” catalyst nanoparticle.

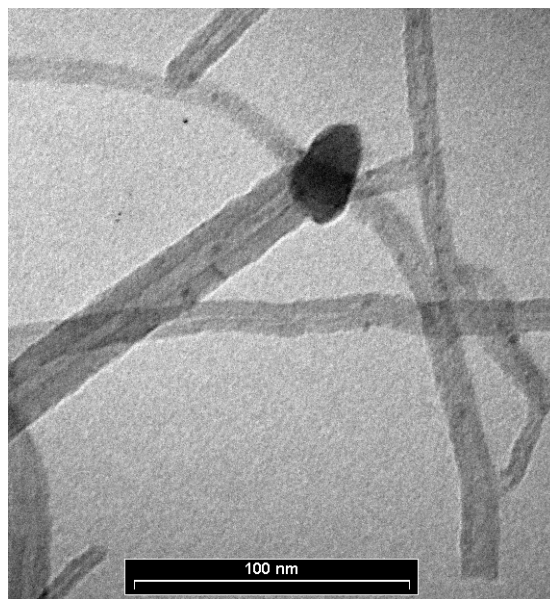


Figure 4.14 Transmission electron micrograph of FutureCarbon MWNT oxidized at 400°C for 3 hours: opened CNT ends, amorphous carbon particles and debris inside the CNTs.

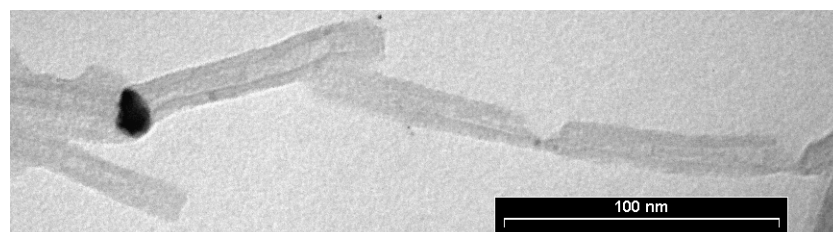


Figure 4.15 Transmission electron micrograph of FutureCarbon MWNT oxidized at 450°C for 3 hours. Large holes in the sidewalls and a spherical amorphous carbon particle can be seen.

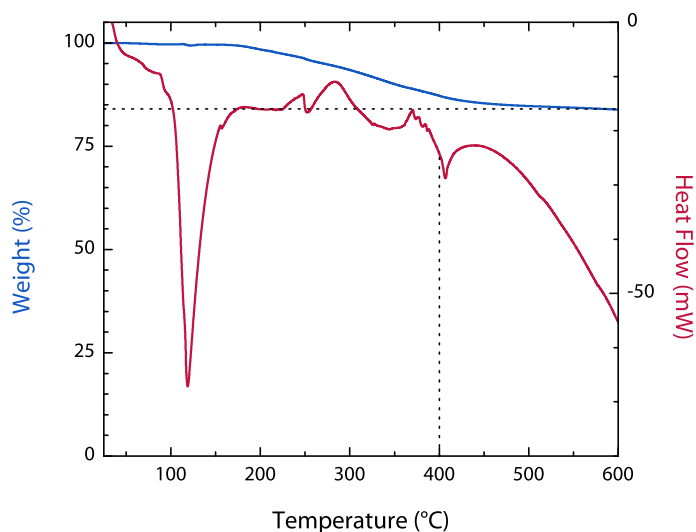


Figure 4.16 TG/DSC analysis of potassium hydroxide in flowing nitrogen: weight (blue) and heat flow (red). The residue at 600°C is 84.1%. Melting peak between 370 and 430°C.

for MWNT filling experiments.

4.2.3 Filling with KOH

This treatment method for MWNT has been developed during this thesis work based on work on single-walled carbon nanotubes carried out by Malcolm Green's group [84, 85, 86]. They use the reaction of SWNT with alkali metal hydroxides (KOH, CsOH) to obtain opened and hydroxide-filled nanotubes. During the filling reaction, which is carried out in a sealed ampoule under vacuum, they remark the generation of a small quantity of gas, attributed to H_2 . They remove the KOH filling by stirring the KOH@SWNT in water. The now empty "hydroxide-opened SWNT" can be refilled with various salts by solution infiltration, for example with uranyl acetate.

Our treatment method for opening FutureCarbon MWNTs has three steps:

1. reaction with molten KOH, followed by washing with water;
2. cleaning with boiling HCl;
3. annealing at 950°C in argon (optional).

For the first step, we mixed pristine FutureCarbon MWNTs with KOH pellets in a mass ratio between 1 : 10 and 1 : 30. The mixture was heated to 400°C for different times (between 45 min and 4 h) in a covered nickel crucible. Upon heating, the KOH liquefies at about 120°C, when its water of constitution (about 15 wt%) is released. The hydroxide effectively dissolves in its own water of constitution, and the high concentration of the solution increases its boiling point. Further heating makes it solidify again because the water evaporates. Finally, KOH itself melts at about

360°C [183, p. 945]. Figure 4.16 shows a TG/DSC analysis of KOH; the endothermic peak at 100–155°C (maximum 120°C) corresponds to the first liquefaction, while the melting peak is at 370–430°C (maximum 406°C). Due to the low density of the nanotubes, they have the tendency to float on the molten hydroxide. This effect can be avoided by putting the KOH pellets on top of the MWNTs; the two phases will mix driven by their specific densities.

Even though we are not working under a protective atmosphere, the oxygen inside the crucible has presumably been displaced by the evaporated water contained in the KOH. A simple calculation proves this assumption: In a typical experiment, 9.0 g of KOH and 0.3 g of MWNT have been heated in a nickel crucible with a volume of 55 mL. The potassium hydroxide typically contains about 15 wt% of water. This value, which is given by the supplier (Sigma-Aldrich), was verified by a TGA experiment in nitrogen (Figure 4.16), which showed a weight loss of 15.9 wt% in the studied temperature range.⁶ 15% of 9.0 g KOH is 1.35 g or 75 mmol of H₂O. From the ideal gas law

$$pV = nRT,$$

we determine that 75 mmol of water vapor have a volume of about 2.4 L at 120°C. This is more than 40 times the volume of the crucible; it is therefore reasonable to assume that the atmosphere in the crucible is only made of water vapor.

Contrary to sodium hydroxide [183, p. 939], potassium hydroxide forms small amounts of peroxides and superoxides (KO₂), which are presumably the highly reactive species attacking the carbon. It is even possible that some metallic potassium will form during the reaction; this has been observed in the “activation” of charcoals.

The aspect of the reaction product in the crucible depends on the ratio C : KOH. For 1 : 10, the product looks like grey sand and is solid even at 400°C. For a 1 : 15 ratio, we get spherical particles with a diameter of several millimeters. For a 1 : 30 ratio, a monolithic block of a black composite material is obtained. When adding water to the “monolith”, it dissolves slowly and with considerable heating. The result is a black CNT sediment and a turbid, slightly green supernatant from Ni(OH)₂ formed by attacking the crucible walls. The suspension is centrifugated at 5000 min⁻¹ for 7 min. The supernatant liquid is decanted, 70 mL of ultrapure water is added, and the sediment is redispersed by a short sonication (about 15 s). This cycle is repeated until the supernatant liquid has the same pH as the pure water (~ 6). After removing the KOH and Ni(OH)₂ by four or five of these sonication–centrifugation cycles, we observe the spontaneous formation of a dispersion without adding any surfactant. In these dispersions, whose concentration is low (under 1 g/L), the zeta potential of the nanotubes is about –36 mV. This means that they are stabilized by electrostatic repulsion between the negatively charged MWNTs. The negative charges are due to the existence of deprotonated acidic functional groups (e. g. carboxylates) on the CNT surface.

⁶For higher temperatures, further weight loss occurs due to sublimation of the KOH to (KOH)₂ molecules in the vapor phase [183, p. 945].

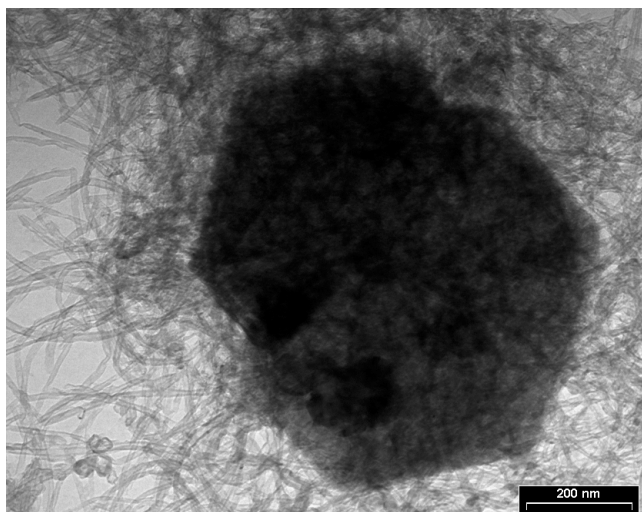


Figure 4.17 TEM micrograph of a water-washed KOH@MWNT sample showing the formation of micron-sized hexagonal platelet crystals.

When this product is dried however, its specific surface area ($60 \text{ m}^2/\text{g}$) is much lower than the one of the pristine CNTs ($222 \text{ m}^2/\text{g}$). This means that contrary to the observations of Green and coworkers on SWNTs, simple washing with water is not sufficient to completely remove the hydroxide from the nanotubes. The hydroxide cannot be completely removed either by stirring the product in boiling water for 16 h.

We tried to see by electron microscopy whether the washed tubes are filled with KOH. During the observation, micron-sized hexagonal platelets crystalized on the sample holder, as shown in Figure 4.17. Unfortunately, the microscope we used for these observations is not equipped with an EDS detector so that the exact chemical composition of this deposit cannot be directly determined. However, looking at the crystal structures, it is unlikely that these crystals are made of KOH. The crystal structure of KOH (Figure 4.18a) is monoclinic (space group $P2_1/m$) and is a slightly distorted variant of the structure of NaOH (orthorhombic, space group $Cmcm$, Figure 4.18b), in which there are linear Na–O–H units [184]. In both structures, the environment of the oxygen atoms is a pyramid with quadratic base; this structure does not give rise to a hexagonal crystal shape. However, nickel hydroxide $\text{Ni}(\text{OH})_2$ crystallizes in the hexagonal $P\bar{3}m1$ space group [185]. Its structure is composed of independent OH–Ni–OH layers; the intra-layer symmetry is hexagonal (Figures 4.18c and d). Thus, the formation of hexagonal platelets seems likely for nickel hydroxide.

HCl treatment. To remove all traces of hydroxides, we boiled the washed nanotubes in hydrochloric acid, diluted 1 : 1 with water (about 6 mol/L), for 16 hours under magnetic stirring. At the end of the reaction, all the MWNT readily precipitate, which means that they are no longer stabilized by charged functional groups. Most of these groups are carboxylic acids ($-\text{COOH}$) which are in their neutral form in an acidic solution. The clear supernatant is light blue while it

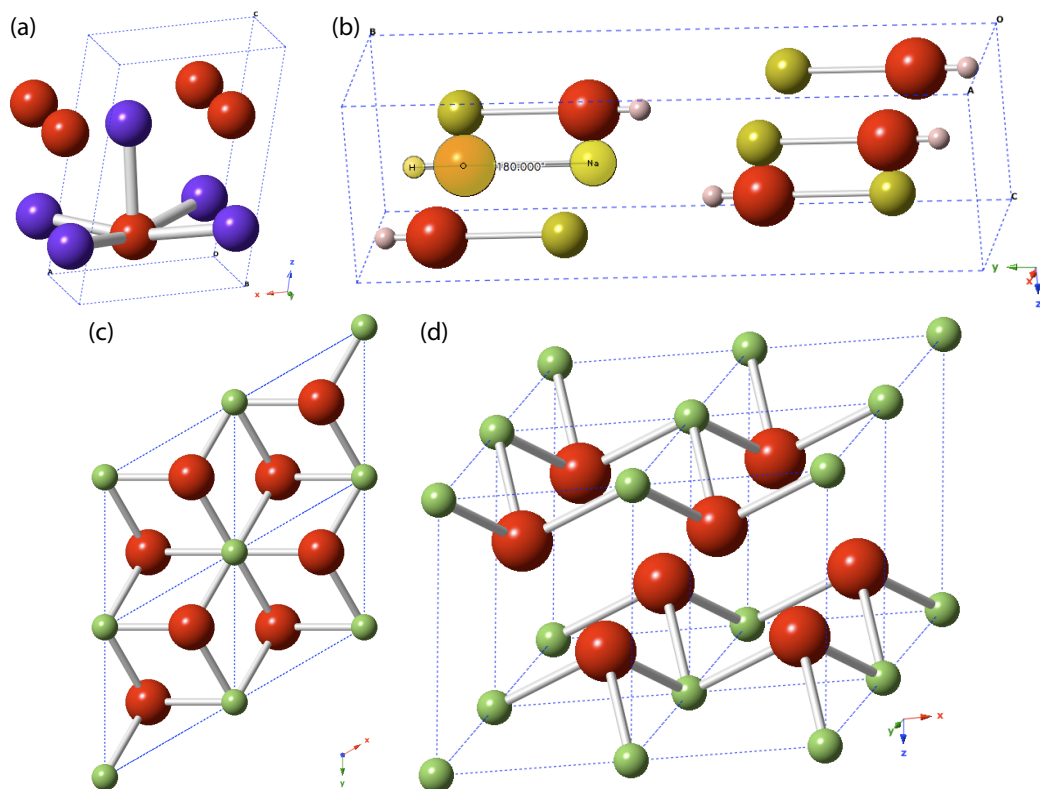
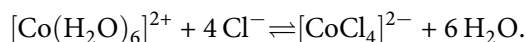


Figure 4.18 Crystal structures of some of the relevant metal hydroxides: KOH (H not shown), with bonds indicating the quadratic-pyramidal environment ($CN = 5$) of oxygen (red) by potassium (violet) (a); NaOH structure for comparison, showing the linear Na-O-H arrangement (b); hexagonal layered structure of nickel hydroxide (H not shown) from the side (c) and from the top (d). Images created from atomic structure data [184, 185] with CrystalMaker.

is near its boiling point and becomes colorless when cooled down to room temperature. This is a sure sign for cobalt(II) ions, as it corresponds to the equilibrium



The hexaquo complex has a pink color that is not seen because of the low concentration of Co^{2+} . The chloro complex, on the other hand, has an intense blue color. The equilibrium is pushed to the right by raising the temperature because there is an increase in entropy by going from five to seven independent particles. The influence of entropy (as in $\Delta G = \Delta H - T\Delta S$) in the position of the equilibrium becomes stronger when the temperature T is higher.

The cobalt comes from catalyst particles in the nanotube samples: the catalyst used for MWNT growth are metallic Co nanoparticles. Even though the tubes had been treated with HCl by the manufacturer before, the KOH treatment opened their walls and made some catalyst particles that had previously been fully covered with graphitic carbon accessible to removal by HCl. The Ni^{2+} ions in the solution have a much weaker color and are not visible.

The cleaned nanotubes are isolated by filtering the suspension over a 450 nm OMNIPORE membrane, abundantly washing with ultrapure water and drying for 2 h at 105°C in an oven [163]. TGA analysis of the HCl-washed carbon nanotubes shows that the ash content is reduced to near zero; the value is too small to be measured with TGA, as the measured residue is slightly negative ($-10 \mu\text{g}$ for a 2 mg sample).

Annealing. Oxygenated functional groups on the CNT surface can act as preferred nucleation sites for metal salts by forming metal carboxylates. To study this phenomenon, we want to tune the quantity of these functional groups on the CNT surface. In order to reduce their number, we annealed the cleaned MWNT at 950°C for 1 h (heating rate 10 K/min) under flowing argon (150 mL/min) in a tubular furnace. Through this process, small adsorbed molecules (“oxidation debris”) is removed by sublimation, and part of the $-\text{COOH}$ groups are removed by decarboxylation and subsequent elimination of CO_2 . It is known that carboxylic acids and anhydrides are the least stable functional groups on carbon surfaces and typically decompose to CO and CO_2 below 600°C, while lactones, quinones, phenols and ethers are eliminated at higher temperatures of 600–1100°C [148]. A small amount of graphitization might also take place; however, complete graphitization occurs only at temperatures of 1500°C and above.

During the reaction, we observe that small amounts of a white substance, which we assume to be oxygenated organic molecules, deposit on the cool part of the quartz tube used for the reaction. This residue is soluble in ethanol, which is what would be expected for polar organic molecules.

Characterization of the products. Figure 4.19 shows the TGA curves in air for a heating rate of 5 K/min of the four product stages: pristine MWNT, after the KOH infiltration, after cleaning with HCl and after annealing. Table 4.5 resumes the analytical data for the samples. The high ash

4 Characterization and treatment of carbon nanotubes

Sample	Ash (wt-%)	T_o (°C)	S_{BET} (m ² /g)	A_D/A_G
Pristine MWNT	1.5	522	222	1.12
KOH-infiltrated	14.2	420	60	
washed with HCl	~ 0 ^a	535	302	0.844
annealed at 950°C	~ 0 ^a	528	315	0.902

^a residue below experimental error, slightly negative result

Table 4.5 Analytical data for the different steps of the filling with KOH: ash content of the sample, oxidation temperature T_o at which the combustion velocity is maximal, specific surface area, ratio of D peak area to G peak area in the Raman spectrum.

Sample	C (wt-%)	O (wt-%)	H (wt-%)	N (wt-%)
Pristine MWNT	94.62	0.82	0.33	< 0.10
washed with HCl	95.14	2.50	0.31	< 0.10
annealed at 950°C	96.84	0.88	< 0.30	< 0.10

Table 4.6 Results of elementary analysis of different steps of the filling of MWNT with KOH: weight percentages for carbon, oxygen, hydrogen and nitrogen.

content of the KOH-infiltrated sample is due to the metallic residues (KOH and Ni(OH)₂) still present after washing. The oxidation temperature T_o is much lower than in either the pristine or the cleaned sample; this fact also points to the presence of transition metal atoms catalyzing the oxidation of carbon. After HCl cleaning however, the oxidation resistance is even slightly higher than in the pristine material. We believe that this effect is mostly due to the removal of the residual catalyst particles. Finally, after annealing the nanotubes at 950°C, the T_o is again slightly decreased, indicating that the nanotube structure has been slightly damaged again.

Table 4.6 shows the results of elementary analyses at different stages of the process. Between the pristine MWNT and the HCl-washed samples, the percentage of carbon atoms increases, which is due to the removal of inorganic impurities. The percentage of oxygen is increased from 0.8 to 2.5 wt-%, confirming the formation of oxygenated functional groups on the nanotube surfaces. After annealing at 950°C, the percentage of oxygen atoms is again decreased and slightly above the initial value, which means that the annealing successfully removed the functional groups created in the KOH treatment.

The Raman spectra (Figure 4.20) show that the relative intensity of the D peak is reduced by about 25% after KOH infiltration and cleaning by HCl.⁷ This means that the mean distance between defect sites has actually *increased*. A possible interpretation of this phenomenon is based on the selectivity of the attack by the oxidative species, which occurs by preference on the sites which are highly defective, or on amorphous carbon impurities. Defect-free sites are attacked

⁷The relative intensities of the D and G peak are given in the rightmost column of Table 4.5.

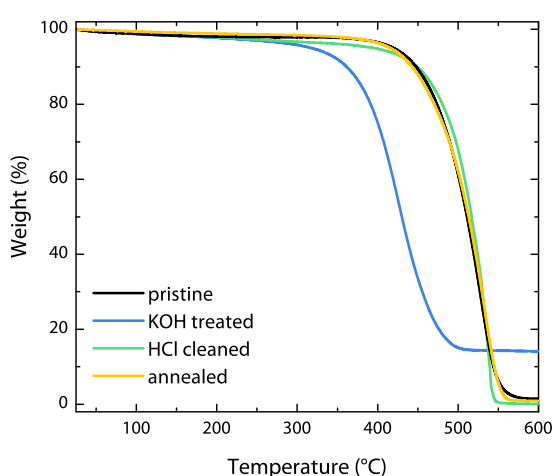


Figure 4.19 Thermogravimetric analysis of pristine FutureCarbon MWNT (black), after KOH treatment at 400°C, before (blue) and after washing with HCl (green) and after the final annealing step (purple).

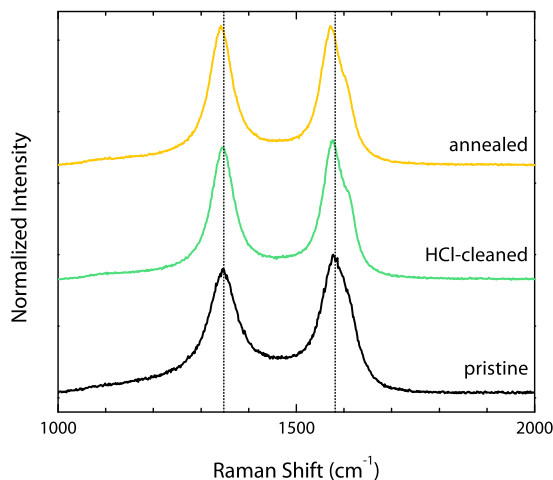


Figure 4.20 Raman spectra between 1000 and 2000 cm^{-1} for the pristine MWNT, the HCl-cleaned nanotubes and after annealing. Dotted lines indicate the peak positions for the pristine nanotubes.

more slowly, thus their relative contribution to the Raman spectrum increases during the treatment. After annealing, the A_D/A_G ratio again increases slightly but is still lower than in the pristine tubes; this confirms the observation from TG results that the removal of oxygenated groups creates new defects in the sp^2 carbon lattice. In both treated samples, there is a slight downshift in the G band center from 1581.3 to 1576.8 cm^{-1} , which is a sign of n-doping. Both the G and the D bands are narrower (by 20 and 40% respectively) in the treated tubes compared to the pristine ones. This also suggests a higher degree of uniformity of the graphitic carbons.

4.2.4 Aqueous KOH treatment

In the KOH filling treatment described in the previous section, slightly higher specific surface areas and some degree of nanotube shortening can be achieved if the concentrated basic solution obtained by dissolving the KOH/MWNT composite is left standing for a day or more at room temperature. The proportions used in that reaction, 9.0 g of KOH in 70 mL of water, result in a concentration of $c = 2.3$ mol/L. Can such a solution attack and possibly damage CNTs at room temperature, resulting in opening and/or cutting? To elucidate this question, we did a systematic study, in which pristine MWNTs are soaked for varying amounts of time in an aqueous KOH solution of the same concentration as above. The effect on morphology and on the specific surface area depending on the reaction time is measured.

For each sample, 100 mg of pristine FutureCarbon MWNT are added to a solution of 3.0 g KOH

4 Characterization and treatment of carbon nanotubes

Reaction time (h)	KOH treated	HCl cleaned	annealed
0	222.0	240.1	246.5
6	243.6	250.9	269.5
24	248.7	–	275.3
72	253.0	–	–
168	255.4	280.3	279.0

Table 4.7 Specific surface areas S_{BET} for MWNT samples treated with aqueous KOH solution for different amounts of time after washing with water, cleaning with HCl and after annealing (see text).

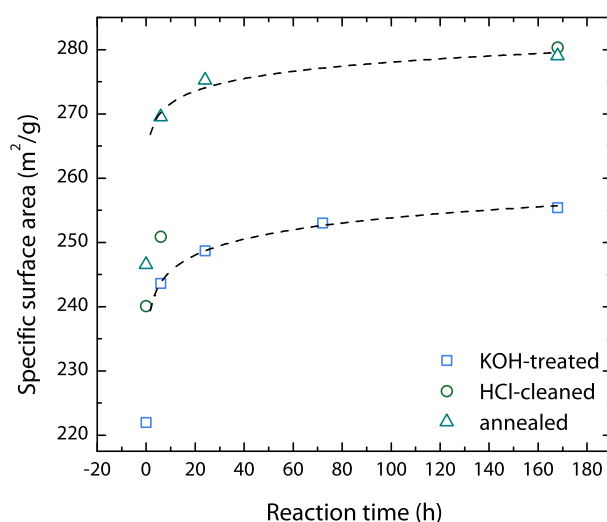


Figure 4.21 Graph of the specific surface area for MWNT samples treated with aqueous KOH solution for different amounts of time, non-linear fits for $S = at^b$ (dashed lines).

(Labosi, ~ 85%) in 25 mL of ultrapure water. After 1 h of magnetic stirring, the samples are left for a given time at ambient conditions. For the last 60 minutes of the treatment, the suspension is stirred again. The total reaction times used were 6, 24, 72 and 168 hours (one week). After this time, the KOH is removed by five sonication–centrifugation cycles as above, until a neutral pH of the supernatant is observed. The water is removed, and each sample is dried for 2 h at 110°C.

In the next step, the samples from above are added to 70 mL of concentrated HCl (Prolabo) diluted by an additional 70 mL of H₂O and stirred under reflux for 16 h. The nanotubes are again isolated by repeated cycles of washing and centrifugation as above and dried under the same conditions.

The third step, as before, consists in annealing the sample at 950°C (10 K/min heating rate, 1 h dwell time) in a tubular furnace under an argon flow of 150 mL/min.

Results. The specific surface areas measured on the products after each step of the treatment are given in Table 4.7 and in Figure 4.21. Contrary to the molten KOH infiltration discussed

in the last section, simply washing with water is sufficient to eliminate all traces of KOH after the treatment. This corroborates the assumption that the residual impurity before really was a transition metal hydroxide.

In the first few hours, S_{BET} rapidly increases; for higher durations, the increase in surface area becomes slower and approaches a limiting value of about $280 \text{ m}^2/\text{g}$. It should be noted that this value does not correspond to a complete opening of the ends of the nanotube, thus complete opening of the ends cannot be achieved with KOH at room temperature. On a double logarithmic plot, the $S_{\text{BET}} = f(t)$ values for treated samples lie on a straight line. They can thus be well fitted by a function of the form

$$S_{\text{BET}} = at^b,$$

where a and b are parameters and t is the treatment time. The resulting values are the following:

$$\begin{aligned} a_{\text{KOH}} &= 237.6 \text{ m}^2/\text{g}; & b_{\text{KOH}} &= 0.014 \\ a_{\text{annealed}} &= 265.4 \text{ m}^2/\text{g}; & b_{\text{annealed}} &= 0.010 \end{aligned}$$

The difference of the specific surface area between the KOH-treated and the annealed samples is almost constant at $25 \text{ m}^2/\text{g}$.

To verify the influence of this mild treatment on the graphitic lattice, we performed Raman spectroscopy on the most strongly oxidized sample, the one that has been immersed in the KOH solution for 168 hours. To our surprise, the Raman spectra (not shown) of this series of products are virtually identical to the one of the pristine nanotubes. The $A_{\text{D}}/A_{\text{G}}$ ratio is between 1.10 and 1.15 for all products, the differences are in the error margin of the determination method. The same downshift of the G peak is observed for the treated products; however, it is only 2 cm^{-1} , which is almost negligible for a peak width (FWHM) of 80 cm^{-1} . We conclude that a room-temperature aqueous KOH treatment does not significantly damage the graphitic lattice or introduce large number of defects.

4.3 Conclusion of this chapter

In this chapter, we showed how selective oxidation treatments are able to open the closed ends of multi-walled carbon nanotubes (MWNT). The treatments lead to the formation of oxygenated functional groups on the CNT surface; they can be removed again by annealing at 950°C . For thermal oxidation, the selectivity and the damage pattern depends on the temperature: the lower the temperature, the more selectively the oxidation proceeds. Filling with KOH seems to be a the best method of the ones presented here to open the ends of the CNTs while having good yields.

Chapter 5

Filling of carbon nanotubes with metal oxides

In this chapter, we will fill the four types of carbon nanotubes (SWNT, DWNT, MWNT, CNF) discussed in chapter 4 with four different metal oxides (manganese, chromium, vanadium and copper oxide) using three different techniques – infiltration of molten precursors, infiltration of an aqueous solution of a precursor, and “reactive infiltration”. Table 5.1 shows which products will be prepared by what method. The choice of the method depends on the properties of the oxide and of its precursor.

In the first part of the chapter, we will study the properties of the chosen precursor salts, which can all be decomposed by heating to form the corresponding metal oxide. The next sections each contain the result of filling experiments with one oxide. First, we use the reactive infiltration technique to prepare manganese oxide-filled carbon nanotubes, comparing the properties of the products depending on the type of nanotubes; this allows to select the nanotube types that are best suited for being filled with oxides. We will also use this system to explain many of the effects encountered during CNT filling experiments. Due to its low melting point (see below), we then try to infiltrate molten manganese nitrate into the carbon nanotubes.

The remainder of the experiments is carried out with the two types of nanotubes (MWNT and CNF) that seem to work best for filling experiments. The following short section (5.3) shows the reactive infiltration of MWNT with chromium oxide; while this system has a limited interest for the preparation of nanothermites, it shows that the synthesis technique is easily adapted to other oxides.

For vanadium and copper oxide, we used only the infiltration from aqueous precursor solutions, for different reasons: ammonium metavanadate precipitates in acidic solutions, while the solubility of copper(II) nitrate in nitric acid is relatively low. In both cases, we show results on MWNTs, followed by CNFs.

The most interesting products from each series, i. e. those with high a metal oxide loading, will be used for preparing nanothermite formulations in chapter 6.

	calcination temp.	melt	aqueous solution	reactive infiltration
MnO _x @SWNT	225°C			x
MnO _x @DWNT	225°C			x
MnO _x @MWNT	190°C ^a 225°C ^b	x		x
MnO _x @CNF	225°C	x		x
Cr ₂ O ₃ @MWNT	225°C			x
V ₂ O ₅ @MWNT	325°C		x	
V ₂ O ₅ @CNF	325°C		x	
CuO@MWNT	325°C		x	
CuO@CNF	325°C		x	

^a melt infiltration

^b reactive infiltration

Table 5.1 Overview of the filled nanotube systems presented in this chapter, the temperatures at which they were calcined and the methods they were prepared with (x means a prepared product).

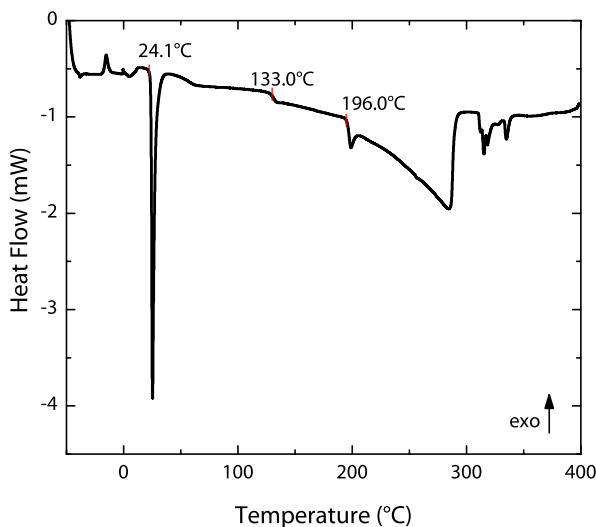


Figure 5.1 DSC trace of manganese nitrate $\text{Mn}(\text{NO}_3)_2 \cdot 4\text{H}_2\text{O}$ in a sealed hermetic crucible at 2 K/min. The onset temperatures of the melting point and decomposition reactions are annotated.

5.1 Study of the thermal stability of the metal oxide precursors

5.1.1 Manganese nitrate tetrahydrate

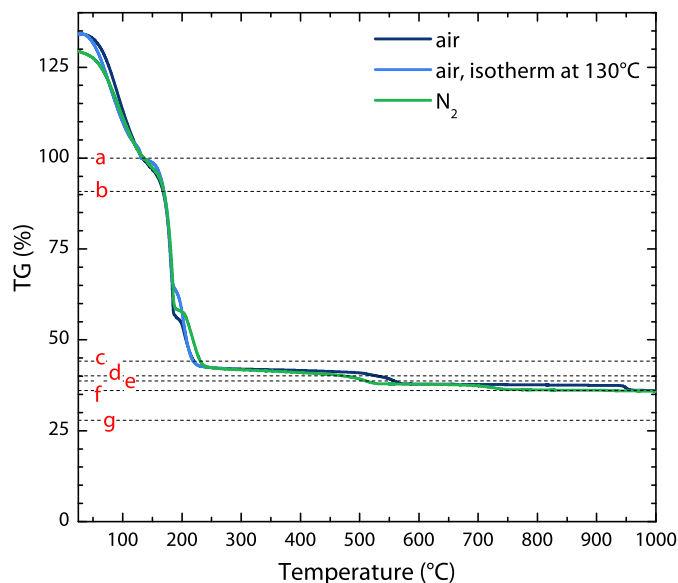
Manganese nitrate tetrahydrate $\text{Mn}(\text{NO}_3)_2 \cdot 4\text{H}_2\text{O}$ is a rose-colored manganese salt. It contains manganese in the +II oxidation state. It is strongly hygroscopic and oxidizing. Its most surprising property, perhaps, is the very low melting point of only 24°C, which can be seen in the DSC trace in Figure 5.1. Accordingly, the salt has to be stored at +4°C. It is extremely well soluble in water, acetone and ethanol, to the point of being miscible in almost any quantity with it. The solubility in higher alcohols, such as 2-propanol, decreases with an increasing length of the alkyl chain. The dissolution is very slow in these solvents, while it is fast in water and acetone.

According to the Material Safety Data Sheet (MSDS), the thermal decomposition occurs somewhere beyond 130°C. The onset is indeed found at 133°C in the DSC; however, for the higher temperatures, there is a distortion of the DSC trace due to the generation of gas because the analysis was carried out in a sealed hermetic crucible.

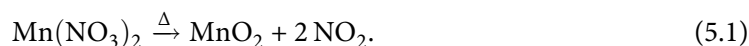
The thermal decomposition of manganese nitrate leads to the formation of manganese oxide. Manganese has a rich chemistry in its oxides, with oxidation states that can range from +II to +IV. The main phases are:

- ▶ MnO (+II)
- ▶ Mn_3O_4 (= $\text{MnO} \cdot \text{Mn}_2\text{O}_3$; +II and +III)
- ▶ Mn_2O_3 (+III)
- ▶ MnO_2 (+IV)

Figure 5.2 Thermogravimetric analysis of manganese nitrate $\text{Mn}(\text{NO}_3)_2 \cdot 4\text{H}_2\text{O}$ in an open alumina crucible at 5 K/min under air (blue) and nitrogen atmosphere (green). The end of the evaporation of the water of constitution was taken as 100 wt-%; horizontal dashed lines indicate stoichiometric phases: $\text{Mn}(\text{NO}_3)_2 \cdot \text{H}_2\text{O}$ (a), anhydrous $\text{Mn}(\text{NO}_3)_2$ (b), MnO_2 (c), Mn_2O_3 (d), Mn_3O_4 (e), MnO (f), Mn metal (g).

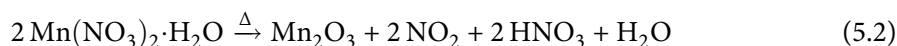


According to literature, manganese nitrate decomposes directly to MnO_2 as a result of a redox reaction between manganese and nitrogen following the reaction



This is not the observed behavior however, as can be seen on the thermogravimetric analysis reported in Figure 5.2. First, we could not isolate the anhydrous salt. An isothermal hold at 130°C produced the monohydrate $\text{Mn}(\text{NO}_3)_2 \cdot \text{H}_2\text{O}$, which then decomposes directly. For comparison, this monohydrate was defined as the 100% reference point. The stoichiometric manganese oxide phases are indicated as dashed horizontal lines for reference in Figure 5.2.

It can be seen that the initial water content is variable due to the hygroscopic behavior of the salt. Regardless of the atmosphere (oxidizing or non-oxidizing), a non-stoichiometric product is reproducibly obtained at about 225°C; its formula is approximately equal to $\text{MnO}_{1.7}$. The density of this product was determined by helium pycnometry to be $(5.10 \pm 0.03) \text{ g/cm}^3$. We therefore propose a second decomposition equation with an incomplete oxidation of the manganese, leading to manganese(III) oxide and the elimination of nitric acid:



The real decomposition is likely to be somewhere in between reactions (5.1) and (5.2), with the non-stoichiometric oxide as the result.

At a temperature of 500°C in air or about 450°C in nitrogen, the oxide loses some oxygen and forms a sub-stoichiometric Mn_3O_4 of the approximate formula $\text{MnO}_{1.2}$. Upon even further

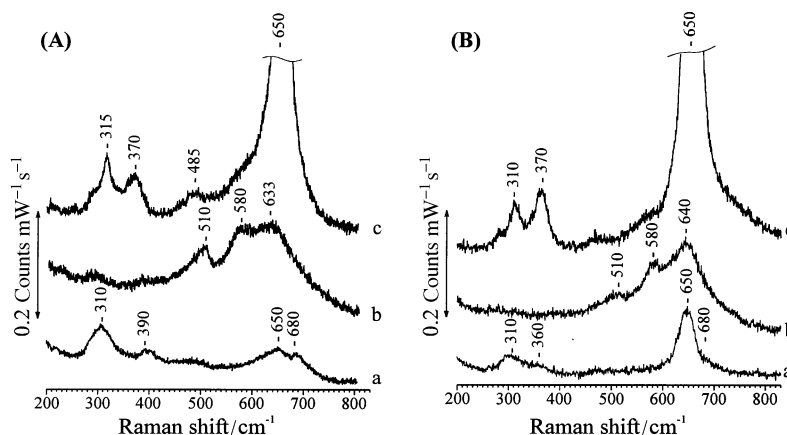


Figure 5.3 Raman spectra of Mn_2O_3 (a), MnO_2 (b) and Mn_3O_4 (c), recorded using $\lambda = 647.1$ (A, left) and 514.5 (B, right) laser lines. From [186].

heating, at 950°C in air or 700°C in nitrogen, stoichiometric MnO is formed. From this point, the oxygen content cannot decrease further without forming metallic $\text{Mn}(0)$. This analysis is very well reproducible over several runs and always forms the same products.

For the composite products with CNTs, we will show that the phase compositions formed are slightly different, due to the presence of carbon, which is a reducing agent, and due to nanoscale encapsulation effects.

Raman spectra of manganese oxides. The Raman spectra of the different manganese oxides show characteristic peaks for each phase, which allows to distinguish them from one another. Bucuman and coworkers [186] give reference spectra for Mn_2O_3 , MnO_2 and Mn_3O_4 with different laser excitation wavelengths. Of these, the blue laser at 458 nm is the least useful, resulting in weak signals. The two other ones, for 647 and 514 nm excitation, have been reproduced in Figure 5.3.

The strongest peak, at 650 cm^{-1} , is obtained for the Mn_3O_4 phase, which also gives weaker peaks at 310 – 315 and 370 cm^{-1} . The characteristic peaks for MnO_2 are located at 510 (weak) and 580 cm^{-1} , while the peak at 633 – 640 cm^{-1} is attributed to the formation of γ - Mn_2O_3 , a distorted, hausmannite-like intermediate form in the transition from MnO_2 to Mn_3O_4 . The peaks of Mn_2O_3 , seen in the bottom curve of Figure 5.3, are mostly due to the formation of Mn_3O_4 during the recording of the spectrum (310 , 360 and 650 cm^{-1}). The authors consider the weak signal at 680 cm^{-1} as being the only characteristic one for Mn_2O_3 .

This illustrates an important problem for the acquisition of Raman spectra of manganese oxides: as the laser beam heats the sample, the oxide can change its degree of oxidation from $\text{MnO}_2 \rightarrow \text{Mn}_2\text{O}_3 \rightarrow \text{Mn}_3\text{O}_4$, like we saw in the thermogravimetric analysis earlier. This means that the existence of a peak at 650 cm^{-1} , for instance, is not necessarily a sign of the presence of

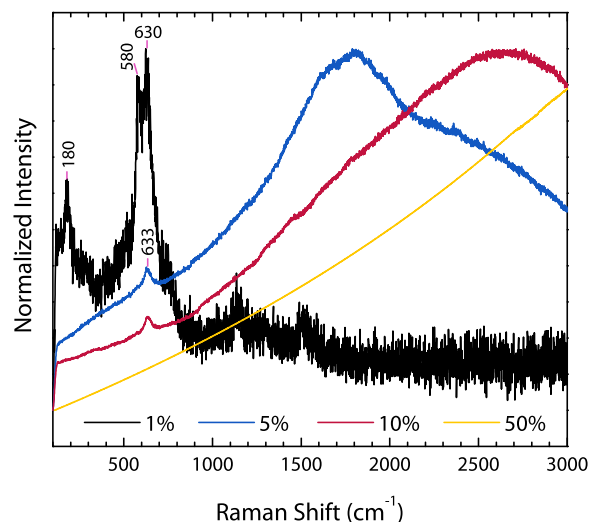


Figure 5.4 Raman spectrum of MnO₂ nanorods, recorded at 633 nm excitation with different laser powers: 1%, 5%, 10%, and 50%. The sample is completely destroyed after the 50% observation.

Mn₃O₄ in the initial sample – the sample composition may have changed by heating. It also means that the Raman spectra are highly dependent on the incident laser power. This point is further illustrated by Figure 5.4, which shows the Raman spectrum for MnO₂ nanorods depending on the incident laser power. For 1% power, corresponding to about 0.2 mW, Raman peaks at 180, 580 and 633 cm⁻¹ are seen, which clearly corresponds to the characteristic MnO₂ peaks described above. At 5 and 10%, only one peak at 633 cm⁻¹ can be distinguished, corresponding to γ -Mn₂O₃ formation by the decomposition of the manganese dioxide. The baseline is more and more distorted going to higher laser powers. Finally, after the illumination at 50% power (~ 10 mW), the sample is completely destroyed, and only a flat line is observed. This example strikingly illustrates that one has to be very careful in choosing the right laser power for analyzing the sample.

5.1.2 Chromium nitrate nonahydrate

Chromium nitrate nonahydrate Cr(NO₃)₃ · 9 H₂O is a dark violet, hygroscopic oxidizing salt of chromium(+III). It is very soluble in water and can be decomposed by heating. Figure 5.5 shows is TG/DSC analysis under nitrogen. The first endothermic peak on the DSC trace with its onset at 78°C is the melting of the salt, which is accompanied by a rapid loss of the water of constitution. The second endothermic peak, with its onset at 130°C, corresponds to the thermal decomposition of the nitrate. The endothermic behavior is caused by the hot gases leaving the crucible and evacuating a certain amount of heat. At about 300°C, a plateau in the mass is reached. It corresponds to a hydrated chromium oxide of the formula CrOOH or Cr₂O₃ · H₂O. This oxyhydroxide is finally dehydrated at 430°C to form pure stoichiometric Cr₂O₃. A small endothermic peak can be seen in the DSC curve at this temperature. Contrary to the case of manganese (see section 5.1.1),

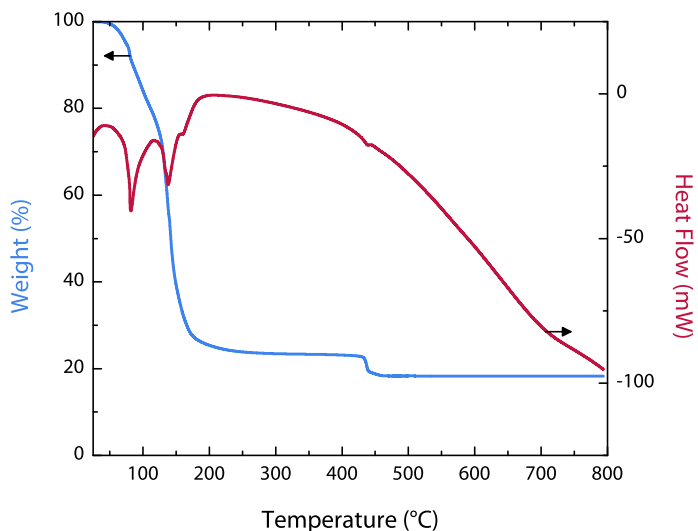


Figure 5.5 Thermogravimetric analysis (TG/DSC) of chromium nitrate nonahydrate in nitrogen: weight (—) and heat flow (—).

there is no redox reaction between the metal ion and the nitrate involved; we only deal with a single oxidation state, namely +III.

The analysis of the decomposition products by X-ray diffraction (Figure 5.6) confirms this mechanism: after heating to 300°C, the product is an amorphous form of chromium oxide hydroxide (lower part); the only noticeable feature in the diffractogram is a very large peak centered at about $2\theta = 27^\circ$, which corresponds to the position of the most intense reflection of CrOOH (guyanaite, 20-312), the (110) peak at 27.6° . After heating to 500°C, the product shows relatively intense peaks that clearly belong to the Cr₂O₃ phase (eskolaite, 38-1479). A crystallite size determination via the Full Pattern Matching (FPM) routines in the EVA software gives a mean size of 35.0 nm.

A very interesting property of chromium nitrate is its natural tendency to foam. The thermal decomposition is accompanied by a large increase in volume; every drop forms a large hemispherical oxide “dome” that contains much empty space (see Figure 5.7). It is very brittle, and one can easily crush it with a pestle. At lower temperatures, up to about 300°C, the color of the oxyhydroxide is a very dark violet with metallic shine. Upon further heating and crystallization, the color progressively changes to green; the green dome shown in the photo corresponds to well-crystallized chromium(III) oxide.

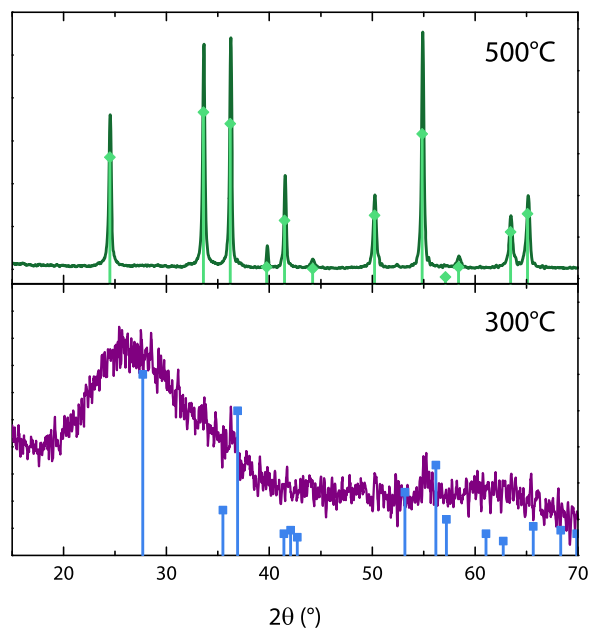


Figure 5.6 X-ray diffraction of the decomposition products of chromium nitrate: largely amorphous CrOOH and its pattern (guyanaite, 20-312) below; well-crystallized Cr_2O_3 with the corresponding JCPDS pattern (eskolaite, 38-1479) above.



Figure 5.7 Photo of a “dome” of Cr_2O_3 foam obtained by thermogravimetric analysis of chromium nitrate, residue from the test in Figure 5.5.

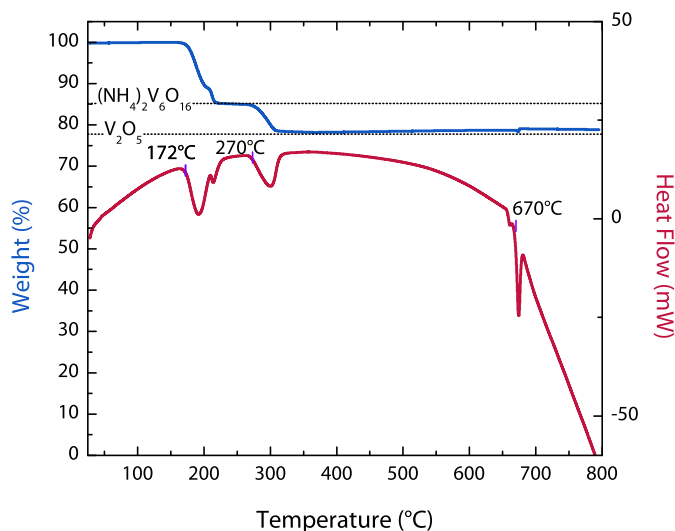


Figure 5.8 Thermogravimetric analysis (TG/DSC) of ammonium metavanadate NH_4VO_3 under nitrogen atmosphere (heating rate 5 K/min). Horizontal lines indicate the percentages corresponding to ammonium hexavanadate $(\text{NH}_4)_2\text{V}_6\text{O}_{16}$ and vanadium(V) oxide V_2O_5 . The annotated temperatures correspond to the peak onset values.

5.1.3 Ammonium metavanadate

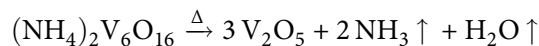
Vanadium oxide is an interesting compound for nanothermite applications for a number of reasons. It has a high percentage of oxygen due to the formation of a pentoxide containing V(+V) ions. Vanadium also has the tendency to change its oxidation state rather easily—at least in its aqueous chemistry, where a large number of differently colored vanadium and vanadyl (e. g. VO_2^+) cations are known.

The precursor chosen in this case is not a nitrate but an ammonium salt, ammonium metavanadate NH_4VO_3 . Like nitrates, ammonium salts are known to decompose upon heating. During the decomposition, no redox processes involving the vanadium atom are necessary as it is already in the +V oxidation state. This should make the reaction very clean and robust and result in a pure vanadium pentoxide.

The result of a TG/DSC measurement under non-oxidizing atmosphere is shown in Figure 5.8. The first reaction (onset temperature of 172°C) is a decomposition that seems to proceed in two steps to give ammonium hexavanadate as the intermediary product:



The next step, with its onset at 270°C, is the decomposition of the hexavanadate to vanadium pentoxide:



In order to confirm the assignment of the different phases, the crystalline phases in the intermediate products were analyzed by X-ray diffraction, as shown in Figure 5.9. The color of the products can be seen in the photos of the powders given in Figure 5.10. The product heated to

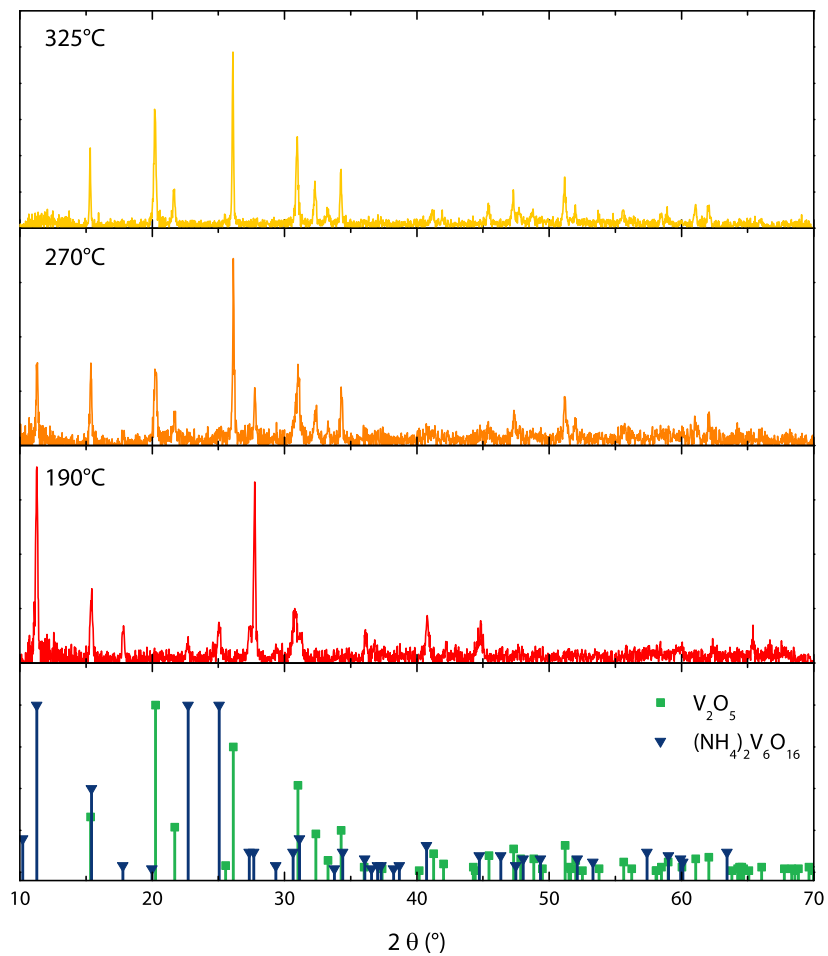


Figure 5.9 X-ray diffraction results for ammonium metavanadate NH_4VO_3 calcined at different temperatures: 190°C, 270°C, 325°C. The indexed phases (bottom) are ammonium hexavanadate $(\text{NH}_4)_2\text{V}_6\text{O}_{16}$ (JCPDS file 22-1046, blue) and vanadium oxide V_2O_5 (Shcherbinaite, 41-1426, green).



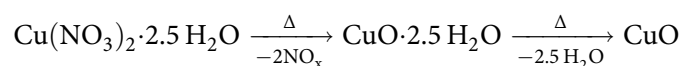
Figure 5.10 From left to right: Photos of ammonium metavanadate and the decomposition products after heating to 190°C, 270°C and 325°C.

190°C (in the middle of the first weight loss peak) consists entirely of ammonium hexavanadate $(\text{NH}_4)_2\text{V}_6\text{O}_{16}$, corresponding to the JCPDS file 22-1046. At 270°C (the onset temperature of the second weight loss step), the product is a mixture of ammonium hexavanadate and vanadium pentoxide. Looking closely at the photo, one can distinguish grains of different color, indicating that some of the grains have already reacted while others have not. Finally, at 325°C, we find only the peaks corresponding to vanadium pentoxide, or Shcherbinaite (JCPDS file 41-1426). The corresponding photo shows the typical orange-yellow color of V_2O_5 .

The vanadates are the secondary group analog of the phosphates. When ammonium metavanadate is brought into contact with acidic solutions, the a polyanion is formed, finally leading to vanadium pentoxide powder. This is analogous to the formation of polyphosphates. It is also the reason why no reactive infiltration experiments can be carried out for the CNT/vanadium oxide system. Another disadvantage of ammonium metavanadate is its high toxicity: due to the chemical similarity with phosphates, vanadates can displace phosphate ions in biochemically active molecules, such as enzymes, in the body.

5.1.4 Copper nitrate hemi(pentahydrate)

Copper nitrate hemi(pentahydrate) $\text{Cu}(\text{NO}_3)_2 \cdot 2.5 \text{H}_2\text{O}$ is a deep blue colored, hygroscopic copper(II) salt. As the other transition metal nitrates, it can be thermally decomposed to yield the oxide. The TG/DTA curves are shown in Figure 5.11. Contrary to manganese and chromium nitrate, the water of constitution seems to be more tightly bound in this compound, as it is not given off at low temperatures; instead, the mass stays constant up to the first endothermic peak, which corresponds to the melting of the compound (onset 113°C). The melting also initiates the decomposition (second endothermic peak), which proceeds through a removal of NO_x first and the evaporation of the water of constitution in a second step (onset 225°C):



The end product of the thermal decomposition is Copper(II) oxide CuO .

Even though copper nitrate is very soluble in H_2O (about 1500 g/L), it is considerably less soluble in its “parent acid”, concentrated HNO_3 . This is because there is a *solubility product*, which is equal to the product of the ionic concentrations $[\text{Cu}^{2+}][\text{NO}_3^-]$. In nitric acid, $[\text{NO}_3^-]$ is already high so that the solubility of copper nitrate is lower.

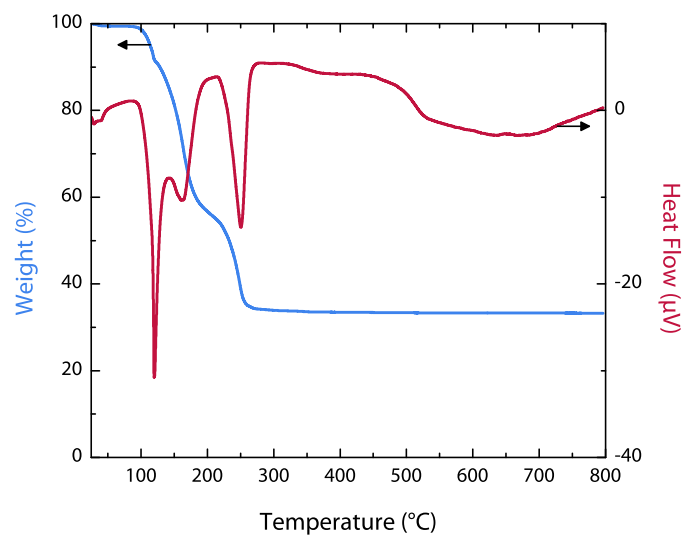


Figure 5.11 Thermogravimetric analysis (TG/DTA) of copper nitrate hemi(pentahydrate) $\text{Cu}(\text{NO}_3)_2 \cdot 2.5\text{H}_2\text{O}$ in air at 5 K/min: weight (—) and heat flow (—).

5.2 Filling with manganese oxide

5.2.1 Reactive infiltration: comparison of CNT types

The systematic study presented here was intended to elucidate the influence of the nanotube type and size on the properties and the morphology of the final product. To do this, we prepared $\text{MnO}_x\text{@CNT}$ nanocomposites from three types of carbon nanotubes – SWNT, DWNT and MWNT – with the reactive infiltration method. This method has the merit of being easy to perform, as it combines the opening of the nanotube ends and their endohedral filling in a single step. This study was presented as an oral communication at the *Carbon 2009* conference [187].

The different types of CNTs have already been presented with their properties and typical dimensions in Table 4.1 in the last chapter.¹ Let us now calculate the **maximum metal oxide loading** that can be obtained for each CNT type. Like in the calculation of the specific surface area for opened and closed CNTs,² we call the inner radius of the nanotube r (diameter d) and the outer radius R (diameter D) and approximate the perfectly filled nanotube as two concentric cylinders of length l . In the following, we use the index 1 for the manganese oxide and 2 for the CNT; ρ_1 and ρ_2 are the densities of the manganese oxide and the CNTs, respectively. The MnO_x content in wt-% Y_1 is thus

$$\begin{aligned}
 Y_1 &= \frac{m_1}{m_1 + m_2} \\
 &= \frac{\pi r^2 l \rho_1}{\pi r^2 l \rho_1 + \pi (R^2 - r^2) l \rho_2} \\
 &= \frac{d^2 \rho_1}{d^2 \rho_1 + (D^2 - d^2) \rho_2}.
 \end{aligned} \tag{5.3}$$

The final form of this expression uses the diameter instead of the radius, the factor $1/4$ being simplified in the division. As for the densities, we use the density measured by helium pycnometry from the last section for the MnO_x ($\rho_1 = 5.10$) and the density calculated from the position of the (002) X-ray diffraction peak for the MWNTs,³ which is $\rho_2 = 2.17$. To account for the distribution in tube diameters and wall thicknesses, we will calculate a highest and a lowest estimate for the maximum loading, considering all the tubes are completely filled without exocrystallization.

For the smallest SWNTs, whose inner cavity is just 0.35 nm wide (comparable to a fullerene), a complete filling corresponds to only 23 wt-% of MnO_x . From the ionic radii (80 pm for Mn^{2+} , 140 pm for O^{2-}), only a 2×2 or 3×3 atomic column would fit in such a nanotube, comparable to what has been obtained for potassium iodide [102]. For a larger SWNTs, whose nucleus-to-nucleus diameter is $d_t = 1.6$ nm (corresponding to $d = 1.25$ nm and $D = 1.95$ nm), the theoretical

¹See page 61.

²See section 3.4.2, page 45ff.

³See the explanations in section 4.1.3, page 63ff.

Sample	theoretical maximum loading (wt-%)
MnO _x @CNF	31–65
MnO _x @MWNT	33–65
MnO _x @DWNT	23–72
MnO _x @SWNT	23–62

Table 5.2 Theoretical maximum loading with manganese oxide obtainable for the different types of MnO_x@CNT composites, as calculated by a geometrical model.

maximum is 62 wt-% of oxide. As the SWNTs are composed of a range of different diameters between these values, the real maximum is somewhere in between these values. For MnO_x@DWNT, the maximum metal load obtainable for a hypothetical double-walled tube with $D = 5.0$ nm and $d = 3.6$ nm is 72 wt-%. For a more realistic double-walled nanotube with $D = 2.8$ nm and $d = 1.4$ nm, the maximum obtainable loading would be 44 wt-%; we found inner tubes with such a diameter by analyzing the RBM peaks in the Raman spectrum on as-received DWNT samples.⁴ The DWNT samples also contain some single-walled CNTs; in the case of a fullerene-like size, the maximum loading would again be only around 23 wt-%. Concerning filled MWNTs, the maximum loadings that could be obtained are between 33 wt-% ($D = 12$ nm, $d = 5$ nm) and 65 wt-% of oxide ($D = 15$ nm, $d = 10$ nm). For Pyrograf nanofibers (CNF), we have between 31 wt-% ($D = 100$ nm, $d = 40$ nm) and 65 wt-% of theoretical oxide loading ($D = 120$ nm, $d = 80$ nm).

The result of this calculation is thus that the quantity of metal oxide that we can fill into the different types of carbon nanotubes are in a similar range (Table 5.2). *We can expect loadings on the order of 20–60 wt-% of MnO_x for all the types of carbon nanotubes.* Even if their *absolute* sizes are very different, the *relative* dimensions – i. e. the ratio between inner and outer diameter – are similar.

Thermal behavior. The first reaction step, refluxing in the manganese nitrate solution in nitric acid, oxidizes the tube ends while possibly also creating defects and holes in the sidewalls or even removing (parts of) the outer shells for MWNTs. Simultaneously, manganese nitrate can enter through these newly created holes into the interior of the nanotubes, with nanocapillarity as a driving force. At the same time, the precursor solution is also trapped in the interstitial spaces, i. e. at the interior of larger aggregates and between the nanotubes in bundles.

Presumably, the liquid phase stays inside the nanotubes under the filtration conditions. Thus, after completion of the first step, some HNO₃ is still present. During the slow heating on calcination, the nitric acid evaporates, leaving liquid manganese nitrate, which then decomposes.

The synthesis method results in an intimate contact between the CNTs and the manganese oxide. To get an idea of the influence on the thermal behavior, it was compared to a model system.

⁴See section 4.1.2, page 63.

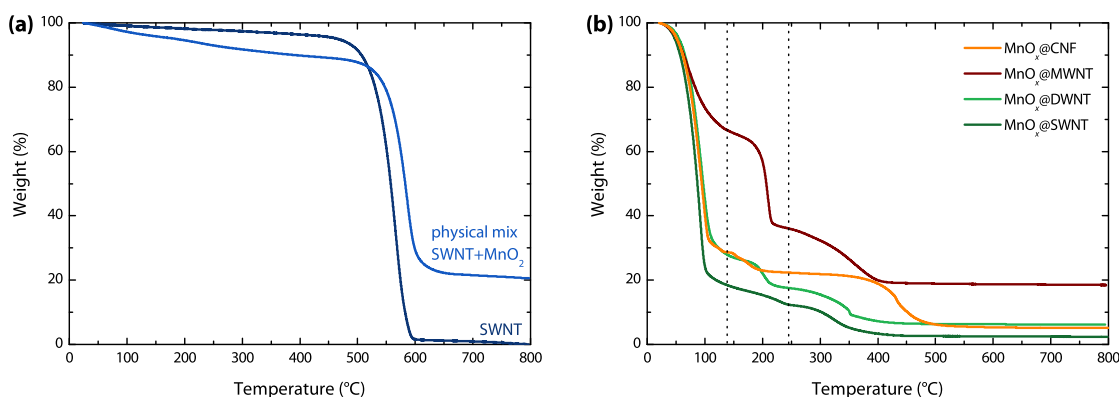


Figure 5.12 Thermogravimetric oxidation curves recorded in air at 5 K/min of as-received SWNT and SWNT physically mixed with MnO₂ nanoparticles (a); TG curves of MnO_x@CNT nanocomposites prepared by the reactive infiltration technique (b).

In this system, as-received SWNTs have been physically mixed with 22 wt-% of MnO₂ nanoparticles by sonication in hexane (a non-solvent) followed by evaporation. As shown in Figure 5.12a, the thermal stability of the carbon nanotubes is very similar to their pristine state, and the onset of their oxidation is located at 530°C. On the other hand, the thermogravimetry results for the MnO_x@CNT composites before their calcination (Figure 5.12b) show that the oxidation temperatures (T_0) of the carbon nanotubes (Table 5.3) are strongly reduced compared to the as-received tubes shown in Table 4.1. This means that there is a strong catalytic effect of the manganese oxide towards carbon oxidation, while the effect is completely absent in the physically mixed sample.

The TGA curves of the four samples show a characteristic three-step weight loss, which also allows choosing the right calcination temperature. The weight loss up to about 100°C corresponds to the evaporation of residual nitric acid. The second step is the thermal decomposition of manganese nitrate to manganese oxide. The third step, at temperatures above 250°C, corresponds to the oxidation of the CNTs in the air atmosphere.

We saw in the last section that the onset of the decomposition of the pure salt is 133°C. In the case of the composites here, the reaction is shifted to higher temperatures; Table 5.3 gives the values for the different samples. The smaller the nanotubes, the higher the onset temperature. The Pyrograf nanofibers only show a slight increase, while it is much more marked for the other types. This is somewhat surprising, as reaction temperatures are generally expected to be lower for smaller particle sizes. We attribute this behavior to a *confinement effect*, which means that the confinement inside a small nanotube somehow makes it more difficult for the manganese nitrate to decompose. It has been shown that molecular movements in pores are slower than in the bulk, and that this effect is inversely proportional to pore size [188]. Ravindra and coworkers have shown that proteins in the pores of mesoporous silica are significantly more stable against

5 Filling of carbon nanotubes with metal oxides

Sample	onset (°C)	T_o (°C)	ΔT_o (K)	oxide loading (wt-%)	S_{BET} (m ² /g)
MnO _x @CNF	146	427	-323	24	68.6
MnO _x @MWNT	179	357	-167	51	90.1
MnO _x @DWNT	187	350	-182	35	114
MnO _x @SWNT	190	320	-242	22	17.8

Table 5.3 Numerical results of the thermogravimetric analysis of the manganese nitrate-filled CNTs, prepared by reactive infiltration, before their calcination: onset of the decomposition of manganese nitrate to manganese oxide, oxidation temperature T_o of the CNTs, difference ΔT_o of the oxidation temperature of the composite to the one of the as-received CNTs, oxide contents of the composites.

temperature-induced unfolding compared to the protein in bulk solution [189]. We propose that the effect here is similar to these literature examples.

From the weight loss percentage associated with the different decomposition steps, the relative amount of manganese oxide in each composite can be assessed. From the weight loss m_{CNT} in the third step (burning of nanotubes) and the residue m_{res} , the proportion Y_{MnO_x} of manganese oxide in the composite is calculated as

$$Y_{\text{MnO}_x} = \frac{m_{\text{res}}}{m_{\text{CNT}} + m_{\text{res}}}. \quad (5.4)$$

The amount of NO_x (second weight loss step) can be useful to check the experimentally determined residue weight as the fraction $m_{\text{NO}_x}/m_{\text{MnO}_x}$ is constant and given by the stoichiometry. The quantity of nitric acid (first weight loss step) is not used for this calculation. The manganese oxide content of the nanocomposites, determined using equation (5.4), is shown in the rightmost column of Table 5.3. The loading is the lowest for the SWNT sample and increases with the diameter for DWNT and MWNT. However, the CNF sample shows again a lower loading. As the inner tube diameter is considerably larger in this sample than in the others, we suppose that it is easier to remove the manganese nitrate solution inside the tube by the vacuum filtration step.

Determination of the manganese oxide phase. We saw in the last section that the ideal reaction product of the decomposition of manganese nitrate is MnO₂ according to eqn. (5.1) and that the decomposition of the bulk nitrate gives non-stoichiometric manganese oxides. Heating pure Mn(NO₃)₂ · 4 H₂O to 225°C gave an oxide with the approximate composition MnO_x, with $1.6 \leq x \leq 1.7$, i. e. between Mn₂O₃ and MnO₂. Which manganese oxide phase is formed in the presence of carbon nanotubes?

Crystalline phases can be easily identified using **X-ray diffraction**. Figure 5.13 shows the X-ray diffractogram for three of the nanocomposites. In all cases, we identify three phases: graphitic carbon [56-159], MnO₂ in the pyrolusite structure [24-735] and Mn₂O₃ of the bixbyite-C type [41-1442].

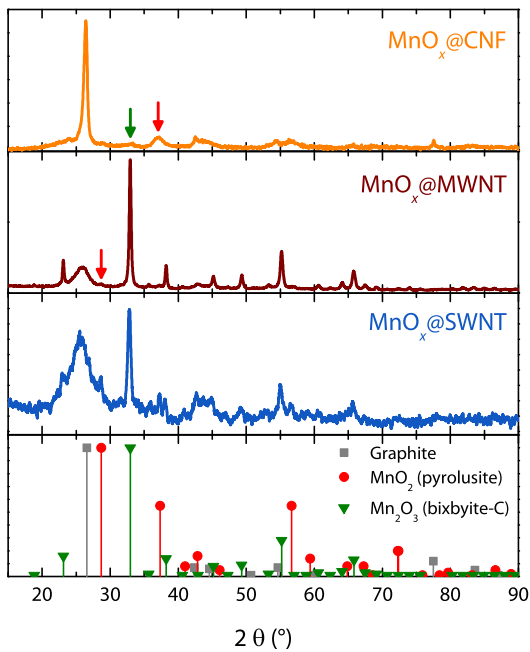


Figure 5.13 X-ray diffraction of different MnO_x @CNT nanocomposites prepared by reactive infiltration. The identified phases are graphite [56-159], MnO_2 (pyrolusite) [24-735] and Mn_2O_3 (bixbyite-C) [41-1442]. Arrows: see text.

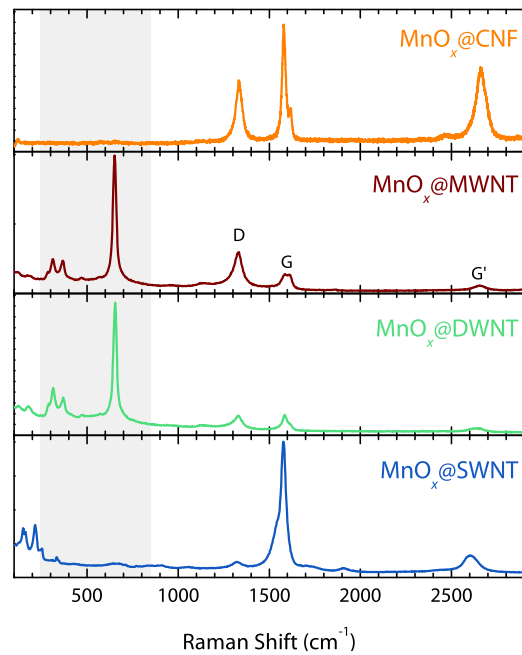


Figure 5.14 Raman spectra of different MnO_x @CNT nanocomposites prepared by reactive infiltration, taken at 633 nm laser excitation wavelength. The position D, G and G' peaks for graphitic carbon is indicated for the MWNT curve. The shaded area is where the manganese oxide peaks are expected.

In the case of the CNF composite (top), the diffractogram is clearly dominated by the peaks of the graphitic carbon. The oxide peaks are weak and large, indicating poorly crystallized oxide nanoparticles. The Mn_2O_3 peaks are weak but remain visible, especially the (222) reflection at $2\theta = 33.0^\circ$ (green arrow). The main reflection of MnO_2 (110) seems to be absent, however the (101) reflection ($2\theta = 37.3^\circ$) is well visible (red arrow). Based on full pattern matching for the whole MnO_x @CNF diffractogram, we get a 4 : 1 ratio of MnO_2 : Mn_2O_3 , which means that the stoichiometry of the manganese oxide in this sample is near $\text{MnO}_{1.9}$. The corresponding crystallite sizes, calculated with the Scherrer formula, are in the 8–10 nm range for both oxide phases.

For the MnO_x @MWNT composite, the diffraction pattern is clearly dominated by the bixbyite (Mn_2O_3) peaks, which are even stronger than the ones of graphitic carbon. The reflections for pyrolusite (MnO_2) are very weak but still visible, for example the (110) reflection at $2\theta = 28.7^\circ$ (red arrow). As the bixbyite reflections are obviously much more intense than the pyrolusite ones, the stoichiometry of the oxide is much closer to Mn_2O_3 . The stoichiometry determined from TG measurements is MnO_x with $x \approx 1.61$. The crystallite size of the manganese(III) oxide, determined again by the Scherrer formula for reflection broadening, is in the 20–30 nm range. Crucially, this is much larger than the cavity of the MWNTs; this is a sign that the reflections due to the oxide are mainly from material *outside* the MWNTs.

Regarding the MnO_x @SWNT composite, both the bixbyite and the pyrolusite phase show visible reflections, with an approximately 1 : 2 ratio of MnO_2 : Mn_2O_3 , corresponding to a $\text{MnO}_{1.65}$ oxide phase.⁵ The crystallite sizes from the line broadening are near 15 nm for both oxide phases, which is again much larger than the diameter of the SWNT cavities (0.7–1.5 nm). This means that, as with the MWNT sample, the main contribution to the diffractogram is from exocrystallized oxide particles.

Looking now at the **Raman spectra** of the different composites (Figure 5.14), we can gain some more information about both their phase and their morphology. For technical reasons, the top curve (MnO_x @CNF) was recorded on a different instrument (Renishaw inVia) than the rest (Jobin Yvon LabRAM). In the Raman spectrum for the MnO_x @CNF nanocomposite, there are no visible Raman peaks for manganese oxide. In the corresponding curve recorded at 514 nm (not shown), there is a very weak MnO_x signal at 650 cm^{-1} . However, we know from TGA and XRD that the sample does contain manganese oxide. We suppose that the sample mainly contains filled nanotubes as opposed to exocrystallized particles, and that the relatively thick carbon walls of the herringbone nanotubes (at least 20 nm) are completely opaque for the laser light. It thus seems that at least in this sample, *Raman spectroscopy does not account for the inside of the nanotubes*. The G peak of this sample shows an interesting feature: it appears as *two* separate peaks at 1579 and 1618 cm^{-1} . Their intensity ratio varies with the place being imaged on the

⁵The ratios of the different oxide phases have been determined by the “Full Pattern Matching” function in the EVA software using the graphite pattern with corrected *c* spacing, the pyrolusite and the bixbyite-C pattern as inputs.

sample but the upshifted peak is always weaker than the unshifted one. The lower-wavenumber peak is the same as in the unfilled CNFs as shown in Figure 4.3⁶ while the upshifted one appears only in the filled samples. This upshift is due to *p*-doping of the sample, which is likely due to the oxide filling of the nanotubes. This means that manganese oxide acts as an electron acceptor with respect to the CNTs. The presence of the unshifted peak means that *there is a significant number of nanotubes that does not contain manganese oxide*. Another possible explanation for the upshift is the intercalation of HNO₃ molecules between graphitic layers; as the sample has been calcined at 225°C however, this explanation seems less likely. Intercalation of nitric acid in SWNT bundles has been shown to lead to *p*-doping and an upshift in the G band Raman shift, but also to a partial quenching of the peak intensity [190]. The intensity ratio between the two peaks is thus not directly a measurement for the amount of doped/filled tubes.

In the MnO_x@MWNT sample, the same splitting of the G peak is observed; as the peaks are much larger, they overlap significantly. The peak centers are at 1586 and 1615 cm⁻¹. Contrary to the CNF sample, the signals from manganese oxide are visible with a high intensity. There are peaks at 312 (m), 369 (m) and 652 cm⁻¹ (s), which indicate the presence of Mn₃O₄. As XRD did not show this phase, it is either amorphous or (more likely) it has formed due to localized heating with the laser beam. According to Figure 5.2,⁷ this means that the sample has been heated locally to at least 550°C. There is also a small shoulder at 575 cm⁻¹, which is tentatively attributed to a small content of MnO₂. The intensity of these bands compared to the graphitic ones varies depending on the observed region of the sample, indicating a heterogenous structure in which various amounts of exohedral material is present. The high intensity of these peaks is also taken as a sign for exocrystallization.

The Raman spectrum of the MnO_x@DWNT nanocomposite gives essentially the same information as the MnO_x@MWNT one. It has the split G peak at 1585 and 1617 cm⁻¹; the two peaks have a significant overlap so that the upshifted one appears as a shoulder. Spectra taken at different spots on the sample have varying intensities of the manganese oxide peaks. This intensity seems to be correlated with the amount of G band splitting. For a spot that does not show any MnO_x peaks, the G band has an almost perfectly Lorentzian shape. For the spot shown in Figure 5.14, the manganese oxide bands are similar in shift and intensity: there are the Mn₃O₄ bands located at 313 (m), 371 (m) and 654 cm⁻¹ (s) as well as the small shoulder at 573 cm⁻¹ indicating the presence of MnO₂.

The Raman spectrum of the MnO_x@SWNT sample is different from the other ones: as in the case of the CNF sample, the graphitic bands are much stronger than the ones from manganese oxides. However, no upshift in the G band position and no G band splitting could be detected. The G band is asymmetric on the left hand side due to the Breit-Wigner-Fano resonance asymmetry for metallic SWNTs that has already been mentioned in section 4.1.1.⁸ The only manganese

⁶See page 65.

⁷Page 92.

⁸Page 61.

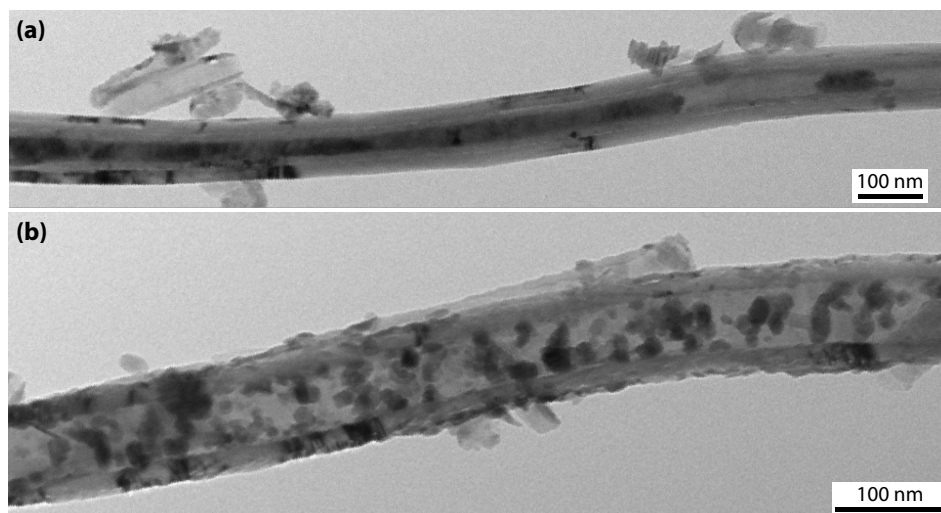


Figure 5.15 Transmission electron micrographs of MnO_x -filled CNFs (herringbone nanotubes) showing two types of filling morphology: long, continuous nanowires (a) and discrete endohedral oxide particles (b).

oxide peak that can be detected is a weak signal at 660 cm^{-1} , corresponding to the Mn_3O_4 phase. The peak width (FWHM of 70 cm^{-1}) is larger than for example in the MnO_x @MWNT sample (FWHM of 25 cm^{-1}). The peak at 335 cm^{-1} is a RBM signal, as it is also found in the untreated SWNTs (Figure 4.1). As the micro-Raman probe is the most sensitive to the sample surface, this unusual behavior might be related to the sample morphology, indicating the presence of SWNTs on the outside of the macroscopic grains. The manganese oxide could be located in the interstitial spaces of nanotube bundles and aggregates. Thus, it is necessary to take a closer look at the morphology of the final composites.

Morphology. TEM observation in bright-field mode reveals a wide variety of morphologies. The highest amount of filling is found in the MnO_x @CNF product, shown in Figure 5.15. The sample contains many small nanofiber fragments, which had not been present in the as-received carbon nanofibers (Figure 4.6). It seems that the nitric acid has cleaved the fibers along graphitic planes. In Figure 5.15b, the CVD overlayer on the outside of the fibers is partly detached from the herringbone part on the inside; this is visible for example in the top right of the image. The fragments in the top left part of Figure 5.15a do seem to have the overlayer completely removed. As for the filling with manganese oxide, there are essentially two morphologies:

- The first type, shown in Figure 5.15a, is a long, continuous nanowire, seen as a dark line in the TEM; the long part seen on the left is about $1.1\text{ }\mu\text{m}$ in length and $25\text{--}30\text{ nm}$ in diameter, for a total tube diameter of $D = 100\text{ nm}$. In higher magnifications including HRTEM

observations, it seems that the “nanowire” is not a homogeneous object but merely a dense aggregate of approximately spherical particles, which overlap so much that the individual particles become indistinguishable. In the figure reproduced here, random contrast variations along the object can be seen. In higher magnifications however, the small focus depth and the scattering by the nanotube walls make it impossible to see more details or diffraction planes from individual crystallites.

- The second type of morphology is a looser aggregate of oxide particles much smaller than the inner diameter d of the tube. The tube in Figure 5.15b shows an example for this morphology; the outer diameter of the tube is $D \approx 100$ nm like in the other tube, however the cavity has an inner diameter d between 45 and 55 nm. The oxide particles themselves have sizes in the range of 10–25 nm, with the majority at about 15 nm.

Though it is difficult to say from the micrographs, it seems that the oxide particles stick to the inside walls of the CNFs. These walls have a herringbone structure with graphitic planes at an angle (about 15°) with respect to the tube axis. This means that the *edges* of graphitic planes are exposed on the inside. These edges are functionalized with high efficiency with oxygen-containing functional groups – especially carboxylic acids – by the nitric acid treatment. The hydrophilic surface shows good wetting by the precursor-containing solution. Furthermore, a carboxylic acid can react with a Mn^{2+} cation and form a manganese salt, “trapping” the cation and forming a seed for the growth of a manganese oxide particle. *We propose that these carboxylic acid groups act as anchoring points for oxide crystal growth.*

In the other three products, the filling yields are more disappointing. In all three, a large part of the manganese oxide is found in exocrystallized particles outside the CNTs. Even if a few partially filled nanotubes are presented here, they do not represent the majority of the carbon nanotubes in the samples, which are empty.

Figure 5.16 shows transmission electron micrographs for MnO_x @MWNT. In subfigure (a), an aggregate of highly entangled MWNTs with manganese oxide particles between them is visible. The typical particle sizes of the manganese oxide in this micrograph are 20–60 nm, much larger than the cavity of the MWNTs, which is only 5 nm in diameter. Some bigger oxide grains, up to 2 μm in length, are also found. However, most of the tube ends in the micrograph seem to be opened. In Figure 5.16b, a HRTEM observation on a single MWNT with two particles inside is shown. The inset gives the result of an energy-dispersive X-ray spectroscopy (EDS) measurement on this nanotube. The strong signal from copper is due to the TEM observation grid; the other signals are from C, O and Mn, which confirms that the particle is made of manganese oxide, even in the absence of visible diffraction planes from the filling.

For the MnO_x @DWNT nanocomposite (Figure 5.17), a very similar morphology is found. The left micrograph (a) shows DWNTs with sizes of 2–6 nm, opened and mostly empty. Some of the bigger tubes are likely to be MWNT with more than two walls. Again, few tubes are filled with

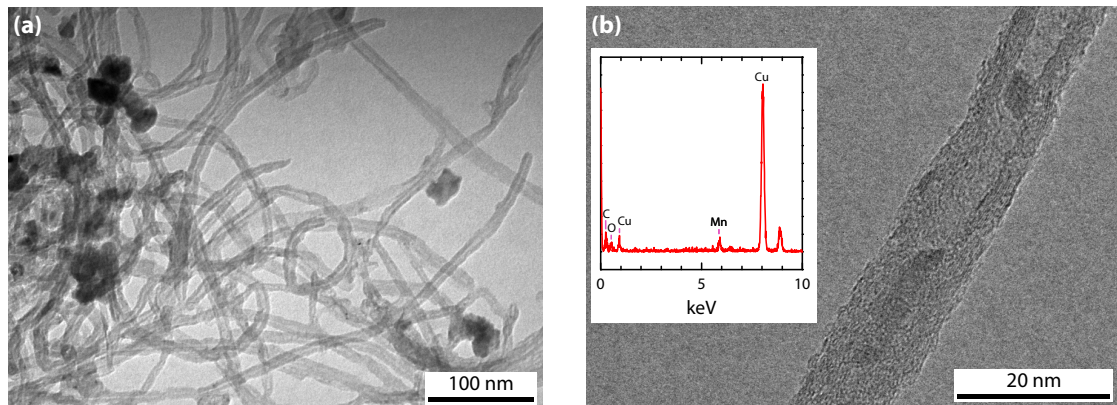


Figure 5.16 Low-magnification transmission electron micrograph of MnO_x @MWNT nanocomposite prepared by the reactive infiltration method showing mostly empty nanotubes and exocrystallized manganese oxide (a) and HRTEM micrograph of a partially filled MWNT (b) with the corresponding EDS data (inset) showing Mn, C and O as well as Cu from the sample holder.

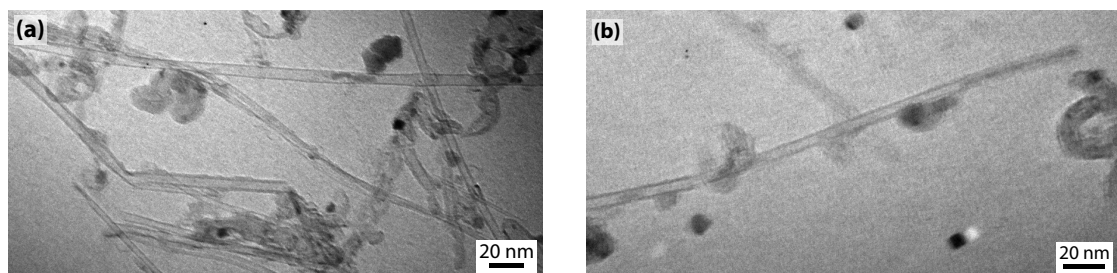


Figure 5.17 Transmission electron micrographs of MnO_x @DWNT nanocomposite prepared by the reactive infiltration method: nanotube fragments with exocrystallized manganese oxide and polyhedral carbon nanoparticle impurities (a); partially filled DWNT (b).

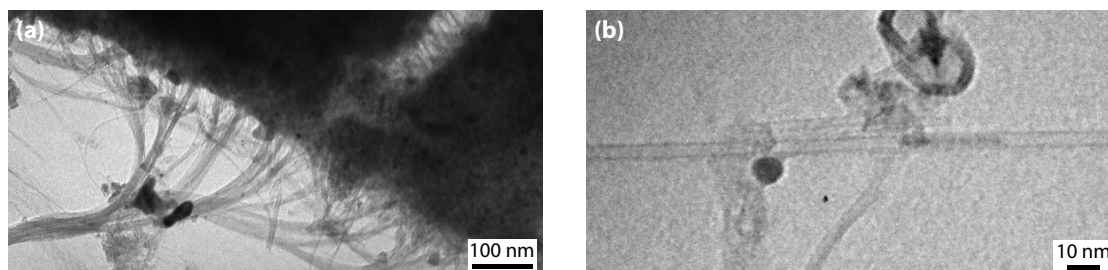


Figure 5.18 Transmission electron micrographs of MnO_x @SWNT nanocomposite prepared by the reactive infiltration method: big composite grain with a bundle of unfilled SWNTs protruding from it (a); zoom on a particle inside a large-diameter SWNT (b).

elongated particles (for example the large horizontal nanotube in the upper half), and most of the oxide is found in particles of 10 nm and larger. The second micrograph (b) shows a tube whose end is filled with a nanowire about 55 nm in length. As no EDS was available on the microscope where this micrograph was recorded, it is not clear if this nanowire consists of manganese oxide or of amorphous carbon. HRTEM observations suggest that many of the particles inside the CNTs are actually composed of amorphous carbon because the corresponding EDS data does not show the manganese $K\alpha$ peak at $E = 5.9$ keV. However, it is not clear to what extent the X-ray photons produced by whatever is inside the CNT are quenched, scattered or absorbed by the carbon walls; it is possible that the absence of a Mn signal is just related to reabsorption or an insufficient sensitivity of the detector.

The MnO_x @SWNT nanocomposite (Figure 5.18) shows a morphology that is best described as a nanotube-reinforced manganese oxide matrix. The left micrograph (a) shows the edge of a very large (about 0.1 mm) grain of manganese oxide. Everywhere on the surface, nanotubes are protruding from it and organize in bundles. On the fracture site in the top right part of the image, parallel SWNTs spanning the gap between the two parts can be seen. During the synthesis, the nanotubes and the nitric acid solution are separated by filtration; the product formed is thus a form of “buckypaper”. The partial alignment during the filtration step explains the seemingly ordered structure of the composite material. Manganese nitrate is trapped in the interstitial spaces of this buckypaper and removed from the surface by the filtration, which explains that the Raman spectra showed little manganese oxide on the grain surface. Macroscopically, this product consists of flakes about a millimeter in thickness that are very difficult to grind in a mortar, due to the high strength of the single-walled carbon nanotubes. The resolution of the microscope used for the observations⁹ is barely sufficient to image the inside of the smallest SWNTs; in any case, the filling efficiency seems low. The partially filled horizontal nanotube shown in Figure 5.18b is exceptionally large, about 4 nm. In the top part of this figure, a polyhedral carbon nanoparticle

⁹Philips/FEI Morgagni 268D, 80 kV acceleration voltage.

can be seen.

The presence of very large oxide particles also strongly reduces the **specific surface area**, from 680 m²/g in the as-received SNWTs to only 17.8 m²/g in the final composite. For interpreting the specific surface areas of the other composites, let us construct a simple and “pessimistic” model: Starting from the hypothesis that the nanotubes and the oxide particles are completely independent and that their specific surface is just the weighted sum of the specific surface of the components, and assuming furthermore that the specific surface area of the oxide is negligibly small, the specific surface area of the composite can be calculated from the nanotube contents and the S_{BET} value of the nanotubes treated with HNO₃ under the same conditions but without the addition of manganese nitrate. For the MnO_x@MWNT composite, we get a hypothetical value of

$$S = 0.49 \cdot 269 \text{ m}^2/\text{g} = 132 \text{ m}^2/\text{g}.$$

For the MnO_x@DWNT composite, the value is

$$S = 0.65 \cdot 262 \text{ m}^2/\text{g} = 170 \text{ m}^2/\text{g}.$$

Both of these values are higher than the ones found experimentally (Table 5.1), which are 90.1 and 114 m²/g respectively. In addition to the embedding effect just explained for the SWNT-containing composite, another mechanism that can cause this reduction in surface is the blocking of CNT ends by manganese oxide (or carbon) particles, which prevents the nitrogen gas from entering into the nanotube, thus making the inner surface of a CNT unavailable to the measurement. There is a corresponding reduction in the total pore volume measured with the BJH method between the nanotubes treated only with HNO₃ and the nanocomposites: from 1.27 mL/g to 0.14 mL/g for the MWNTs and from 0.35 to 0.14 mL/g in the case of the DWNTs.

On the other hand the specific surface area of the MnO_x@CNF nanocomposite (68.6 m²/g) is even slightly higher than the one of the HNO₃-treated fibers (66.5 m²/g). This means that the specific surface area of the manganese oxide particles is about the same as the one of the nanotubes, when neglecting the direct interaction, i. e. the direct MnO_x-CNF interface. Assuming spherical particles, their mean diameter can be determined by the equation

$$S_{\text{BET}}\rho = \frac{6}{d}. \quad (5.5)$$

Inserting the density of the manganese oxide measured by helium pycnometry ($\rho = (5.10 \pm 0.03) \text{ g/cm}^3$), we get a mean particle diameter of about 16 nm. This is consistent with the particle sizes measured in the transmission electron micrographs. This result means that (a) the tube ends are not completely blocked when filling the CNFs and that (b) there are very few large exocrystallized oxide particles – both phenomena would drastically reduce the specific surface area of the nanocomposite.

The most important result of this comparative study is that *larger nanotubes are easier to fill*. This is illustrated by the fact that the best filling yields with more endohedral than exohedral material were achieved for the herringbone nanotubes, which are the largest CNTs in the investigation. The filled SWNT and DWNT that were presented in the transmission electron micrographs were among the largest ones found in the respective sample. At first, this may seem curious, as the macroscopic capillarity laws go into the opposite direction – i. e. the smaller the capillarity, the farther the liquid column enters into it. However, as stated in the bibliography, the laws of nanocapillarity are different from the macroscopic ones because the assumption that most of the liquid molecules do not interact directly with the wall of the capillary breaks down for nanometer-sized capillaries.

We also saw that despite its simplicity, the reactive infiltration method does not work very well for the manganese oxide–CNT system. For $\text{MnO}_x\text{@CNF}$, the oxide loading of 24 wt-% is not sufficient for the preparation of a nanothermite mixture, which is of course the goal of the filling experiments. The other three nanocomposites do not show sufficient amounts of filling to even be called “manganese oxide-filled carbon nanotubes”. Nonetheless, the $\text{MnO}_x\text{@MWNT}$ nanocomposite has been selected for preparing a nanothermite mixture.¹⁰

5.2.2 Infiltration of MWNTs with molten manganese nitrate

Molten manganese nitrate tetrahydrate was infiltrated into FutureCarbon MWNTs opened by reaction with molten KOH.¹¹ In order to empty their cavities, the CNTs were outgassed under vacuum before bringing them in contact with the molten salt; this procedure is used in many pore filling techniques, for example in mesoporous silica foams. The method we used was presented in section 3.1.3. Manganese(II) nitrate tetrahydrate was used in a large excess with a weight ratio of 25 : 1 to the CNTs, typically 80 mg of opened MWNT with 2.0 g of $\text{Mn}(\text{NO}_3)_2 \cdot 4 \text{H}_2\text{O}$. The products were calcined at 190°C.

However, the manganese oxide loadings that can be obtained are quite low, on the order of 14–16 wt-%, which is insufficient for preparing a nanothermite. The manganese oxide has about the same oxygen deficiency ($\text{MnO}_{1.65}$) as in the products of the reactive infiltration method. A typical morphology obtained after 72 h of reaction time for the infiltration is shown in Figure 5.19. It shows the open end of a multi-walled carbon nanotube with a manganese oxide nanorod extending about 50 nm from the end into the CNT cavity. The oxide appears darker than the carbon walls on the micrograph, which is an important criterion for distinguishing it from amorphous carbon debris.

¹⁰See section 6.2.1.

¹¹See section 4.2.3.

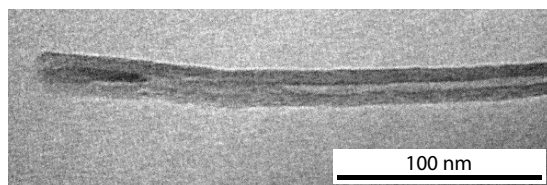


Figure 5.19 Transmission electron micrograph of an MnO_x @MWNT nanocomposite obtained by infiltration of molten manganese nitrate for 72 h. The manganese oxide has entered the nanotube over a distance of about 50 nm from its open end.

5.2.3 Infiltration of herringbone CNFs with molten manganese nitrate

The most interesting product of the last section is the MnO_x @CNF nanocomposite, as it has the highest number of filled carbon nanotubes. However, we said that the 24 wt-% metal oxide loading is not sufficient for the preparation of a nanothermite mixture. To achieve higher loadings, the CNFs were infiltrated with molten manganese nitrate using the “simplified” melt infiltration presented in section 3.1.4.¹² Manganese(II) nitrate tetrahydrate was used in a large excess with a weight ratio of 25 : 1 to the CNTs. In a typical synthesis, 0.3 g of CNFs and 7.5 g of molten $\text{Mn}(\text{NO}_3)_2 \cdot 4 \text{H}_2\text{O}$ were stirred together for 72 h at 50°C, filtered and then calcined at 225°C (1 h) with a heating rate of 1 K/min under flowing argon (9 L/h).

If the product is prepared by infiltrating as-received Pyrograf PR-24-HHT carbon nanofibers, the oxide loading obtained is about 16 wt-%, like in the MnO_x @MWNT composites prepared by melt infiltration. However, if the CNFs are treated with hot HNO_3 for 16 hours before the infiltration reaction, we obtain a much higher metal oxide loading of 48.6 wt-%. This is attributed to a difference in wetting behavior: graphitic surfaces, such as the MWNT sidewalls, or the unfunctionalized CNF walls, are not wet by the molten nitrate, which is highly polar. The acid treatment creates $-\text{COOH}$ functional groups on the inner surface of the CNFs only, because the inner surface consists of graphene *edges* while the outer surface consists of the π system, due to the synthesis process. The $-\text{COOH}$ groups are anchoring points for the manganese nitrate, and consequently for the oxide particles, due to the formation of $-\text{COOMn}^+$ moieties. In the following, we will look only at the composite with 48.6 wt-% manganese oxide loading.

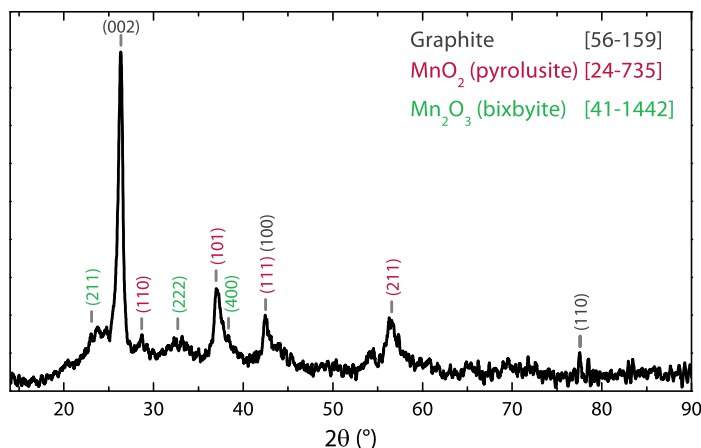
The X-ray diffractogram of the nanocomposite, shown in Figure 5.20, is very similar to the one from the MnO_x @CNF product prepared by reactive infiltration (Figure 5.13, top curve).¹³ However, the manganese oxide reflections are better visible, simply because the loading is higher. While the reflections from Mn_2O_3 are weak and large, the ones from MnO_2 (pyrolusite, 24-735) are quite intense, which indicates a good crystallinity of the particles. From the intensity ratio of the crystalline phases, the stoichiometry of the manganese oxide is calculated to be approximately $\text{MnO}_{1.9}$, which is significantly higher than the $\text{MnO}_{1.65}$ obtained for the MWNT product.

The specific surface area S_{BET} of the MnO_x @CNF product is 66.1 m²/g, practically unchanged from the value of 66.5 m²/g for the oxidized nanofibers alone, and close to the value of 68.6 m²/g

¹²Page 40.

¹³Page 105.

Figure 5.20 X-ray diffractogram of an MnO_x @CNF nanocomposite (48.6 wt-% of oxide) prepared by infiltration of molten manganese nitrate. The indicated crystalline phases are graphite (56-159, grey), bixbyite (Mn_2O_3 , 41-1442, green) and pyrolusite (MnO_2 , 24-735, red).



for the reactive infiltration product with 24 wt-% metal oxide loading. This shows that the specific surface area does not depend much in the composition in this system. The mean particle size of the manganese oxide particles, determined with equation (5.5) is around 16 nm, using the same reasoning as above.

Figure 5.21 shows a high-resolution micrograph of a manganese oxide-filled CNF with well-resolved diffraction planes. In the lower left of Figure 5.21b, the CVD overlayer is visible. The darker area next to it is the catalytically grown nanotube wall; the visible graphitic planes are nearly vertical. In the top right, oxide particles can be seen. EDS data for this spot indicates the presence of manganese, carbon, oxygen and copper (from the support). On one of the particles, we have highlighted a set of diffraction planes. Their measured distance is 316 pm; the (110) distance for pyrolusite (MnO_2) is 311 pm, which is within 2% of the measured value. This proves unambiguously that the particles inside the CNTs are MnO_2 .

5.3 Filling MWNTs with chromium(III) oxide by reactive infiltration

Chromium nitrate has very similar properties to manganese nitrate. It can thus be used in the same experimental conditions as for the manganese oxide-based products. A Cr_2O_3 @MWNT nanocomposite was prepared by the reactive infiltration method¹⁴ with the same proportions as in the case of manganese oxide – 80 mg of MWNT with 2.0 g of $\text{Cr}(\text{NO}_3)_3 \cdot 9\text{H}_2\text{O}$ in 5 mL of concentrated HNO_3 . The product is calcined at 225°C (1 h, 1 K/min) to decompose the chromium nitrate into the oxide. It contains 37 wt-% of chromium oxide.

The X-ray diffractogram for the product calcined at 225°C (Figure 5.22, top curve) is virtually identical to the one of the pristine MWNTs, indicating that the chromium oxide is amor-

¹⁴See section 3.1.1, page 39.

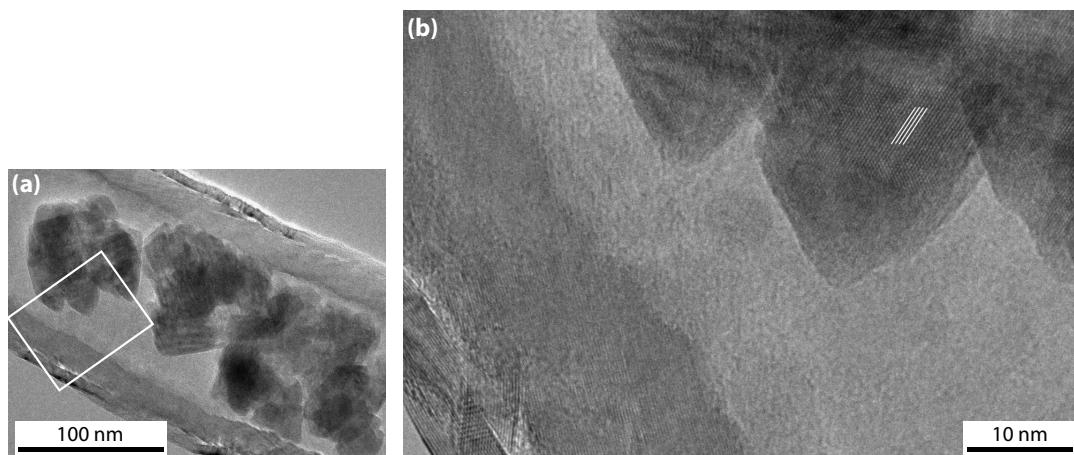


Figure 5.21 High-resolution transmission electron micrographs of MnO_x @CNF prepared by infiltrating molten manganese nitrate: view of the whole tube (a) and zoomed image of the highlighted region (b) showing the (110) diffraction planes of MnO_2 at the top right.

phous. After annealing the nanocomposite at 500°C under argon, large, ill-defined reflections from chromium(III) oxide (eskolaite, JCPDS file 38-1479) become visible (middle curve). After annealing at 600°C (bottom curve), sharper reflections for Cr_2O_3 appear. This is different from the decomposition product of pure chromium nitrate, which is well-crystalline after heating to 500°C (Figure 5.6). In the case of Cr_2O_3 @MWNT, the presence of MWNT constitutes a geometrical constraint for the crystallization of the oxide, which means that more energy is required to obtain a crystalline material. Even in the sample that was calcined at 600°C , it is questionable if the sharper reflections, whose intensity is quite weak, are really due to the material inside the cavity of the nanotubes, or if the exocrystallized oxide particles (outside the MWNTs) crystallize first.

In HRTEM observations on the Cr_2O_3 @MWNT nanocomposite treated at 600°C , (Figure 5.23a), we found more or less spherical or rod-shaped chromium oxide particles inside the MWNTs. Many of the nanotubes (more than half) are at least partly filled with these particles. However, it seems that at least half of the chromium oxide present is actually exocrystallized in the form of aggregated particles outside the MWNTs. We were unable to resolve any lattice fringes for the endohedral chromium oxide particles, which leads us to believe that they are amorphous even after having been heated to 600°C . However, the energy-dispersive X-ray spectrum (EDS) shown in Figure 5.23b, which corresponds to the particles seen inside the tube in the micrograph, shows the $K\alpha$ line of Cr at 5.417 keV and its $L\alpha_1$ line at 0.519 keV, which confirms that the particles are in fact made of chromium oxide.

Figure 5.22 X-ray diffraction of Cr_2O_3 @MWNT nanocomposites calcined at different temperatures (225, 500 and 600°C), with the JCPDS reference peaks of graphite (56-159) and Cr_2O_3 (eskolaite, 38-1479).

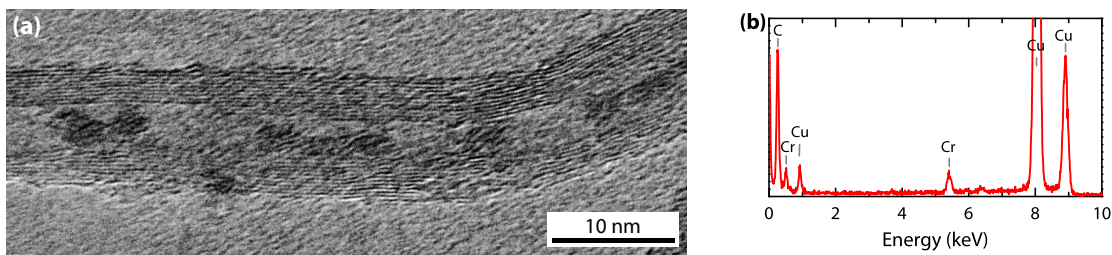
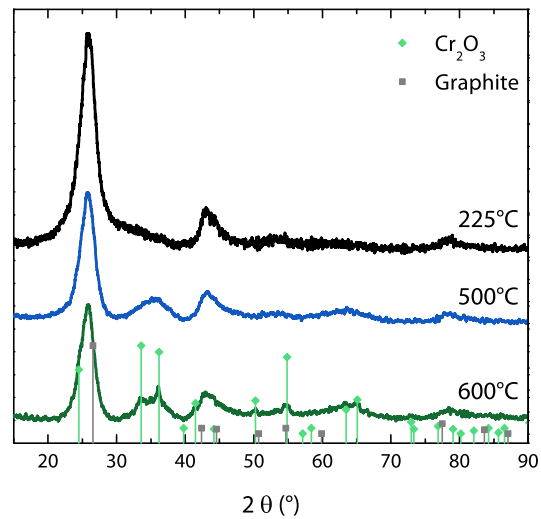


Figure 5.23 High-resolution transmission electron micrograph of Cr_2O_3 @MWNT prepared by reactive infiltration (a) and the corresponding EDS spectrum for the particles inside the MWNT (b) showing peaks for copper (from the sample holder), carbon and chromium.

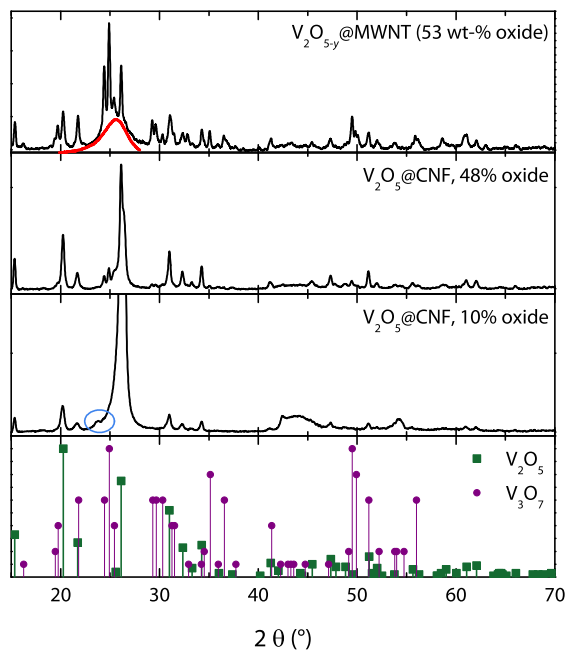


Figure 5.24 X-ray diffractograms of $V_{2}O_{5-y}@MWNT$ (top) and $V_{2}O_{5}@CNF$ at 48 wt-% (middle) and 10 wt-% oxide loading. In the top curve, the shape of the graphite (002) peak is indicated in red.

5.4 Filling with vanadium oxide

5.4.1 Filling MWNT with vanadium oxide

As the precursor for obtaining vanadium oxide, ammonium metavanadate, immediately forms a precipitate in acidic solutions, the reactive infiltration technique could not be used with this system. Thus, we infiltrated an aqueous NH_4VO_3 solution into the opened MWNTs with the technique presented in section 3.1.2. 120 mg of opened MWNTs were mixed with 10 mL of a saturated ammonium metavanadate solution in water, and the suspension was stirred at 60–70°C until all the water was evaporated. An orange deposit was visible on the wall of the flask, indicating that not all the NH_4VO_3 was deposited on or in the nanotubes. The black MWNT composite was collected and calcined at 325°C (1 h).

The oxide content in the obtained $V_{2}O_{5}@MWNT$ product was determined to be 53 wt-% by a TG/DTA measurement in air. X-ray diffraction showed the presence of vanadium oxide as $V_{2}O_{5}$ (shcherbinaite, 41-1426) and monoclinic $V_{3}O_{7}$, i. e. vanadium(IV,V)-oxide $VO_2 \cdot V_2O_5$ [27-940]. The reflections of the two oxides are similar in intensity; from full pattern matching, we get a weight ratio of about 5 : 7 for $V_{2}O_{5} : V_{3}O_{7}$. This leads to a mean stoichiometry of $VO_{2.40}$ – a slightly oxygen-deficient product. The (002) reflection from the graphitic carbon is covered by several sharp vanadium oxide reflections. In Figure 5.24, the shape of this peak is indicated in red. The red curve is a part of the X-ray diffractogram of pure, as-received MWNTs.

TEM observation of the nanocomposite shows that a large part of the vanadium oxide exists

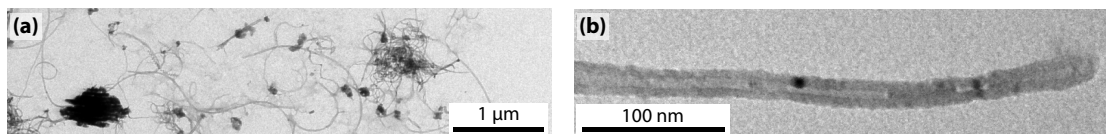


Figure 5.25 Transmission electron micrographs of $V_2O_5@MWNT$ nanocomposites: low-magnification image showing exocrystallized vanadium oxide nanoparticles (a), zoom on one partially filled multi-walled carbon nanotube (b).

as particles outside the nanotubes, as shown in the low-magnification overview in Figure 5.25a. However, there are some partially filled nanotubes, although it seems difficult to estimate their proportion from the micrographs. Figure 5.25b shows such a CNT end, which is partially filled with an oxide nanorod in the right part of the image. Although we do not have a corresponding EDS spectrum to prove that the filling is really composed of vanadium oxide, there is nevertheless a strong indication: to the left and right of the nanorod, small bright spots are visible. This is due to the diffraction of the electron beam by a crystalline compound, strongly suggesting that the particle is an oxide crystal and not just an amorphous carbon impurity.

Another argument for the presence of filled CNTs can be derived from the specific surface area of the nanocomposite, which is $S_{BET} = 98 \text{ m}^2/\text{g}$. The surface area of the opened MWNTs is about $300 \text{ m}^2/\text{g}$. If the product was simply a physical mix between the nanotubes and the oxide particles, its specific surface area would simply be equal to the weighted sum of the one of the constituents. However, the area from the CNTs alone would be

$$0.47 \cdot 300 \text{ m}^2/\text{g} = 141 \text{ m}^2/\text{g},$$

which is more than the observed value. This means that some of the nanotube surface must have become inaccessible; the easiest explanation for this is pore blocking due to filling of the endohedral space of the nanotubes.

Looking at the sample in the optical microscope, some large vanadium oxide particles (tens of microns) can be distinguished. Correspondingly, depending on the spot chosen for recording the Raman spectrum, anything between a pure vanadium oxide spectrum and a pure carbon nanotube spectrum can be obtained. This means that the product is inhomogeneous on a micro-metric scale. Figure 5.26b (middle curve) shows a the low-shift part of such a Raman spectrum, in which the Raman bands of the vanadium oxides can be seen. The visible peaks correspond to both the ones of vanadium(V) oxide (Figure 5.26a), indicated in black, and the ones of vanadium(IV) oxide, indicated in red. This indicates that there is a mixture of vanadium(IV) and (V) oxide in the sample and confirms the result of the X-ray diffraction.

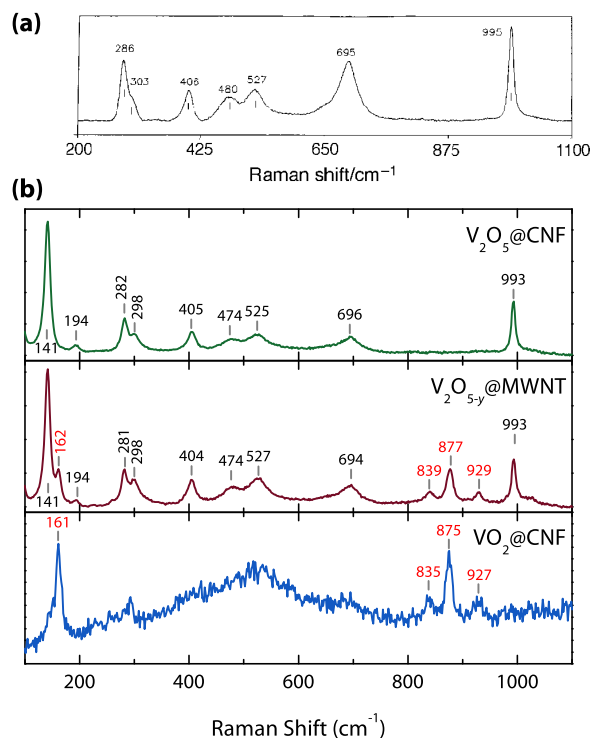


Figure 5.26 Reference Raman spectrum for vanadium(V) oxide, recorded at $\lambda = 632$ nm, reproduced from [191], © Royal Society of Chemistry 1997 (a). Raman spectra, recorded at $\lambda = 514$ nm, for $V_2O_5@CNF$, $V_2O_{5-y}@MWNT$ and annealed $VO_2@CNF$ (b). Black numbers indicate V_2O_5 bands, red numbers indicate VO_2 bands.

5.4.2 Filling Pyrograf CNF with vanadium oxide

Using the same method as for the $V_2O_5@MWNT$ nanocomposite, we prepared vanadium oxide-filled herringbone carbon nanotubes (Pyrograf carbon nanofibers). Instead of using an excess of ammonium metavanadate however, the quantity was adapted to achieve control over the metal oxide loading. To demonstrate this control, two products, one containing about 50 wt-% of oxide and the other with about 10 wt-%, have been prepared. The nanofibers used in the synthesis had been acid-functionalized by heating them in HNO_3 for 3 hours, followed by washing and drying.¹⁵

The solubility of NH_4VO_3 in water is strongly dependent on the temperature. According to Wikipedia, the solubility is 4.8 g/L at 20°C, 24.2 g/L at 60°C and even 70 g/L at 100°C. This means that an infiltration reaction at 60°C can start from a concentrated solution, so that only a small volume of H_2O must be evaporated. To obtain the 50 wt-% product, 200 mg of functionalized CNFs were added to a solution of 257 mg of NH_4VO_3 (taking into account the weight loss of 22% on decomposition) in 20 mL of ultrapure water. The suspension was stirred at 70°C for 16 hours in an open beaker, leading to the slow evaporation of the water. The dry, black product is calcined at 325°C for 1 h under argon. The product with a 10 wt-% oxide loading was prepared with the

¹⁵Cf. section 4.2.

same method, only adjusting the quantity of ammonium metavanadate.

The obtained oxide loadings, as determined by TG/DTA measurements in air, are slightly below the desired values (48.6 wt-% and 8.9 wt-% respectively). The reason is that a part of the metavanadate does not crystallize on the CNF surface but on the wall of the beaker.

The X-ray diffractograms of the two nanocomposites are shown in the middle curves of Figure 5.24. As before, we find graphite [56-159], vanadium(V) oxide [41-1426] and vanadium(IV,V) oxide V_3O_7 [27-940]. Compared to the MWNT-based composite, the intensity of the V_3O_7 phase is much weaker, leading to an estimated stoichiometry of $VO_{2.45}$ for the product with 48.6 wt-% loading. For the 8.9 wt-% product, the V_3O_7 peaks have all but disappeared, as indicated by the blue circle. In both products, the (002) reflection of the graphitic carbon covers the (110) reflection of vanadium(V) oxide at $d = 340.8$ pm ($2\theta = 26.1^\circ$).

The Raman spectrum of the V_2O_5 @CNF composites, like in the MWNT case, depends strongly on the location on the sample surface that is chosen, indicating inhomogeneities on a micrometric scale. Indeed, the corresponding image in the optical microscope shows some bright spots that seem to be exocrystallized vanadium oxide particles; their size is in the range of 1–20 μm . In the case of 8.9 wt-% loading, the number of these micron-sized particles is much smaller. The low-frequency part of a Raman spectrum with well-visible oxide bands is shown in Figure 5.26b (top curve). The spectra for both oxide loadings are the same. The Raman spectrum is identical to the reference spectrum of V_2O_5 shown in Figure 5.26a, and no vanadium(IV) oxide bands, which would be located at 160, 840, 877 and 930 cm^{-1} , are visible. This means that the vanadium(IV) content is below the sensitivity level of the Raman spectrum, and it confirms the X-ray diffraction results.

TEM observations of the V_2O_5 @CNF nanocomposites reveal that only very few oxide particles adhere on the outside of the nanofiber. Not all nanotubes are filled; those that contain vanadium oxide reveal a particular morphology, a vanadium oxide foam (Figure 5.27a and b), in which gas bubbles, presumably filled with the gases formed during the decomposition, are trapped. Vanadium oxide foams are well-known in the literature; this morphology has for example been used for the synthesis of highly active catalysts [192]. Figure 5.27c shows the EDS spectrum corresponding to the inside of the nanotube shown in Figure 5.27b and confirms that the foam phase is really composed of vanadium oxide. Due to the disordered morphology, it was not possible to obtain a micrograph with visible diffraction planes in order to determine the crystalline phase. Figure 5.27d shows the reaction of the vanadium oxide foam when subjected to the electron beam (80 kV) in the TEM for 5–10 minutes: the morphology changes completely as the particles melt and recrystallize into larger ones, and the gas bubbles are removed. The melting point of the oxide is around 660°C; it seems that this temperature has been reached in the sample.

The V_2O_5 @CNF sample with the 48.6 wt-% oxide loading was selected for the preparation of a V_2O_5 @CNF/Al nanothermite mixture; see section 6.4 for details.

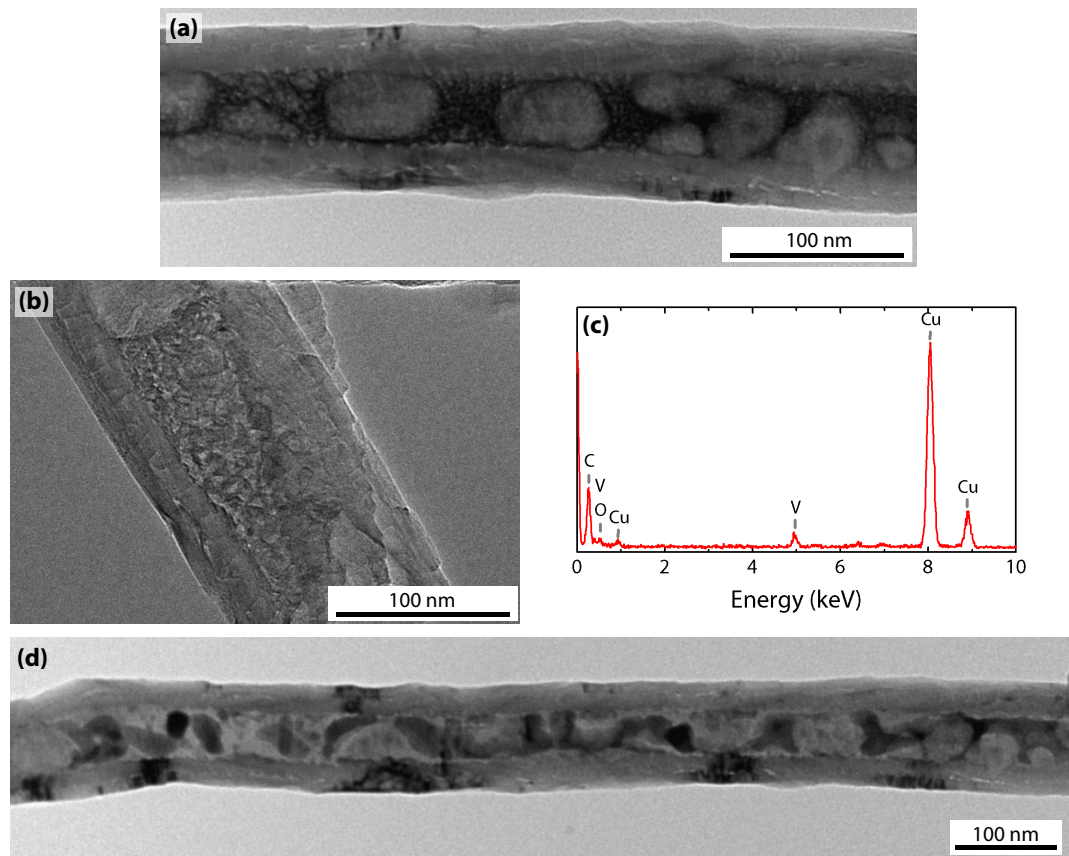


Figure 5.27 Transmission Electron micrograph, recorded at 80 kV, of a $V_2O_5@CNF$ nanocomposite showing a vanadium oxide foam inside the CNT (a); higher resolution micrograph, recorded at 200 kV (b) with the corresponding selected-area EDS spectrum (c) showing peaks due to vanadium, oxygen, carbon and copper (from the sample holder); melting and recrystallization of the vanadium oxide foam after about 10 min of observation in the TEM at 80 keV (d) on the same nanotube as in the first micrograph.

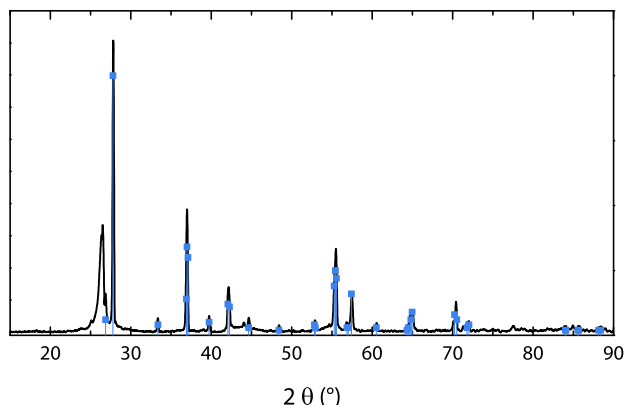


Figure 5.28 X-ray diffractogram of the annealed VO₂@CNF nanocomposite. Blue squares indicate the VO₂ phase [43-1051].

Effect of annealing. In order to see whether we could recreate the melting of the foam in a macroscopic sample, a V₂O₅@CNF nanocomposite was annealed at 700°C for 1 h under argon, above the melting point of the vanadium oxide.

After the annealing, the specific surface area of the product was reduced from 35.2 to 26.6 m²/g, indicating that crystal growth had occurred. The oxide loading of the composite was more or less unchanged at 48.1 wt-%. The X-ray diffractogram, however, showed that there was a major change in the oxide phase (Figure 5.28). The only vanadium oxide phase found in the diffractogram is vanadium(IV) oxide VO₂ [43-1051]. The mean crystal size of the oxide, as estimated from the peak broadening by the Scherrer formula, is 68 nm, which is larger than the diameter of most of the CNF cavities. The Raman spectrum of the composite, the low-frequency part of which is shown in Figure 5.26 (bottom curve), shows very weak vanadium(V) oxide bands at 280 and 695 cm⁻¹. The major features, however, are new peaks at 161 cm⁻¹ (s) as well as 839 (w), 875 (m) and 927 cm⁻¹(w). We attribute these bands to vanadium(IV) oxide. The overall intensities in the Raman spectrum of this composite are quite small compared to the V₂O₅@CNF. This is due to the fact that V₂O₅ is orange and thus has a strong optical absorption near 500 nm, which means that it is strongly in resonance with the 514 nm (green) laser excitation. VO₂ however is bluish-black in color [183, p. 1075], thus it is not *a priori* in resonance.

TEM observation of the nanocomposite (Figure 5.29) shows that most of the vanadium oxide was in fact ejected from the nanotube cavities. This could be due to the trapped gas bubbles expanding during the heating of the nanocomposite. The vanadium oxide forms aggregates, which are several hundred nanometers in diameter, of particles between 40 and 80 nm (Figure 5.29a) or coats the outside surface of the nanotubes (Figure 5.29b); in the second micrograph, some oxide is still present at the opening of the CNF, which seems to indicate that molten material has been ejected from the tube cavity. It should be noted that the melting point of VO₂ is 1970°C, which means that it is solid at the annealing temperature, while V₂O₅ is liquid. This means that the reduction of the vanadium oxide triggers its solidification.

In conclusion, this product can reasonably be called VO₂@CNF. In section 6.4, it will be used

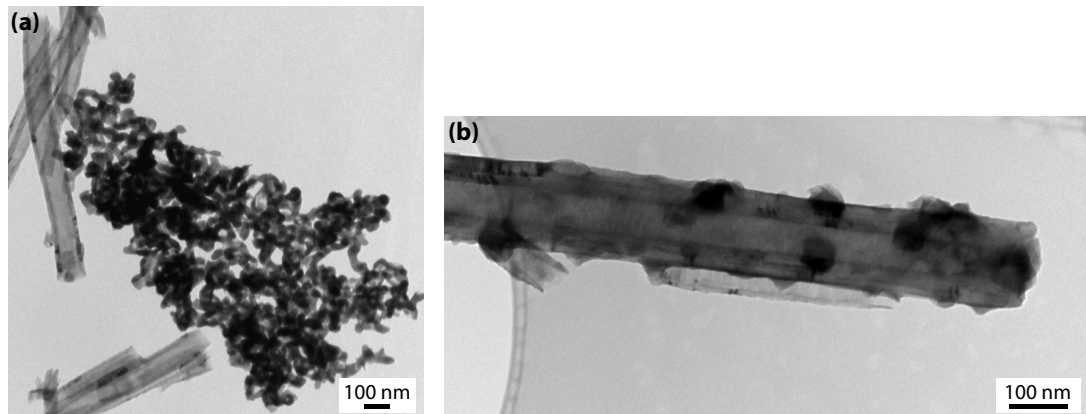


Figure 5.29 TEM observation of “VO₂@CNF” showing the formation of aggregated of vanadium oxide particles outside the CNFs (a) and the deposition of oxide on the outside and the ends of the CNFs (b).

for preparing a “VO₂@CNF/Al” nanothermite mixture and compared to the performances of a V₂O₅@CNF/Al thermite prepared from the non-annealed composite.

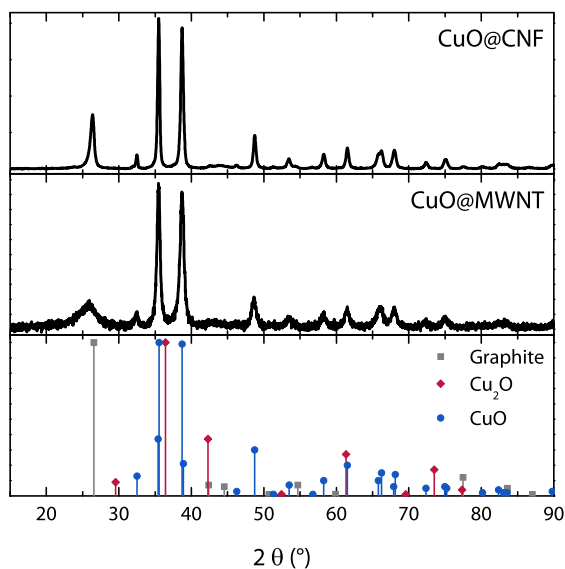


Figure 5.30 X-ray diffraction of CuO@MWNT (middle) and CuO@CNF (top) nanocomposites prepared by infiltration of a copper nitrate solution; reflections for graphite [56-159], cuprite Cu₂O [5-667] and tenorite CuO [48-1548].

5.5 Filling with copper(II) oxide

5.5.1 Filling MWNT with copper oxide

As copper nitrate is much less soluble in nitric acid than in water, as explained above, we did not use the reactive infiltration technique for preparing copper oxide-filled carbon nanotubes. Thus, we prepared a CuO@MWNT nanocomposite by infiltrating opened MWNTs (treated with KOH and defunctionalized by annealing at 950°C) with an aqueous solution of copper nitrate, according to the procedure given in section 3.1.2. To get an oxide loading of about 50 wt-%, 585 mg of Cu(NO₃)₂ · 2.5 H₂O were dissolved in 10 mL of ultrapure water, and 200 mg of the opened MWNTs were added. After the slow evaporation of the solvent, the dry paste was calcined at 325°C with a 1 K/min heating rate under argon.

After the calcination, the nanocomposite contains 47.05 wt-% of copper oxide, slightly less than the desired value. Like in the case of V₂O₅@CNE, this is because a part of the nitrate solidifies on the wall of the beaker instead of in the MWNTs. The X-ray diffraction of the calcinated product is shown in the bottom curve of Figure 5.30. The identified phases are mainly graphitic carbon [56-159] and tenorite CuO [48-1548]. A small amount of copper(I) oxide (cuprite, Cu₂O, 5-667) can also be distinguished, although the reflections are mostly lost in the background noise. The mean crystallite size for CuO, determined by the Scherrer formula, is 16 nm, which is larger than the diameter of the MWNT cavity (5 nm). This means that the copper oxide exists mainly in the form of exocrystallized particles, outside the MWNTs.

However, TEM observation of the CuO@MWNT nanocomposite (Figure 5.31) shows that a significant number (estimated to about 1/4) of the MWNTs is at least partly filled with copper

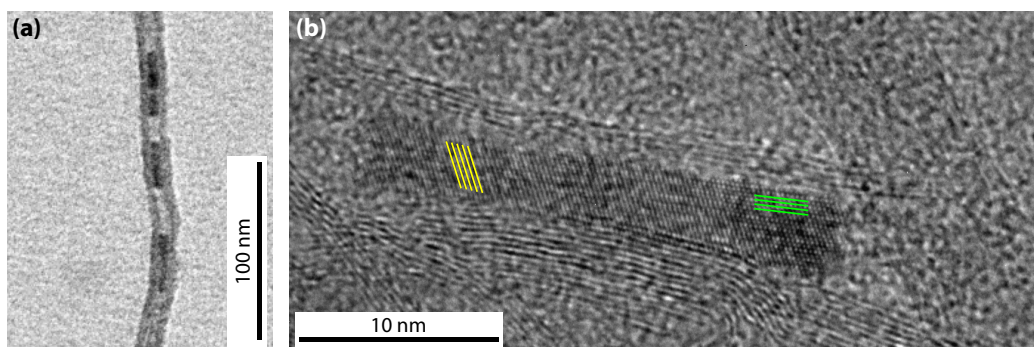


Figure 5.31 TEM observation of CuO@MWNT: micrograph showing a nanotube that is partially filled with oxide particles (a); high-resolution micrograph of oxide particles inside an MWNT (b). The spacing of the highlighted lattice fringes is 2.12 Å (yellow) and 1.95–1.97 Å (green).

oxide particles. The lower resolution micrograph on the left shows that these particles are found in the form of elongated, discontinuous nanorods inside the MWNTs. They appear darker in the micrograph than the surrounding carbon shell, similar to what was observed in Figure 5.19 for MnO_x@MWNT. Contrary to the case of manganese oxide-filled MWNTs, the oxide particles are not only found at the ends of the CNTs in this sample; we attribute this effect to the lower viscosity of the copper nitrate solution compared to the molten manganese nitrate, which enables the precursor to penetrate further into the cavity. In the HRTEM micrograph shown in Figure 5.31b, close observation shows that the nanorod in the MWNT cavity is actually composed of two particles that show different lattice fringes. Two sets of such fringes have been highlighted in yellow and in green in the figure. The yellow planes have a distance of 2.12 Å from one another. This corresponds to the (200) spacing of cuprite (Cu₂O), which is 2.14 Å, to within an accuracy of 1%. The green set of planes has a measured spacing of 1.95–1.97 Å. This corresponds to the (11 $\bar{2}$) distance in tenorite (CuO), which is 1.96 Å. This means that one of the two crystals seen in the HRTEM micrograph consists of copper(I) oxide, while the other one consists of copper(II) oxide.

5.5.2 Filling CNF with copper oxide

We also prepared a CuO@CNF nanocomposite with exactly the same method and the same proportions as for CuO@MWNT. 500 mg of acid-treated herringbone nanotubes (treated for 3 h) were mixed with 1.46 g of Cu(NO₃)₂ · 2 · 5 H₂O dissolved in 25 mL of ultrapure water in a beaker. After slow evaporation of the water at 60°C under magnetic stirring (about 16 h), the dry paste was calcined at 325°C with a heating rate of 1 K/min under argon. The product contains 48.3 wt-% of copper oxide, as determined by a TG/DTA analysis in air.

The X-ray diffractogram (shown in Figure 5.30, top curve) shows no reflections due to copper(I) oxide, only CuO [48-1548] and graphitic carbon [56-159]. This means that *a priori*, the

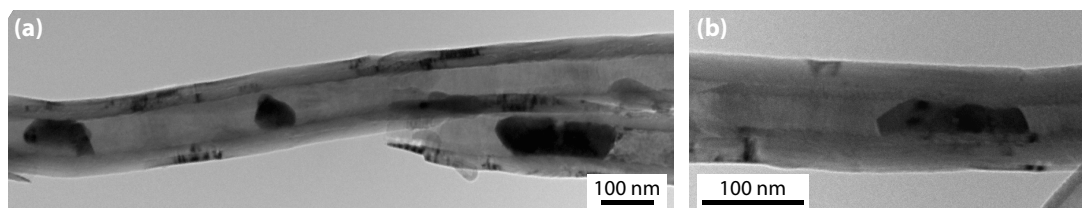


Figure 5.32 TEM observation of CuO@CNF: most nanotubes are partially filled with faceted oxide particles that span the entire cavity.

product has the “ideal” CuO@CNF stoichiometry and is not oxygen-deficient. The crystallite size of CuO, as estimated by the Scherrer formula, is 40 nm, which is equal to the typical width of the cavities in the herringbone nanotubes. From this measurement, we expect the CuO particles to occupy the whole cavity of the CNF – contrary to $\text{MnO}_x\text{@CNF}$, where the oxide is in the form of small particles stuck to the walls. The TEM observation (Figure 5.32) shows that this is in fact the case. The copper oxide is found as nanoparticles or nanorods inside the CNF cavities, most tubes (about 3/4) are at least partially filled with oxide particles. Some exocrystallized material, in the form of 50–100 nm particles, is also found. The particles shown in the two micrographs have widths of 30–60 nm and clearly visible crystal facets. In Figure 5.32, a copper oxide particle completely blocks the inner cavity.

This product will be used in section 6.5¹⁶ to prepare a CuO@CNF/P nanothermite by physically mixing it with red phosphorus.

5.6 Conclusion of this chapter

In this chapter, we showed the filling of carbon nanotubes with four different oxides – manganese, chromium, vanadium and copper oxide. The precursors were metal nitrates or (in the case of vanadium) ammonium salts; both can be decomposed to form the oxide by heating. The larger carbon nanotubes give higher filling yields, and the best results were obtained with the herringbone nanotubes (CNFs). In many cases, the oxides formed are oxygen-deficient because the carbon acts as a reducing agent.

¹⁶Page 156.

Reduced-sensitivity nanothermites containing carbon nanotubes

In this chapter, we will prepare new nanothermite formulations that contain carbon nanotubes. The goal is to reduce their mechanical sensitivity, particularly in response to friction stress. First, we will look at two “reference” systems that do not contain carbon nanotubes and that have been described in recent articles, MnO_2/Al and CuO/P . $\text{V}_2\text{O}_5/\text{Al}$ nanothermites have not been described in the literature, as it is difficult to get vanadium(V) oxide nanopowders. After this, we will test formulations that consist of filled nanotubes mixed with a reducing agent, where the oxidizer and the fuel are spatially separated; other formulations will simply be physically mixed with carbon nanotubes in order to see how much of the effect is only due to “dilution” of the reaction mixture with an inert material.

Table 6.1 gives an overview over the products that we will investigate in this chapter. In the formulas, the solidus (/) stands for a physical mix while the at sign (@) means filling.

The materials were prepared by physical mixing in a non-solvent, either *n*-hexane or acetonitrile. For $\text{MnO}_x@\text{MWNT}/\text{Al}$, we directly compared the properties of a formulation mixed in *n*-hexane with the corresponding one that was mixed in acetonitrile. In the case of $\text{MnO}_x@\text{CNF}/\text{Al}$ (using filled herringbone nanotubes), we investigated the influence of the oxygen balance by comparing a formulation with 20% excess of fuel with a “fuel-rich” one containing a 140% excess of fuel. For vanadium oxide-based nanothermites, we compared the properties of a $\text{V}_2\text{O}_5@\text{CNF}/\text{Al}$ formulation containing vanadium(V) oxide with a $\text{VO}_2@\text{CNF}/\text{Al}$ formulation, where the filled nanotubes had been annealed to form vanadium(IV) oxide. Finally, we investigate the properties of a $\text{CuO}@\text{CNF}/\text{P}$ nanothermite, which contains (micron-sized) phosphorus as the fuel.

For each formulation, we look at its sensitivities (Table 6.1) and the apparent density of pellets compressed at three different compressions (44, 99 and 210 MPa, Table 6.2); the pellets are ignited in a time-resolved cinematography (TRC) experiment, and their combustion is recorded. This experiment gives the ignition delay time (IDT), activation energy (E_A) and the combustion velocity. Finally, we look at the morphology and composition of the combustion residues to gain information about the combustion mechanism.

6 Reduced-sensitivity nanothermites containing carbon nanotubes

Composition	Impact (J)	Friction (N)	Electrostatic discharge (mJ)
MnO ₂ /Al ^a	31.9	< 5	1.04
MWNT/MnO ₂ /Al ^a	17.2	> 360	–
CNF/MnO ₂ /Al ^b	29.4	> 360	1800
MnO _x @MWNT/Al ^a	24.5	> 360	–
MnO _x @CNF/Al ^b	44.2	> 360	34.7
MnO _x @CNF/Al fuel-rich ^b	24.5	> 360	5300
V ₂ O ₅ @CNF/Al ^b	34.3	> 360	5.79
CuO/P ^a	39.2	8	0.21
CuO@CNF/P ^a	> 49	> 360	61.6

^a mixed in *n*-hexane

^b mixed in acetonitrile

Table 6.1 Overview of the types of nanothermite formulations investigated in this chapter with their respective mechanical and electrostatic discharge (ESD) sensitivity threshold values.

6.1 Reference systems (without CNTs)

6.1.1 MnO₂/Al

As the reference for the investigation of reduced-sensitivity nanothermites, the MnO₂/Al nanothermite presented by our laboratory in 2008 [162] will be used. It is composed of manganese oxide nanoparticles and Al 50 P aluminum nanoparticles physically mixed in *n*-hexane. The reaction equation for the thermite reaction is



A 20% excess of aluminum, which has been recognized as the optimum for other nanothermite systems, is used for the formulation, resulting in

- ▶ 55.07 wt-% of nano-MnO₂ and
- ▶ 44.93 wt-% of Al 50 P containing 60.85 wt-% of metallic aluminum.

Table 6.3 shows the amount of each constituent in the thermite.

The motivation for preparing nanothermites with this formulation was the low toxicity of the elements in group 7 of the periodic table (Mn, Tc, Re) compared to other transition metals; the resulting thermites are thus environmentally friendly, and the fumes released by the combustion are less hazardous than for, say, thermites based on lead oxide. The other motivation was the development of a synthesis procedure for extremely fine (3–5 nm) manganese oxide particles; as a rule, the smaller the particles, the higher the reaction velocity of a thermite. Details on the synthesis of the manganese dioxide nanoparticles are given in section 3.3.

6.1 Reference systems (without CNTs)

Formula	p (MPa)	ρ (g/cm ³)	%TMD	IDT (ms)	E_A (mJ)	ν (mm/s)
MnO ₂ /Al ^a	99	1.33 ± 0.09	32 ± 2	3.66 ± 0.3		730 ± 80
MWNT/MnO ₂ /Al ^a	99	0.59 ± 0.05	17 ± 1.5	9.3 ± 3	10.0 ± 4	14.4 ± 2
	210	0.68 ± 0.09	20 ± 2	8.4 ± 4	9.3 ± 3	9.9 ± 4
MnO _x @MWNT/Al ^a	99	1.26 ± 0.02	38.6 ± 0.5	20 ± 5	76 ± 26	irr.
	210	1.47 ± 0.06	45.3 ± 2	26 ± 4	115 ± 16	irr.
MnO _x @MWNT/Al ^b	44	1.17 ± 0.05	36.1 ± 1.5	13.3 ± 4	43 ± 25	irr.
	99	1.31 ± 0.02	40.4 ± 0.7	13.5 ± 4	50 ± 30	irr.
MnO _x @CNF/Al ^b	44	1.29 ± 0.05	37.3 ± 1.3	11.1 ± 9	20 ± 15	3.3 ± 1
	99	1.35 ± 0.03	39.2 ± 0.7	11.2 ± 5	25 ± 10	3.5 ± 1
MnO _x @CNF/Al fuel-rich ^b	99	1.40 ± 0.1	41.2 ± 4	13.5 ± 3	40 ± 20	5.1 ± 2
V ₂ O ₅ @CNF/Al ^b	44	0.83	28	8.2	12	8.8
	99	0.92	31	7.5 ± 5	10 ± 15	5.9 ± 1
	210	1.02 ± 0.1	35 ± 5	8.6 ± 1.3	12 ± 8	6.2 ± 3
VO ₂ @CNF/Al annealed ^b	44	0.91 ± 0.07	28.6 ± 2	13 ± 4	24 ± 12	irr.
	99	0.95 ± 0.04	30.1 ± 1	12	25	irr.
	210	1.06 ± 0.02	33.5 ± 0.7	16 ± 6	40 ± 10	irr.
CuO@CNF/P ^a	44	1.14 ± 0.04	31 ± 1	16 ± 9	39 ± 15	–
	99	1.25 ± 0.09	34 ± 3	19 ± 9	43 ± 20	–
	210	1.38 ± 0.1	38 ± 3	25 ± 5	114 ± 15	–

^a mixed in *n*-hexane ^b mixed in acetonitrile

Table 6.2 Results of pelletizing and TRC experiments for nanothermite pellets compressed at different pressures p : apparent density ρ of the pellet, percentage of the theoretical maximum density (TMD) of the formulation, ignition delay time (IDT), activation energy E_A and combustion velocity ν (irr.: irregular).

Sample	TMD (g/cm ³)	%MnO ₂	%Mn ₂ O ₃	%Al	%Al ₂ O ₃	%C (CNT)
MnO ₂ /Al ^a	4.204	55.07	–	27.34	17.59	–
MWNT/MnO ₂ /Al ^a	3.434	33.37	–	16.57	10.66	39.40
CNF/MnO ₂ /Al ^b	3.478	34.60	–	17.18	11.05	37.16
MnO _x @MWNT/Al ^a	3.293	8.52	26.70	15.24	9.22	39.40
MnO _x @MWNT/Al ^b	3.276	8.12	25.72	14.64	8.48	42.10
MnO _x @CNF/Al ^b	3.445	28.09	7.02	16.87	9.78	37.16
MnO _x @CNF/Al “fuel-rich” ^b	3.293	21.99	5.50	26.42	15.31	29.09

^a mixed in *n*-hexane ^b mixed in acetonitrile

Table 6.3 Theoretical maximum density (TMD) and contents in wt-% of each constituent phase in the different manganese oxide-based nanothermite formulations. The two MnO_x@MWNT/Al formulations use different batches of MnO_x@MWNT and nano-Al, which is why their composition is slightly different.

In their survey on the thermochemical properties of thermite systems, Fischer and Grubelich [156] find an adiabatic reaction temperature of 2918 K when taking phase changes into account. This is slightly lower than in the $\text{Fe}_2\text{O}_3/\text{Al}$ or MoO_3/Al systems but still quite high. At these temperatures, Al_2O_3 is in its molten state while the Mn metal is gaseous. The heat of reaction of 4.84 kJ/g however is much higher than the one of $\text{Fe}_2\text{O}_3/\text{Al}$ (3.95 kJ/g) or even MoO_3/Al (4.70 kJ/g). Manganese oxide-based thermites thus have very good energetic performance in theory.

The results from Time-Resolved Cinematography (TRC) experiments¹ on pellets compressed at 99 MPa are shown in the first line of Table 6.2. It can be seen that the density of the pellet is only 1/3 of the theoretical maximum. This is typical for nanoparticle-based formulations; the pellets are nonetheless cohesive, even without the addition of a binder. Two effects are found at this small percentage of the TMD: On the one hand, the energy transfer by the heat wave going through the material is less effective, as more of the energy is dissipated. On the other hand, for the same molar reaction velocity, the distance traveled by the combustion front is greater. In any case, the ignition delay time of only 4 ms corresponds to a low thermal activation energy.

Figure 6.1 shows a “timeline” image of the combustion of a MnO_2/Al pellet. Let us rapidly introduce how to read this type of image, which has been generated by the software in appendix A.2. The image has been generated by taking one line of each frame of the high-speed video and gluing them below one another. Each line of the image shows in fact the same part of the sample; the x position thus corresponds to the horizontal position, which has been calibrated and converted to millimeters. The pellet is on the right of the image, and the laser beam strikes from the left. The y axis corresponds to the time and is read from top to bottom. In the top right part of the image, the combustion front is visible. In fact, the front reaches the end of the pellet after approximately 6 ms. In the 2008 paper, the combustion velocity was approximated by a linear rate law for the second half of the pellet, resulting in the 730 mm/s (0.73 m/s) value given in Table 6.2. However, a parabolic rate law would provide a better fit to the propagation, which accelerates as it progresses.

Table 6.1 shows the sensitivity thresholds for this thermite. While its impact sensitivity (corresponding to an impact of the 5 kg hammer from 65 cm) is relatively low, the friction sensitivity is extremely high, to the point that the lowest stress the testing machine can apply initiates the reaction. Friction stress is common in the handling of nanothermite materials, for example when removing them from the flask after evaporation of the non-solvent or when pressing them into pellets. The electrostatic discharge (ESD) sensitivity, which was not in the original paper, is also at a high level. The human body can deliver discharges of up to 156 mJ according to experts from SME (the largest producer of energetic materials in France), so the threshold of about 1 mJ means that the product can easily be initiated by an operator who is not correctly grounded. This means that the MnO_2/Al nanothermite is a hazardous product. As it does not fulfill the criteria of the

¹For an explanation of the TRC method, see section 3.5.3, page 56.

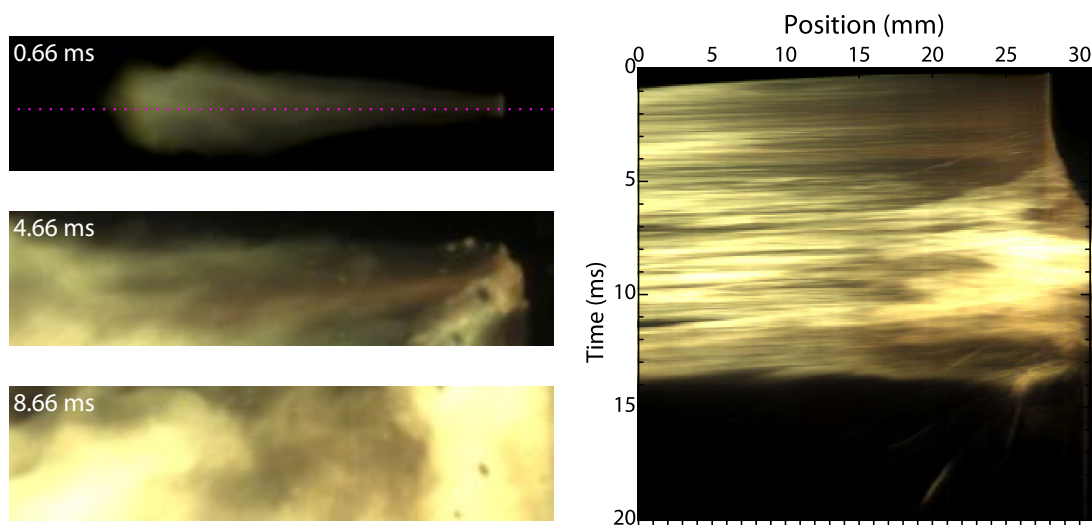


Figure 6.1 Selected screenshots from the combustion video of a MnO_2/Al nanothermite pellet compressed at 99 MPa (left); “Timeline” image of the combustion (right). The pellet is on the right side, the laser comes from the left. The dotted line in the top left picture indicates the area shown in each line of the timeline image.

UN norm on the transport of dangerous goods [6], it cannot be transported on public roads.

In Ref. [162], the authors prepared gas-generating nanothermites (GGNT) from MnO_2/RDX nanocomposites mixed with aluminum. In the case of the material containing 27.6 wt-% of RDX, the friction sensitivity is lower (threshold 9 N) than for the product without RDX. This is attributed to the fact that the RDX layer on the surface of the manganese dioxide particles disadvantages the interactions between MnO_2 and Al nanoparticles. This is exactly the effect that we want to achieve with the nanotube-containing hermites in the following sections: *decrease the direct interaction between oxidizer and fuel by spatially separating them.*

6.1.2 CuO/P

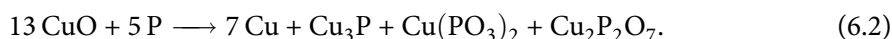
Nanothermites that use phosphorus instead of aluminum as the fuel are a recent development of our laboratory [193, 194, 195]. The idea is to use an alternative reducing agent to avoid the problems in the supply of aluminum nanopowders. Contrary to aluminum, phosphorus is only available in the form of micron-sized particles, which means that the mixtures presented here are micro-/nanothermites. The reactivity of different metal oxides with phosphorus, in ascending order, is



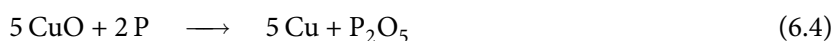
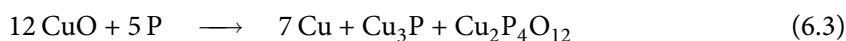
Copper(II) oxide provides a good reactivity without being as toxic as lead(IV) oxide.

A CuO/P nanothermite was prepared from copper oxide nanoparticles (Sigma-Aldrich) and micron-sized red phosphorus (Sigma-Aldrich) by mixing in *n*-hexane according to procedure A (section 3.2). The sensitivity levels of a formulation with a 20% excess of phosphorus (corresponding to 15.7 wt-% of P) are given in Table 6.1 (line “CuO/P^a”). While the impact sensitivity is low, the sample is quite sensitive to friction stress, and its sensitivity to electrostatic discharges is extremely high. For more fuel-rich formulations (30.0 or 50.0 wt-% of phosphorus), the friction and ESD sensitivities are too low to measure them (< 5 N and < 0.12 mJ respectively). These formulations are among the most ESD-sensitive materials known; this makes them very dangerous to handle. The low impact sensitivity is explained by the low hardness of the phases; the Mohs hardness of copper(II) oxide and red phosphorus are 3.5 and 0.5 respectively. The CuO particles tend to be inserted into the phosphorus matrix upon an impact stress. Concerning the extreme ESD sensitivity, the start of the reaction in the material creates metallic copper, which is a good electrical conductor. Therefore, the conductivity of the material is increased, facilitating the flow of current and further accelerating the reaction.

The combustion mechanism of the CuO/P nanothermites is complex; it depends on the proportions in the formulation, the atmosphere and the heating rate. Contrary to aluminum-based nanothermites, atmospheric oxygen plays an important role in the combustion of these mixtures. In the presence of oxygen, the reaction starts by the combustion of phosphorus in air, which initiates the combustion of the nanothermite. Heating the formulation with 20% excess of fuel at 2 K/min in argon to 500°C results in the formation of metallic copper, copper phosphide, copper phosphate and copper pyrophosphate; no P₄O₁₀ is formed in the reaction. The proposed reaction equation [194] is



In the same conditions, the fuel-rich formulation (containing 30.0 wt-% of phosphorus) reacts according to the following reactions:



In a TRC experiment with a 7 W CO₂ laser, the CuO/P pellets react in two steps: in the first few milliseconds, the laser evaporates some of the phosphorus, which begins burning in contact with the air. Then, the thermite reaction starts, initiated by the burning phosphorus. In addition, if copper phosphide is formed, it will react quickly with the oxygen in the air and be oxidized further. The fumes released by the combustion make it difficult to observe the propagation of the combustion front. The combustion velocity of a pellet compressed at 99 MPa is about 27 mm/s. The combustion residues (Figure 6.2) are spheres of resolidified molten material. SEM observations at higher magnification [194] show that the macroscopic spheres are themselves made of fused spherical nanoparticles, a sort of fractal structure.

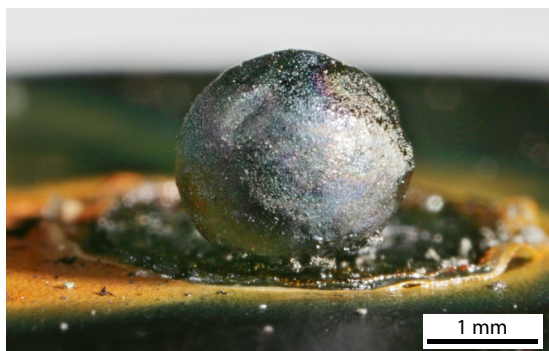


Figure 6.2 Photography of the combustion residue of a CuO/P nanothermite formulation after a TRC experiment: sphere of resolidified molten copper.

6.2 Nanothermites containing manganese oxide-filled CNTs

6.2.1 $\text{MnO}_x\text{@MWNT/Al}$

The first of these formulations is based on the “ $\text{MnO}_x\text{@MWNT}$ ” nanocomposite prepared by reactive infiltration of FutureCarbon MWNTs with manganese nitrate in nitric acid.² The manganese oxide in this composite is less oxygenated ($\text{MnO}_{1.621}$) and mostly contained as exocrystallized particles, i. e. outside the CNTs. For the calculation of the oxygen balance, the oxygen content in CNT end groups was neglected, and only the oxygen contained as manganese oxide was taken into account. The formulation, with a 20% excess of aluminum, contains

- ▶ 74.6 wt-% of $\text{MnO}_x\text{@MWNT}$, which contains 47.2 wt-% of MnO_x with $x = 1.621$ and
- ▶ 25.4 wt-% of Al 50 P, of which 60.04 wt-% is metallic aluminum.

Table 6.3 shows the amount of each constituent in the thermite.

Mixing in *n*-hexane. There is a practical problem for the preparation of the mixture: the oxide nanocomposite is in the form of millimetric grains that are not dispersible in *n*-hexane. Thus, the product is first ground in a mortar and then dispersed in ultrapure water by sonicating with a sonotrode at 300 W. The resulting black dispersion is distilled on a rotary evaporator, and the resulting fine powder is dried under vacuum. Then, the powder is mixed normally with aluminum and *n*-hexane according to procedure A (section 3.2).

The friction sensitivity test shows that this formulation (> 360 N) is in fact much less sensitive than the one that does not contain any carbon nanotubes (< 5 N). This is an important result because it shows that the basic premise of separating oxidizer and fuel does work. This product is among the least sensitive nanothermites known! On the other hand, it is slightly more reactive to impact stress than the MnO_2/Al formulation.

²See section 5.2.1, page 101ff.

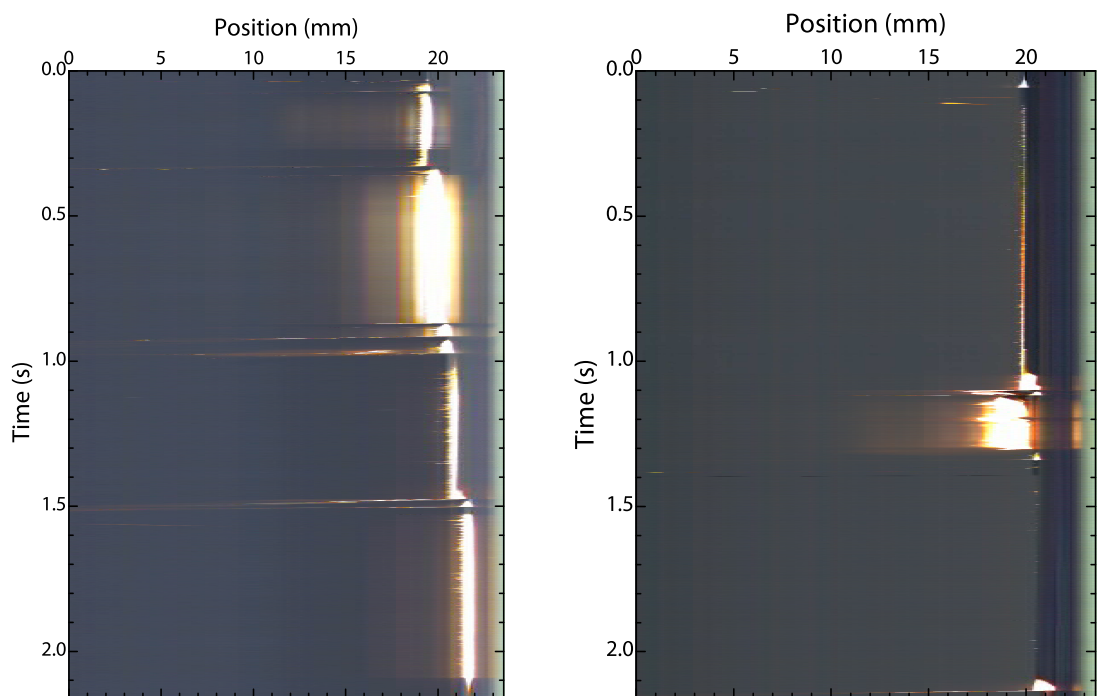


Figure 6.3 “Timeline” images of the combustion of the $\text{MnO}_x\text{@MWNT/Al}$ nanothermite mixed in *n*-hexane. The vertical axis is the time going from top to bottom.

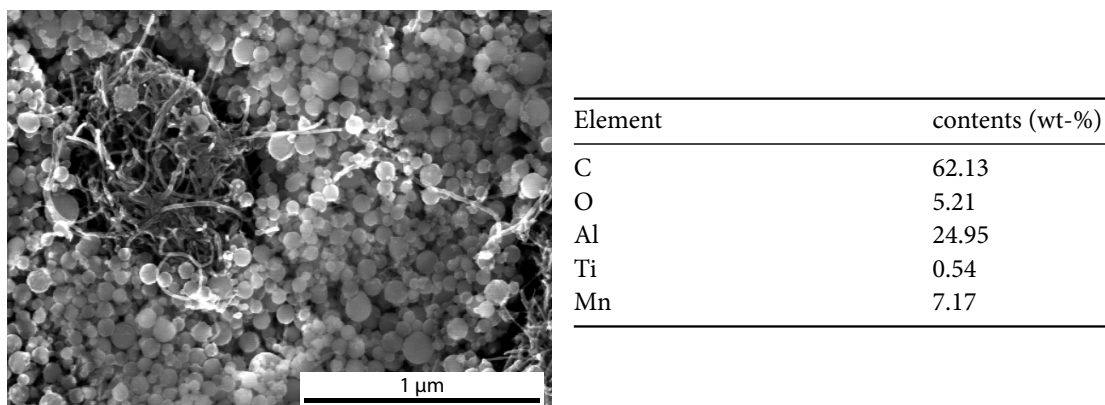


Figure 6.4 SEM micrograph of the surface of a $\text{MnO}_x\text{@MWNT/Al}$ pellet, showing the agglomeration of aluminum particles on the outermost layer of the pellet (left); quantitative results of EDS analysis on the pellet surface (right).

After physical mixing and drying, the nanothermite powder was pressed into pellets of about 50 mg each and with a diameter of about 4 mm. The apparent densities obtained from the pellets are given in Table 6.2. The theoretical maximum density (TMD), calculated from the bulk densities of the constituents, is 3.249. Both types of pellets (99 and 210 MPa) have less than half of the TMD. However, the apparent density is almost as high as for MnO_2/Al (1.26 vs 1.33), giving a higher compaction ratio (39% of TMD vs 32%). This seems to be mostly due to the higher mean grain size of the manganese oxide. Still, even with their residual porosity, the $\text{MnO}_x\text{@MWNT/Al}$ pellets are very cohesive and can be handled without breaking.

The pellets have a grey color and a metallic shine. Where does this effect come from? Figure 6.4 shows a scanning electron micrograph of the smooth upper surface of a $\text{MnO}_x\text{@MWNT/Al}$ pellet compressed at 210 MPa. The surface is covered more or less continuously with aluminum particles, which can be distinguished by their characteristic spherical shape. However, the EDS results (right) taken on this surface show that the surface composition is very similar to the proportions of the formulation; specifically, the aluminum content is 24.95 wt-%, compared to 25.38 wt-% in the overall formulation. This is explained by the penetration depth of the EDS microanalysis. At an energy of 20 keV, the EDS spectrum is representative for the mean composition in a surface layer of about 5 μm . Thus, there are compositional inhomogeneities on a submicrometric scale in the pellet. Similarly, if the pellet is broken apart mechanically, the fracture surfaces (not shown here) are significantly lower in aluminum, indicating that the mechanical fractures happen where there are agglomerated MWNTs.

Figure 6.3 shows two timeline images of the combustion of an $\text{MnO}_x\text{@MWNT/Al}$ nanocomposite mixed in *n*-hexane, compressed at 99 (left) and 210 MPa (right). The combustion of the $\text{MnO}_x\text{@MWNT/Al}$ pellets is very irregular, which makes it impossible to define a combustion

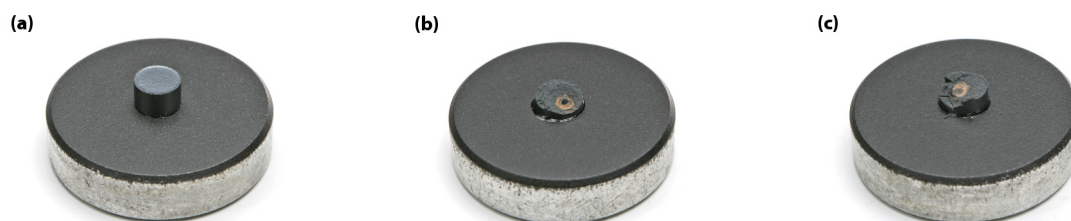


Figure 6.5 Photos of $\text{MnO}_x\text{@MWNT/Al}$ nanothermite pellets glued to the duraluminum supports used for TRC: before ignition (a) and residues after 2 s laser illumination for $p = 99$ MPa (b) and 210 MPa (c).

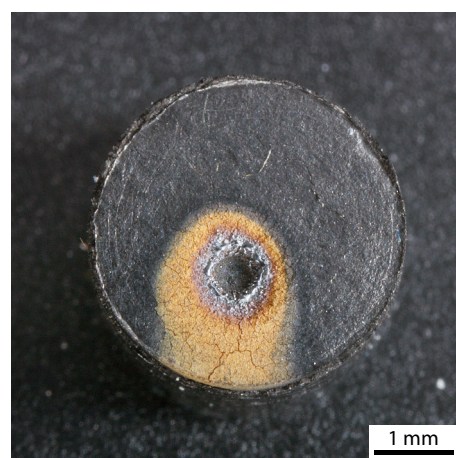


Figure 6.6 Macro photograph of a pellet consisting only of $\text{MnO}_x\text{@MWNT}$, without addition of aluminum, after 2 s of laser illumination in the TRC setup.

velocity. Most of the time, the combustion front is stationary, and small particulates are ejected to the left. At some points, there are short bursts of activity with a rapidly advancing combustion front, for example in Figure 6.3a between 0.35 and 0.4 s. The thermite reaction creates an intense light output of the reacting part of the pellet. Very suddenly (e. g. at around 0.85 s), there is a rupture in the image, when the burning part of the pellet (and often some unburned material) is ejected. Just before this ejection, a fissure can be seen to appear in the videos. The ejected parts can be up to half of the pellet. In the more strongly compressed pellet (Figure 6.3b), the time between the subsequent “bursts” of activity is much longer. There is one such burst just after $t = 1.0$ s and another at the bottom of the image ($t = 2.1$ s). During the bursts, the combustion propagates very rapidly, with a speed of up to 35 mm/s, for a distance of 1 mm or less. However, as the time delays between subsequent material ejections and the size of the ejected pieces is essentially random, it makes no sense to define an overall propagation velocity.

From the residues shown in Figure 6.5b and c, it is clear that the pellets did not completely react in the 2 s of CO_2 laser illumination at $P = 7$ W. The pellets compressed at 210 MPa have a larger unreacted residue, which means that they burn more slowly than the ones compressed at

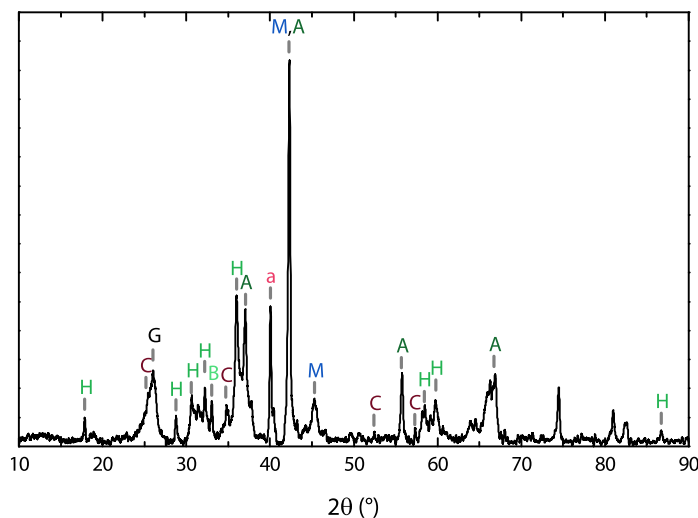


Figure 6.7 X-ray diffractogram of the collected combustion residues of the $\text{MnO}_x\text{@MWNT/Al}$ nanothermite mixed in *n*-hexane. The annotated phases are Graphite (56-159, **G**), Akhtensite (MnO_2 , 30-820, **A**), Hausmannite (Mn_3O_4 , 24-734, **H**), Bixbyite (Mn_2O_3 , 24-508, **B**), manganese metal ($\gamma\text{-Mn}$, 17-910, **M**), Corundum ($\alpha\text{-Al}_2\text{O}_3$, 10-173, **C**) and aluminum carbide (Al_4C_3 , 35-799, **a**).

99 MPa. The point where the focused laser impacted on the pellets is clearly visible. Around the impact spot, a light brown ring can be seen. To achieve a better understanding of the processes during the combustion and of the residues, a control experiment, in which a pellet consisting only of $\text{MnO}_x\text{@MWNT}$ nanocomposite without aluminum was tested by TRC, was carried out. Figure 6.6 shows a macro photograph of the residue of this pellet. At the spot where the laser struck the pellet, there is a small crater; on the edge, small frozen droplets of manganese metal can be seen in the optical microscope. The area around the laser spot has a light brown color from manganese oxides (“Braunstein”), as it has been heated by diffusion.

The combustion video of the pellet without aluminum shows a stationary combustion front with the ejection of small, incandescent particles – exactly like in the stationary combustion phases of the nanothermite pellets. Thus, we know that the phases in which the combustion front does not advance (for example in Figure 6.3b between 0.1 and 1.0 s) is due an inhomogeneous composition of the pellet: at the spot where the laser hits the sample, no or too little aluminum to start the combustion is present. Only when a part of the pellet with a more stoichiometric composition is heated enough by diffusion does the reaction start. The thermal expansion of the pellet induces mechanical stress that creates fissures in the pellet, which act as barriers for the reaction, stopping the propagation.

The combustion residues that detach from the pellet during the TRC experiment have a light brown color on the outside, just like in Figure 6.6, and are black on the inside. They also contain

some unreacted, grey nanothermite material. Figure 6.7 shows the results of X-ray diffraction of the collected residues; an effort was made to separate reacted from unreacted material. The diffractogram shows a large number of peaks; the assignment to crystalline phases is difficult because of the large number of possible products and the structural similarity for some of them. We find graphite (from the CNTs), manganese metal (γ -Mn), manganese oxides (MnO_2 , Mn_2O_3 and Mn_3O_4), α - Al_2O_3 and aluminum carbide Al_4C_3 . The presence of aluminum carbide means that some of the aluminum reacts with the CNTs according to the reaction



The presence of manganese metal is a sign that the thermite reacted as stated in reaction (6.1). The manganese oxides are either a sign of incomplete reduction due to the “loss” of aluminum because of reaction (6.5), or of reoxidation of the formed manganese metal with oxygen from the air. Interestingly, the MnO_2 is not found in the pyrolusite structure (rutile-type) but in the less ordered akhtensite (ϵ - MnO_2) structure. As akhtensite is usually converted irreversibly into pyrolusite at 250–300°C [196], this suggests that the MnO_2 is formed by reoxidation of the manganese metal at lower temperatures. On the other hand, hausmannite is the most stable manganese oxide at a temperature between 900 and 1200°C [183, p. 1112ff.], suggesting that it is formed from the residual manganese oxide that has not directly reacted with the aluminum.

Mixing in acetonitrile. The analysis of the combustion behavior above suggests that the nanothermite pellets were not homogeneously mixed. In order to improve the mixing, we tried using acetonitrile instead of *n*-hexane. It has been shown in a recent thesis on WO_3/Al nanothermites that dispersing in acetonitrile results in more homogeneous mixing [197]. From a practical point of view, the $\text{MnO}_x@\text{MWNT}$ composite dispersed very well in acetonitrile, so the water redispersion step could be skipped. The nanothermite was directly prepared from the ground composite material and nano-aluminum according to procedure B, as given in section 3.2.

Table 6.2 (the line labeled “ $\text{MnO}_x@\text{MWNT}/\text{Al}^b$ ”) shows that the pellets compressed at 99 MPa have indeed a much shorter IDT than the product mixed in *n*-hexane (13.5 vs 20 ms), which corresponds to a considerable gain in activation energy (50 vs 76 mJ). This performance gain is due to the more homogeneous mixing that can be achieved in acetonitrile. There is also a slight increase in the apparent density of the pellets (1.31 vs 1.26) but this is probably not significant.

As the activation energy of the other pellets was considerably higher when compressed at 210 MPa compared to 99 MPa, one could formulate the hypothesis that a less strongly compressed pellet is also more reactive. However, the pellets compressed at 44 MPa show exactly the same ignition delay time as the ones compressed at 99 MPa.

As for their combustion behavior, the thermite mixed in acetonitrile shows the same irregular combustion with frequent ejections of material. While the combustion of the pellets compressed at 99 MPa is very similar to the *n*-hexane-mixed material, the pellets compressed at 44 MPa break

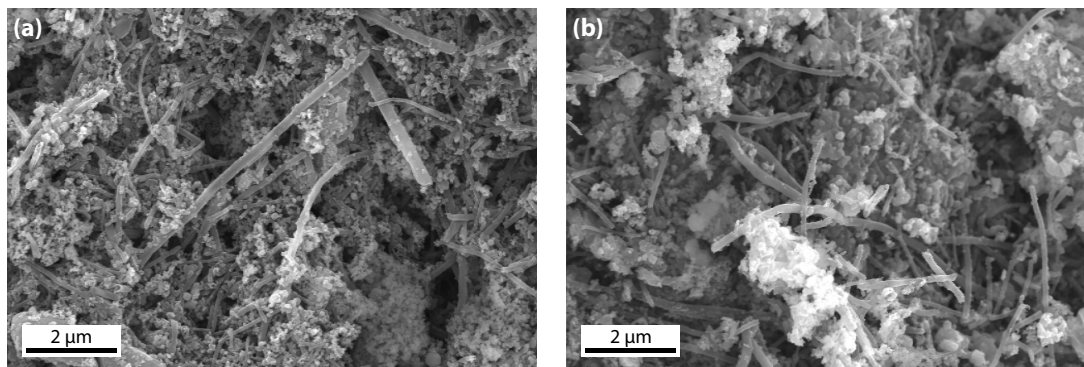


Figure 6.8 Scanning electron micrographs (10 000 \times) of the $\text{MnO}_x\text{@CNF/Al}$ nanothermite mixture before (a) and after burning (b).

even more easily on mechanical stress. As a result, the ejected pieces are mostly composed of unreacted material, and most of the pellet is simply ejected unreacted instead of burning. This makes the determination of combustion velocities meaningless.

6.2.2 $\text{MnO}_x\text{@CNF/Al}$

This second nanothermite composition is based on the manganese-oxide filled herringbone nanotubes (Pyrograf PR-24) prepared by the infiltration of molten manganese nitrate. This manganese oxide in this nanocomposite is essentially filled in the cavities of the nanotubes, and there is very little exocrystallized oxide. Even though the Pyrograf nanofibers have a higher diameter than the MWNTs, the mean diameter of the manganese oxide particles is actually smaller. Furthermore, the manganese oxide phase is closer to MnO_2 than in the $\text{MnO}_x\text{@MWNT}$ sample before.

As before, for the determination of the oxygen balance of the nanothermite, the CNF are assumed to be completely inert in the thermite reaction, and 1.2 times the stoichiometric amount of aluminum is added. This gives a formulation containing

- ▶ 72.3 wt-% of $\text{MnO}_x\text{@CNF}$, which contains 48.58 wt-% of $\text{MnO}_{1.9}$, and
- ▶ 27.7 wt-% of Al 50 P, which contains 60.85 wt-% of metallic aluminum.

The resulting percentages for each constituent phase are given in Table 6.3. The mixing is done in acetonitrile according to procedure B, as given in section 3.2. The scanning electron micrograph shown in Figure 6.8a shows a homogeneous mix of the nanofibers and the spherical aluminum particles.

The sensitivity of this nanothermite formulation is given in Table 6.1 (line “ $\text{MnO}_x\text{@CNF/Al}^b$ ”). Like all the nanotube-containing thermites presented in this work, it is completely insensitive to

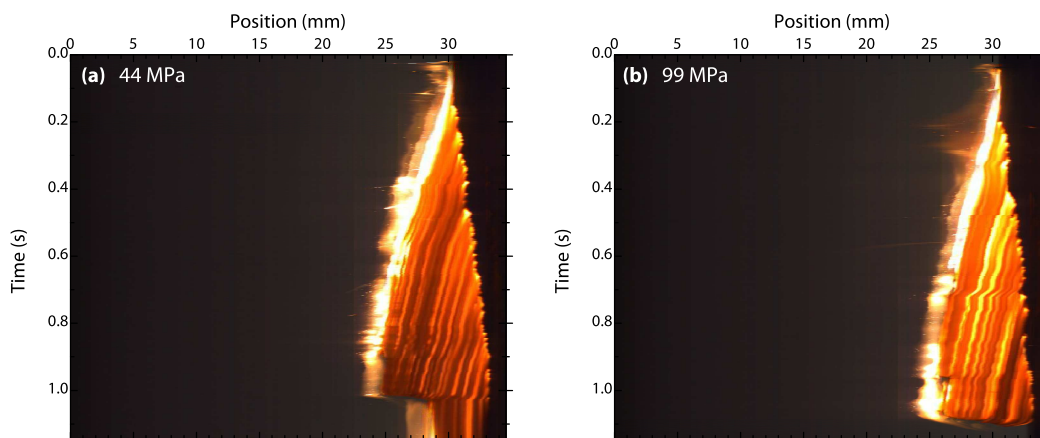


Figure 6.9 “Timeline” images of the combustion of $\text{MnO}_x\text{@CNF/Al}$ pellets compressed at 44 (a) and 99 MPa (b).

friction stress. However, unlike the $\text{MnO}_x\text{@MWNT/Al}$ nanothermite presented in the last section, it also has a low impact sensitivity – lower, in fact, than the $\text{MnO}_2\text{/Al}$ mixture that does not contain any nanotubes (44.2 vs 31.9 J). This is attributed to the low amount of exocrystallized manganese oxide, which means that there is no (or very little) direct contact between oxidizer and fuel. The cavity of the CNFs is typically 40 nm large, while the mean diameter of the aluminum particles is 50 nm. It is thus unlikely that aluminum particles enter the CNF cavities during mixing. The ESD sensitivity of the formulation is also lowered by more than an order of magnitude (threshold of 34.7 vs 1.04 mJ); however, this value is still below the capacity of the human body (156 mJ).

The ignition delay time of the compressed pellets, determined by a TRC experiment with a 7 W CO_2 laser, is lower than for both $\text{MnO}_x\text{@MWNT/Al}$ nanothermites. The activation energy is lowered by a factor of two or more (25 vs 50 or 76 mJ for 99 MPa compression). However, the energetic performance is still vastly below the $\text{MnO}_2\text{/Al}$ nanothermite.

Nonetheless, the most important advantage of the CNF-containing formulation compared to the one presented earlier is its *cigarette-like combustion with an approximately linear propagation of the reaction in the pellet*, allowing to measure the combustion velocity v . As before, there is almost no difference between the 44 MPa and the 99 MPa compression, neither in the combustion velocity nor in the ignition delay. Figure 6.9 gives “timeline” images for two pellets compressed at 44 and 99 MPa respectively. The difference with Figure 6.3 is immediately obvious: the combustion proceeds in a continuous fashion without the ejection of bigger, partially reacted pieces. During the combustion, the pellet expands in the direction of the combustion; the burning proceeds layer by layer. Each layer (of a few hundred microns thickness) rapidly starts burning, moving the combustion front to the right, and then expands in length, moving the combustion

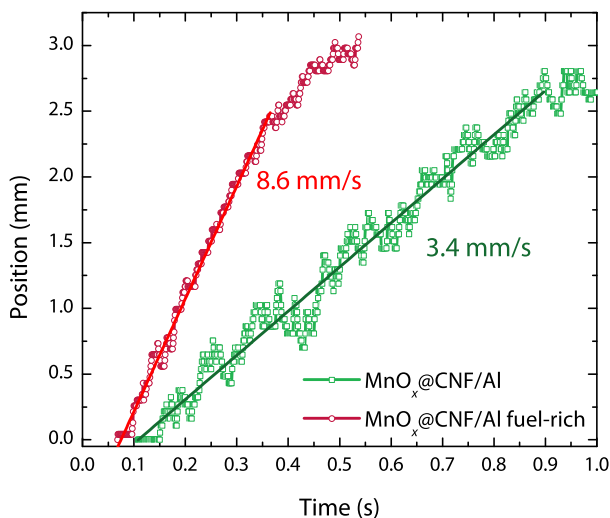


Figure 6.10 Propagation of the combustion front with time ($x = f(t)$) for a normal (green) and a fuel-rich $\text{MnO}_x@CNF/Al$ nanothermite (red), compressed at 44 MPa, with the corresponding linear regression and combustion velocity.

front to the left again. These characteristic oscillations are visible in the timeline as a zigzag line. The expanded ash of the pellet either detaches from the support (such as in Figure 6.9b) or stays on it (as in Figure 6.9a) and is heated by the laser for the remaining time of the experiment (two seconds in total). In the figure, this part has been cut because nothing more happens: the nanothermite is completely burned, and the burning of the carbon nanotubes in air is very slow compared to the thermite reaction. Their combustion happens on a timescale of several minutes.

For a fully quantitative analysis of the combustion propagation, i. e. for determining v , we retraced the position of the combustion front in the image with the help of the “nt-decode” software presented in appendix A.3. Reconverting the pixel positions into millimeters and tracing them as a graph results in Figure 6.10. The oscillation of the front position, which was explained above, is well visible in this graph, too. However, a linear regression over the whole propagation, as indicated by the black line, gives an excellent fit ($R^2 = 0.97$ for the 44 MPa sample pictured) and a meaningful “macroscopic” combustion velocity of about 3.4 mm/s. It is obvious that the velocities for the two samples shown in the graph are almost identical. This is indeed the result obtained by taking the mean of three pellets per compression, shown in Table 6.2 (3.3 mm/s for 44 MPa and 3.5 mm/s for 99 MPa).

To draw a parallel to the irregular combustion of the $\text{MnO}_x@MWNT/Al$ nanothermites, the rapid progression of a layer corresponds to what we earlier called “bursts”, while the expansion of the pellet corresponds to the ejection of material. One of the reasons for the missing ejections is that the structural cohesion of the pellet on a micrometric scale is greater with the Pyrograf CNFs, as they have lengths of tens of microns and, more importantly, less kinks and bends in their structure. While the MWNT with their flexibility entangle into smaller aggregates, the CNFs are able to assure the cohesion over a longer length scale.

The residue of the combustion of the nanothermite pellets, shown in Figure 6.11, resembles



Figure 6.11 Macro photograph of the residue of a $\text{MnO}_x\text{@CNF/Al}$ pellet after combustion.

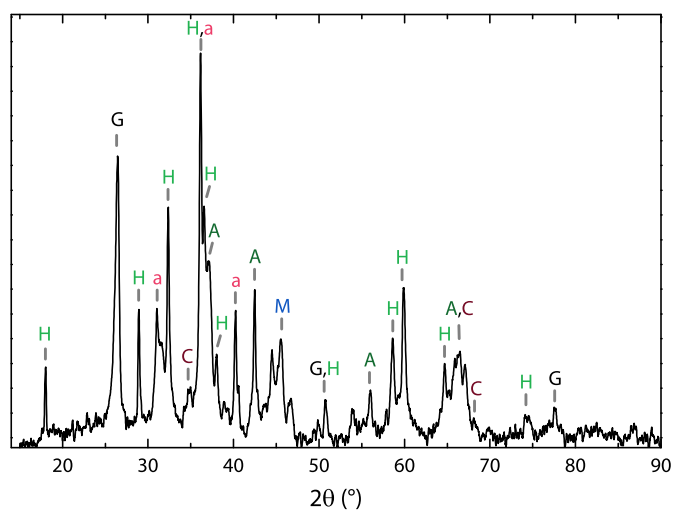


Figure 6.12 X-ray diffractogram of the collected combustion residues of the $\text{MnO}_x\text{@CNF/Al}$ nanothermite mixed in acetonitrile. The annotated phases are Graphite (56-159, **G**), Akhtensite (MnO_2 , 30-820, **A**), Hausmannite (Mn_3O_4 , 24-734, **H**), manganese metal ($\gamma\text{-Mn}$, 17-910, **M**), Corundum ($\alpha\text{-Al}_2\text{O}_3$, 10-173, **C**) and aluminum carbide (Al_4C_3 , 35-799, **a**).

cigarette ash. As a result of the axial expansion, there are slit-like voids in the cylinder. The color of the residue is light brown on the outside and dark brown/black on the inside. This is visible in the top part, where a piece of the brittle residue has been detached. A scanning electron micrograph of the residue (Figure 6.8b) shows that *the carbon nanotubes are not completely destroyed by the combustion of the thermite*. They seem to be largely intact.

The crystalline phases in the residues were determined by X-ray diffraction. The results are shown in Figure 6.12. The diffractogram is very similar to the one of the $\text{MnO}_x\text{/MWNT/Al}$ nanothermite residues: As before, we find MnO_2 in the disordered akhtensite structure, whose formation is likely due to reoxidation of manganese formed by the thermite reaction, as well as Mn_3O_4 and $\gamma\text{-Mn}$. However, the peaks from the initial oxide phases – pyrolusite-type MnO_2 and Mn_2O_3 as bixbyite – have disappeared, indicating that the reaction is completed. The manganese metal reflections are less pronounced than in the MWNT-based product; presumably, the long “stationary phases” in the combustion of the latter product, in which there was only a reaction between the laser beam and the $\text{MnO}_x\text{/MWNT}$ composite, contributed to the formation of well-crystallized metal. Due to the more regular combustion of the CNF-based formulation, the residues contain less Mn metal. Like in the MWNT-based thermite, aluminum carbide Al_4C_3 was formed as a byproduct during the reaction. However, any aluminum that forms the carbide can no longer participate in the thermite reaction. As a consequence, the quantity of aluminum metal in the formulation might be below the optimum; in this case, the Mn_3O_4 residues are the sign of an incomplete thermite reaction because Mn_3O_4 is formed upon heating of other manganese oxides.

Fuel-rich formulation. To test the hypothesis that the $\text{MnO}_x\text{/CNF/Al}$ thermite formulation does not contain enough aluminum for a complete reaction with the manganese oxide, we prepared a “fuel-rich” $\text{MnO}_x\text{/CNF/Al}$ nanothermite formulation. In this product, the quantity of aluminum has been doubled – i. e. 2.4 times the stoichiometric amount instead of 1.2 times. The sensitivity thresholds of this formulation are given in Table 6.1 (under “ $\text{MnO}_x\text{/CNF/Al}$ fuel-rich^b”). The product is more sensible to impact stress than the previous formulation (24.5 vs 44.2 J). On the other hand, the ESD sensitivity of the formulation is extremely decreased, by more than two orders of magnitude compared to the previous formulation (5300 vs 34.7 mJ). This is due to the fact that aluminum is a good electrical conductor. As the conductivity of the sample is much higher, the spark heats the sample much less, which increases the discharge energy necessary to initiate a combustion.

Regarding the combustion of compressed pellets of the fuel-rich formulation, the ignition delay time and activation energy (Table 6.2) is higher than for the previous one, i. e. they are more difficult to initiate. On the other hand, its combustion velocity is slightly higher. This is shown by the fact that a pellet of 50 mg compressed at 99 MPa takes 840 ms to burn for the fuel-rich formulation vs 1030 ms for the previous one. However, the propagation of the combustion, as

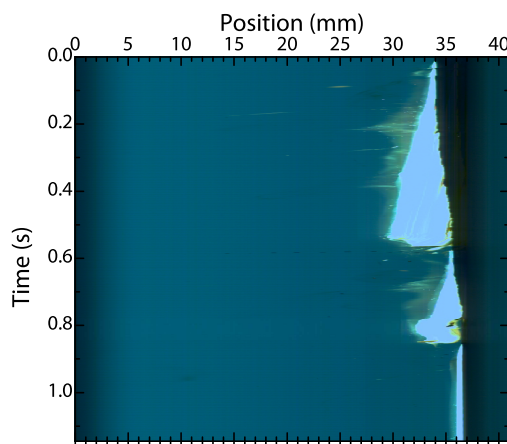


Figure 6.13 Timeline image of the combustion of a fuel-rich $\text{MnO}_x\text{@CNF/Al}$ nanothermite pellet. The blue tint is due to technical reasons.

shown in the timeline image in Figure 6.13, is less regular, due to the ejection of burning pieces of the pellet. The rupture in the image near $t = 0.55$ s is due to the entire piece of residue falling down. It seems that the reduction in CNT content, as given in Table 6.3, causes a decrease in the mechanical cohesion of the compressed material. The propagation of the combustion front of one pellet is also illustrated by the red points in Figure 6.10. While an increase in the combustion velocity can be seen, it is close to the margin of experimental error.

In any case, the fact that the velocity is higher means that the aluminum content of the original formulation was in fact not sufficient. However, it is likely that this fuel-rich formulation is in fact too rich in aluminum, and that the optimal aluminum content is somewhere between these formulations. A systematic study of the influence of the oxygen balance (i. e. the fuel content) on the properties of the nanothermite formulations should be done in the future in order to achieve optimal energetic performances.

6.3 MnO_2/Al nanothermites physically mixed with CNTs

In order to investigate the effect of filling and confinement on the reactivity of manganese oxide thermites, we prepared two formulations, with MWNT and CNF, based on purely physical mixing of the reagents instead of manganese oxide/carbon nanotube composites. Both of these formulations are based on empty nanotubes, MnO_2 nanoparticles (3–5 nm) and Al 50 P aluminum nanoparticles about 50 nm in diameter. The oxygen balance, as in the other thermites, has been chosen so that aluminum is added in 1.2 times its stoichiometric quantity. The proportion of carbon nanotubes has been chosen to be equal to the directly comparable formulation based on manganese oxide-filled carbon nanotubes ($\text{MnO}_x\text{@MWNT/Al}$ and $\text{MnO}_x\text{@CNF/Al}$, respectively).

The MWNT-based formulation (MWNT/ MnO_2/Al), which was mixed in *n*-hexane like the

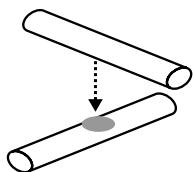


Figure 6.14 Illustration for the mechanism that sensitizes the CNT-containing MnO₂/Al thermites to impact stress: thermite particles (grey) between two crossed CNTs.

corresponding MnO_x@MWNT/Al formulation, contains

- ▶ 39.40 wt-% of as-received MWNTs,
- ▶ 33.37 wt-% of MnO₂ nanoparticles and
- ▶ 27.23 wt-% of Al 50 P, containing 60.85 wt-% of metallic aluminum.

The CNF-based formulation (CNF/MnO₂/Al), on the other hand, was mixed in acetonitrile and contains

- ▶ 37.16 wt-% of CNFs oxidized for 16 h in nitric acid,
- ▶ 34.60 wt-% of MnO₂ nanoparticles and
- ▶ 28.24 wt-% of Al 50 P, containing 60.85 wt-% of metallic aluminum.

Both formulations were prepared according to procedure A presented in section 3.2.

While both formulations are insensitive to friction stress (threshold over 360 N), they are actually more sensitive to impact than the reference formulation without nanotube addition. We think that this is a consequence of the confinement of oxidizer and fuel *between* the CNTs, which are highly entangled and enclose the two reagents in the voids and interstices of the CNT aggregates. The fact that the MWNT/MnO₂/Al has a higher sensitivity than its CNF counterpart (17.2 vs 29.4 J) is due to the lower size of the MWNTs (which provides a nanoscale confinement) and their flexibility (which creates a much stronger short-ranged entanglement than in the CNF case). The confinement effect is thus much weaker for the CNFs. The impact sensitivity of these formulations is also higher than in the case of the nanothermites containing manganese oxide-filled nanotubes. This is a *direct consequence of the spatial separation between oxide and fuel* in the case of the filled CNTs, which lowers their sensitivity.

There is also a geometrical argument that can be proposed to explain the increased impact sensitivity. Let us imagine two nanotubes crossed at an angle of 90°, with some manganese dioxide and aluminum particles between them, like in the schematic illustration in Figure 6.14. Geometrically, the contact between two crossed cylinders is equal to the contact between a sphere and a plane, which is why this geometry is applied in the Surface Force Apparatus developed by Israelachvili [198] for measuring the interaction between spherical surfaces. In our nanothermite model, the impact stress will make the upper nanotube impact violently on the lower one.

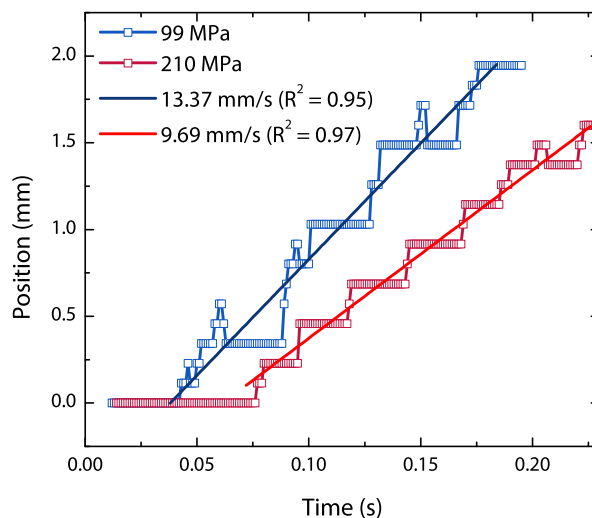


Figure 6.15 Graph showing the propagation of the combustion front of MWNT/MnO₂/Al pellets, compressed at 99 MPa (blue) and 210 MPa (red), in the high-speed video recorded during a TRC experiment with 7 W of optical power.

The contact surface between the tubes is near zero, which means that a much higher pressure will build up between the two tubes, *concentrating the impact stress in one point* (“hot spot”). The higher localized stress then initiates the thermite reaction.

The electrostatic discharge sensitivity of the CNF-containing nanothermite³ is extremely decreased compared to the MnO₂/Al reference (1800 vs 1.04 mJ). This is due to the higher conductivity of the sample, like in the case of the fuel-rich MnO_x@CNF/Al formulation: Presumably, CNF content is above the percolation threshold, thus the spark passes along a high-conductivity path spontaneously formed in the sample and causes less heating of the sample. The effect is also related to the efficient heat transport provided by the CNTs, leading to a rapid dissipation of the discharge energy throughout the bulk of the sample.

The big problem of these formulations is their behavior during the compression into pellets for the TRC tests: The empty carbon nanotubes with their high flexibility act as springs and cause the pellets to reexpand when ejected from the pressing mold. Thus, while the nominal diameter of the mold is 4.08 mm, the final pellet diameter is up to 4.21 mm. In many cases, the pellets form macroscopic voids by reexpanding, which makes them brittle, prone to breaking and difficult to handle. This is in sharp contrast to the excellent cohesion observed in the case of the nanothermites containing manganese oxide-filled CNTs. Accordingly, the percentage of the theoretical maximum density of the pellets, shown in Table 6.2, is the lowest one of all the formulations observed (only 17% and 20% for MWNT/MnO₂/Al compressed at 99 and 210 MPa, respectively).

In terms of the energetic performance, however, the compositions containing unfilled nanotubes are much better than their filled-nanotube counterparts. The MWNT/MnO₂/Al nanothermite ignites much faster and with less laser energy than the other formulations ($E_A = 10$ mJ)

³The ESD sensitivity of the MWNT/MnO₂/Al formulation was not measured because the experiments were done before the acquisition of the ESD testing device.

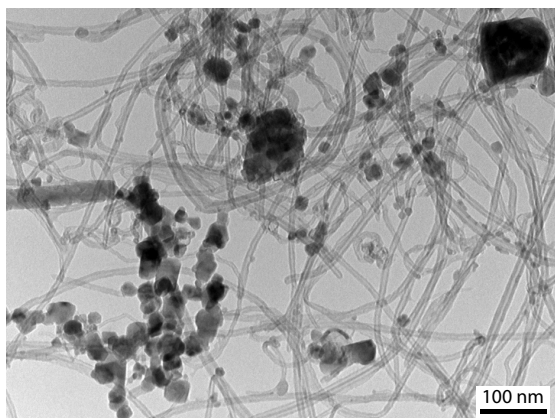


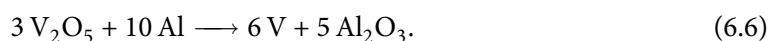
Figure 6.16 Transmission electron micrograph (80 kV acceleration voltage) of the combustion residues of MWNT/MnO₂/Al.

vs at 50 mJ and more for MnO_x@MWNT/Al). The combustion velocity, for which values between 6.5 and 16 mm/s have been measured for the two compression levels (mean values are given in Table 6.2), is at least twice as high than for the MnO_x@CNF/Al. Furthermore, contrary to MnO_x@MWNT/Al, the combustion of these pellets proceeds in a regular, linear fashion. Figure 6.15 shows two exemplary propagation traces, obtained from the analysis of the high-speed videos of the combustion of MWNT/MnO₂/Al using the “nt-timeline” and “nt-decode” programs given in the appendix. The position resolution in these traces is of one pixel, which is why there are discrete steps in the graph. The sloped lines show the corresponding linear regressions, which provide very good fits for the data. Table 6.2 gives the mean values and errors, obtained from three (99 MPa) and four pellets (210 MPa) respectively. In each case, one extra pellet broke apart during handling.

An electron microscopic investigation of the combustion residues of MWNT/MnO₂/Al (Figure 6.16 shows that the MWNTs are still intact after the thermite reaction. This confirms the result obtained for the MnO_x@CNF/Al nanothermite (Figure 6.8b), where the Pyrograf nanofibers were found to be intact after the combustion of the thermite. In the transmission electron micrograph, the small manganese dioxide nanorods (about 3 nm in diameter and 20 nm in length) are no longer found; they have completely reacted. Instead, we find many spherical particles with diameters similar to the one of the Al 50 P nanoparticles (about 50 nm), as well as a few particles larger than 100 nm.

6.4 Nanothermites containing vanadium oxide-filled CNTs

Vanadium(V) oxide is an interesting material for preparing thermite mixtures. Compared to MnO₂, for instance, its oxygen content is higher. The reaction equation for this system is



6 Reduced-sensitivity nanothermites containing carbon nanotubes

Sample	TMD (g/cm ³)	%V ₂ O ₅	%VO ₂	%Al	%Al ₂ O ₃	%C (CNT)
V ₂ O ₅ @CNF/Al	2.936	29.79	4.34	19.42	11.25	34.99
VO ₂ @CNF/Al annealed	3.161	6.57	26.28	19.27	11.17	35.48

Table 6.4 Theoretical maximum density (TMD) and contents in wt-% of each constituent phase in the different vanadium oxide-based nanothermite formulations.

This reaction, at 950°C, is used for the technical preparation of vanadium metal [183, p. 1071]. In the technical process, where the reaction is done much more slowly than for a thermite, aluminum is added in excess, and an Al/V alloy is formed. This alloy is heated under vacuum to 1700°C to distill the aluminum, leading to pure vanadium.

Like manganese oxides, vanadium oxide can change its oxidation state very easily between +V, +IV, +III and +II, making it a valuable catalyst for a large number of oxidation and reduction reactions. This property is also very interesting for a thermite, as it means that the reaction will proceed readily.

According to theoretical calculations by Fischer and Grubelich [156], the adiabatic reaction temperature is slightly higher than in the MnO₂/Al system when taking phase changes into account (3273 vs 2918 K), and the heat of reaction is comparable (4.56 kJ/g for V₂O₅/Al vs 4.84 kJ/g for MnO₂/Al). Until now, no V₂O₅/Al nanothermites have been prepared in our laboratory; thus, we cannot directly compare the properties of the thermites investigated here with a reference product, as in the case of manganese dioxide.

We prepared two nanothermite mixtures based on vanadium oxide-filled herringbone carbon nanofibers, with the goal of achieving higher reactivities and combustion velocities than for the manganese oxide-based systems. The first one is based on CNFs that have been infiltrated with an aqueous ammonium metavanadate solution and calcined at 325°C. The oxide is a slightly sub-stoichiometric VO_{2.45}. The formulation consists of

- ▶ 68.1 wt-% of V₂O₅@CNF, containing 48.6 wt-% of vanadium oxide and
- ▶ 31.91 wt-% of Al 50 P, containing 60.85 wt-% of metallic aluminum.

The exact amounts of each phase contained in the nanothermite formulation are given in the upper line of Table 6.4. The formulation was prepared according to procedure B given in section 3.2.

Like the other nanotube-containing thermites prepared in this chapter, the V₂O₅@CNF/Al nanothermite is insensitive to friction stress. Its impact sensitivity is slightly higher than for its manganese oxide counterpart (34.3 vs 44.2 J) but still moderate. On the other hand, the thermite is quite sensitive to electrostatic discharges, more so than the MnO_x@CNF/Al thermite (5.8 vs 34.7 mJ). This could be due to a lower initiation energy of the thermite reaction (6.6) compared to reaction (6.1), or due to the higher amount of exocrystallization (i. e. vanadium oxide particles

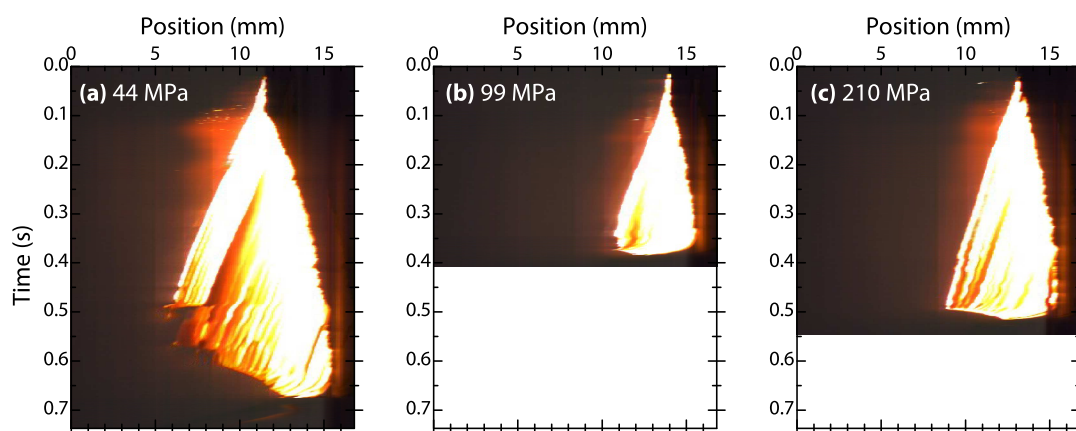


Figure 6.17 Timeline images of $V_2O_5@CNF/Al$ nanothermite pellets ignited by a 7 W CO_2 laser beam. The pellets have been formed at a pressure of 44 MPa (a), 99 MPa (b) and 210 MPa (c).

between the tubes or on the outer nanotube surface) observed for the $V_2O_5@CNF$ samples. For the ESD, exocrystallization could prevent the building of a high-conductivity percolation path through the bulk of the sample by reducing direct nanotube–nanotube contacts; this effect would decrease the ESD sensitivity threshold. The lower activation energy hypothesis is confirmed by the ignition delay time measurements on the (non-annealed) $V_2O_5@CNF/Al$ samples shown in Table 6.2, showing a 50% reduction in the E_A values compared to $MnO_x@CNT/Al$.

During compression of pellets for the combustion tests, we observed a strong reexpansion of the pellets when removing them from the pressing mold. This results in the formation of voids, giving a low apparent density of the pellets. For instance, the only usable, unbroken pellet obtained for $p = 44$ MPa has an apparent density of only 0.83,⁴ 1/3 less than the manganese oxide based-formulation under the same conditions. Moreover, the adhesion of the pellet to the compression piston was often stronger than the cohesion of the pellet itself, resulting in a typical breakage pattern which is shown in Figure 6.18. The form of the fissure is a result of the mechanical stress when the pellet is removed from the mold and reexpands perpendicular to the pressing axis. Wiping the piston with a small amount of silicone oil helped somewhat, but still, many pellets were unusable or broke apart during the handling. We are unsure about the reason for this behavior, which might be related to the mechanical properties of the vanadium(V) oxide itself, more specifically to its compression modulus and elastic behavior. For what it is worth, the same mechanical behavior has been observed in the physically mixed nanotube/ MnO_2/Al formulations presented in the previous section.

The combustion of the nanothermite pellets, which was investigated in the TRC setup, was

⁴See Table 6.2, page 131. Values where no error is given are the result of investigating only one pellet.

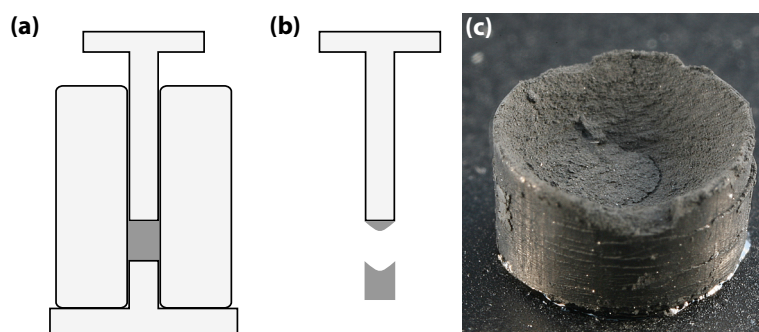


Figure 6.18 Schematical drawing (not to scale) of a pellet (dark grey) between the two pistons during the uniaxial compression step (a), characteristically broken $V_2O_5@CNF/Al$ pellet with a piece adhering to the upper piston (b); macro photograph of a broken pellet (c).

accompanied by a very bright, orange flame – much brighter than for the manganese oxide thermites. Figure 6.17 shows representative timeline images of one pellet for each compression level. The total burning durations do not directly correlate with the velocity, as some of the pellets (specifically the one in Figure 6.17b) are just pieces of broken pellets. Like in the $MnO_x@CNF/Al$ thermites, the pellets expand significantly in the propagation direction of the combustion front. The residues are mostly found intact, although some strongly fissured pellets (like the one in Figure 6.17a) break apart along the fissure during the combustion, which is visible in the timeline images, specifically Figure 6.17a, where a part on the left side breaks off during the combustion.

The results of a quantitative analysis of the combustion front position for these pellets are shown in the graph in Figure 6.19. They show a linear progression of the combustion front, and the linear regressions all have R^2 values between 0.95 and 0.98. Curiously, the dependency of the velocity on the forming pressure is not monotonous, with the 99 MPa pellets slightly slower than the ones pressed at 210 MPa, although the difference is probably not statistically significant. Taking into account the uncertainty of the measurement, the combustion velocity is about the same.

The combustion residues of one V_2O_5/Al nanothermite pellet are shown in Figure 6.20a. They closely resemble the ones achieved in the case of the $MnO_x@CNF/Al$ nanothermites (Figure 6.11). The same cigarette-like combustion leads to the same final morphology. Both pellets are strongly expanded along the combustion direction, while the lateral dimension stays the same. The pellets are whitish yellow on the outside and brown to black on the inside. The X-ray diffractogram of the collected, ground combustion residues (Figure 6.21a) shows that the redox reaction did not result in the formation of metallic vanadium, unlike in the case of the manganese oxide-based thermites. However, there are no more traces of vanadium(V) oxide, which means that the oxide has completely reacted. The oxide has been reduced mostly to the +IV and +III oxidation states, i. e. VO_2 and V_2O_3 . A large quantity (judging from the peak intensities) of the vanadium has reacted with the carbon nanotubes, forming cubic vanadium carbide V_8C_7 , which is indicated by

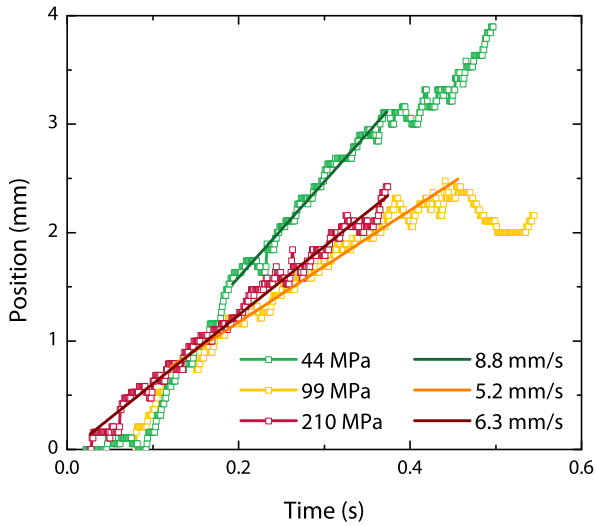


Figure 6.19 Propagation of the combustion front in $V_2O_5@CNF/Al$ nanothermite pellets, determined by analysis of timeline images, and corresponding linear regressions for finding the combustion velocity v .

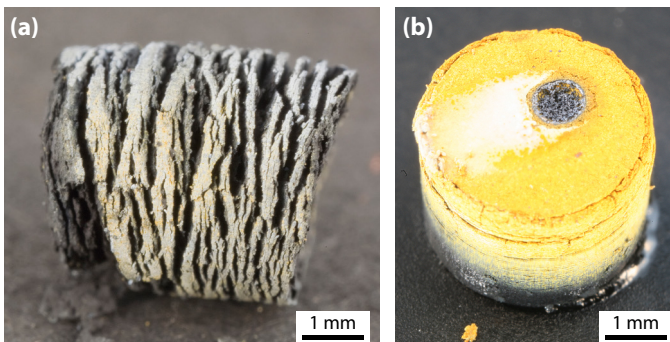


Figure 6.20 Macro photographs of the combustion residue for the $V_2O_5@CNF/Al$ nanothermite (a) and for the same formulation using annealed $VO_2@CNF$ (b).

a blue C in the figure. The graphite reflections, especially the (002) at $2\theta = 26.54^\circ$, are still visible, which means that the nanofibers are not completely destroyed by the combustion; we showed the same behavior for the other thermites earlier. The aluminum is completely converted to α - and γ - Al_2O_3 .

“Annealed” product. In the V_2O_5 -filled carbon nanofiber composite, the vanadium oxide is contained as a foam inside the CNFs. A foam contains trapped gas bubbles, which can be released during the combustion of the nanothermite. This could be the reason for the expansion of the V_2O_5 @CNF/Al pellets during their combustion. To explore the effect further, we prepared another nanothermite, in which the vanadium-oxide filled CNFs had been annealed at 700°C for 1 h under argon prior to mixing them with the aluminum nanoparticles. Thus, “annealed” does not refer to the nanothermite directly but to the nanocomposite from which they have been prepared.

As explained in section 5.4.2,⁵ the composite is essentially VO_2 @CNF. Compared to the non-annealed nanothermite, the combustion behavior is different and quite peculiar. The ignition delay times (Table 6.2) are in the range of 12–16 ms, which is much higher than for the non-annealed thermite; correspondingly, the activation energy is approximately twice as high. The IDT is in the same range as for the fuel-rich MnO_x @CNF/Al nanothermite; indeed, as the oxide is less oxygenated, it seems that we are also in fuel-rich conditions.

Contrary to all other nanotube-containing nanothermite formulations investigated in this chapter, the VO_2 @CNF/Al nanothermite pellets do not expand during their combustion, they keep their form perfectly. Figure 6.20b shows a pellet after combustion. Its original form is intact, only the bright yellow color shows that it has reacted. The reaction stopped somewhere in the middle of the pellet, as the lower part is still black. At the spot where the laser impacted on the pellet, there is a small crater, similar to the pellet in Figure 6.6 (which is not a nanothermite though as it does not contain any aluminum). Figure 6.22 shows a timeline image of the combustion of a typical “annealed” pellet. During the first two seconds, the pellet is illuminated with a focused 7 W CO_2 laser. The only effect that this has is to heat up the zone immediately around the impact, indicated by a white glow. Only when the laser is switched off does the solid-state reaction start. It seems very gentle and develops less heat than in the case of the “normal” V_2O_5 @CNF/Al nanothermite; the reddish-orange glow observed in the reaction zone corresponds to an estimated reaction temperature of about 700 – 900°C , while the white hot residues in the other thermite have an estimated temperature of at least 1200°C .

Curiously, while the thermite before the combustion contained almost no vanadium(V) oxide according to X-ray diffraction, the combustion residues (Figure 6.21b) do contain significant amounts of this oxide in addition to the other phases found in the V_2O_5 @CNF/Al nanothermite. This means that the oxidation state of some of the vanadium oxide has actually increased during

⁵Page 120ff.

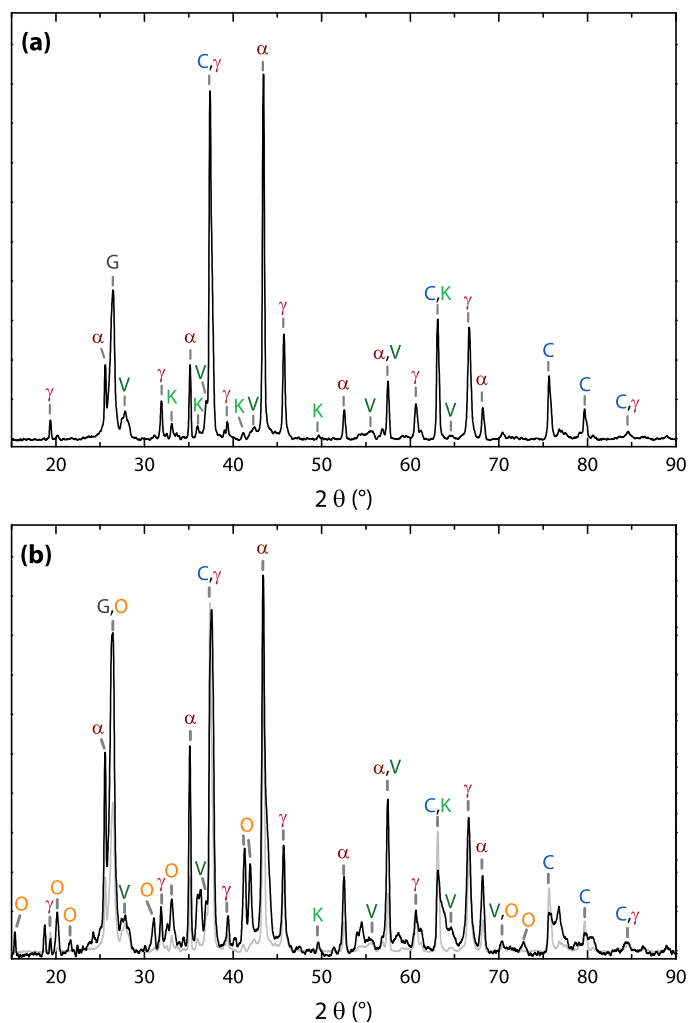


Figure 6.21 X-ray diffractogram of the combustion residues of the V_2O_5 @CNF/Al nanothermite (a) and of the same formulation using annealed VO_2 @CNF (b). The annotated phases are Graphite (56-159, **G**), vanadium(IV) oxide (44-252, **V**), Karelianite (vanadium(III) oxide, V_2O_3 , 34-187, **K**), vanadium carbide (V_8C_7 , 35-786, **C**), Corundum (α - Al_2O_3 , 10-173, α) and γ - Al_2O_3 (50-741, γ), plus Shcherbinaite (vanadium(V) oxide, V_2O_5 , 41-1426, **O**) for b. The diffractogram from subfigure a is in light grey in subfigure b for reference.

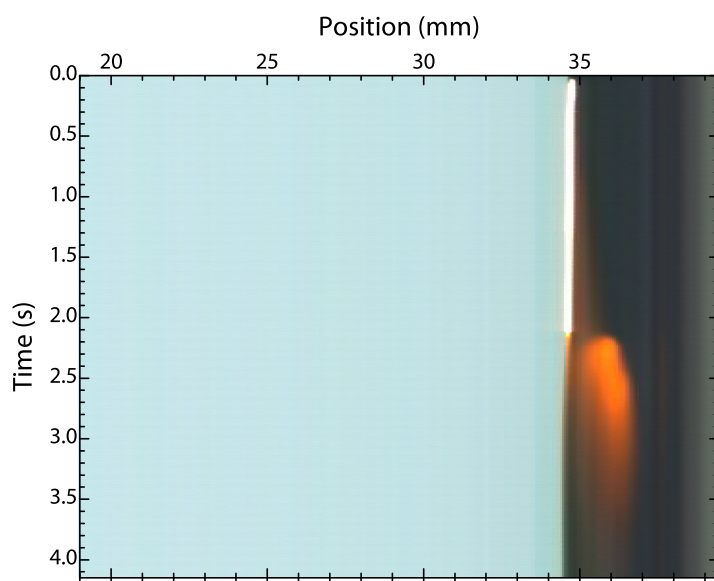


Figure 6.22 Timeline image of the combustion of a pellet containing annealed $V_2O_{5-y}@CNF/Al$, compressed at 99 MPa. Note that the laser is only active during the first 2.0 seconds.

the reaction! We attribute this to a reaction with the oxygen from the air at the surface of the pellets during their combustion. In any case, this would explain the bright yellow color of the combustion residues (Figure 6.20b), which could be a mixture of vanadium(V) oxide (orange-yellow) and aluminum oxide (white). No reflections due to metallic aluminum are found in the X-ray diffractogram of the combustion residues, meaning that all of the Al 50 P reacted during the nanotube combustion; the partially reacted pellets were cut and only the yellow part was investigated by XRD. It is likely that some of the aluminum burned with the help of oxygen from the atmosphere.

To conclude, while this experiment showed that the annealing of the oxide-filled CNTs does prevent the expansion of the nanothermite pellets during their combustion, it is still not clear why. This thermite, compared to the other vanadium oxide-based one, has a lower mean oxidation state of the vanadium, which in turn lowers the reaction velocity and temperature. Furthermore, gas bubbles that were trapped in the V_2O_5 foam structure have been released by the annealing treatment, which also increased the particle size of the oxide.

6.5 Phosphorus-based nanothermites: $CuO@CNF/P$

We prepared a phosphorus-based nanothermite from copper(II) oxide-filled herringbone carbon nanotubes ($CuO@CNF/P$) in order to evaluate the difference in reactivity and sensitivity to the pure CuO/P nanothermite mixture without carbon nanotubes. Like in the case of CuO/P , the formulation was mixed in *n*-hexane according to procedure A (section 3.2). The proportions were

chosen to be slightly richer in fuel, with a 50% excess of phosphorus (1.5 times the stoichiometric amount for reaction (6.4)). The formulation consists of

- ▶ 90.0 wt-% of CuO@CNF, containing 48.3 wt-% of copper oxide and
- ▶ 10.0 wt-% of red phosphorus.

The sensitivity thresholds for this formulation are given in the bottom line of Table 6.1. The CuO@CNF/P nanothermite is completely insensitive against both impact and friction (thresholds of > 49 J and > 360 N respectively) and 300 times less sensitive to electrostatic discharges. This is an impressive decrease in sensitivity.

The combustion behavior of the CuO@CNF/P nanothermites was investigated by a TRC experiment using a 7 W CO₂ laser for the ignition of pellets compressed at 44, 99 and 210 MPa. The ignition delay times (IDT), given on the bottom of Table 6.2, are very similar to the ones for the MnO_x@MWNT/Al thermite; this suggests that the laser illumination of the CuO@CNF/P nanothermite first leads to heating of the nanotubes, whereupon the reaction starts when enough heat has been transported by diffusion into the core of the pellet. This is different from the initiation mechanism for CuO/P and is one of the reasons for the desensitization. The combustion timeline for a pellet that was compressed at 99 MPa is shown in Figure 6.23, along with selected screenshots from the combustion video. The bright area on the left side is just the spot that is directly hit by the laser, the propagation of the reaction itself is not accompanied by any visible flame. Again, this is different than in the case of CuO/P, where a bright flame was visible. The absence of light at the combustion front means that the combustion velocity cannot be determined by the method we used for the other nanotube-containing thermite formulations. We can only make a rough estimation by evaluating the time for a complete combustion of the pellet. According to this estimation, the combustion velocity is in the range of 3.5–5 mm/s for a pellet compressed at 99 MPa, which is similar to the other nanotube-containing formulations.

During the combustion, the pellet expands in a similar fashion as for the MnO_x@CNF/Al and V₂O₅@CNF/Al nanothermites. The combustion residues stay in this expanded form, as seen in Figure 6.24b. At several points in the photo, the typical color of metallic copper can be distinguished, showing that Cu(0) was formed by the combustion. The X-ray diffractogram of the collected and ground combustion residues (Figure 6.24a) shows a very large number of reflections, which is why not all reflections for all found phases were indicated in the graphic. The phases which were identified are copper metal and CuO, copper phosphates (Cu(PO₃)₂ and Cu₂P₂O₇) and two copper phosphide phases (CuP₂ and Cu₂P₇). This is similar to the results obtained with CuO/P, with one important exception: during the combustion of CuO/P in air, the phosphides react with oxygen from the air to form phosphates in a secondary reaction. This reaction does not happen in the case of the nanotube-containing thermite here. This is attributed to the fact that the carbon is a reducing agent, which prevents the secondary oxidation. This can also explain

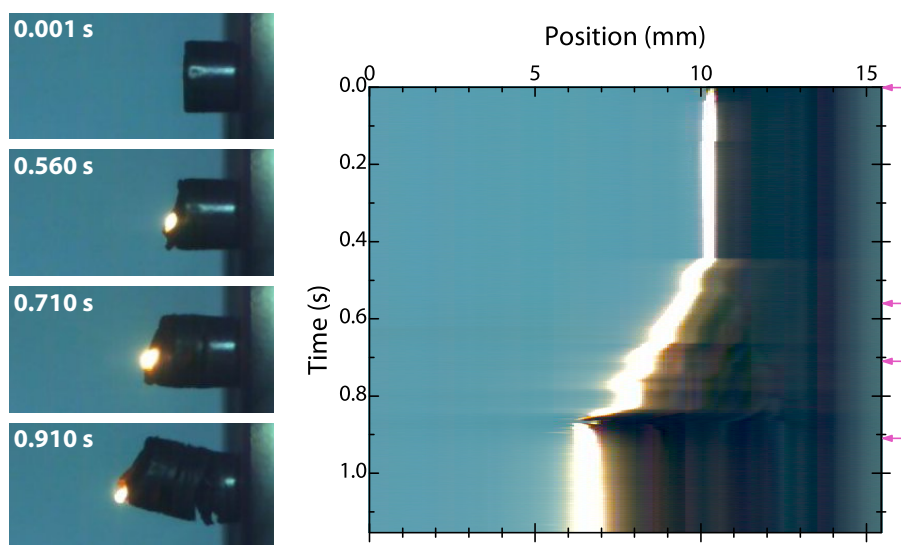


Figure 6.23 Selected screenshots from the combustion of a CuO@CNF/P pellet compressed at 99 MPa (left); timeline image of the combustion (right), the pink arrows indicate the time at which each screenshot was taken.

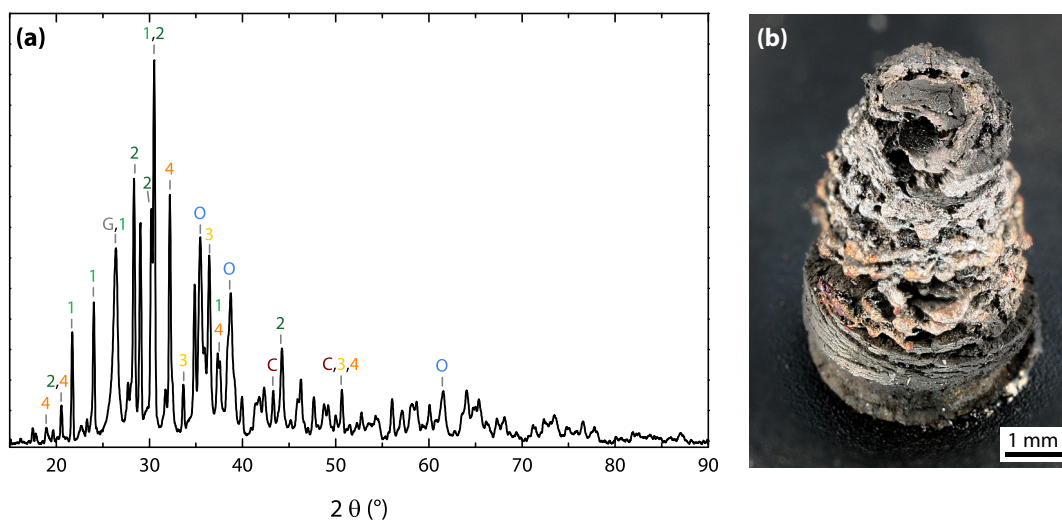


Figure 6.24 X-ray diffraction of the combustion residue of CuO@CNF/P pellets (a); photo of an intact pellet residue after the combustion, showing the typical color of copper metal (b). Due to the large number of peaks, not all reflections have been indicated for each phase. The indicated phases are graphitic carbon (G, JPCDS file 56-159), copper metal (C, 4-836), copper(II) oxide (tenorite, O, 48-1548), copper phosphate $\text{Cu}(\text{PO}_3)_2$ (1, 29-572), copper pyrophosphate $\text{Cu}_2\text{P}_2\text{O}_7$ (2, 44-182), copper phosphide CuP_2 (3, 18-452) and copper phosphide Cu_2P_7 (4, 47-1566).

the absence of a flame; the flame is associated with the burning of phosphorus in air, which is prevented by the presence of large amounts of carbon, which creates a reducing environment.

6.6 Conclusion of this chapter

In this chapter, we investigated three fuel/oxidizer (“nanothermite”) systems – manganese oxide/aluminum, vanadium oxide/aluminum, copper oxide/red phosphorus – and compared “classical” nanoparticle mixtures with nanothermite formulations containing filled and unfilled carbon nanotubes. All the nanotube-containing formulations have a strongly reduced sensitivity to mechanical stress (notably an absence of friction sensibility) and electrostatic discharges. However, the spatial separation between oxidizer and fuel, induced by the use of filled CNTs, also slows down the combustion. Formulations in which empty nanotubes are mixed with the oxidizer and the fuel in the form of nanoparticles burn faster but are more sensitive to impact stress. The vanadium(V) oxide-based formulations burn faster and with a higher temperature than the ones based on manganese oxide. The CuO@CNF/P nanothermite burns without a visible flame.

Chapter 7

Conclusion

In this work, we show how the incorporation of metal oxide-filled carbon nanotubes lowers the sensitivity of nanothermite mixtures. The results are presented in three steps – opening, filling, pyrotechnical use – that build on one another. The opened and functionalized CNTs are the basis for the filling reactions, and the filled nanotubes are the basis for the reduced-sensitivity nanothermite formulations.

7.1 Opening of carbon nanotubes

In chapter 4, after characterizing four different CNT types bought from commercial suppliers, we investigated the effects of different oxidation treatments on two forms of carbon nanotubes, MWNT and CNF.

When the CNFs are heated in concentrated nitric acid, the graphitized “overlayer” that forms the outside surface of the nanotube is partly detached from the inner herringbone structure. At the same time, the inside surface of the CNFs, which consists of graphene edges, is functionalized with oxygen-containing functional groups. Furthermore, the mean length of each fiber decreases by the exfoliation of two adjacent herringbone layers. Presumably, this is due both to the effect of the nitric acid, which can intercalate between two graphitic layers, and to the mechanical stress when stirring the suspension for a prolonged time.

Mild oxidation treatments of MWNT are able to open their closed ends, as they are able to exploit the small reactivity difference between pentagons and hexagons in the graphitic structure; the pentagons induce a positive curvature, five of them form an end cap. Three types of treatment were presented:

- ▶ heating with concentrated oxidizing acids (especially HNO_3),
- ▶ isothermal oxidation in air at different temperatures and
- ▶ filling with KOH.

For each type of treatment, we tried to find the typical damage pattern in the structure of the MWNTs from TEM observations of the most strongly damaged samples. The specific surface

area S_{BET} was used to estimate the percentage of opened carbon nanotubes; as soon as one of the ends is opened, the inner surface of the tube becomes accessible for the nitrogen molecules, which increases the value of S_{BET} . From the Raman spectra, we were able to gather information on the degree of damage to the graphitic lattice and on eventual n or p doping, by looking at the fitted area A_{D} of the D peak, at peak widths or positions.

Regarding thermal oxidation, we found that the velocity of this reaction has an Arrhenius-type dependency on the temperature, which allows determining the activation energy E_A of the reaction. We found a value of (114 ± 2) kJ/mol, which is much lower than the value of about 225 kJ/mol found by Ajayan *et al* on arc-discharge MWNTs. As the arc-discharge process takes place at much higher temperatures than the CVD synthesis, CVD nanotubes have a higher amount of defects in their graphitic lattice. This means that the activation energy for thermal oxidation is a measure for the number of defects in the graphitic lattice, similar to the oxidation temperature T_o .

Filling with KOH is an original method for opening MWNTs, which has been developed in this work. The nanotubes are mixed with solid KOH, and the mixture is heated to 400°C, melting the hydroxide. After cooling and washing the excess with water, the product still contains KOH filled into the tubes or intercalated between the layers. Nickel hydroxide, from the reaction of the crucible wall, is also found. Washing with HCl removes the hydroxides and the residual catalyst particles, which are made of cobalt. This product contains 2.5 wt-% of oxygen in surface functional groups. Finally, the product can be annealed at 950°C under argon in order to remove these functional groups (defunctionalization) and to lower the oxygen content to its initial value of about 0.8 wt-%.

Finally, we saw that MWNTs can be opened under extremely mild conditions by leaving them in 2.3 M aqueous KOH solution for long times of up to a week. While these treatments increase the specific surface area (indicating that the ends have been opened), they have remarkably little incidence on the Raman spectra, which means that they do not significantly damage the graphitic lattice.

7.2 Filling of carbon nanotubes with metal oxides

In chapter 5, we presented the filling of different types of carbon nanotubes with four metal oxides:

- ▶ manganese oxide,
- ▶ chromium(III) oxide,
- ▶ vanadium(IV) and (V) oxide and
- ▶ copper(II) oxide.

We used metal nitrates as precursors, except in the case of vanadium, where the precursor was an ammonium salt. All the precursor salts used decompose when heated to form the corresponding metal oxide.

Three techniques were used for infiltrating the precursor into the nanotubes: infiltrating opened nanotubes with a molten salt (for manganese nitrate) or with an aqueous solution; or infiltrating the as-received nanotubes with a solution of the metal nitrate in nitric acid. This last method reacts with the nanotube ends to open them and fills the inner cavities at the same time, which is why we called it “reactive infiltration”.

The maximum amount of metal oxide for completely filled CNTs was determined by a simple geometrical calculation. Despite their different sizes, all the types of carbon nanotubes employed in this work – SWNT, DWNT, MWNT and herringbone nanotubes – have similar ratios of the inner and the outer diameter, which leads to similar maximum metal oxide loadings. Because there is always a diameter distribution, a pessimistic and an optimistic estimate were given. We found that for all nanotube types, the maximum loading of manganese oxide, whose density is 5.1, is on the order of 20–60 wt-%.

In practice, we found that as a rule, larger nanotubes are easier to fill. The best filling yields were thus consequently achieved for the filling of the “Pyrograf” herringbone nanotubes ($\text{MO}_x\text{@CNF}$). Larger nanotubes do not necessarily mean larger metal oxide particles. In the case of $\text{MnO}_x\text{@CNF}$, for instance, the oxide particles are much smaller (about 10–20 nm) than the cavity of the nanotube (about 40 nm) and stick to the CNF walls. We attributed this to the fact that the inner surface of the wall is strongly functionalized with oxygen-containing groups (such as $-\text{COOH}$), which act as “anchoring points” for the nitrate – by the formation of metal carboxylates – and for the oxide after calcining. In the case of $\text{V}_2\text{O}_5\text{@CNF}$, the vanadium oxide formed a foam structure in which gas bubbles, presumably of the gases developed during the precursor deposition, were trapped. These foams recrystallized under the electron beam in the TEM, leading to larger crystals. On the other hand, copper(II) oxide formed large crystals that occupy the entire cavity in the CuO@CNF nanocomposites. These crystals show well-developed facets and have a typical size of about 40 nm. It should be noted that according to the literature, the preparation of copper oxide-filled nanotubes by infiltrating copper(II) nitrate does not work; we show this affirmation to be incorrect.

In each case, the evidence for a successful experiment, i. e. a non-zero filling yield, was found by TEM observation. However, in the lower magnification images, which were recorded at 80 kV of acceleration voltage, it is easy to confound carbon particles (amorphous carbon or debris from the nanotube walls) with genuine oxide filling. Thus, we only took TEM micrographs where the filling appeared darker than the carbon walls into account. In most cases, to fully confirm the identity of the endohedral particles, we looked at the lattice fringes on HRTEM micrographs or at energy-dispersive X-ray spectra, in which the metals give characteristic peaks.

X-ray diffraction and Raman spectroscopy also allow to get information about the oxides, especially about the oxidation state of the metal. Most of the oxides in the nanocomposites are

oxygen-deficient. The smallest oxygen deficiency was found in the CNF composites. As these composites also contain the lowest amount of exocrystallized metal oxide, there seems to be a correlation between the oxygen deficiency and the ratio of metal oxide *outside* and *inside* the nanotubes: the higher this ratio, the more under-oxygenated the oxide. This can be seen very well by comparing for example the $\text{MnO}_x\text{@DWNT}$ product ($x \approx 1.6$) to $\text{MnO}_x\text{@CNF}$ ($x \approx 1.9$).

A possible explanation for this phenomenon comes from the decomposition mechanism of the nitrates in combination with the *confinement*. The decomposition of the nitrate usually produces stoichiometric amounts of nitric acid (and/or NO_x). The nitric acid is confined inside the cavity, and the pressure builds up. The boiling point of the acid is increased because of the pressure, and the oxide formation happens in “pseudo-hydrothermal”, oxidizing conditions. The CNT cavity acts in effect as a nanoreactor.

The most interesting products prepared in this chapter were used for the next step: the preparation of reduced-sensitivity nanothermites.

7.3 Reduced-sensitivity nanothermites containing carbon nanotubes

In chapter 6, we investigated reduced-sensitivity nanothermites in the manganese oxide/aluminum, vanadium oxide/aluminum and copper oxide/phosphorus redox systems. There are two types of nanotube-containing formulations: those where the oxidizer (the metal oxide) is replaced by metal-oxide filled CNTs – which is the basic idea behind this work – and two formulations that consist of fuel and oxidizer nanoparticles physically mixed with empty CNTs (MWNT/ MnO_2/Al and CNF/ MnO_2/Al).

For MnO_2/Al and CuO/P , reference compositions that do not contain CNTs were described in recent articles from our laboratory. Both of these are highly sensitive and hazardous materials, especially regarding their friction and electrostatic discharge (ESD) sensitivity. These are in the range of primary explosives, while CuO/P is even one of the most highly ESD-sensitive materials known.

In comparison, the nanotube-containing formulations have a strongly reduced sensitivity; all of them are insensitive to friction (threshold > 360 N). The electrostatic discharge sensitivity was also reduced by more than one order of magnitude, which is likely due to the fact that the carbon nanotubes are relatively good electrical conductors. The discharge can quickly pass through percolation paths without creating a high amount of hot spots. The impact sensitivity is also reasonable in the nanotube-containing formulations. Some of the manganese oxide-based formulations are more sensitive to impact stress than the pure MnO_2/Al , notably the physically mixed nanothermites. We explained this phenomenon by a concentration of the stress at certain points (“hot spots”); for instance, the contact surface of two crossed cylinders is very small. If a fuel and

an oxidizer particle are confined between two crossed nanotubes, the force of the impact will be concentrated in one point, initiating the decomposition more easily.

For assessing their performance, the nanothermites were compressed into pellets at three different compression levels (44, 99 and 210 MPa). The pellets were ignited by a CO₂ laser, and the combustion was recorded using a high-speed camera and an oscilloscope. This experiment, called TRC, allows to determine the ignition delay time (IDT) and consequently the activation energy E_A , as well as the combustion velocity v . The latter is determined from the high-speed videos (1000 frames per second in our experiments); we developed an original technique using two programs (given in the appendix) to create $x-t$ diagrams, which we call “timeline” images. Each line in the timeline image shows the same location at a given time. The pellet is always on the right, the laser strikes from the left side. The combustion front can be easily seen by the light output from the reaction. The timeline technique allows to recognize a variety of phenomena, for example the parabolic rate law of MnO₂/Al pellets or the back-and-forth oscillation of the combustion front for MnO_x@CNF/Al and V₂O₅@CNF/Al. It also allows to determine the mean combustion velocity by linear regression of the combustion front position $x = f(t)$.

During their combustion, the nanothermites containing filled CNF expand along the combustion direction – similar to an accordion – but not perpendicular to it. We attributed this to the high structural cohesion of the CNF-containing pellets over a length scale of several tens of micrometers. On the other hand, the MWNTs tend to entangle into smaller aggregates which are harder to break up (thus giving an inhomogeneous composition) and not connected to one another, behaving essentially as spherical, micron-sized entities.

Compared to the “reference systems”, the combustion of the reduced-sensitivity thermites is much slower. In the case of MnO₂/Al, the velocity is reduced from almost 1 m/s to a value between 3 and 15 mm/s. This strong reduction is due to the high amount of carbon, which is pyrotechnically almost inert. The carbon content of most of these thermites is on the order of 40 wt-%, considerably “diluting” the pyrotechnical reaction. The physically mixed composition, in which all the reactants are on the outside of the CNTs, burns three to five times faster than the compositions using manganese oxide-filled CNTs. This is because the spatial separation of oxidizer and fuel, as beneficial as it is for reducing the sensitivity, makes the redox reaction even more difficult.

Comparing the different metal oxides, the vanadium(V) oxide-based nanothermite formulations burn faster and reach higher temperatures, as shown by the very bright flame. On the other hand, the CuO@CNF/P nanothermite burns without any visible flame.

7.4 Perspectives

The metal oxide-filled carbon nanotubes presented in this work are not only interesting in the context of fuel/oxidizer mixtures. Manganese and vanadium oxides can easily change their oxidation state, which means that these nanocomposites could be used as electrochemical pseudocapacitors. There has been research on these composites, notably with MnO_2 [199, 200], which showed that high energy storage densities can be obtained. V_2O_5 @CNF composites are also possible materials for applications in nonlinear optical limitation.

For these alternative applications, it is important to find a way to *selectively remove the metal oxide outside the CNT cavities*. We had some limited success with rapidly washing the composites with HCl in a vacuum filtration apparatus, so that the acid is only in contact with the material for a few seconds. Such techniques merit further research; preparing a nanothermite from such a material (ideally without any exohedral oxide) should allow to determine whether the ignition of these mixtures always starts from exohedral oxides, and to understand the reaction mechanism better. It would also be conceivable to prepare nanothermite formulations containing oxide-coated instead of filled nanotubes.

The high carbon content of the nanotube-containing nanothermite formulations (on the order of 40 wt-%) seriously impacts their energetic performance, especially their combustion velocity. It is thus important to find a way to increase the oxide loading even further, in order to obtain nanocomposites containing more than 60 wt-% of metal oxide. There are two ways to obtain a higher loading:

- ▶ Reduce the number of empty nanotubes, by doing multiple infiltrations or by physically separating the empty CNTs from the filled ones. The separation could be done by density gradient ultracentrifugation (DGU) based on the different densities of filled and unfilled nanotubes.
- ▶ Use nanotubes with thinner walls and a large cavity, for example Pyrograf PR-25, which have the same 40 nm cavity as the PR-24 type we used in this work but a lower outer diameter D .

The slower combustion of the reduced-sensitivity nanothermite formulations presented in this work burn does not mean that these products are useless. There are applications, such as pyrotechnical delay compositions, where the low velocity can actually be beneficial. There is an actual industrial need for new delay formulations. Nonetheless, these applications need highly tunable, reproducible ignition delays and combustion velocities, thus demanding a highly homogeneous composition of the material.

Appendix

Appendix A

Software

A.1 An algorithm for calculating atomic positions in carbon nanotubes

The chirality and the diameter of a carbon nanotube are unambiguously defined by a pair of integers (n_1, n_2) describing a roll-up vector

$$\mathbf{R} = n_1 \mathbf{R}_1 + n_2 \mathbf{R}_2$$

in the graphene lattice plane. A detailed description was given in section 2.1.

The application of trigonometric relations leads to the following numerical values for the two primitive vectors, with L being the C–C bond length (142 pm):

$$\mathbf{R}_1 = \begin{pmatrix} \sqrt{3}L \\ 0 \end{pmatrix}; \quad \mathbf{R}_2 = \begin{pmatrix} \frac{\sqrt{3}}{2}L \\ \frac{3}{2}L \end{pmatrix} \quad (\text{A.1})$$

The paper by White, Robertson, and Mintmire [8] proposes an easy algorithm for finding the atomic positions in a carbon nanotube. First, the two carbon atoms at

$$\mathbf{d} = \frac{\mathbf{R}_1 + \mathbf{R}_2}{3}$$

and $2\mathbf{d}$ (highlighted in Figure 2.2 on page 4) are mapped on the cylinder surface. Two symmetry operations are then carried out:

- ▶ a C_N axis, where N is the largest common divisor of n_1 and n_2 and
- ▶ a $\mathcal{S}(h, \alpha)$ screw operation, which allows tiling the helical motif along the length of the nanotube. Armchair nanotubes with $n_2 = 0$ have an easy solution with $h = 3L/2$ and $\alpha = \pi/N$ radians. For the other cases, a vector

$$\mathbf{H} = p_1 \mathbf{R}_1 + p_2 \mathbf{R}_2$$

with minimal indices $p_1 \geq 0$ and p_2 must be found so that

$$p_2 n_1 - p_1 n_2 = \pm N.$$

We then have

$$\alpha = 2\pi \frac{\mathbf{H} \cdot \mathbf{R}}{\mathbf{R}^2}$$

and

$$h = N \frac{|\mathbf{R}_1 \times \mathbf{R}_2|}{|\mathbf{R}|}.$$

A.1.1 Implementation in Limbo under Inferno

The algorithm described above has been successfully implemented in a Limbo program. In order to understand the program code, it is necessary to give a very short introduction into the language.

Limbo is the native programming language of the Inferno operating system, which has been created by many of the same people who wrote UNIX in the 1970s. Inferno is free software and can run either directly on the hardware or under a host operating system (such as Windows, Mac OS, or Linux) in a virtual machine called *dis*.

Limbo shares many similarities with the C programming language, while the variable declarations resemble Pascal (variablename: typename). Comments start with a #. The code is organized into *modules*. Functions in other modules are called via modulename→function, the arrow being typed as ->. Execution starts at the init function, which is given the command line arguments in a variable argv. There are two types of assignment: variable = value just assigns a value, while variable := value initializes and declares the variable with the correct type. Tuples—such as the return value from the solve_p1p2() function below—, lists, and arrays are first-class data types. Only two operations are possible on lists: **hd**, which gets the first element, and **tl** (for tail), which gets everything but the first element. The operator :: constructs a list. All casts (change of variable type) are explicit; for example **real hd** argv converts the first element of argv to a floating-point value.—

Vectors are implemented in the program as an **array of real**, i. e. an array of floating-point numbers. The Math module already provides the dot function to calculate the scalar product; scaling, addition, and the cross product are implemented in the Vector module shown here.

The program uses two types of vectors: three-dimensional cartesian coordinates (x,y,z) and cylinder coordinates. The latter are represented as two-dimensional vectors (φ,z) ; the radius r is always the same because all points lie on a cylinder surface. This choice of coordinates makes rotations and translations along the cylinder axis trivial.

The init routine reads the command line arguments (see below) and calls the calc_nanotube with these values. It first determines the values of the vectors \mathbf{R}_1 , \mathbf{R}_2 , \mathbf{R} , \mathbf{d} as well as the radius r and the values for h and α . The very first point can be on an arbitrary position, thus $(\varphi = 0, z = 0)$ is

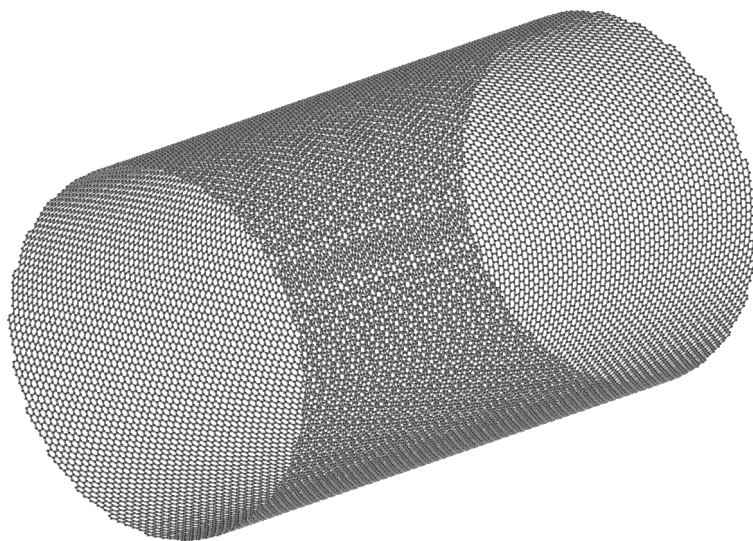


Figure A.1 Ball-and-stick model of a chiral (125,25) carbon nanotube; its length is 20 nm and its diameter about 10.7 nm. Image created using OpenRasmol.

the logical choice. The position of the second point is stored in a variable `tmp` for later use. The heart of the algorithm is the double `for` loop below. The outer loop corresponds to the N -fold rotational axis while the inner loop represents the helical symmetry operation. In each iteration, the two points undergo i rotations and j helical operations, after which they are prepended to the list containing all calculated point positions.

The output is done in the `.xyz` format, originally introduced by the XMol program. The format is really extraordinarily simple. The first line of the file contains the total number of atoms in the molecule. The second line contains a descriptive text, which includes the indices, the radius, and the length in this program. All other lines contain four columns: the first one is the element symbol (always C for us), the other three are the x , y , and z positions in Ångströms with five decimal places.

Usage. The compiled program can be called with either two or three arguments. The first two are the indices n_1 and n_2 . The third, optional argument is the desired length of the nanotube, determining the number of times the $\mathcal{S}(\alpha, h)$ screw operation is carried out. The output can be written to a file like this:

```
nanotube 12 0 > output.xyz
```

For the graphical visualization, a range of different molecule viewers can be employed. OpenRasmol is free and available on most platforms. As it has been designed for peptides, it copes

very well with large numbers of atoms. The (125,25) nanotube with 10.7 nm diameter and 20 nm length shown in Figure A.1, for instance, contains 26550 carbon atoms.

A.1.2 The source code

A.1.2.1 vector.m

```
1 # $Id: /mirror/These/trunk/limbo/vector.m 405 2009-10-07T07:42:51.822266Z SIEGERT $
2 #
3
4     vec: type array of real;
5
6 Vector: module {
7     PATH: con "/n/limbo/vector.dis";
8
9     scale: fn (a: real, v: vec): vec;
10    add: fn (v1: vec, v2: vec): vec;
11    xprod3: fn (v1: vec, v2: vec): vec;
12    cyl2vec: fn(radius, phi, z: real): vec;
13 };
```

A.1.2.2 vector.b

```
1 # $Id: /mirror/These/trunk/limbo/vector.b 405 2009-10-07T07:42:51.822266Z SIEGERT $
2 #
3
4 implement Vector;
5
6 include "vector.m";
7 include "math.m";
8
9     m: Math;
10
11 # multiply with a scalar
12 scale(a: real, v: vec): vec
13 {
14     rv := array[len v] of real;
15     for (i := 0; i < len v; i++)
16         rv[i] = v[i] * a;
17     return rv;
18 }
19
20 # add two vectors
21 add(v1: vec, v2: vec): vec
```

```

22 {
23     rv := array[len v1] of real;
24     for (i := 0; i < len v1; i++)
25         rv[i] = v1[i] + v2[i];
26     return rv;
27 }
28
29 # cross product for three dimensions
30 xprod3(v1: vec, v2: vec): vec
31 {
32     # (a2*b3 - a3*b2, a3*b1 - a1*b3, a1*b2 - a2*b1);
33     return array[3] of {
34         v1[1]*v2[2] - v1[2]*v2[1],
35         v1[2]*v2[0] - v1[0]*v2[2],
36         v1[0]*v2[1] - v1[1]*v2[0]
37     };
38 }
39
40 # convert cylinder coordinates to cartesian coordinates
41 cyl2vec(radius, phi, z: real): vec
42 {
43     if (m == nil)
44         m = load Math Math→PATH;
45
46     return array[3] of {
47         radius * m→cos(phi),
48         radius * m→sin(phi),
49         z
50     };
51 }

```

A.1.2.3 nanotube.b

```

1  # $Id: /mirror/These/trunk/limbo/nanotube.b 700 2010-07-15T13:10:07.570572Z SIEGERT $
2  #
3
4  implement Nanotube;
5
6  include "sys.m";
7  include "draw.m";
8  include "math.m";
9  include "vector.m";
10
11 # modules used by this program

```

```
12     sys: Sys;
13     m: Math;
14     vector: Vector;
15
16 # constants
17     bondlen: con 1.42; # Angstroms
18
19 Nanotube: module {
20     ggt: fn (a, b: int): int;
21     solve_p1p2: fn(n1, n2: int): (real, real);
22     calc_nanotube: fn(n1, n2: int, nt_length: real);
23     init: fn (nil: ref Draw→Context, argv: list of string);
24 };
25
26
27 # find the largest common divisor of a and b
28 ggt(a, b: int): int
29 {
30     i, min: int;
31
32     if (a < b)
33         min = a;
34     else
35         min = b;
36
37     for (i = min; i > 0; i--) {
38         if ((a % i) == 0 && (b % i) == 0)
39             break;
40     }
41
42     if (i == 0)
43         return a;
44     else
45         return i;
46 }
47
48 # solve "p2n1 - p1n2 = N"
49 solve_p1p2(n1, n2: int): (real, real)
50 {
51     p1, p2: int;
52
53     # shortcut path
54     if (n2 == 0)
55         return (0.0, 1.0);
```

A.1 An algorithm for calculating atomic positions in carbon nanotubes

```

56
57     N := ggt(n1, n2);
58     for (p1 = 1; ((p1*n2 + N) % n1) != 0; p1++);
59     p2 = (p1*n2 + N) / n1;
60
61     return (real p1, real p2);
62 }
63
64 # do the actual calculation of a (n1, n2) nanotube with a length
65 # of nt_length nm
66 calc_nanotube(n1, n2: int, nt_length: real)
67 {
68     R1, R2: vec; # the unit vectors
69     R: vec; # the resulting chiral vector, i.e. n1*R1 + n2*R2
70     radius: real; # the radius of the nanotube
71     points: list of vec = nil; # calculated atomic positions, in cylinder coordinates
72                               # (phi and z, the radius is always the same)
73     num: int = 0; # number of points
74     N: int; # largest common divisor of n1 and n2
75     h, alpha: real; # angle and translation for the helical symmetry operator
76
77     # initialize the basic vectors of the coordinate system,
78     # of which n1 and n2 are the multiples
79     R1 = array[] of {m→sqrt(3.0) * bondlen, 0.0, 0.0};
80     R2 = array[] of {m→sqrt(3.0)/2.0 * bondlen, 1.5 * bondlen, 0.0};
81     R = vector→add(vector→scale(real n1, R1), vector→scale(real n2, R2));
82
83     radius = m→sqrt(m→dot(R, R)) / 2.0 / m→Pi;
84     N = ggt(n1, n2);
85
86     # the first two points are easy. The first is (phi = 0, z = 0),
87     # the second is stored in tmp for access later:
88     d := vector→scale(1.0/3.0, vector→add(R1, R2));
89     dR := vector→xprod3(d, R); # d x R
90     tmp := array[2] of {
91         2.0 * m→Pi * m→dot(d, R) / m→dot(R, R),
92         m→sqrt(m→dot(dR, dR)) / m→dot(R, R)
93     };
94
95     # we get the rest of the helical motif by applying the C_N rotational axis.
96
97     # apply a helical symmetry operation to the whole helical motif (2N points):
98     # translation by h along the z axis
99     # and rotation by alpha (in radians)

```

```
100     if (n2) {
101         (p1, p2) := solve_p1p2(n1, n2);
102         h = real N * 1.5 * m→sqrt(3.0) * bondlen * bondlen
103             / m→sqrt(m→dot(R, R));
104         alpha = 2.0 * m→Pi * m→dot(vector→add(vector→scale(p1, R1),
105             vector→scale(p2, R2)), R) / m→dot(R, R);
106     } else {
107         # zigzag (n, 0) nanotube
108         h = 1.5 * bondlen;
109         alpha = m→Pi / real N;
110     }
111
112     for (i := 0; i < N; i++) { # C_N loop
113         for (j := 0; j <= int (10.0 * nt_length / h); j++) { # S(h, alpha) loop
114             points = array[2] of {(2.0 * m→Pi / real N * real i
115                 + real j*alpha, real j*h} :: points;
116             points = array[2] of {(tmp[0] + 2.0 * m→Pi / real N * real i
117                 + real j*alpha, tmp[1] + real j*h} :: points;
118             num += 2;
119         }
120     }
121
122     # now print all points, in correct .xyz format
123     sys→print("%d\n(%d, %d) nanotube, diameter = %f nm, length = %f nm\n",
124         num, n1, n2, radius / 5.0, nt_length);
125     cyl, cart: vec;
126     for (; points != nil; points = tl points) {
127         cyl = hd points;
128         cart = vector→cyl2vec(radius, cyl[0], cyl[1]);
129         sys→print("C\t%.5f\t%.5f\t%.5f\n", cart[0], cart[1], cart[2]);
130     }
131 }
132 }
133
134
135 init(nil: ref Draw→Context, argv: list of string)
136 {
137     sys = load Sys sys→PATH;
138     m = load Math Math→PATH;
139     vector = load Vector Vector→PATH;
140     if (vector == nil) {
141         sys→fprint(sys→fildes(2), "vector load: %r\n");
142         raise "fail:load";
143     }
```

```

144
145     # jump over program name
146     argv = tl argv;
147
148     if (len argv < 2) {
149         sys→fprint(sys→fildes(2), "Usage: nanotube n1 n2 [length_in_nm]\n\n");
150         raise "fail:args";
151     }
152
153     n1 := int hd argv;
154     argv = tl argv;
155     n2 := int hd argv;
156     if (n2 > n1) {
157         sys→print("The argument n1 must be greater than or equal to n2!\n");
158         raise "fail:args";
159     }
160     argv = tl argv;
161     nt_length := 20.0; # default length
162     if (argv != nil)
163         nt_length = real hd argv;
164
165     calc_nanotube(n1, n2, nt_length);
166 }

```

A.2 Extracting “timeline” images of nanothermite combustion movies

The combustion rate of a nanothermite pellet in a CRT experiment¹ is determined from the high-speed video recording. The height and diameter of the pellet to be measured have been measured before the experiment, allowing to determine how many pixels in the video correspond to 1 mm. Usually, two or more frames (for example, near the beginning and the end of the combustion) are selected, the horizontal position of the combustion front is measured; the distance (converted to mm) divided by the time difference gives the combustion velocity

$$\bar{v} = \frac{\Delta x}{\Delta t}.$$

However, this evaluation method gives a mean combustion velocity, supposing that the combustion is perfectly linear, and does not allow finding instantaneous velocities. A continuous evaluation using single video frames is tedious and time-consuming.

In the videos, the laser beam strikes the target horizontally, and the position of the combustion front is evaluated at the center of the laser heating spot. The idea behind the software presented

¹See section 3.5.3.

here is to take just one horizontal line of pixels from every frame of the video and glue them vertically one below the other. The result is one image, in which the vertical axis corresponds to the time. For example, for 1000 frames per second, one pixel is equal to 1 ms. The horizontal axis corresponds to a horizontal position and allows evaluating the position of the combustion front at each moment t . In a sense, these images are a snapshot of the whole combustion process.

A.2.1 Implementation in Go

The Go programming language is developed by Google and seen by some as the successor to Limbo, which was used in the previous section. Without going into details, the syntax resembles both C and Limbo. In this program, we benefit from the fact that modules for JPEG (read-only) and PNG images (read/write) are included in the distribution.

The input to the program consists of JPEG images (given on the command line), each one corresponding to one video frame. These image collections are the default output format for the Photon Fastcam software we used in our CRT experiments. The program opens the first input file to determine its width and whether the line number to extract (given by the `-l` option) is valid. The default line number is 104, as the images usually have a size of 640×208 pixels. Then the output file is opened for writing, and the main calculation is done in line 85 by a call to the `createOutput()` function. This function creates a new, empty image in memory, opens each of the files in turn and “blits” (copies) one line of pixels into the output. The raw image is returned, immediately encoded to PNG and written to the file. For a typical movie with 1200 frames, the program takes about 20–30 seconds on a recent Mac Book Pro (2.2 GHz).

Usage. The program is normally called from the command line in a directory containing the results of a shot. There are two flags that can be given: `-o` to set the output file name (default is “out.png”), `-l` to set the line number to extract. After the flags, the source images have to be given on the command line, using wildcards (*). For example, the program could be called as follows:

```
nt-timeline -o NT4_A3.png NT4_A3_image*.jpg
```

A.2.2 The source code

A.2.2.1 nt-timeline.go

```
1 package main
2
3 import (
4     "flag"
5     "fmt"
6     "image"
7     "image/jpeg"
```

```

8     "image/png"
9     "os"
10    "./w32glob"
11    "runtime"
12 )
13
14 var line = flag.Int("l", 104, "line number of each input file")
15 var outputfile = flag.String("o", "out.png", "name of the output file")
16
17 // Open the image at filename, decode it as a jpeg and return
18 // the decoded image.
19 func decodeImage(filename string) image.Image {
20     var f *os.File
21     var err os.Error
22     var img image.Image
23
24     f, err = os.Open(filename, os.O_RDONLY, 0666)
25     defer f.Close()
26     if err != nil {
27         fmt.Fprintln(os.Stderr, err)
28         os.Exit(1)
29     }
30
31     img, err = jpeg.Decode(f)
32     if err != nil {
33         fmt.Fprintln(os.Stderr, err)
34         os.Exit(1)
35     }
36
37     return img
38 }
39
40 // The principal function of this program. For each of the files,
41 // copy exactly one horizontal line into the output.
42 func createOutput(minX, maxX int, files []string) image.Image {
43     var img image.Image
44     out := image.NewNRGBA(maxX-minX, len(files))
45
46     for i, file := range files {
47         img = decodeImage(file)
48         for j := minX; j < maxX; j++ {
49             out.Set(j, i, img.At(j, *line))
50         }
51     }

```

```
52
53     return out
54 }
55
56
57 func main() {
58     var bounds image.Rectangle
59
60     runtime.GOMAXPROCS(2)
61
62     flag.Usage = func() {
63         fmt.Fprintf(os.Stderr, "Usage: %s [flags] imagefile ...\n\nFlags:\n", os.Args[0])
64         flag.PrintDefaults()
65     }
66     flag.Parse()
67     if flag.NArg() == 0 {
68         flag.Usage()
69         os.Exit(2)
70     }
71
72     files, err := w32glob.Glob(flag.Args())
73     if err != nil {
74         fmt.Fprintln(os.Stderr, err)
75         os.Exit(2)
76     }
77
78     // open the first input file to determine the width and to check if the
79     // line number is valid
80     bounds = decodeImage(files[0]).Bounds()
81     if *line < bounds.Min.Y || *line > bounds.Max.Y {
82         fmt.Fprintf(os.Stderr, "%s: value for line is out of range, must be between %d and %d\n",
83             os.Args[0], bounds.Min.Y, bounds.Max.Y)
84         os.Exit(2)
85     }
86
87     // now build and write the output
88     f, err := os.Open(*outputfile, os.O_WRONLY|os.O_CREAT|os.O_TRUNC, 0644)
89     if err != nil {
90         fmt.Fprintln(os.Stderr, "while opening output file:", err)
91         os.Exit(3)
92     }
93     defer f.Close()
94     err = png.Encode(f, createOutput(bounds.Min.X, bounds.Max.X, files))
95     if err != nil {
```

```

95         fmt.Fprintln(os.Stderr, "while writing output file:", err)
96         os.Exit(3)
97     }
98 }

```

A.2.2.2 w32glob.go

This helper package is needed on Windows to find the names of the image files.

```

1  package w32glob
2
3  import (
4      "container/vector"
5      "os"
6      "strings"
7      "syscall"
8  )
9
10 func Glob(patterns []string) ([]string, os.Error) {
11     var path, name string
12     var i, errno int
13     var handle int32
14     var f syscall.Win32finddata
15
16     files := make(vector.StringVector, 0)
17
18     for _, p := range patterns {
19         i = strings.LastIndexFunc(p, func(r int) bool {
20             return r == '\\' || r == '?' || r == '/'
21         })
22         if i != -1 {
23             path = p[0 : i+1]
24         } else {
25             path = ""
26         }
27
28         handle, errno = syscall.FindFirstFile(syscall.StringToUTF16Ptr(p), &f)
29         if handle == -1 { // INVALID_HANDLE_VALUE
30             return nil, os.NewError(syscall.Errstr(errno))
31         }
32         defer syscall.FindClose(handle)
33         for errno == 0 {
34             name = syscall.UTF16ToString(f.FileName[0:])
35             if name != "." && name != ".." {
36                 files.Push(path + name)

```

```
37         }
38         _, errno = syscall.FindNextFile(handle, &f)
39     }
40     if errno != syscall.ERROR_NO_MORE_FILES {
41         return nil, os.NewError(syscall.Errstr(errno))
42     }
43 }
44 return files, nil
45 }
```

A.3 Decoding combustion front images for numerical analysis

The “timeline” images created with the nt-timeline program presented in the last section contain useful information for qualitatively assessing the combustion of a nanothermite pellet. However, a *quantitative* determination of the combustion velocity v , i. e. of the propagation of the reaction front, is still difficult. For a linear regression or even a determination of the instantaneous velocity dx/dt , it is necessary to have a table containing the position of the combustion front in each video frame, i. e. in each line of the timeline graphic. However, it is difficult to find this position with a software algorithm; a human can indicate it much faster.

The idea behind the “nt-decode” program presented here is the following: The timeline image is opened in an image manipulation program such as GIMP or Photoshop. The user creates a new, transparent layer above the image and indicates the position of the combustion front by drawing a line with an 1×1 pixel brush in the image. This layer is then saved as a new image. In each row, one pixel is set to a non-background color, indicating the position x of the combustion front for frame number y . The “nt-decode” program reads such an image, in the png format, and writes a text file containing the y and x positions of the set pixels to the standard output.

Implementation. Like nt-timeline, the program is written in Go. It has two flags that can be given on the command line. The `-d` flag only generates a line in the output file if the x position is different from the one in the line above. The `-i` flag suppresses the output of output lines where no pixel is set. If it is not given, a line with “# invalid” is output instead, taken as an invalid point by the graphing software (Gnuplot or Origin) in which the data file is imported. In order to create an output file, a command line like in the following example is used:

```
nt-decode NT4A1.png > NT4A1.dat
```

A.3.1 The source code: nt-decode.go

```
1 package main
```

```
2
3 import (
4     "bufio"
5     "flag"
6     "fmt"
7     "image"
8     "image/png"
9     "io"
10    "os"
11 )
12
13 // Command line flags
14 var diff = flag.Bool("d", false, "only write lines where value is different")
15 var invalid = flag.Bool("i", false, "jump over invalid points")
16
17 const NotFound = -1
18
19 type Comparator func(image.Color) bool
20
21 // It is difficult to compare two Colors, so this function returns a closure
22 // that compares other colors against this one.
23 func NewComparator(c image.Color) Comparator {
24     var myR, myG, myB, myA uint32
25
26     myR, myG, myB, myA = c.RGBA()
27     return func(color image.Color) bool {
28         r, g, b, a := color.RGBA()
29         if r == myR && g == myG && b == myB && a == myA {
30             return true
31         }
32         return false
33     }
34 }
35
36 // Open the image at filename, decode it as a png and return
37 // the decoded image.
38 func decodeImage(filename string) image.Image {
39     var f *os.File
40     var err os.Error
41     var img image.Image
42
43     f, err = os.Open(filename, os.O_RDONLY, 0666)
44     defer f.Close()
45     if err != nil {
```

```
46         fmt.Fprintln(os.Stderr, err)
47         os.Exit(1)
48     }
49
50     img, err = png.Decode(f)
51     if err != nil {
52         fmt.Fprintln(os.Stderr, err)
53         os.Exit(1)
54     }
55
56     return img
57 }
58
59 func outputData(img image.Image, w io.Writer) {
60     var isBG Comparator
61     var pos, oldpos int
62
63     bw := bufio.NewWriter(w)
64     bounds := img.Bounds()
65     oldpos = NotFound
66
67     // use heuristics to guess background color
68     isBG = NewComparator(img.At(0, 0))
69     if !isBG(img.At(1, 0)) {
70         isBG = NewComparator(img.At(bounds.Max.X-1, 0))
71     }
72
73     for i := bounds.Min.Y; i < bounds.Max.Y; i++ {
74         pos = NotFound
75         for j := bounds.Min.X; j < bounds.Max.X; j++ {
76             if !isBG(img.At(j, i)) {
77                 pos = j
78                 break
79             }
80         }
81         if pos == NotFound {
82             if *invalid == false {
83                 fmt.Fprintf(bw, "%v\t#invalid\n", i)
84             }
85         } else if *diff == false || pos != oldpos {
86             fmt.Fprintf(bw, "%v\t%v\n", i, pos)
87         }
88         oldpos = pos
89     }
```

```
90     bw.Flush()
91 }
92
93
94 func main() {
95     flag.Usage = func() {
96         fmt.Fprintf(os.Stderr, "Usage: %s [flags] imagefile \n\nFlags:\n", os.Args[0])
97         flag.PrintDefaults()
98     }
99     flag.Parse()
100    if flag.NArg() == 0 {
101        flag.Usage()
102        os.Exit(2)
103    }
104
105    for _, file := range flag.Args() {
106        outputData(decodeImage(file), os.Stdout)
107    }
108 }
```


Appendix B

Supplementary characterization results

B.1 Manganese dioxide nanorods

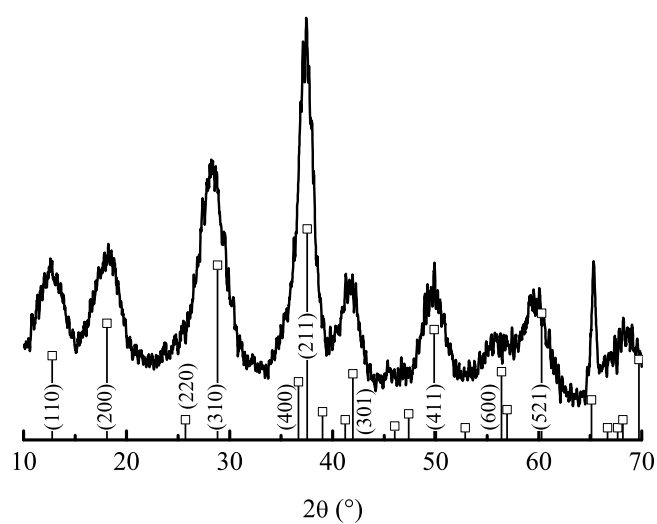


Figure B.1 X-ray diffractogram for manganese dioxide nanorods synthesized by the reduction of potassium permanganate with ethanol. Indicated diffraction peaks and (hkl) indices conform to α - MnO_2 (JCPDS file 44-141).

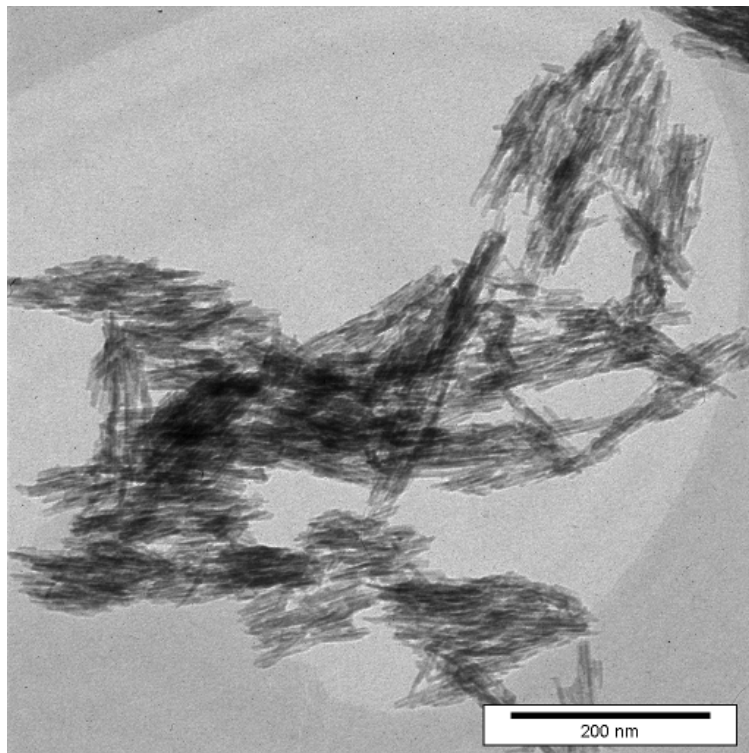


Figure B.2 Transmission Electron Micrograph of manganese dioxide nanorods.

Bibliography

- [1] M. Monthioux, E. Flahaut, Meta- and hybrid-CNTs: a clue for the future development of carbon nanotubes, *Mat. Sci. Eng. C* **27** 1096–1101 (2007).
- [2] M. Comet, D. Spitzer, Des thermites classiques aux composites interstitiels métastables, *Actualité chimique* **299** 20–25 (2006).
- [3] K. C. Walter, D. R. Pesiri, D. E. Wilson, Manufacturing and performance of nanometric Al/MoO₃ energetic materials, *J. Propulsion and Power* **23** (4) 645–650 (2007).
- [4] S. Apperson, R. V. Shende, S. Subramanian, D. Tappmeyer, S. Gangopadhyay, Z. Chen, K. Gangopadhyay, P. Redner, S. Nicholich, D. Kapoor, Generation of fast propagating combustion and shock waves with copper oxide/aluminum nanothermite composites, *Appl. Phys. Lett.* **91** (24) 243109 (2007).
- [5] K. T. Higa, Energetic nanocomposite lead-free electric primers, *J. Propulsion and Power* **23** (4) 722–727 (2007).
- [6] UN recommendations on the transport of dangerous goods: Manual of test and criteria, ST/SG/AC.10/11/Rev.4/Amend.2, United Nations, New York and Geneva (2008).
URL
http://www.unece.org/trans/danger/publi/manual/Rev4/English/02E_part1.pdf
- [7] M. Comet, B. Siegert, V. Pichot, P. Gibot, D. Spitzer, Preparation of explosive nanoparticles in a porous chromium(III) oxide matrix: a first attempt to control the reactivity of explosives, *Nanotechnology* **19** 285716 (2008).
- [8] C. T. White, D. H. Robertson, J. W. Mintmire, Helical and rotational symmetries of nanoscale graphitic tubules, *Phys. Rev. B* **47** (9) 5485–5488 (1993).
- [9] L. V. Radushkevich, V. M. Lukyanovich, *Zurn. Fisic. Chim (Russia)* **26** 88–95 (1952).
- [10] M. Monthioux, Who should be given the credit for the discovery of carbon nanotubes?, *Carbon (Guest Editorial)* **44** 1621–1623 (2006).
- [11] R. H. Boughman, A. A. Zakhidov, W. A. de Heer, Carbon nanotubes—the route toward applications, *Science* **297** 787–792 (2002).
- [12] H. Moustafa, N. Durent, M. Owzarek, P. Brender, J.-N. Munsch, P. Ziegler, D. Schwartz, M. F. Vallat, B. Haidar, Carbon nanotubes as filler for elastomers: Expectation and reality, *Kautschuk Gummi Kunststoffe* **11** 574–579 (2009).
- [13] G. Viswanathan, N. Chakrapani, H. Yang, B. Q. Wei, H. Chung, K. Cho, C. Y. Ryu, P. M. Ajayan, Single-step in situ synthesis of polymer-grafted single-wall nanotube composites, *J. Am. Chem. Soc.* **125** 9258–9259 (2003).

- [14] Q. Ye, A. M. Cassell, H. Liu, J. Han, M. Meyyappan, Integrating carbon nanotubes for Atomic Force Microscopy imaging applications, *Mat. Res. Soc. Symp. Proc.* **820** 107–112 (2004).
- [15] N. Sinha, J. Yeow, Carbon nanotubes for biomedical applications, *IEEE Trans. Nanobiosci.* **4** (2) 180–195 (2005).
- [16] Z.-P. Yang, L. Ci, J. A. Bur, S.-Y. Lin, P. M. Ajayan, Experimental observation of an extremely dark material made by a low-density nanotube array, *Nano Lett.* **8** (2) 446–451 (2008).
- [17] A. Barreiro, R. Rurali, E. R. Hernández, J. Moser, T. Pichler, L. Forró, A. Bachtold, Subnanometer motion of cargoes driven by thermal gradients along carbon nanotubes, *Science* **320** 775–778 (2008).
- [18] Y. J. Lü, M. Chen, Oscillation of gas molecules in carbon nanotubes, *Nanotechnology* **19** 215707 (2008).
- [19] D. S. Sholl, J. K. Johnson, Making high-flux membranes with carbon nanotubes, *Science* **312** 1003–1004 (2006).
- [20] J. K. Holt, H. G. Park, Y. Wang, M. Stadermann, A. B. Artyukhin, C. P. Grigoropoulos, A. Noy, O. Bakajin, Fast mass transport through sub-2-nanometer carbon nanotubes, *Science* **312** 1034–1037 (2006).
- [21] B. J. Hinds, N. Chopra, T. Rantell, R. Andrews, V. Gavalas, L. G. Bachas, Aligned multiwalled carbon nanotube membranes, *Science* **303** 62–65 (2004).
- [22] L. Zhu, D. W. Chang, L. Dai, Y. Hong, DNA damage induced by multiwalled carbon nanotubes in mouse embryonic stem cells, *Nano Lett.* **7** (12) 3592–3597 (2007).
- [23] A. Yan, A. von dem Bussche, A. B. Kane, R. H. Hurt, Tocopheryl polyethylene glycol succinate as a safe, antioxidant surfactant for processing carbon nanotubes and fullerenes, *Carbon* **45** 3463–2470 (2007).
- [24] Y. Zhao, G. Xing, Z. Chai, Are carbon nanotubes safe?, *Nature Nanotechnology* **3** 191–192 (2008).
- [25] X. Liu, L. Guo, D. Morris, A. B. Kane, R. H. Hurt, Targeted removal of bioavailable metal as a detoxification strategy for carbon nanotubes, *Carbon* **46** 489–500 (2008).
- [26] V. Raffa, G. Ciofani, S. Nitodas, T. Karachalios, D. D’Alessandro, M. Masini, A. Cuschieri, Can the properties of carbon nanotubes influence their internalization by living cells?, *Carbon* **46** (12) 1600–1610 (2008).
- [27] A. Bianco, K. Kostarelos, M. Prato, Applications of carbon nanotubes in drug delivery, *Current Opinion in Chemical Biology* **9** 674–679 (2005).
- [28] S. V. Torti, F. Byrne, O. Whelan, N. Levi, B. Ucer, M. Schmid, F. M. Torti, S. Akman, J. Liu, P. M. Ajayan, O. Nalamasu, D. L. Carroll, Thermal ablation therapeutics based on CN_x multi-walled nanotubes, *Int. J. Nanomedicine* **2** (4) 707–714 (2007).
- [29] S. K. Pillai, S. S. Ray, M. Moodley, Purification of single-walled carbon nanotubes, *J. Nanosci. Nanotechnol.* **7** (9) 3011–3047 (2007).

- [30] C. Journet, W. K. Maser, P. Bernier, A. Loiseau, M. L. la Chapelle, S. Lefrant, P. Deniard, R. Leek, J. E. Fischer, Large-scale production of single-walled carbon nanotubes by the electric-arc technique, *Nature* **388** 756–758 (1997).
- [31] S. K. Pillai, W. G. Augustyn, M. H. Rossouw, R. I. McCrindle, The effect of calcination on multi-walled carbon nanotubes produced by DC-arc discharge, *J. Nanosci. Nanotechnol.* **8** 3539–3544 (2008).
- [32] M. Q. Tran, C. Tridech, A. Alfrey, A. Bismarck, M. S. P. Shaffer, Thermal oxidative cutting of multi-walled carbon nanotubes, *Carbon* **45** 2341–2350 (2007).
- [33] M. S. P. Shaffer, X. Fan, A. H. Windle, Dispersion and packing of carbon nanotubes, *Carbon* **36** (11) 1603–1612 (1998).
- [34] S. Hofmann, R. Sharma, C. Ducati, G. Du, C. Mattevi, C. Cepek, M. Cantoro, S. Pisana, A. Parvez, F. Cervantes-Sodi, A. C. Ferrari, R. Dunin-Borkowski, S. Lizzit, L. Petaccia, A. Goldoni, J. Robertson, In situ observations of catalyst dynamics during surface-bound carbon nanotube nucleation, *Nano Lett.* **7** (3) 602–608 (2007).
- [35] G. Bertoni, C. Cepek, F. Romanato, C. S. Casari, A. L. Bassi, C. E. Bottani, M. Sancrotti, Growth of multi-wall and single-wall carbon nanotubes with in situ high vacuum catalyst deposition, *Carbon* **42** (2) 440–443 (2004).
- [36] K. H. Choi, J. P. Bourgoïn, S. Auvray, D. Esteve, G. S. Duesberg, S. Roth, M. Burghard, Controlled deposition of carbon nanotubes on a patterned substrate, *Surf. Sci.* **462** 195–202 (2000).
- [37] H. W. Zhu, C. L. Xu, D. H. Wu, B. Q. Wei, R. Vajtai, P. M. Ajayan, Direct synthesis of long single-walled carbon nanotube strands, *Science* **296** 884–886 (2002).
- [38] CoMoCAT process fundamentals,
<http://www.ou.edu/engineering/nanotube/comocat.htm> (2010).
- [39] P. Nikolaev, M. J. Bronikowski, R. K. Bradley, F. Rohmund, D. T. Colbert, K. A. Smith, R. E. Smalley, Gas-phase catalytic growth of single-walled carbon nanotubes from carbon monoxide, *Chem. Phys. Lett.* **313** 91–97 (1999).
- [40] M. J. Bronikowski, P. A. Willis, D. T. Colbert, K. A. Smith, R. E. Smalley, Gas-phase production of carbon single-walled nanotubes from carbon monoxide via the HiPco process: A parametric study, *J. Vac. Sci. Technol. A* **19** (4) 1800–1805 (2001).
- [41] K. Hata, D. N. Futaba, K. Mizuno, T. Namai, M. Yumura, S. Iijima, Water-assisted highly efficient synthesis of impurity-free single-walled carbon nanotubes, *Science* **306** 1362–1364 (2004).
- [42] The ‘secret’ behind “super growth” of SWNT, Asia Pacific Nanotech Weekly, URL
<http://unit.aist.go.jp/nanotech/apnw/articles/library3/pdf/3-4.pdf> (2005).
- [43] M. Lin, J. P. Ying Tan, C. Boothroyd, K. P. Loh, E. S. Tok, Y.-L. Foo, Direct observation of single-walled carbon nanotube growth at the atomistic scale, *Nano Letters* **6** (3) 449–452 (2006). URL <http://pubs.acs.org/doi/abs/10.1021/nl052356k>
- [44] J. Gavillet, A. Loiseau, C. Journet, F. Willaime, F. Ducastelle, J.-C. Charlier, Root-growth mechanism for single-wall carbon nanotubes, *Phys. Rev. Lett.* **87** (27) 275504 (2001).

Bibliography

- [45] G. A. Forrest, A. J. Alexander, Quantitative inhibiting effect of group I–III cations on the growth of carbon nanotubes, *Carbon* **46** 818–821 (2008).
- [46] T. W. Ebbesen (Ed.), *Carbon Nanotubes—Preparation and Properties*, CRC Press, Boca Raton, New York, London, Tokyo, 1997.
- [47] M. Audier, M. Colon, Kinetic and microscopic aspects of catalytic carbon growth, *Carbon* **23** (3) 317–323 (1985).
- [48] A. T. Matveev, D. Golberg, V. P. Novikov, L. L. Klimkovich, Y. Bando, Synthesis of carbon nanotubes below room temperature, *Carbon* **39** 155–158 (2001).
- [49] G. J. Bodwell, Growth potential, *Nature Nanotechnology* **5** (2) 103–104 (2010).
- [50] E. H. Fort, P. M. Donovan, L. T. Scott, Diels-Alder reactivity of polycyclic aromatic hydrocarbon bay regions: Implications for metal-free growth of single-chirality carbon nanotubes, *J. Am. Chem. Soc.* **131** 16006–16007 (2009).
- [51] M. S. Dresselhaus, G. Dresselhaus, R. Saito, Physics of carbon nanotubes, *Carbon* **33** (7) 883–891 (1995).
- [52] F. Papadimitrakopoulos, S.-Y. Ju, Purity rolled up in a tube, *Nature (News and Views)* **450** 486–487 (2007).
- [53] D. Tasis, K. Papagelis, D. Douroumis, J. R. Smith, N. Bouropoulos, D. G. Fatouros, Diameter-selective solubilization of carbon nanotubes by lipid micelles, *J. Nanosci. Nanotechnol.* **8** 420–423 (2008).
- [54] J. Graham, *Biological Centrifugation*, BIOS Scientific Publishers Ltd, Oxford, 1996.
- [55] M. S. Arnold, S. I. Stupp, M. C. Hersam, Enrichment of single-walled carbon nanotubes by diameter in density gradients, *Nano Lett.* **5** (4) 713–718 (2005).
- [56] M. S. Arnold, A. A. Green, J. F. Hulvat, S. I. Stupp, M. C. Hersam, Sorting carbon nanotubes by electronic structure using density differentiation, *Nature Nanotechnology* **1** 60–65 (2006).
- [57] A. A. Green, M. C. Hersam, Ultracentrifugation of single-walled nanotubes, *Materials Today* **10** (12) 59–60 (2007).
- [58] A. A. Green, M. C. Duch, M. C. Hersam, Isolation of single-walled carbon nanotube enantiomers by density differentiation, *Nano Res.* **2** 69–77 (2009).
- [59] M. C. Hersam, Progress towards monodisperse single-walled carbon nanotubes, *Nature Nanotechnology* **3** (7) 387–394 (2008).
- [60] L. Vaisman, H. D. Wagner, G. Marom, The role of surfactants in dispersion of carbon nanotubes, *Adv. Coll. Interf. Sci.* **128–130** 37–46 (2006).
- [61] D. H. Marsh, G. A. Rance, M. H. Zaka, R. J. Whitby, A. N. Khlobystov, Comparison of the stability of multiwalled carbon nanotube dispersions in water, *Phys. Chem. Chem. Phys.* **9** 5490–5496 (2007).

- [62] J. Liu, M. J. Casavant, M. Cox, D. A. Walters, P. Boul, W. Lu, A. J. Rimberg, K. A. Smith, D. T. Colbert, R. E. Smalley, Controlled deposition of individual single-walled carbon nanotubes on chemically functionalized templates, *Chem. Phys. Lett.* **303** 125–129 (1999).
- [63] F. Inam, H. Yan, M. J. Reece, T. Peijs, Dimethylformamide: an effective dispersant for making ceramic–carbon nanotube composites, *Nanotechnology* **19** 195710 (2008).
- [64] D. F. Shriver, P. W. Atkins, Chimie inorganique, De Boeck Université, Louvain-la-Neuve and Paris, 2001.
- [65] J. Hilding, E. A. Grulke, Z. G. Zhang, F. Lockwood, Dispersion of carbon nanotubes in liquids, *J. Disp. Sci. Technol.* **24** 1–41 (2003).
- [66] S. Badaire, Etude de suspensions et de fibres de nanotubes de carbone, Thèse, Université Bordeaux I (2005).
- [67] L. Jiang, L. Gao, J. Sun, Production of aqueous colloidal dispersions of carbon nanotubes, *J. Colloid Interf. Sci.* **260** 89–94 (2003).
- [68] W. Wenseleers, I. Vlasov, E. Goovaerts, E. Obraztsova, A. Lobach, A. Bouwen, Efficient isolation and solubilization of pristine single-walled nanotubes in bile salt micelles, *Adv. Funct. Mater.* **14** (11) 1105–1112 (2004).
- [69] C.-H. Xue, R.-J. Zhou, M.-M. Shi, Y. Gao, G. Wu, X.-B. Zhang, H.-Z. Chen, M. Wang, The preparation of highly water-soluble multi-walled carbon nanotubes by irreversible noncovalent functionalization with a pyrene-carrying polymer, *Nanotechnology* **19** 215604 (2008).
- [70] R. Shvartzman-Cohen, Y. Levi-Kalishman, E. Nativ-Roth, R. Yerushalmi-Rozen, Generic approach for dispersing single-walled carbon nanotubes: The strength of a weak interaction, *Langmuir* **20** 6085–6088 (2004).
- [71] Y.-C. Tsai, C.-C. Chiu, M.-C. Tsai, J.-Y. Wu, T.-F. Tseng, T.-M. Wu, S.-F. Hsu, Dispersion of carbon nanotubes in low pH aqueous solutions by means of alumina-coated silica nanoparticles, *Carbon* **45** 2823–2827 (2007).
- [72] D. J. Mann, W. L. Hase, Direct dynamics simulations of the oxidation of a single wall carbon nanotube, *Phys. Chem. Chem. Phys.* **3** 4376–4383 (2001).
- [73] T. C. Dinadayalane, J. Leszczynski, Stone–wales defects with two different orientations in (5, 5) single-walled carbon nanotubes: A theoretical study, *Chem. Phys. Lett.* **434** 86–91 (2007).
- [74] M. A. Hamon, H. Hui, H. M. E. Itkis, R. C. Haddon, Ester-functionalized soluble single-wall carbon nanotubes, *Appl. Phys. A* **74** 333–338 (2002).
- [75] M. Haluska, M. Hulman, M. Hirscher, M. Becher, S. Roth, I. Stepanek, P. Bernier, Hydrogen storage in mechanically treated single wall carbon nanotubes, in: H. Kuzmany (Ed.), CP591, Electronic Properties of Molecular Nanostructures, American Institute of Physics, 2001, pp. 603–608.
- [76] P. M. Ajayan, T. W. Ebbesen, T. Ichihashi, S. Iijima, K. Tanigaki, H. Hiura, Opening carbon nanotubes with oxygen and implications for filling, *Nature* **362** 522–525 (1993).

- [77] B. C. Satishkumar, A. Govindaraj, J. Mokofeng, G. N. Subbanna, C. N. R. Rao, Novel experiments with carbon nanotubes: opening, filling, closing and functionalizing nanotubes, *J. Phys. B: At. Mol. Opt. Phys* **29** 4925–4934 (1996).
- [78] G. Zhang, S. Sun, D. Yang, J.-P. Dodelet, E. Sacher, The surface analytical characterization of carbon fibers functionalized by H₂SO₄/HNO₃ treatment, *Carbon* **46** 196–205 (2008).
- [79] J. Zhang, H. Zou, Q. Qing, Y. Yang, Q. Li, Z. Liu, X. Guo, Z. Du, Effect of chemical oxidation on the structure of single-walled carbon nanotubes, *J. Phys. Chem. B* **107** 3712–3718 (2003).
- [80] T. Hemraj-Benny, T. J. Bandosz, S. S. Wong, Effect of ozonolysis on the pore structure, surface chemistry, and bundling of single-walled carbon nanotubes, *J. Coll. Interf. Sci.* **317** 375–382 (2008).
- [81] D. B. Mawhinney, V. Naumenko, A. Kuznetsova, J. T. Yates, J. Liu, R. E. Smalley, Infrared spectral evidence for the etching of carbon nanotubes: Ozone oxidation at 298 K, *J. Am. Chem. Soc.* **122** 2383–2384 (2000).
- [82] Y. Lian, Y. Maeda, T. Wakahara, T. Akasaka, S. Kazaoui, N. Minami, T. Shimizu, N. Choi, H. Tokumoto, Nondestructive and high-recovery-yield purification of single-walled carbon nanotubes by chemical functionalization, *J. Phys. Chem. B* **108** 8848–8854 (2004).
- [83] A. Vinu, K. Z. Hossian, P. Srinivasu, M. Miyahara, S. Anandan, N. Gokulakrishnan, T. Mori, K. Ariga, V. V. Balasubramanian, Carboxy-mesoporous carbon and its excellent adsorption capability for proteins, *J. Mater. Chem.* **17** 1819–1825 (2007).
- [84] L. Shao, G. Tobias, Y. Huh, M. L. H. Green, Reversible filling of single walled carbon nanotubes opened by alkali hydroxides, *Carbon* **44** 2855–2856 (2006).
- [85] Y. Huh, L. Shao, G. Tobias, M. L. H. Green, Opening and reversible filling of single-walled carbon nanotubes with various materials, *J. Nanosci. Nanotechnol.* **6** 3360–3363 (2006).
- [86] N. Thamavaranukup, H. A. Höpfe, L. Ruiz-Gonzalez, P. M. F. J. Costa, J. Sloan, A. Kirkland, M. L. H. Green, Single-walled carbon nanotubes filled with MOH (M = K, Cs) and then washed and refilled with clusters and molecules, *Chem. Commun.* 1686–1687 (2004).
- [87] Y. K. Chen, R. C. Haddon, S. Fang, A. M. Rao, P. C. Eklund, W. H. Lee, E. C. Dickey, E. A. Grulke, J. C. Pendergrass, A. Chavan, B. E. Haley, R. E. Smalley, Chemical attachment of organic functional groups to single-walled carbon nanotube material, *J. Mater. Res.* **13** (9) 2423–2431 (1998).
- [88] J. Chen, M. A. Hamon, H. Hu, Y. Chen, A. M. Rao, P. C. Eklund, R. C. Haddon, Solution properties of single-walled carbon nanotubes, *Science* **282** 95–98 (1998).
- [89] R. Verdejo, S. Lamoriniere, B. Cottam, A. Bismarck, M. Shaffer, Removal of oxidation debris from multi-walled carbon nanotubes, *Chem. Commun.* 513–515 (2007).
- [90] S. Fogden, R. Verdejo, B. Cottam, M. S. P. Shaffer, Purification of single walled carbon nanotubes; the problem with oxidation debris, *Chem. Phys. Lett.* **in Press**.
- [91] A. Kuznetsova, D. B. Mawhinney, V. Naumenko, J. T. Yates, J. Liu, R. E. Smalley, Enhancement of adsorption inside of single-walled carbon nanotubes, *Chem. Phys. Lett.* **321** 292–296 (2000).
- [92] M. Monthieux, Filling single-wall carbon nanotubes, *Carbon* **40** 1809–1823 (2002).

- [93] M. Monthieux, E. Flahaut, J.-P. Cleuziou, Hybrid carbon nanotubes: Strategy, progress, and perspectives, *J. Mater. Res.* **21** (11) 2774–2793 (2006).
- [94] M. Wilson, P. A. Madden, Growth of ionic crystals in carbon nanotubes, *J. Am. Chem. Soc.* **123** 2101–2102 (2001).
- [95] M. Wilson, Structure and phase stability of novel ‘twisted’ crystal structures in carbon nanotubes, *Chem. Phys. Lett.* **366** 504–509 (2002).
- [96] M. R. Pederson, J. Q. Broughton, Nanocapillarity in fullerene tubules, *Phys. Rev. Lett.* **69** (18) 2689–2692 (1992).
- [97] E. Maccallini, G. Kalantzopoulos, T. Tsoufis, R. G. Agostino, G. Chiarello, V. Formoso, T. Caruso, A. Policicchio, D. Gournis, E. Colavita, Metallic tin-filling effects on carbon nanotubes revealed by atomically resolved spectro-microscopies, *J. Nano Res.* **3** 1–6 (2008).
- [98] W. Luo, Y. Xie, F. Zheng, The large-scale synthesis and characterization of carbon nanotubes filled with long continuous inorganic nanowire in supercritical CS₂, *Nanotechnology* **17** 5702–5706 (2006).
- [99] E. Dujardin, T. W. Ebbesen, H. Hiura, K. Tanigaki, Capillarity and wetting of carbon nanotubes, *Science* **265** 1850–1852 (1994).
- [100] J. Sloan, J. Cook, A. Chu, M. Zwiefka-Sibley, M. L. H. Green, J. L. Hutchison, Selective deposition of UCl₄ and (KCl)_x(UCl₄)_y inside carbon nanotubes using eutectic and noneutectic mixtures of UCl₄ with KCl, *J. Sol. State Chem.* **140** 83–90 (1998).
- [101] P. M. F. J. Costa, D. Golberg, M. Mitome, S. Hampel, A. Leonhardt, B. Buchner, Y. Bando, Stepwise current-driven release of attogram quantities of copper iodide encapsulated in carbon nanotubes, *Nano Lett.* **8** (10) 3120–3125 (2008).
- [102] J. Sloan, M. C. Novotny, S. R. Bailey, G. Brown, C. Xu, V. C. Williams, S. Friedrichs, E. Flahaut, R. L. Callender, A. P. E. York, K. S. Coleman, M. L. H. Green, R. E. Dunin-Borkowski, J. L. Hutchison, Two layer 4:4 co-ordinated KI crystals grown within single walled carbon nanotubes, *Chem. Phys. Lett.* **329** 61–65 (2000).
- [103] A. F. Holloway, K. Toghill, G. G. Wildgoose, R. G. Compton, M. A. H. Ward, G. Tobias, S. A. Llewellyn, B. Ballesteros, M. L. H. Green, A. Crossley, Electrochemical opening of single-walled carbon nanotubes filled with metal halides and with closed ends, *J. Phys. Chem. C* **112** 10389–10397 (2008).
- [104] J. Sloan, D. M. Wright, H.-G. Woo, S. Bailey, G. Brown, A. P. E. York, K. S. Coleman, J. L. Hutchison, M. L. H. Green, Capillarity and silver nanowire formation observed in single walled carbon nanotubes, *Chem. Commun.* 699–700 (1999).
- [105] R. M. Zakalyukin, B. N. Mavrin, L. N. Dem’yanets, N. A. Kiselev, Synthesis and characterization of single-walled carbon nanotubes filled with SnF₂, *Carbon in Press*.
- [106] M. Hulman, H. Kuzmany, P. M. F. J. Costa, S. Friedrichs, M. L. H. Green, Light-induced instability of pbo-filled single-wall carbon nanotubes, *Appl. Phys. Lett.* **85** (11) 2068–2070 (2004).

Bibliography

- [107] P. M. Ajayan, O. Stephan, P. Redlich, C. Colliex, Carbon nanotubes as removable templates for metal oxide nanocomposites and nanostructures, *Nature* **375** 564–567 (1995).
- [108] Y. Li, R. Hatakeyama, W. Oohara, T. Kaneko, Formation of p–n junction in double-walled carbon nanotubes based on heteromaterial encapsulation, *Applied Physics Express* **2** (9) 095005 (2009).
- [109] T. Shimizu, T. Kato, W. Oohara, R. Hatakeyama, Electrical transport properties of calcium-encapsulated single-walled carbon nanotubes realized using calcium plasma, *Jpn. J. Appl. Phys.* **49** 02BD05 (3pp) (2010).
- [110] S. Chen, K. Kobayashi, Y. Miyata, N. Imazu, T. Saito, R. Kitaura, H. Shinohara, Morphology and melting behavior of ionic liquids inside single-walled carbon nanotubes, *J. Am. Chem. Soc.* **131** (41) 14850–14856 (2009).
- [111] G. Chen, J. Qiu, H. Qiu, Filling double-walled carbon nanotubes with AgCl nanowires, *Scripta Materialia* **58** 457–460 (2008).
- [112] J. Sloan, J. Hammer, M. Zwiefka-Sibley, M. L. H. Green, The opening and filling of single walled carbon nanotubes (SWTs), *Chem. Commun.* 347–348 (1998).
- [113] A. Capobianchi, S. Foglia, P. Imperatori, A. Notargiacomo, M. Giammateo, T. del Buono, E. Palange, Controlled filling and external cleaning of multi-wall carbon nanotubes using a wet chemical method, *Carbon* **45** 2205–2208 (2007).
- [114] A. Chu, J. Cook, R. Heesom, J. Hutchison, M. Green, J. Sloan, Filling of carbon nanotubes with silver, gold, and gold chloride, *Chem. Mater.* **8** (12) 2751–2754 (1996).
- [115] C. Wang, S. Guo, X. Pan, W. Chen, X. Bao, Tailored cutting of carbon nanotubes and controlled dispersion of metal nanoparticles inside their channels, *J. Mater. Chem.* **in Press**.
- [116] J. Cook, J. Sloan, R. J. R. Heesom, J. Hammer, M. L. H. Green, Purification of rhodium-filled carbon nanotubes using reversed micelles, *Chem. Commun.* **23** 2673–2674 (1996).
- [117] Q. Fu, G. Weinberg, D.-S. Su, Selective filling of carbon nanotubes with metals by selective washing, *New Carbon Materials* **23** (1) 17–20 (2008).
- [118] E. Borowiak-Palen, Iron filled carbon nanotubes for bio-applications, *Materials Science-Poland* **26** (2) 413–418 (2008).
- [119] Z. L. Zhang, B. Li, Z. J. Shi, Z. N. Gu, Z. Q. Xue, L.-M. Peng, Filling of single-walled carbon nanotubes with silver, *J. Mater. Res.* **15** (12) 2658–2661 (2000).
- [120] S. H. S. Zein, L.-C. Yeoh, S.-P. Chai, A. R. Mohamed, M. E. M. Mahayuddin, Synthesis of manganese oxide/carbon nanotube nanocomposites using wet chemical method, *J. Mater. Processing Technol.* **190** 402–405 (2007).
- [121] S. I. A. Razak, A. L. Ahmad, S. H. S. Zein, A. R. Boccaccini, MnO₂-filled multiwalled carbon nanotube/polyaniline nanocomposites with enhanced interfacial interaction and electronic properties, *Scripta Materialia* **61** (6) 592–595 (2009).
URL <http://dx.doi.org/10.1016/j.scriptamat.2009.05.030>

- [122] N. Keller, C. Pham-Huu, C. Estournès, J.-M. Grenèche, G. Ehret, M. J. Ledoux, Carbon nanotubes as a template for mild synthesis of magnetic CoFe₂O₄ nanowires, *Carbon* **42** 1395–1399 (2004).
- [123] N. Keller, C. Pham-Huu, T. Shiga, C. Estournès, J.-M. Grenèche, M. J. Ledoux, Mild synthesis of CoFe₂O₄ nanowires using carbon nanotube template: a high-coercivity material at room temperature, *J. Magnetism Magnet. Mater.* **272–276** 1642–1644 (2004).
- [124] S. C. Tsang, Y. K. Chen, P. J. F. Harris, M. L. H. Green, A simple chemical method of opening and filling carbon nanotubes, *Nature* **372** 159–162 (1994).
- [125] Y. Saito, K. Yanagi, N. Hayazawa, H. Ishitobi, A. Ono, H. Kataura, S. Kawata, Vibrational analysis of organic molecules encapsulated in carbon nanotubes by tip-enhanced raman spectroscopy, *Jpn. J. Appl. Phys.* **45** (12) 9286–9289 (2006).
- [126] K. Yanagi, Y. Miyata, H. Kataura, Highly stabilized β -carotene in carbon nanotubes, *Adv. Mater.* **18** 437–441 (2006).
- [127] J. Mittal, M. Monthieux, H. Allouche, O. Stephan, Room temperature filling of single-wall carbon nanotubes with chromium oxide in open air, *Chem. Phys. Lett.* **339** 311–318 (2001).
- [128] Y. K. Chen, A. Chu, J. Cook, M. L. H. Green, P. J. F. Harris, R. Heesom, M. Humphries, J. Sloan, S. C. Tsang, J. F. C. Turner, Synthesis of carbon nanotubes containing metal oxides and metals of the d-block and f-block transition metals and related studies, *J. Mater. Chem.* **7** (3) 545–549 (1997).
- [129] Y. F. Li, R. Hatakeyama, T. Kaneko, T. Izumida, T. Okada, T. Kato, Synthesis and electronic properties of ferrocene-filled double-walled carbon nanotubes, *Nanotechnology* **17** 4143–4147 (2006).
- [130] S. Kawasaki, Y. Iwai, M. Hirose, Electrochemical lithium ion storage properties of single-walled carbon nanotubes containing organic molecules, *Carbon* **47** (4) 1081–1086 (2009).
- [131] H. Kataura, Y. Maniwa, T. Kodama, T. Kikuchi, K. Hirahara, K. Suenaga, S. Iijima, S. Suzuki, Y. Achiba, W. Krätschmer, High-yield fullerene encapsulation in single-wall carbon nanotubes, *Synthetic Metals* **121** 1195–1196 (2001).
- [132] B. Bouteaux, A. Claye, B. W. Smith, M. Monthieux, D. E. Luzzi, J. E. Fischer, Abundance of encapsulated C₆₀ in single-wall carbon nanotubes, *Chem. Phys. Lett.* **310** 21–24 (1999).
- [133] R. Kitaura, H. Shinohara, Carbon-nanotube-based hybrid materials: Nanopeapods, *Chem. Asian J.* **1** (5) 646–655 (2006).
- [134] R. Kitaura, H. Shinohara, Endohedral metallofullerenes and nano-peapods, *Jpn. J. Appl. Phys.* **46** (3A) 881–891 (2007).
- [135] B. W. Smith, M. Monthieux, D. E. Luzzi, Encapsulated C₆₀ in carbon nanotubes, *Nature* **396** 323–324 (1998).
- [136] H. Ulbricht, T. Hertel, Dynamics of C₆₀ encapsulation into single-wall carbon nanotubes, *J. Phys. Chem. B* **107** 14185–14190 (2003).
- [137] A. N. Khlobystov, D. A. Britz, J. W. Wang, S. A. O’Neil, M. Poliakoff, G. A. D. Briggs, Low temperature assembly of fullerene arrays in single-walled carbon nanotubes using supercritical fluids, *J. Mater. Chem.* **14** 2852–2857 (2004).

Bibliography

- [138] F. Kokai, T. Shimazu, K. Adachi, A. Koshio, Y. Takahashi, Fabrication of completely filled carbon nanotubes with copper nanowires in a confined space, *Appl. Phys. A* **97** 55–62 (2009).
- [139] D. Haase, S. Hampel, A. Leonhardt, J. Thomas, N. Mattern, B. Büchner, Facile one-step-synthesis of carbon wrapped copper nanowires by thermal decomposition of copper(II)-acetylacetonate, *Surf. Coat. Technol.* **201** (22–23) 9184–9188 (2007).
- [140] A. Leonhardt, M. Ritschel, R. Kozhuharova, A. Graff, T. Mühl, R. Huhle, I. Mönch, D. Elefant, C. M. Schneider, Synthesis and properties of filled carbon nanotubes, *Diamond and Related Materials* **12** 790–793 (2003).
- [141] C. Müller, D. Elefant, A. Leonhardt, B. Büchner, Incremental analysis of the magnetization behavior in iron-filled carbon nanotube arrays, *J. Appl. Phys.* **103** 034302 (2008).
- [142] V. Pichot, P. Launois, M. Pinault, M. Mayne-L’Hermite, C. Reynaud, Evidence of strong nanotube alignment and for iron preferential growth axis in multiwalled carbon nanotube carpets, *Appl. Phys. Lett.* **85** (3) 473–475 (2004).
- [143] R. Lv, A. Cao, F. Kang, W. Wang, J. Wei, J. Gu, K. Wang, D. Wu, Single-crystalline permalloy nanowires in carbon nanotubes: Enhanced encapsulation and magnetization, *J. Phys. Chem. C* **111** 11475–11479 (2007).
- [144] R. Lv, S. Tsuge, X. Gui, K. Takai, F. Kanga, T. Enoki, J. Wei, J. Gao, K. Wang, D. Wu, In situ synthesis and magnetic anisotropy of ferromagnetic buckypaper, *Carbon* **47** (4) 1141–1145 (2009).
- [145] R. Klingeler, S. Hampel, B. Büchner, Carbon nanotube based biomedical agents for heating, temperature sensing and drug delivery, *Int. J. Hyperthermia* **24** (6) 496–505 (2008).
- [146] J. Y. Chen, A. Kutana, C. P. Collier, K. P. Giapis, Electrowetting in carbon nanotubes, *Science* **310** 1480–1483 (2005).
- [147] J. Chancelon, Remplissage des nanotubes de carbone – effet du confinement, Thèse de doctorat, Université d’Orléans (2004).
- [148] J.-P. Tessonnier, D. Rosenthal, F. Girgsdies, J. Amadou, D. Bégin, C. Pham-Huu, D.-S. Su, R. Schlögl, Influence of the graphitisation of hollow carbon nanofibers on their functionalisation and subsequent filling with metal nanoparticles, *Chem. Commun.* 7158–7160 (2009).
- [149] E. Castillejos, P.-J. Debouttière, L. Roiban, A. Solhy, V. Martinez, Y. Kihn, O. Ersen, K. Philippot, B. Chaudret, P. Serp, An efficient strategy to drive nanoparticles into carbon nanotubes and the remarkable effect of confinement on their catalytic performance, *Angew. Chem. Int. Ed.* **121** (14) 2567–2571 (2009).
- [150] C. Alba-Simionesco, B. Coasne, G. Dosseh, G. Dudziak, K. E. Gubbins, R. Radhakrishnan, M. Sliwinska-Bartkowiak, Effects of confinement on freezing and melting, *J. Phys.: Condens. Matter* **18** (6) R15–R68 (2006).
- [151] W. Wu, G. H. Nancollas, A new understanding of the relationship between solubility and particle size, *Journal of Solution Chemistry* **27** (6) 521–531 (1998).

- [152] G. Brown, S. R. Bailey, M. Novotny, R. Carter, E. Flahaut, K. S. Coleman, J. L. Hutchison, M. L. H. Green, J. Sloan, High yield incorporation and washing properties of halides incorporated into single walled carbon nanotubes, *Appl. Phys. A* **76** 457–462 (2003).
- [153] Y. Xiao, B. Zhu, S. Guo, Y. Wang, Z. Pan, Structures of Au nanowires encapsulated in carbon nanotubes, *Nuclear Instruments and Methods in Physics Research B: Beam Interactions with Materials and Atoms* **267** (18) 3067–3071 (2009).
- [154] F. R. Hung, G. Dudziak, M. Sliwinska-Bartkowiak, K. E. Gubbins, Freezing/melting behaviour within carbon nanotubes, *Mol. Phys.* **102** (2) 223–234 (2004).
- [155] J. Köhler, R. Meyer, Explosivstoffe, 9th Edition, Wiley-VCH, Weinheim, 1998.
- [156] S. H. Fischer, M. C. Grubelich, A survey of combustible metals, thermites and intermetallics for pyrotechnic applications, in: 32nd AIAA/ASME/SAE/ASEE Joint Propulsion Conference, Lake Buena Vista, FL, USA, 1996.
URL <http://www.osti.gov/bridge/servlets/purl/372665-kjTA0r/webviewable/372665.pdf>
- [157] V. Pichot, M. Comet, E. Fousson, C. Baras, A. Senger, F. Le Normand, D. Spitzer, An efficient purification method for detonation nanodiamonds, *Diamond and Related Materials* **17** 13–22 (2008).
- [158] M. Comet, V. Pichot, B. Siegert, J.-P. Moeglin, Y. Boehrer, D. Spitzer, Use of nanodiamond as a reducing agent in a chlorate-based energetic composition, *Propellants Explosives Pyrotechnics* **34** (2) 166–173 (2009).
- [159] M. Comet, V. Pichot, D. Spitzer, Elaboration and characterization of nano-sized RDX using a charcoal mesoporous matrix as template, in: 38th International Annual Conference of ICT, Karlsruhe, DE, 2007.
- [160] Q. S. M. Kwok, C. Badeen, K. Armstrong, R. Turcotte, D. E. G. Jones, V. Y. Gertsman, Hazard characterization of uncoated and coated aluminium nanopowder compositions, *J. Propulsion and Power* **23** (4) 659–668 (2007).
- [161] Wolfram|Alpha knowledge base, Wolfram Mathematica ChemicalData, <http://www.wolframalpha.com/> (2010).
- [162] M. Comet, V. Pichot, D. Spitzer, B. Siegert, F. Ciszek, N. Piazzon, P. Gibot, Elaboration and characterization of manganese oxide (MnO₂) based “green” nanothermites, in: 39th ICT Conference, Karlsruhe, DE, 2008.
- [163] S. Freiman, S. Hooker, K. Migler, S. Arepalli (Eds.), NIST Recommended Practice Guide: Measurement Issues in Single Wall Carbon Nanotubes, National Institute of Standards and Technology, Washington, DC, 2008.
- [164] S. Brunauer, P. H. Emmett, E. Teller, Adsorption of gases in multimolecular layers, *J. Am. Chem. Soc.* **60** 309–319 (1938).
- [165] S. Brunauer, L. S. Deming, W. E. Deming, E. Teller, On a theory of the van der Waals adsorption of gases, *J. Am. Chem. Soc.* **62** (7) 1723–1732 (1940).

Bibliography

- [166] K. S. W. Sing, D. H. Everett, R. A. W. Haul, L. Moscou, R. A. Pierotti, R. Rouquérol, T. Simienewska, Reporting physisorption data for gas/solid systems with special reference to the determination of surface area and porosity, *Pure and Appl. Chem.* **57** (4) 603–619 (1985).
- [167] S. J. Gregg, K. S. W. Sing, Adsorption, Surface Area and Porosity, 2nd Edition, Academic Press, London, 1982.
- [168] E. P. Barrett, L. G. Joyner, P. P. Halenda, The determination of pore volume and area distributions in porous substances. I. computations from nitrogen isotherms, *J. Am. Chem. Soc.* **73** 373–380 (1951).
- [169] L. G. Joyner, E. P. Barrett, R. Skold, The determination of pore volume and area distributions in porous substances. II. comparison between nitrogen isotherm and mercury porosimeter methods, *J. Am. Chem. Soc.* **73** 3155–3158 (1951).
- [170] J. B. Condon, Surface Area and Porosity Determinations by Physisorption: Measurements and Theory, Elsevier Science, Amsterdam, 2006.
- [171] M. S. Dresselhaus, A. Jorio, M. Hofmann, G. Dresselhaus, R. Saito, Perspectives on carbon nanotubes and graphene Raman spectroscopy, *Nano Lett.* **10** (3) 751–758 (2010).
- [172] R. Graupner, Raman spectroscopy of covalently functionalized single-wall carbon nanotubes, *J. Raman Spectrosc.* **38** (6) 673–683 (2007).
- [173] M. S. Strano, M. L. Usrey, P. W. Barone, D. A. Heller, S. Baik, The Selective Chemistry of Single Walled Carbon Nanotubes, Ch. 6, in: Rotkin and Subramoney [201].
- [174] C. Jiang, K. Kempa, J. Zhao, U. Schlecht, U. Kolb, T. Basché, M. Burghard, A. Mews, Strong enhancement of the Breit-Wigner-Fano Raman line in carbon nanotube bundles caused by plasmon band formation, *Phys. Rev. B* **66** 161404 (2002).
- [175] U. Fano, Effects of configuration interaction on intensities and phase shifts, *Phys. Rev.* **124** (6) 1866–1878 (1961).
- [176] L. Duclaux, Review of the doping of carbon nanotubes (multiwalled and single-walled), *Carbon* **40** (10) 1751–1764 (2002).
- [177] I. Loa, Raman spectroscopy on carbon nanotubes at high pressure, *J. Raman Spectrosc.* **34** 611–627 (2003).
- [178] S. Maruyama, Kataura-plot for resonant raman, URL <http://www.photon.t.u-tokyo.ac.jp/~maruyama/kataura/kataura.html> (2002).
- [179] H. Kataura, Y. Kumazawa, Y. Maniwa, I. Umezū, S. Suzuki, Y. Ohtsuka, Y. Achiba, Optical properties of single-wall carbon nanotubes, *Synthetic Metals* **103** (1–3) 2555–2558 (1999).
- [180] H. J. Park, M. Park, J. Y. Chang, H. Lee, The effect of pre-treatment methods on morphology and size distribution of multi-walled carbon nanotubes, *Nanotechnology* **19** 335702 (2008).
- [181] M. Sućeska, Test Methods for Explosives, Springer Verlag, New York and Berlin, 1995.
- [182] F. Simon, R. Pfeiffer, C. Kramberger, M. Holzweber, H. Kuzmany, The Raman response of double wall carbon nanotubes, in: Rotkin and Subramoney [201], Ch. 8, pp. 203–226.

- [183] A. F. Holleman, E. Wiberg, Lehrbuch der anorganischen Chemie, 91st Edition, de Gruyter, Berlin and New York, 1985.
- [184] H. Jacobs, J. Kockelhorn, T. Tacke, Hydroxide des Natriums, Kaliums und Rubidiums: Einkristallzüchtung und röntgenographische Strukturbestimmung an der bei Raumtemperatur stabilen Modifikation, *Z. anorg. allg. Chem.* **531** 119–124 (1985).
- [185] R. W. Cairns, E. Ott, X-ray studies of the system nickel–oxygen–water. I. Nickelous oxide and hydroxide, *J. Am. Chem. Soc.* **55** 527–533 (1933).
- [186] F. Bucioaman, F. Patcas, R. Craciun, D. R. T. Zahn, Vibrational spectroscopy of bulk and supported manganese oxides, *Phys. Chem. Chem. Phys.* **1** 185–190 (1999).
- [187] B. Siegert, D. Spitzer, M. Comet, Structure and reactivity of CNT/manganese oxide nanocomposites, in: Proceedings of the World Conference on Carbon 2009, Biarritz, FR, 2009.
- [188] F. Goettmann, C. Sanchez, How does confinement affect the catalytic activity of mesoporous materials?, *J. Mater. Chem.* **17** (1) 24–30 (2007).
- [189] R. Ravindra, S. Zhao, H. Gies, R. Winter, Protein encapsulation in mesoporous silicate: The effects of confinement on protein stability, hydration, and volumetric properties, *J. Am. Chem. Soc.* **126** (39) 12224–12225 (2004).
- [190] W. Zhou, J. Vavro, N. M. Nemes, J. E. Fischer, F. Borondics, K. Kamarás, D. B. Tanner, Charge transfer and Fermi level shift in *p*-doped single-walled carbon nanotubes, *Phys. Rev. B* **71** (20) 205423 (2005).
- [191] J. Twu, C.-F. Shih, T.-H. Guo, K.-H. Chen, Raman spectroscopic studies of the thermal decomposition mechanism of ammonium metavanadate, *J. Mater. Chem.* **7** (11) 2273–2277 (1997).
- [192] P. Krawiec, P. L. D. Cola, R. Gläser, J. Weitkamp, C. Weidenthaler, S. Kaskel, Oxide foams for the synthesis of high-surface-area vanadium nitride catalysts, *Adv. Mat.* **18** 505–508 (2006).
- [193] M. Comet, B. Siegert, V. Pichot, D. Hassler, N. Piazzon, D. Spitzer, Phosphorus as reducing agent for thermites, in: Proceedings of the International Pyrotechnic Automotive Safety Symposium (IPASS 2009), Bordeaux, FR, 2009.
- [194] M. Comet, B. Siegert, F. Schnell, V. Pichot, F. Cizek, D. Spitzer, Phosphorus based nanothermites: A new generation of pyrotechnics illustrated by the example of n-CuO / red P mixtures, in: 36th International Pyrotechnics Seminar (IPS), Rotterdam, NL, 2009.
- [195] M. Comet, V. Pichot, B. Siegert, F. Schnell, F. Cizek, D. Spitzer, Phosphorus based nanothermites: A new generation of energetic materials, *J. Phys. Chem. Solids* **71** (2) 64–68 (2009).
- [196] C. Tsang, A. Manthiram, A new route for the synthesis of LiMn₂O₄ cathode: variation of composition, microstructure, and electrochemical behavior with synthesis temperature, *Solid State Ionics* **89** (3–4) 305–312 (1996).
- [197] N. Le Houx, Synthèse d'oxyde de tungstène à tailles ultimes (inférieure à dix nanomètres de diamètre) en vue de l'élaboration et de l'étude de la réactivité de composés nanothermites, Ph.D. thesis, Université de Strasbourg (2010).

Bibliography

- [198] J. N. Israelachvili, *Intermolecular and Surface Forces*, 2nd Edition, Academic Press, Amsterdam, 1992.
- [199] B. W. V. Subramanian, Hongwei Zhu, Synthesis and electrochemical characterizations of amorphous manganese oxide and single walled carbon nanotube composites as supercapacitor electrode materials, *Electrochem. Commun.* **8** 827–832 (2006).
- [200] G.-X. Wang, B.-L. Zhang, Z.-L. Yu, M.-Z. Qu, Manganese oxide/MWNTs composite electrodes for supercapacitors, *Solid State Ionics* **176** 1169–1174 (2005).
- [201] S. V. Rotkin, S. Subramoney (Eds.), *Applied Physics of Carbon Nanotubes: Fundamentals of Theory, Optics and Transport Devices*, Springer, Berlin, Heidelberg, New York, 2005.

Abstract

Nanothermites are versatile pyrotechnic systems composed of an oxidizer, such as a metal oxide, and a fuel, such as aluminum. However, their sensitivity to mechanical stress (especially friction) and electrostatic discharges, which is often very high, restricts their practical use: the thermite reaction may be triggered accidentally, presenting a considerable hazard. Enclosing the metal oxide inside carbon nanotubes (CNT) – thus separating oxidizer and fuel – is a new way to lower the sensitivity of a nanothermite.

In this work, we filled different types of carbon nanotubes with manganese oxides MnO_x ($1.6 < x < 2.0$), chromium(III) oxide, vanadium(IV) and (V) oxide and copper(II) oxide. Different methods for the infiltration of the precursor salts (solution infiltration, molten salt, reactive infiltration) have been used. Before the infiltration, the tubes were opened and/or functionalized with oxygenated functional groups by oxidation; the oxidation kinetics were investigated, and different oxidation methods (nitric acid, air oxidation, filling with molten KOH) were compared.

The resulting nanocomposites are used to prepare reduced-sensitivity nanothermites, in which the oxidizer is replaced by the metal oxide-filled CNTs. Compared to reference formulations without the addition of CNTs, the electrostatic discharge sensitivity of these compositions is decreased by several orders of magnitude, and they are completely insensitive to friction stress. The combustion of the reduced-sensitivity nanothermites is much slower than the one of the reference formulations. Analysis of the combustion residues indicates that aluminum carbide was formed as a secondary combustion product. This work shows a new route for the design of safer pyrotechnic systems.